First Principles Study of Emergent and Technologically Important Materials

Thesis submitted for the degree of

Doctor of Philosophy (Science)

in

Physics (Theoretical)

by

Samir Rom

Department of Physics

University of Calcutta

2024

Contents

Dedication vi

Acknowledgments vii

Abstract ix

List of Publications xi

List of Figures xii

List of Tables xxii

1 Introduction 1

1.1 Material Background and Phenomena 6

1.1.1 Rare-Earth Lean Permanent Magnets 6

1.1.2 Perovskite Oxide Heterostructures 9

1.1.3 Low-Dimensional Materials: Electronic and Structural Transformations 16

1.2 Overview of present thesis 20

2 Methodology 29

2.1 Introduction 29

2.2 The Many Electron Hamiltonian 29

2.3 Density Functional Theory 31

2.3.1 Reduced Density Matrices 32

2.3.2 The Hohenberg-Kohn (HK) Theorems 33

2.3.3 Kohn-Sham Formulation 35

2.3.4 Exchange-Correlation Functional 39

2.4 Beyond DFT Exchange-Correlation: DFT+U 41

2.4.1 Liechtenstein Method: 42

2.4.2 Dudarev Method: 44

2.5 Various DFT-Based First-Principles Methods 44

2.5.1 Methods Using Fixed Basis Sets 44

2.5.2 Methods Using Partial Basis Sets and Muffin-Tin Approximation . . 47
2.5.3 The Projector Augmented Wave (PAW) Method 52
2.6 Wannier Functions 54
2.6.1 NMTO based Wannier functions 54
2.6.2 Maximally localized Wannier functions 55
2.7 Machine Learning 58
2.7.1 Database Construction 59
2.7.2 Data Pre-processing 59
2.7.3 Model Construction 61
2.7.4 Prediction of New Compounds 66

3 Prediction of the Properties of the Rare-Earth Magnets $Ce_2Fe_{17-x}Co_xCN$: A Combined Machine-Learning and Ab Initio Study* **71**
3.1 Introduction and Motivation 71
3.2 Machine Learning Approach 74
3.2.1 Database construction and training of the model 74
3.2.2 Model evaluation 81
3.3 DFT details 84
3.4 Properties of Predicted Compounds 85
3.4.1 Crystal structure 85
3.4.2 Magnetic moment and electronic structure 86
3.4.3 Magnetocrystalline anisotropy 89
3.4.4 Maximal energy product and anisotropy field 92
3.4.5 Stability 93
3.5 Summary and Discussion 94

4 Magnetism and Unconventional Topology in $LaCoO_3/SrIrO_3$ Heterostructure* **107**
4.1 Introduction and Motivation 107
4.2 Computational Methodology 109
4.3 Results 110
4.3.1 Heterostructure in superlattice geometries and interface characteristics 110
4.3.2 Valence and spin states of transition metal ions in superlattice structures 112
4.3.3 Magnetic exchange interactions and interface magnetism 115
4.3.4 Topology in strained tetragonal ferromagnetic $SrIrO_3$ 116
4.4 Summary and Discussion 119

5 Trend in Interfacial Charge Transfer, Emergent Electronic and Magnetic Structure and Topological Properties in the 3d, 5d Superlattices $LaBO_3$/$SrIrO_3$ (B = Mn, Fe, Co, Ni)* **123**

5.1 Introduction and Motivation . . . 123
5.2 Computational Details . . . 126
5.3 Results . . . 128
5.3.1 Charge Transfer in LBO/SIO Superlattices . . . 128
5.3.2 Magnetic Interactions . . . 135
5.3.3 Topological Properties of SIO . . . 136
5.4 Summary and Discussion . . . 138

6 Centrosymmetric-noncentrosymmetric Structural Phase Transition in the Quasi-one-dimensional Compound $(TaSe_4)_3I$* **145**

6.1 Introduction and Motivation . . . 145
6.2 Computational Methodology . . . 148
6.3 Observations from Experimental Studies . . . 149
6.3.1 Structural phase transition (SPT): broken inversion symmetry . . . 149
6.3.2 Confirmation of phase transition at $T_S \simeq 145\ K$ . . . 152
6.4 Theoretical Caculation . . . 154
6.5 Summary and Conclusions . . . 156

7 Observation of superconductivity and Weak Ferromagnetism in Quasi-1D chain compound, $(TaSe_4)_3I$ at Ambient Pressure* **163**

7.1 Introduction and Motivation . . . 163
7.2 Computational Methodology . . . 165
7.3 Observations from Experimental Studies . . . 165
7.3.1 Crystal Structure & Superconducting Transition . . . 166
7.3.2 Ferromagnetism and Meissner Effect . . . 167
7.4 Theoretical Caculation . . . 168
7.5 Summary and Conclusions . . . 172

8 Summary and Outlook **178**

8.1 Summary . . . 178
8.1.1 Chapter 3 : Prediction of the Properties of the Rare-Earth Magnets $Ce_2Fe_{17-x}Co_xCN$: A Combined Machine-Learning and Ab Initio Study . . . 178
8.1.2 Chapter 4 : Magnetism and Unconventional Topology in $LaCoO_3$/$SrIrO_3$ Heterostructure . . . 179

8.1.3 Chapter 5 : Trend in Interfacial Charge Transfer, Emergent Electronic and Magnetic Structure and Topological Properties in the 3d, 5d Superlattices $LaBO_3/SrIrO_3$ (B = Mn, Fe, Co, Ni) 180
8.1.4 Chapter 6 : Centrosymmetric-noncentrosymmetric Structural Phase Transition in the Quasi-one-dimensional Compound $(TaSe_4)_3I$ . . . 181
8.1.5 Chapter 7 : Observation of superconductivity and Weak Ferromagnetism in Quasi-1D Chain Compound, $(TaSe_4)_3I$ at Ambient Pressure 181
8.2 Outlook 182

Dedicated to my family, whose unwavering support
has guided me through this journey.

Acknowledgments

As I reach this significant milestone in my academic journey, I am filled with gratitude for the remarkable individuals who have shaped my path. Completing this dissertation represents not just years of research and dedication, but also the culmination of countless moments of support, guidance, and encouragement from people around me. To everyone who contributed to this achievement-whether through academic mentorship, words of encouragement, or simply being there during challenging times-I want to express my sincere appreciation.

First and foremost, I would like to express my sincere gratitude to my supervisor, Prof. Tanusri Saha-Dasgupta, for her constant support, encouragement, and invaluable guidance throughout my doctoral studies. Her passion for science, problem-solving mindset, and systematic approach to critical challenges have been a source of inspiration for me. I have learned so much from her, including time management, dedication, and perseverance. Her constant support and motivation kept me focused and helped me complete my research within the desired timeframe.

I would also like to thank Prof. Subhro Bhattacharjee, Dr. Santu Baidya, Dr. Anita Halder, Dr. Mintu Mondal, Dr. Atindra Nath Pal, Mr. Aishwaryo Ghosh, and Mr. Arnab Bera for their collaborative efforts and insightful discussions on various projects. Their expertise and contributions were invaluable to my research.

I feel fortunate to have been part of a dynamic research group filled with wonderful colleagues. I am especially thankful to Shiladitya'da, Shreya'di, Aishwaryo, Rajdeep, Koushik, Manoj, Arnab, Prosanta, Sweta, Rima, Arghya'da, Sourav and Arun'da for their companionship and support. I would like to extend special thanks to Shiladitya'da for being an amazing mentor and Aishwaryo for always being there for me, both personally and professionally. Their assistance in sharpening my computational abilities and their constant support in all circumstances are incredibly important to me.

My heartfelt thanks go to S. N. Bose National Centre for Basic Sciences, which has been my second home since I joined the Integrated Ph.D. program in 2017. I am especially grateful to my IPh.D. batchmates - Partha, Shubham, Harmit, Riju, Nivedita, and Manjuri - for their constant support, companionship, and for making my M.Sc. journey truly memorable. The time spent with them, filled with learning, laughter, and shared experiences, will always hold a special place in my heart. I deeply appreciate the institute's support, which provided an excellent environment for learning and research. I extend my gratitude to the administrative and non-teaching staff, especially Abhijit'da and Deblina'di, for their support in resolving computer-related technical problems.

During my time at S. N. Bose, I made wonderful friends who became my family away from home. I will always cherish the memories I created with Kaka, Manodip, Anirban, and Aishwaryo- together, we called ourselves the “fantastic 5”. The moments of happiness we’ve experienced together will forever remain dear to my heart. We enjoyed late-night jamming, deep scientific discussions, and unforgettable trips throughout our Ph.D. journey together. Being like-minded individuals, we naturally understood each other, creating a space where I could share both my good days and tough moments. Each of them brought something special to the group. Kaka, with his sharp intellect and playful humor, could make even the most stressful days feel lighter. In fact, I learned a few computational tools from him along the way. Aishwaryo, calm and thoughtful, always had a wise perspective to offer. Manodip’s relentless dedication to research inspired me to stay focused and driven, while Anirban’s cool-headed, practical approach to life kept us grounded. These friendships made the long Ph.D. journey not just bearable but truly memorable, filling it with joy, laughter, and unhesitating support.

My heartfelt gratitude goes to my seniors here: Ananda’da, Sourav’da, Samiran’da, Mahebub’da, Monalisa’di, Punam’di, Sumanti’di, Joydeep’da, Sasthi’da, Dhiraj’da, Debayan’da, Achintya’da, Sayan’da, Premasish’da, and Tanmoy’da for their priceless mentorship and insightful advice whenever I required assistance. Their experience and advice have been a constant source of support throughout my journey. Special thanks go to Krishnendu and Dibyendu for their prompt and kind assistance with technical challenges related to computational problems. I am truly grateful for the support and encouragement I received from each of them, which played a significant role in making this journey more enriching and manageable.

Special thanks to Sweta for her valuable suggestions, helpful feedback in creating figures. Her insightful comments played a key role in improving my thesis. Her suggestions made the writing process more productive. I am truly grateful for her support throughout this journey.

Lastly, I extend my heartfelt gratitude to my family for their constant support and encouragement throughout this journey. Special thanks to my grandfather, whose kind guidance and wisdom laid the foundation for my educational path - without him, I would not be where I am today. I am deeply grateful to my parents for their endless love, patience, and sacrifices, which kept me motivated even during challenging times. My brother and uncle have also been constant pillars of support, always ready to uplift me with their words of encouragement. Their belief in me has been a driving force in achieving this milestone.

Abstract

This thesis focuses on the study of technologically important materials using first-principles methods, investigating their electronic, magnetic, and topological properties. The materials studied include Ce-based rare-earth lean permanent magnets, oxide perovskite heterostructures, and the quasi-one-dimensional compound $(TaSe_4)_3I$.

To address the challenges of high cost and limited availability of rare-earth elements, we predict the magnetic properties of $Ce_2Fe_{17-x}Co_xCN$ compounds using a combination of machine learning and density functional theory (DFT). Our analysis identifies potential candidates with high transition temperatures, large saturation magnetization, and desirable magnetocrystalline anisotropy, while also assessing their stability through interstitial vacancy formation energies.

For oxide perovskite heterostructures, we study $LaBO_3/SrIrO_3$ superlattices (B = Mn, Fe, Co, Ni) to understand the trends in interfacial charge transfer, electronic structure, magnetic properties, and topology. Our work reveals that for *p*-type superlattices, charge is transferred to the $SrIrO_3$ block in all cases, with the amount of transfer governed by the strength of B-Ir covalency. In *n*-type superlattices, the direction of charge transfer depends on the *d*-orbital occupancy of B. For B = Co and Ni, charge transfers to the $LaBO_3$ layer, leaving $SrIrO_3$ magnetic. In contrast, for B = Mn and Fe, charge transfers to the $SrIrO_3$ layer, making it non-magnetic. The magnetic $SrIrO_3$ layer exhibits a band structure with $C = 2$ double Weyl points, driven by ferromagnetic Ir-Ir exchange and spin-orbit coupling. This results in a significant intrinsic anomalous Hall conductivity (AHC) for $LaCoO_3/SrIrO_3$ and $LaNiO_3/SrIrO_3$. Only *p*-type $LaMnO_3/SrIrO_3$ and $LaFeO_3/SrIrO_3$ exhibit AHC, with the latter suppressed due to proximity effects from the antiferromagnetic $LaFeO_3$ layer.

Finally, we study the quasi-one-dimensional material $(TaSe_4)_3I$, identifying a structural phase transition at $T \sim 145$ K from a high-temperature centrosymmetric to a low-temperature noncentrosymmetric phase. Raman scattering, specific heat, and transport measurements confirm this transition, while first-principles calculations attribute it to the hybridization energy gain from off-center displacements of Ta atoms, overcoming elastic energy costs. At low temperatures, we observed a unique coexistence of superconductivity ($\sim$2.5 K) and weak ferromagnetism ($\sim$9 K), likely arising from Se dimer vacancies. Furthermore, these vacancies induce small localized magnetic moments, which contribute to the unexpected ferromagnetism via the Ruderman-Kittel-Kasuya-Yosida (RKKY) exchange mechanism. While the highly localized magnetic moments form on the vacancy-bearing chains, the vacancy-free chains remain nonmagnetic, though metallic, and sup-

port superconductivity. This leads to an electronic phase separation in the system, with vacancy-bearing chains acting as the source of magnetism and vacancy-free chains supporting phononic superconductivity due to vacancy-induced metallicity.

Our findings provide valuable insights into these systems, offering a platform to explore complex ground states arising from disorder, low dimensionality, and unique electronic structures. The predictions presented here should also guide future experimental efforts to discover materials with tailored and enhanced properties.

List of Publications

1. *"Prediction of the Properties of the Rare-Earth Magnets $Ce_2Fe_{17-x}Co_xCN$: A Combined Machine-Learning and Ab-Initio Study."*, Anita Halder, **Samir Rom**, Aishwaryo Ghosh, Tanusri Saha-Dasgupta, Phys. Rev. Applied 14, 034024 (2020).*

2. *"Machine learning classification of binary semiconductor heterostructures"*, **Samir Rom**[†], Aishwaryo Ghosh[†], Anita Halder[†], and Tanusri Saha Dasgupta, ([†]These authors contributed equally to this work), Phys. Rev. Materials 5, 043801 (2021).

3. *"Magnetism and unconventional topology in $LaCoO_3/SrIrO_3$ heterostructure"*, **Samir Rom**, Santu Baidya, Subhro Bhattacharjee, and Tanusri Saha-Dasgupta, Appl. Phys. Lett. 122, 021602 (2023).*

4. *"Centrosymmetric-noncentrosymmetric structural phase transition in the quasi-one-dimensional compound $(TaSe4)_3I$"*, Arnab Bera[†], **Samir Rom**[†], Suman Kalyan Pradhan, Satyabrata Bera, Sk Kalimuddin, Tanusri Saha-Dasgupta, and Mintu Mondal, ([†]These authors contributed equally to this work), Phys. Rev. B 108, 035112 (2023).*

5. *"Trend in Interfacial Charge Transfer, Emergent Electronic and Magnetic Structure and Topological properties in the 3d, 5d superlattices $LaBO_3/SrIrO_3$ (B = Mn, Fe, Co, Ni)"*, **Samir Rom** and Tanusri Saha Dasgupta, Under Review.*

6. *"Observation of superconductivity and weak ferromagnetism in quasi-1D chain compound, $(TaSe_4)_3I$ at ambient pressure"*, Arnab Bera, Riju Pal[†], Buddhadeb Pal[†], **Samir Rom**[†], Suchanda Mondal[†], Deepti Rana, Aastha Vasdev, Sandeep Howlader, Manish Jana, Tanmay Maiti, Rafikul Ali Saha, Biswajit Das, Tanusri Saha-Dasgupta, Prabhat Mandal, Atindra Nath Pal, Mintu Mondal, ([†]These authors contributed equally to this work), Under Review.*

Publications marked with * are reported in the thesis.

List of Figures

1.1 Estimated distribution of the global market for permanent magnets, valued at around $9 billion. The figure is taken from Ref. [1]. 3
1.2 The energy product and coercivity ranges for various permanent magnet types are illustrated using the same colour code as in Figure 1.1. The stippled patterns represent bonded magnets. The figure is taken from Ref [14]. . 6
1.3 The cost periodic table (as of November 2011), featuring details on the magnetic properties of the elements. The figure is taken from Ref [14]. . . . 8
1.4 Ideal crystal structure of cubic perovskite ABO_3. Small orange spheres represent oxygen atoms, the red sphere represents the A cation, and the B transition metals are located within the blue-grey BO_6 octahedra. 10
1.5 Crystal field splitting in various metal-oxygen polyhedra: (a) octahedral, (b) tetrahedral, (c) trigonal bipyramidal, (d) square pyramidal, (e) square planar, and (f) trigonal. 11
1.6 Illustration of two breathing modes in Jahn-Teller distortion of metal-oxygen octahedra: (a) Q_2 mode and (b) Q_3 mode. 12
1.7 Schematic diagram comparing the shapes of 3d and 4d/5d states in transition metal oxides. The TM 3d states form narrow bands, whereas the TM 4d/5d states form wider bands in TMOs 13
1.8 Electrostatic model showing the polar catastrophe with atomic layers as charged planes based on ionic formal charges (e/θ). The z-axis is along the [001] direction, perpendicular to the surface. The left panel shows a pristine interface and its increasing electrostatic potential, V, with LAO film thickness. The right panel depicts the stabilized system with a transfer of $-0.5e/\theta$ from the surface to the interface. 14
1.9 Summary of research advancements in magnetic oxide interfaces. The unique properties of these interfaces stem from the complex interplay between spin, charge, orbital, and lattice dynamics, as well as other interactions like exchange interactions and charge carriers. This interplay leads to phenomena such as magnetic switching, multiferroicity, magnetic order, magnetoresistance, interfacial magnetic texture, and magnetocrystalline anisotropy. 15

1.10 (a) Conduction band of a one-dimensional crystal where one-electron states with energy $E_k < E_{k_F}$ are filled and those with $E_k > E_{k_F}$ are empty. The boundaries of the first Brillouin zone are given by $\pm a^*/2$. (b) A 1D crystal exhibiting Peierls lattice distortion (PLD) with a period $q = 2k_F$, showing an energy gap (Δ) in the dispersion at $k = \pm k_F$. The figure is taken from [31]. 18

2.1 The iterative process in Density Functional Theory (DFT) to achieve self-consistency. 37
2.2 Diagram illustrating the effect of the Hubbard U parameter on the electronic structure in LDA. The presence of U causes a relative shift between the occupied and unoccupied orbitals. 42
2.3 Comparison of the all-electron (solid line) and pseudo (dashed line) wave-functions and potentials. Beyond the cut-off radius r_c they converge and match. 46
2.4 Schematic representation of the Muffin-Tin (MT) potential, characterized by a spherically symmetric potential inside the MT radius and a constant potential outside. 48
2.5 Schematic representation of the steps that are used in the machine learning algorithm for the screening of stable compounds. 58
2.6 Generation of a bootstrapped dataset through random re-sampling with replacement from the original dataset. 59
2.7 Identification of outliers using a box plot. (a) The interquartile range (IQR) contains 50% of the data and Q2, the median, divides the distribution into two equal halves. (b) The lower and upper whiskers are defined by Q1-1.5×IQR and Q3+1.5×IQR respectively. In a Gaussian distribution, 99.3% of the values fall within this range, leaving only 0.7% as outliers. 60
2.8 Heatmap showing the correlation between different attributes. The colour intensity indicates the strength of the correlation, with grey boxes indicating weak or no correlation and yellow boxes indicating strong correlation. . . . 61

3.1 Steps of a Machine-Learning-Combined DFT Approach for Predictions of Properties in $Ce_2Fe_{17-x}Co_xCN$ Permanent Magnets. 73
3.2 Heatmap indicating the correlation between different attributes considered to built ML algorithm. The color code is shown in the side panel. The boxes with red represent weak or no correlation, whereas blue boxes represent strong correlation between the attributes. 76
3.3 Coefficient of determination R^2 score of five different ML algorithms applied to the T_c dataset. 78

3.4 Model output from RF algorithm for T_c of RE-TM intermetallics. The left panel shows the comparison of T_c obtained from the literature and predicted T_c. The distribution of absolute error between predicted T_c and actual T_c is shown in the upper right panel, while the lower right panel presents the distribution of relative error for the compounds with $T_c > 600$ K. 80

3.5 Normalized confusion matrix for $\mu_0 M_s$ (violet) and K_u (gray) classification using tenfold cross-validation. Here positive (negative) class represents either compounds with $\mu_0 M_s > (<)$ 1 T, or compounds with uniaxial anisotropy, i.e., $K_u > (<)$ 0 MJ/m^3. True positive and negative or TP and TN are the compounds where their classes are predicted correctly. Whereas false positive (FP) and false negative (FN) are the off-diagonal terms of the matrix where the classes are incorrectly classified. 81

3.6 ML predictions of Curie temperature (T_c) from regression model, and saturation magnetization (M_s) and anisotropy constant (K_u) from classification model. The upper (middle/lower) panel shows the results of T_c (M_s/K_u). The exploration set is $Ce_2Fe_{17-x}Co_xC_yN_z$ where y and z can have values either 0 or 1, and $x = 0 \ldots 8$, acronymed as xyz. In the top panel, noninterstitial compounds, carbonated, nitrogenated, and carbonitrogenated compounds are symbolized by circle, diamond, square, and upper triangle. Different colors specify compounds with different x values. The middle panel shows the ML prediction confidence for M_s. In the lower panel, ML prediction confidence for K_u is illustrated. Here the upper (lower) half having bars with no-fill (shaded) shows the confidence for the compounds with positive (negative) K_u. 82

3.7 Crystal structure of $Ce_2Fe_{17-x}Co_xCN$ magnets. The Ce, Fe/Co, and C/N atoms are shown with large, medium, and small balls, respectively. Four transition metal sublattices 9d, 18f, 18h, and 6c are shown in black, green, magenta, and yellow colored balls, respectively. The left panel shows the crystal structure viewed with the c-axis pointed vertically up, and the right panel shows the crystal structure viewed along the c-axis. 85

3.8 Calculated total moment (black circles), $\mu_0 M$ in T plotted for increasing Co concentrations of $Ce_2Fe_{17-x}Co_xCN$ compounds. Experimental results are also shown [19] (red, square) for $Ce_2Fe_{17-x}Co_xN_y$ compounds measured at room temperature. For comparison between $T = 0$ K calculated moments and experimental data measured at room temperature, the experimental data has been scaled by a factor of 1.3. 87

3.9 Calculated spin (top) and orbital (bottom) moments at Ce, Fe(9d), Fe(18f), Fe(18h), Fe(6c), and Co sites in the representative case of $Ce_2Fe_{15}Co_2CN$ compound. 88

3.10 Left: density of states of the $Ce_2Fe_{15}Co_2CN$ compound, projected onto Ce f (brown), Ce d (shaded green), Fe d (blue), Co d (shaded red), and CN p (shaded orange) characters. Right: density of states of the $Ce_2Fe_{15}Co_2CN$ compound projected onto different Fe d's: Fe($9d$) (shaded indigo), Fe($18h$) (magenta), Fe($18f$) (green), and Fe($6c$) (brown). The zero of the energy is set at Fermi energy. 89

3.11 Top: calculated magnetocrystalline anisotropy constant in MJ/m^3 plotted for increasing Co concentrations of $Ce_2Fe_{17-x}Co_xCN$ compounds. The inset shows the anisotropy in orbital moment (see text for details). Bottom: the GGA+U+SOC DOS projected to Ce f energy states with magnetization axis pointed along easy axis, for Ce_2Fe_{17} (black), $Ce_2Fe_{17}CN$ (red), and $Ce_2Fe_{16}CoCN$ (blue). The zero of the energy is set at Fermi energy, with the unoccupied part shown as shaded. The arrow indicates the shift in the occupied part. 91

3.12 Calculated anisotropy field in tesla (left) and maximal energy product in kJ/m^3 (right) plotted for increasing Co concentrations of $Ce_2Fe_{17-x}Co_xCN$ compounds. 93

4.1 Top: Schematic representation of the LCO/SIO superlattice structure on an STO substrate. The n-type interface (IF) formed between the IrO_2 layer of SIO and the LaO layer of LCO is marked, along with the different transition metal-oxygen (TM-O) layers and the magnetic exchanges J_1, J_2, and J_3. Bottom: The distortion of the CoO_6 and IrO_6 octahedra plotted as a function of the layer index for the $m = 4$ superlattice. Distortion is measured in terms of the tilt angle (left axis), representing the deviation of the TM–O–TM bond angle from 180°, and the tetragonal bond distortion (right axis). 111

4.2 (Color Online) The layer-resolved density of states projected onto Co d (left) and Ir d (right) orbitals in the (IF-l) and (IF+l) layers of CoO_2 and IrO_2 in the LCO and SIO blocks of the $(LCO)_{4.5}/(SIO)_{4.5}$ superlattice. The energy zero point is set at the Fermi energy. The octahedral crystal field split t_{2g} and e_g contributions of Co d and Ir d orbitals are marked. 113

4.3 Top: Computed magnetic moment in the CoO_2 layers adjacent to the interface (IF), labeled as IF-1, and the subsequent layer, labeled as IF-2, for various U and J_H values at the Co site. Bottom: Magnetic moment (left axis) and Bader charge (right axis) at the Co and Ir sites, plotted as a function of the layer index for the $m = 4$ LCO/SIO superlattice. The inset shows the electron occupancy of the Ir and Co d levels split by the octahedral crystal field. 114

4.4 (Color Online) Top: Computed magnetic moment in the CoO_2 layers adjacent to the interface (IF-1) and the next layer (IF-2). Bottom: Computed magnetic moment in the IrO_2 layers adjacent to the interface (IF+1) and the next layer (IF + 2) for various values U and J_H at the Co site. 115

4.5 (Color Online) The five different spin configurations considered to estimate the magnetic exchanges. The top panel diagram illustrates the numbering of the Co (blue) and Ir (violet) atoms. The table in the bottom panel presents the energies (in meV) of each configuration, measured relative to the energy of the ferromagnetic configuration. 115

4.6 Top: The GGA + SOC + U band structure of ferromagnetic (FM), tetragonal $SrIrO_3$ (SIO), with in-plane lattice parameters constrained to those of $SrTiO_3$ (STO) (left), plotted along the high-symmetry directions of the tetragonal Brillouin zone (BZ) (right). Bottom: Left—band structure zoomed along $a = (\pi/a, \pi/a, 0.126\pi/c)$, $A = (\pi/a, \pi/a, \pi/c)$, $b = (0.224\pi/a, 0.224\pi/a, \pi/c)$, and the symmetry-related path $a' = (\pi/a, \pi/a, 0.126\pi/c)$, $A' = (\pi/a, \pi/a, \pi/c)$, $b' = (0.224\pi/a, 0.224\pi/a, \pi/c)$, projected onto the Ir d_{xz}/d_{yz} and the O p_x/p_y orbitals. Middle—calculated Chern numbers and Berry curvatures of the two crossings above and below E_F along a–A–b. Right—the same along a'–A'–b'. See the top right panel for the positioning of a, a', b, and b' in the BZ, with Weyl points of positive and negative chirality colored red and blue, respectively. 117

4.7 Illustrations of various Weyl points with different Chern numbers. (a) A conventional spin-$1/2$ Weyl point characterized by a Chern number of ± 1. (b) A quadratic Weyl point, which involves 2 bands and exhibits Chern numbers of ± 2. (c) A spin-1 Weyl point, consisting of 3 bands with Chern numbers of 0 and ± 2. (d) A charge-2 Dirac point involving 4 bands, characterized by Chern numbers of ± 2. In this context, the quadratic Weyl point, spin-1 Weyl point, and charge-2 Dirac point are categorized as double Weyl points. The figure is adapted from [29]. 118

5.1 (a) The chemical constituents of $ABO_3/A'B'O_3$ superlattices explored in this study with A and A′ chosen as lathanide series element, La and alkaline metal Sr, B chosen as 3d TM elements, Mn, Fe, Co, Ni and B′ chosen as 5d TM element, Ir. (b) The d occupancy of B^{3+} cation in LBO and $B'(Ir)^{4+}$ cation in SIO. (c) LBO/SIO superlattice with two symmetric n-type interfaces in the unit cell. (d) LBO/SIO superlattice with two symmetric p-type interfaces in the unit cell. The La, Sr, Ir, 3d TM and O atoms are shown as large-cyan, large-green, medium-dark green, medium-blue and small-brown balls, respectively. 124

5.2 (a) The calculated magnetic moment at Co and Ir sites at different CoO_2/IrO_2 layers of LCO/SIO superlattices with two symmetric n-type (blue symbols) and p-type (red symbols) IFs in the cell. The IF+L layers belong to the SIO block, while the IF-L layers belong to the LCO block. IF is formed in the IrO_2 (CoO_2) layer in the n-type (p-type) geometry. (b) The nominal occupancy of the octahedral crystal field split t_{2g} and e_g levels of Co and Ir in the n-type and p-type IFs after electronic reconstruction. Up and down electrons are shown as up and down arrows. The δ amount of occupancy of Co $d^{6+\delta}$ due to charge transfer in the n-type IF is shown with a red arrow and a closed symbol. The depletion of δ electrons in Ir $d^{5-\delta}$ due to charge transfer in p-type IF is shown with a red arrow and an open symbol. (c) same as (a), but shown for calculated magnetic moment at Ni and Ir sites at different NiO_2/IrO_2 layers of LNO/SIO superlattices. (d) same as (b), but shown for the d occupancy of Ni and Ir. 129

5.3 (a) The calculated magnetic moment at Fe and Ir sites at different FeO_2/IrO_2 layers of LFO/SIO superlattices with two symmetric n-type (blue symbols) and p-type IFs in the unit cell. The color convention and illustration is same as in Fig. 5.2. (b) The nominal occupancy of Fe and Ir octahdedral crystal field split, t_{2g} and e_g states in the n-type and p-type IFs after electronic reconstruction. Conventions same as in Fig. 5.2. (c) same as (a), but shown for calculated magnetic moment at Mn and Ir sites at different MnO_2/IrO_2 layers of LMO/SIO superlattices. (d) same as (b), but shown for the d occupancy of Mn and Ir. 130

5.4 The layer-decomposed density of states projected to Ir d (top) within SIO block and B d (bottom) states within the LBO block of LBO/SIO n-type heterostructures. The numbering of the layers is same as in Figure 5.2 and Figure 5.3. The zero of the energy is set at Fermi level. Marked are the octahedral crystal field split, t_{2g} and e_g states. Panels in (a)-(b), (c)-(d), (e)-(f), and (g)-(h) show the plots for B = Mn, Fe, Co, Ni, respectively. 131

5.5 Same as in Fig 5.4, but plotted for the LBO/SIO p-type superlattices. 132

5.6 Schematic representation of five spin configurations used in GGA+U total energy calculations. (a) Ferromagnetic (FM) state with parallel alignment of spins at B (blue) and Ir (green) sites. (b)–(e) Different antiparallel alignments (FiM1, FiM2, FiM3, FiM4) B and Ir spins in LBO/SIO. The up and down spins are marked with red and orange arrows, respectively. 135

5.7 Calculated anomalous Hall conductivity in LCO/SIO, LNO/SIO and LMO/SIO superlattices. The values for n-type and p-type are shown in blue and orange, respectively. For LMO/SIO, only p-type superlattice is considered, as for n-type the SIO block becomes essentially non-magnetic. The results are LFO/SIO are also not considered due to non-magnetic nature of SIO in n-type case, and heavily suppressed ferromagnetism in p-type case. Inset shows the representative band structure of n-type LCO/SIO projected onto the Ir d_{xz}/d_{yz} (red) and the O p_x/p_y (green) characters along the path a = (π/a, π/a, $0.126\pi/c$) - A = (π/a, π/a, π/c) - b = ($0.224\pi/a$, $0.224\pi/a$, π/c), revealing two linear band crossings (shown in dashed circles) near the high-symmetry A point. 137

6.1 Schematic models of MX_2, MX_3, and MX_4. The Figure is taken from Ref. [23]. 146

6.2 Single crystal XRDs: Structures and Symmetries of $(TaSe_4)_3I$ single crystal. Schematics of the $(TaSe_4)_3I$ crystal structure at (a) $T = 300$ K (RT) and (b) $T = 100$ K (LT). The "Inversion Centre (IC)" points are indicated with star symbols and are present only in the RT structure. Likewise, mirror planes, depicted in light blue, are observed in the RT structure but are absent in the LT structure. For clarity, different inequivalent Ta sites (Ta(1) and Ta(2) at HT and Ta(1), Ta(2), Ta(3) at LT) are displayed in the same color. (c-d) The distribution of the dihedral angles at HT and LT (refer to text for more details). Experimental observations were conducted by Mintu Mondal's group from IACS, Kolkata. 149

6.3 (a) Temperature variation of bond distances among different Ta atoms and (b) dihedral angles. The solid spheres represent experimental data, while thick solid lines are guides to the eye. 151

6.4 Indicators of phase transition in $(TaSe_4)_3I$: (a) Temperature-dependent resistance measurements of wire-like $(TaSe_4)_3I$ samples down to $T \sim 2$ K. The upper inset (dR/dT vs. T plot) identifies the phase transition occurring around 145 K. The lower inset displays a R vs. T^2 plot for the temperature range of 2.5–30 K, with the red solid line representing a linear fit to the data. (b) Specific heat measurements reveal a distinct jump, highlighted in the upper inset, which indicates a phase transition at approximately $T_S \sim$ 145 K. The lower inset shows C_p/T vs. T^2 with linear behavior at low temperatures. (c) Raman spectra obtained from both powder and single-crystal samples at T = 300 K (for both powder and single-crystal samples), T = 100 K (for powder sample), and T = 110 K (for single-crystal sample). The arrows denote the Raman-active modes P_2, P_6, and P_{10} that emerge in the low-temperature samples below the transition. Experimental observations were conducted by Mintu Mondal's group from IACS, Kolkata. 153

6.5 (a) The band structure of $(TaSe_4)_3I$ at high temperature (T=300 K), plotted along the high symmetry k-points in the tetragonal Brillouin zone (BZ). The zero of the energy is set at the Fermi energy. The band "fatness" indicates the orbital characters (red for Ta-d, cyan for Se-p). The inset shows the $TaSe_4$ chain running along the crystallographic c-axis. (b) Comparison of the band structure for low temperature (T=100 K) with that at room temperature (T=300 K). The change in the band gap between the two temperatures is highlighted in the zoomed-in plot. The inset shows the $TaSe_4$ chains, separated by iodine atoms, in the $(TaSe_4)_3I$ structure, projected in the ab plane. 153

6.6 (a) Schematic diagram illustrating the distribution of Ta-Ta bond lengths in the $TaSe_4$ chain for high-temperature (HT) and low-temperature (LT) crystal structures. The inversion center (marked by a dotted line) in the HT structure is disrupted in the LT structure due to the distortion δ. (b) Elastic energy and (c) force acting on Ta ions as a function of off-centric displacement (δ), as obtained from density functional theory (DFT) calculations. . . 155

7.1 Crystal structure & superconducting transition: (a) Oblique view of the simple tetragonal unit cell. (b) Projected view on the *ab*-plane. (c) Lateral view of the linear chains. (d) Quasi-1D structure as seen in high-resolution transmission electron microscopy (HRTEM). Upper inset: Selected area electron diffraction (SAED). Lower inset: Zoomed image showing an inter-chain separation of ≈ 9.4 Å. (e) Temperature dependence of resistance (R) measured using a conventional 4-probe method. The change in slope around 150 K signifies a charge density wave transition in *n*-TSI. Upper inset: Superconducting transition at zero magnetic field. Lower inset: Linear behavior of R *vs.* T^2 in the 5-25 K range, with zero magnetic field. Experimental observations are discussed in detail in the preprint [37]. 166

7.2 (a) Temperature-dependent magnetization data at low field (1.5 mT), showing the Meissner effect below 3 K. (b) Field-cooled (FC) magnetization curve with $H \parallel c$ showing the paramagnetic-to-ferromagnetic phase transition in *n*-TSI. Experimental observations are further detailed in the preprint [37]. 167

7.3 First-principles Study: (a) The defected chain in $(TaSe_4)_3I$ with Se_2 dimer vacancy. Marked are the three inequivalent Ta atoms, Ta_1, Ta_2 and Ta_3, and the long (L), medium (M) and short (S) Ta-Ta bonds. (b) The calculated magnetic moment at the Ta and Se sites of the defected chain. The boxes correspond to Ta and Se layers, shown in (a). (c) The total density of states of the pristine (red) and vacancy bearing (blue) $(TaSe_4)_3I$, showing the semiconducting and metallic nature, respectively. The positive and negative y-axis correspond to density of states in up and down spin channels, respectively. The zero of the energy is set at Fermi level. The *inset* shows the zoomed plot. (d) The reconstructed density of states at Ta_1 (upper panel), Ta_2 (middle panel) and Ta_3 (bottom panel) sites of the defected chain in vacancy bearing structure (red) compared to that in the pristine structure (green dashed line with shading). (e) The plot of spin density in the vacancy bearing $(TaSe_4)_3I$. The isovalue in the plot is chosen as 0.0015 $1/\text{Å}^3$. (f) The density of states of the undefected chains in vacancy bearing $(TaSe_4)_3I$ for increasing concentration of vacancy, 0.46% to 1.38%. 169

7.4 Phonon band structure of pristine *n*-TSI at low temperature, plotted along the high-symmetry directions Γ-X-M-Γ-Z-R-A-M in the Brillouin zone. The absence of imaginary phonon frequencies across the Brillouin zone confirms the dynamic stability of the *n*-TSI structure, indicating that the lattice vibrations are stable and the crystal structure is robust under varying conditions. 171

List of Tables

3.1 List of 13 different attributes with description, notation, and range used in the ML algorithm. Here "CW" stands for "composition-weighted." 77
3.2 Vacancy formation energy for carbon [E_f(C)], nitrogen [E_f(N)], and nitrogen-carbon [E_f(CN)] in eV in $Ce_2Fe_{17-x}Co_xCN$ compounds. 94

5.1 Structural and magnetic properties of the bulk phases of SIO, LMO, LFO, LCO, and LNO. 126
5.2 Charge transfer (ΔQ) for B-site (ΔQ_B) and Ir (ΔQ_{Ir}) in LBO/SIO heterostructures (B = Mn, Fe, Co, Ni) with n-type and p-type interfaces. Positive values indicate electron gain, while negative values indicate electron loss. 135
5.3 B-B (J_1), Ir-Ir (J_2) and B-Ir (J_3) magnetic exchanges in meV for LBO/SIO superlattices. Negative values indicate ferromagnetic coupling, while positive values indicate antiferromagnetic coupling. 136

6.1 SXRD Refinement results for $(TaSe_4)_3I$ at T = 100 K, and 300 K. 152

1

Introduction

Since the dawn of human existence, materials have played a fundamental role in our progress. From the elementary tools of the *Stone Age* to the advanced technologies of today's *Silicon Age*, also known as the *Information Age*, the development of human civilization has been closely linked to the development and use of a wide range of materials. The discovery of new materials has transformed our technologies at every stage of human history. They have not only shaped our societies, but also driven them forward.

The 18th century was the trans-formative era, driven by the exploitation of coal, iron and other resources. It brought extraordinary progress. Steam engines, railways reshaped our society. The 20th was the beginning of the *information age*, fuelled by the discovery of silicon for semiconductors, polymers for plastics and rare earths for electronics. They have revolutionized communications, transport, healthcare and entertainment. We are on the verge of another materials revolution in the 21st century. From lightweight, high-strength materials for the aerospace industry to novel bio-materials for regenerative medicine, materials are at the forefront of sustainability, energy efficiency and human well-being. In short, materials are not just passive elements, they are the very essence of human creativity and progress.

Based on macroscopic behaviour and observable properties, materials have been classified into three main categories: solids, liquids, and gases. Solids are further divided into two main classes: crystalline and amorphous. Crystalline materials have a highly ordered atomic arrangement, with atoms and molecules arranged in a regular, repeating pattern known as a lattice. This long-range order gives rise to characteristic properties such as sharp melting points, well-defined diffraction patterns and an-isotropic properties. In contrast, amorphous materials do not have the long-range order of crystalline structures, but instead have disordered atomic arrangements.

Materials science, a branch of science, has evolved over time to deal with the synthesis, characterization, understanding, and prediction of materials and their properties. It is a multidisciplinary approach that combines physics, chemistry, and engineering to improve

the quality, utility, and cost-effectiveness of materials. This field allows scientists and engineers to explore the fundamental properties of materials while finding ways to design and optimize them for practical applications. Materials science and technology (MST) operates at the interface between science and technology, where the boundaries between the two are often blurred. Although the boundary between the two is sometimes blurred, it is crucial to understand the fundamental difference between the two. Science, in its broadest sense, is the study of the fundamental principles that govern the natural world. Technology, on the other hand, is driven by the practical need to find solutions to the challenges of human adaptation to the environment. In essence, science asks questions and seeks answers, whereas technology addresses problems and provides solutions.

Recently, the concept of designed materials has emerged as a cornerstone of modern materials science. With the increasing demand for energy and the urgent need for cost-effective and environmentally friendly solutions, the development of materials with improved performance and sustainability is becoming increasingly important. This requires a road-map for materials design using computational modelling and simulation. Computer simulation, particularly ab-initio techniques such as Density Functional Theory (DFT) and machine learning (ML), has emerged as a powerful tool in the search for next-generation materials. Researchers can predict and understand the properties of materials with excellent accuracy and efficiency, ranging from semiconductors, rare earth (RE) lean magnets to superconductors and energy storage materials, complementing experimental investigations. By integrating computational modelling, simulation and experimental investigation, it is possible to discover new materials and develop next-generation technologies with major implications for the advancement of society.

In this thesis, we focus on several technologically important materials and provide understanding and predictions using physics concepts. The materials studied in this thesis are:

- Rare-earth lean permanent magnets.
- Perovskite oxide heterostructures.
- Low-dimensional transition metal compounds, specifically the transition metal tetrachalcogenides $(TaSe_4)_3I$.

Below, we describe the technological applications of these materials:

Rare-Earth Lean Permanent Magnets: The field of permanent magnets has undergone a significant evolution over the past six decades, moving from a limited range of applications to becoming an integral component in a diverse array of consumer goods, medical devices, and industrial products. Initially employed in niche applications, magnets

have now become a common component in many household items, though often unnoticed. The revolution in magnetic materials has been the primary driver of this evolution, resulting in a dramatic increase in the number of households owning magnets. Today, they are primarily used in electromagnetic energy conversion devices, including motors, actuators and generators, and computer hard-disk drives. This widespread use has led to the average middle-class family owning hundreds of magnets, a significant increase from just a few decades ago. Traditional magnets, like $SmCo_5$ and $Nd_2Fe_{14}B$, rely heavily on rare-earth (RE) elements. Due to the scarcity of RE elements like Nd and Sm, there's a push to develop alternatives with lower RE content. Researchers are working to enhance performance, lower costs, and discover sustainable substitutes for rare earth elements to ensure the ongoing advancement of magnet technology. Figure 1.1 presents an estimate of the distribution of magnet production by market value.

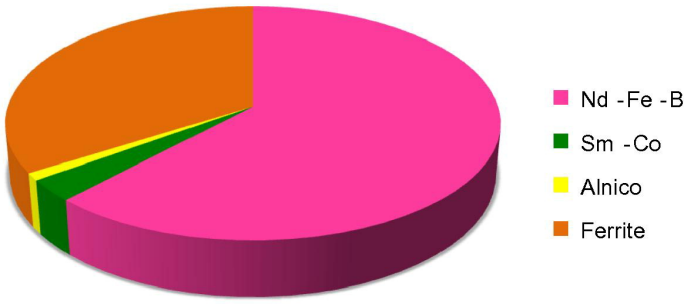

Figure 1.1: *Estimated distribution of the global market for permanent magnets, valued at around $9 billion. The figure is taken from Ref. [1].*

Perovskite Oxide Heterostructures:

Perovskite Oxides

Perovskite structure (ABO_3) allows compositional flexibility, as we can incorporate different elements into the A and B sites, leading to a rich variety of materials with tailored properties. The transition metals in the perovskite compounds exhibit multiple oxidation states, which in turn influence the properties of the materials. One of the most important properties of perovskite compounds is their ability to exhibit ferroelectricity. For example, $BaTiO_3$ (barium titanate) has a spontaneous electrical polarization that can be controlled by an external electric field, leading to applications in memory devices, capacitors and piezoelectric sensors. Perovskite materials also exhibit all possible magnetic orders, including ferromagnetism, antiferromagnetism and ferrimagnetism. For example, $LaMnO_3$ (lanthanum manganite) exhibits colossal magnetoresistance, a phenomenon where the electrical resistance of the material changes with the external magnetic field, leading to applications in magnetic sensors and data storage devices. Another aspect of these types of materials is

their potential for high temperature superconductivity. In particular, copper-based (cuprate) perovskites exhibit zero electrical resistance below a certain critical temperature, leading to applications in magnetic levitation, MRI machines and efficient power transmission. There are also some organic-inorganic hybrid perovskites, such as methylammonium lead iodide ($MAPbI_3$), which are revolutionizing solar cell technology due to their high absorption coefficients and tunable band gaps, leading to sustainable energy solutions. In addition, we can now design heterostructures with different perovskite layers by stacking them to create the interface with novel properties. These heterostructures can exhibit enhanced functionalities such as charge transfer, strain effects, orbital reconstruction and topological properties. They are now at the forefront of research in electronics, spintronics and quantum computing.

Oxide Heterostructures

Herbert Kroemer's Nobel address, "The interface is the device," [2] is particularly relevant to correlated oxides as well. Controlling the interface is crucial for these materials, whether in terms of atomic structure, magnetism, orbital states, or potential gradients. Transition metal oxides (TMOs) exhibit a variety of electronic orders, including charge, spin, and orbital orders. At interfaces, these orders interact through processes like charge transfer, hybridization, and spin/orbital exchange, leading to unique emergent properties. Potential research outcomes for oxide interfaces include:

- **Mottronics**: Electronic functions emerging from the Mott transition, such as the metal-insulator transition in correlated-electron systems. This can lead to resistive switching memory functions for applications like resistance random-access memory (ReRAM) [3].

- **Orbitronics**: Controlling the orbital state of d-electrons can significantly alter magnetic, transport, and optical properties. Research is focusing on electric-field control or current switching of orbital states at interfaces, with potential applications in high-temperature superconductivity [4, 5].

- **Spintronics**: Modulating d-electron magnetism at interfaces can lead to spintronic functions. Despite challenges like degradation of tunneling magneto-resistance (TMR) characteristics at high temperatures, controlling toroidal moments through gate electric fields could result in new magneto-electric functions.

- **Relativistic-electronics**: Utilizing the relativistic spin-orbit interaction (SOI) in TMOs, such as in Sr_2IrO_4, where spin-orbit splitting is significant [6]. This can lead to magneto-electric coupling in spin transistors [7] and the spin-galvanic effect [8, 9]

Future research may also explore topological phenomena like the quantized anomalous Hall effect [10] and the quantum spin Hall effect in oxide interfaces [11, 12]. Advances in experimental techniques are expected to enhance the preparation and probing of these interface electronic states.

Low-Dimensional Materials:

Low-dimensional materials offer a wide range of applications in different fields. Researchers are developing products that use these materials for numerous technical purposes. These materials include two-dimensional (2D) systems like graphene and transition metal dichalcogenides (TMDs), and one-dimensional (1D) systems like carbon nanotubes and nanowires. The reduced thickness of low-dimensional materials allows for the development of unique properties and potential applications, particularly in the fields of energy storage and next-generation electronics.

Features and Applications:

- Low-dimensional materials have a high surface area relative to their volume, making them perfect for uses where a large surface-to-volume ratio is important, like in batteries and supercapacitors for energy storage.
- These materials have outstanding mechanical and electrical qualities. For instance, graphene is well-known for its incredible strength and excellent electrical conductivity.
- Low dimensionality can lead to quantum effects, allowing the exploitation of quantum properties such as quantum confinement and tunneling. This can lead to new phenomena and applications.
- Nanomaterials, for example, have a wide range of applications in fields as diverse as energy storage, electronics, medicine and optics. They are used in advanced batteries, solar cells, medical diagnostics and treatments, light-emitting devices such as LEDs and OLEDs, and even in aerospace and defence technologies for their exceptional mechanical and electrical properties.

Low-dimensional materials are leading a new wave in materials science. As research progresses, we can expect more innovative discoveries and applications, highlighting the importance of these remarkable materials in our everyday lives.

1.1 Material Background and Phenomena

1.1.1 Rare-Earth Lean Permanent Magnets

In the 1950s, significant advancements in the Netherlands revolutionized the production of hard magnetic materials, enabling them to be manufactured in any shape without the risk of self-demagnetization. This innovation marked a major shift from the conventional bar and horseshoe magnets, which were specifically designed to minimize self-demagnetizing fields. An understanding of hard magnets is dependent upon the concept of a hysteresis loop, which describes the relationship between magnetization (M) and magnetic field (H). Ideal permanent magnets are identified by a square or rectangular hysteresis loop, indicative of high coercivity and remanent magnetization. Magnetic materials can be categorized into several types based on their compositions, which will be outlined briefly as follows:

Alnico Permanent Magnets

Alnico magnets are primarily composed of aluminium (Al), nickel (Ni) and cobalt (Co), with iron (Fe) and sometimes other elements such as copper (Cu) and titanium (Ti), and are known for their strong magnetic fields and high coercivity. There are several types, depending on the weight percentage of the constituents. They were the strongest permanent magnets before the advent of RE magnets in 1970. Alnico magnets can generate magnetic fields of up to 0.15 T, with a remanence field of up to 1.2 T [13]. Figure 1.2 illustrates the range of energy product and coercivity for the primary magnets produced in the present days. They have a high Curie temperature of about 850°C, but the maximum working temperature is about 550°C [13].

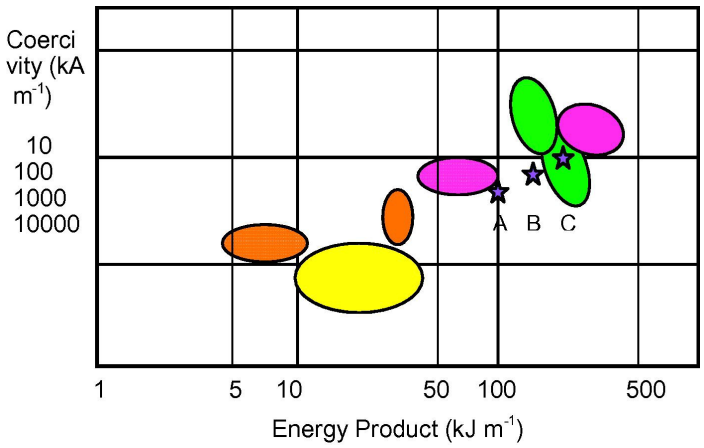

Figure 1.2: *The energy product and coercivity ranges for various permanent magnet types are illustrated using the same colour code as in Figure 1.1. The stippled patterns represent bonded magnets. The figure is taken from Ref [14].*

Ceramic (Ferrite) Permanent Magnets

Ceramic (ferrite) magnets are made from iron oxide (Fe_2O_3) and strontium carbonate. They have high coercivity and high remanence as describe in Figure 1.2 after magnetization and can produce a magnetic field of about 0.35 T, which is lower than RE magnets, and are quite brittle, they can break if dropped on a hard surface. The Curie temperature is 450°C and can be operated up to 400°C [15]. They are inexpensive and easy to produce, making them widely used despite their lower energy product.

Rare-Earth (RE) Permanent Magnets

The term "rare earth" (RE) refers to a group of 14 similar metallic elements in the lanthanide series, ranging from atomic numbers 58 to 71 (Ce to Lu). These elements, discovered between 1787 and the 1940s, all occur naturally with the exception of promethium (Pm). Due to structural similarities, scandium (Sc), yttrium (Y) and lanthanum (La) are also considered to belong to this group. Lanthanides have similar outer electron configurations and valence electrons, leading to uniform behaviour in metal combinations. However, their physical properties vary considerably and are influenced by the number of electrons in the 4f shell, which affects spin and orbital moments.

For a material to qualify as a permanent magnet, the hardness parameter κ must exceed one [16, 17]. This criterion is expressed mathematically as $\kappa = \left(\frac{K}{\mu_0 M_s^2}\right)^{1/2} > 1$, which means that K must be greater than $\mu_0 M_s^2$ and should exceed 2 MJ/m^3. Achieving such high K values requires magnetocrystalline anisotropy resulting from spin-orbit coupling. The highest anisotropy possible by shaping nanoscale magnetized regions, as is done with Alnico [18], is only a quarter of this value. Significant spin-orbit coupling requires the incorporation of heavy elements from the 4d, 5d or 4f series [17]. These elements are expensive, as shown in the cost periodic table in Figure 1.3.

Rare earth (RE) magnets are powerful permanent magnets made from rare earth alloys. These magnets generate much stronger magnetic fields than ceramic or alnico magnets, typically around 1.2 T compared to the 0.5 to 1 T range for ceramic magnets. However, they are extremely brittle and prone to corrosion and typically require protective coatings to prevent damage. There are two main types of RE magnets: neodymium ($Nd_2Fe_{14}B$) and samarium cobalt ($SmCo_5$). Rare earths (lanthanides) are ferromagnetic metals like iron (Fe), but their Curie temperature is below room temperature. When combined with transition metals (TM) such as iron (Fe), nickel (Ni) and cobalt (Co), they form compounds with Curie temperatures well above room temperature. These compounds are used to make permanent RE magnets. The strength of RE magnets is due to two main factors. First, their crystalline structure provides high magnetic anisotropy, resulting in high coercivity. Sec-

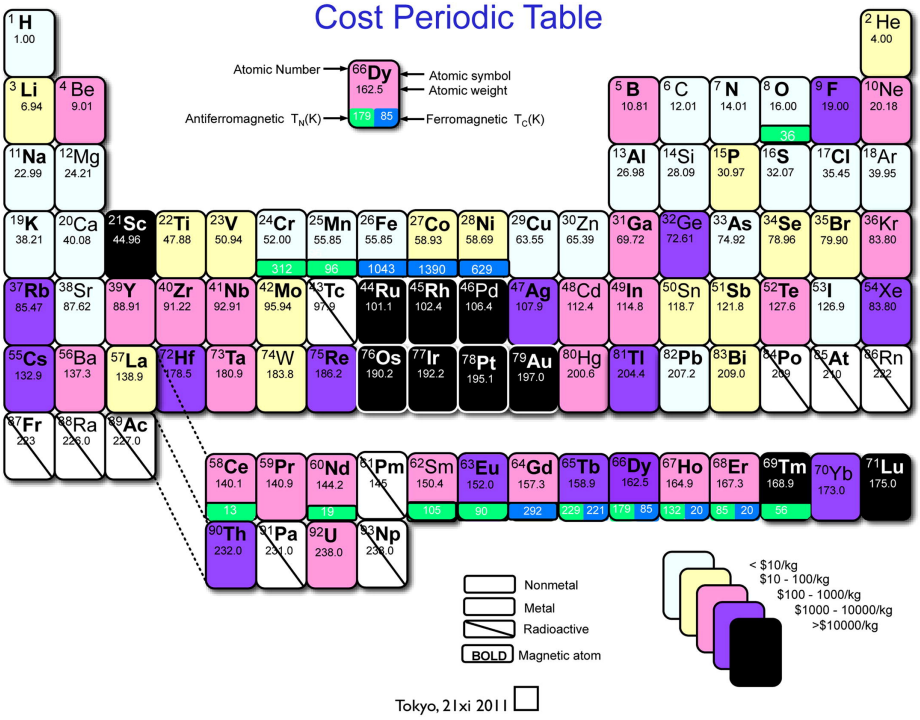

Figure 1.3: *The cost periodic table (as of November 2011), featuring details on the magnetic properties of the elements. The figure is taken from Ref [14].*

ond, rare earth atoms have high magnetic moments due to the many unpaired electrons in their electronic structure, resulting in high remanence. This gives RE magnets a high magnetic energy product, making them much stronger than conventional magnets as depicted in Figure 1.2.

The other key properties to consider when comparing permanent magnets are: remanence (B_r), which indicates the strength of the magnetic field; coercivity (H_{ci}), which measures the resistance to demagnetization; maximum energy product (B-H_{max}), which indicates the magnetic energy density; and Curie temperature (T_c), the point at which magnetism is lost. Rare earth (RE) magnets, such as neodymium ($Nd_2Fe_{14}B$) and samarium-cobalt ($SmCo_5$), typically exhibit superior performance in terms of remanence, coercivity, and energy product. However, it is important to note that $Nd_2Fe_{14}B$ has a relatively lower Curie temperature in comparison to other permanent magnets.

The compounds formed with RE and 3d TM elements have attracted considerable attention. The discovery of giant magnetoresistance and giant magnetocaloric effect [19] in RE intermetallics has increased interest in exploring the magnetic properties of various RE-based compounds and alloys. These magnetic properties are mainly controlled by the delicate balance between Ruddermann-Kittel-Kasuay-Yosida (RKKY) [20] exchange interactions and magnetocrystalline anisotropy [21]. This work focuses on RE-TM intermetallic compounds. In these compounds there are mainly three types of magnetic interactions, which include the RE-RE, TM-TM and RE-TM interactions. The RE-TM interaction is one

of the strongest among them, arising from the RKKY type indirect interaction. The TM-TM interaction arises from the strong overlap between the TM-3d wavefunctions, leading to the formation of energy bands and effective exchange interactions. The magnetic behaviour of RE-TM compounds depends on the coupling between the RE and TM sublattices, with heavy RE elements showing antiparallel coupling and light RE elements showing parallel coupling.

Rare-Earth (RE) Lean Permanent Magnets

The high cost of RE magnets has limited their use to cases where both compact size and high magnetic field strength are essential. This motivates the need for RE lean permanent magnets for sustainable development and the advancement of green technologies, including electric vehicles and renewable energy systems. Traditional permanent magnets such as $Nd_2Fe_{14}B$, $SmCo_5$ are composed of rare earth elements such as neodymium (Nd), samarium (Sm) to achieve high magnetic performance. However, rare earth elements are not only expensive, but also face environmental and geopolitical challenges. To address these issues, researchers have focused on developing RE lean or free permanent magnets that can provide comparable magnetic properties. In this work, we have predicted some rare earth lean magnets, specifically $Ce_2Fe_{17-x}Co_xCN$, using a combination of machine learning and first-principles calculations. The ability to predict and improve their magnetic properties using a combination of machine learning and first-principles calculations has significant implications for their practical use.

1.1.2 Perovskite Oxide Heterostructures

Perovskite Oxides

Perovskite compounds derive their name from the mineral perovskite, $CaTiO_3$, first discovered by Gustav Rose in Russia in 1839 and named in honour of the Russian mineralogist Lev Perovski. These materials have a crystal structure represented by the formula ABO_3, where A is either a rare earth or alkaline earth metal, B is a transition metal and O is oxygen. In a simplified cubic unit cell of such a compound, the 'A' atom occupies the cube corner position (0, 0, 0), the 'B' atom is at the body centre position (1/2, 1/2, 1/2) and the oxygen atoms are at the face centred positions (1/2, 1/2, 0), (1/2, 0, 1/2) and (0, 1/2, 1/2). The ideal form of perovskite can be described as an array of BO_6 octahedra with shared corners, as shown in Figure 1.4. And in this ideal form, the stable structural form is cubic with <B-O-B angle of 180°, but most of them are distorted and this angle deviates from 180°. One of the key dimensionless parameters used to quantify the stability and degree of distortion in perovskites is the Goldschmidt tolerance factor (t). This tolerance factor can

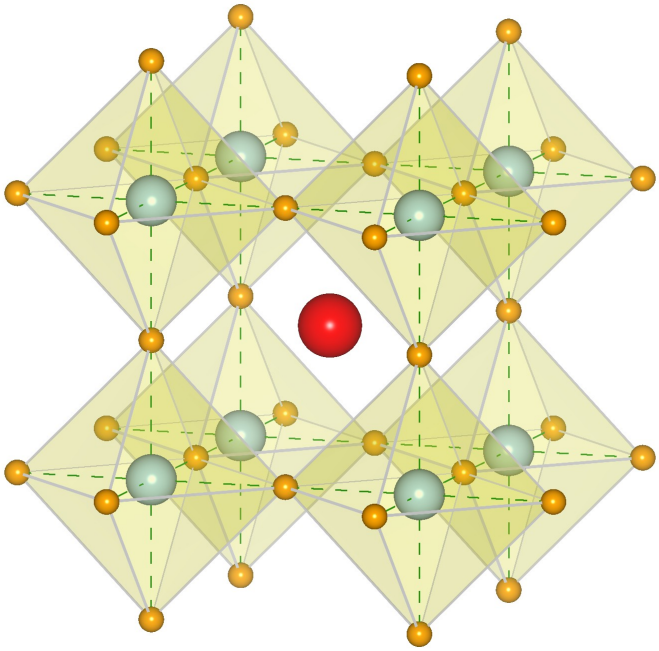

Figure 1.4: *Ideal crystal structure of cubic perovskite ABO_3. Small orange spheres represent oxygen atoms, the red sphere represents the A cation, and the B transition metals are located within the blue-grey BO_6 octahedra.*

be calculated from the ratio of the ionic radii of the constituent ions and is given by the formula:

$$t = \frac{r_A + r_O}{\sqrt{2}(r_B + r_O)} \tag{1.1.1}$$

The ionic radii of the A and B cations are denoted as r_A and r_B, respectively, while r_O represents the ionic radius of the oxygen anion. The perovskite structure is ideally cubic when the value of t is equal to or close to 1, but when it is less than 1, it tends to tilt and rotate the BO_6 octahedra, leading to different distortions such as orthorhombic or rhombohedral phases. The compounds with t>1 are generally found to have hexagonal symmetry.

The metal-oxygen polyhedra (BO_n) are key to their properties, with different shapes affecting the crystal field splitting, which is influenced by the geometry of the oxygen polyhedra and the TM-O covalency strength. These polyhedra can take various forms such as octahedra, square pyramids, square planar configurations, tetrahedra, pentagonal bipyramids and trigonal bipyramids etc. In these materials, the surrounding oxygen tends to have a negative valence and removes the s-electrons from the TM atoms, thereby subjecting the d-orbitals of the TM ions to an anisotropic field known as the crystal field. This interaction causes the initially degenerate d orbitals to split, and this splitting depends on the geometry of the oxygen polyhedra, which is known as crystal field splitting (see Figure 1.5).

The spatial arrangement of the oxygen atoms determines how the d-orbitals interact with these oxygen atoms. For example, in a perfect octahedral geometry the d orbitals split

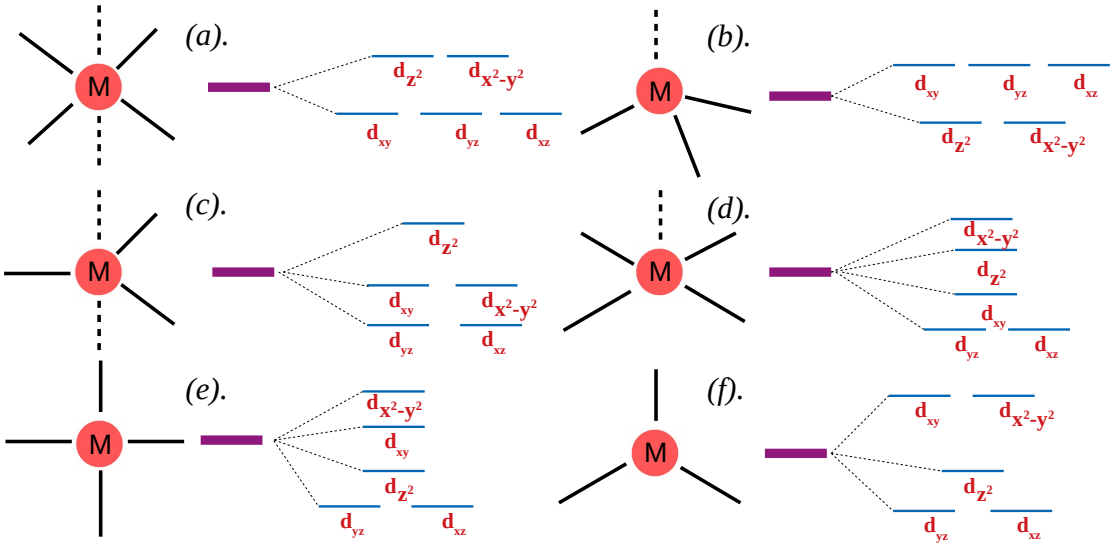

Figure 1.5: *Crystal field splitting in various metal-oxygen polyhedra: (a) octahedral, (b) tetrahedral, (c) trigonal bipyramidal, (d) square pyramidal, (e) square planar, and (f) trigonal.*

into two sets: the lower energy t_{2g} orbitals (d_{xy}, d_{yz}, d_{xz}) and the higher energy e_g orbitals (d_{z^2}, $d_{x^2-y^2}$). The electrons in the e_g orbitals experience strong electrostatic repulsion as the lobes of the e_g orbitals point directly at the oxygen atoms and gain energy as a result. On the other hand, the lobes of the t_{2g} orbitals do not point directly at the oxygen atoms, but between two atoms. When the e_g orbitals are partially occupied, they tend to lower the energy by removing the degeneracy through the octahedral distortion, known as the Jahn-Teller effect. This results in a lower symmetry structure which is more stable. The Jahn-Teller distortions can be described using normal mode coordinates, specifically the Q_2 and Q_3 modes as shown in Figure 1.6, which represent different types of distortion in an octahedral geometry. The Q_2 and Q_3 modes can be described as follows:

Q_2 mode: When the octahedron goes into Q_2 mode, the distortion changes the geometry of the octahedron equally along all three axes. It changes the energy level of both e_g orbitals equally, thus lifting the degeneracy by changing the overall symmetry and reducing the degeneracy.

Q_3 mode: When the octahedron undergoes Q_3 mode distortion, the geometry changes from a perfect octahedron to an elongated or compressed form. In this type of distortion, the elongation is along one axis and the compression is along the perpendicular axis. For example, if the elongation happens along the z-axis, the d_{z^2} orbital (which points directly towards the z-axis) will decrease in energy, while the $d_{x^2-y^2}$ orbital (which lies in the xy-plane) will increase in energy. This removes the degeneracy of the e_g orbitals.

The Jahn-Teller effect, named after Hermann Jahn and Edward Teller, provides a mechanism for removing degeneracies in the d-orbitals of transition metal compounds by distort-

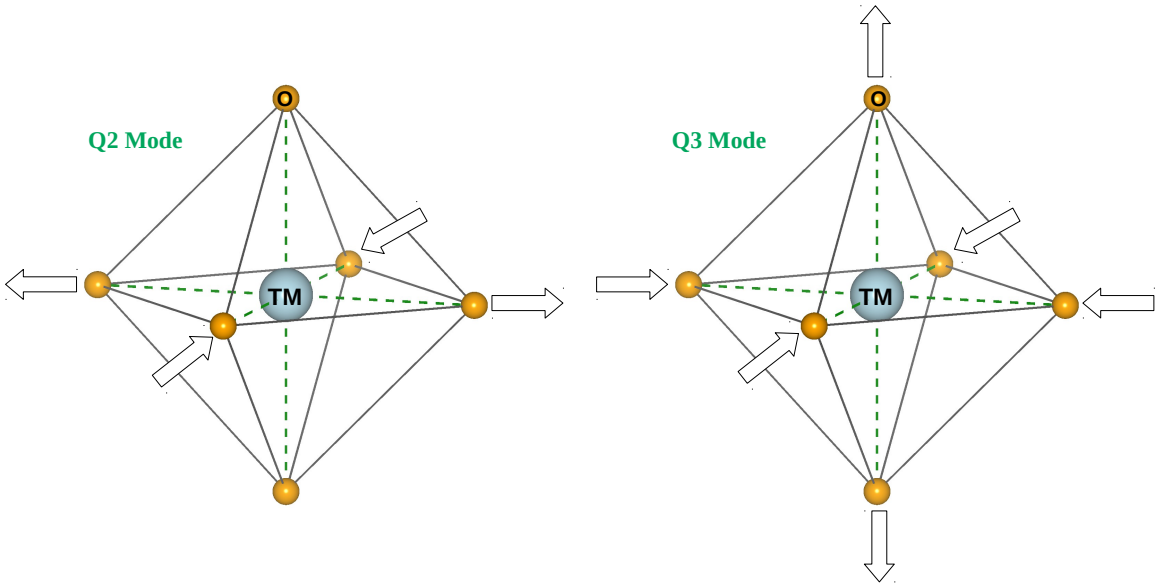

Figure 1.6: *Illustration of two breathing modes in Jahn-Teller distortion of metal-oxygen octahedra: (a) Q_2 mode and (b) Q_3 mode.*

ing their geometric configuration. In contrast, a tetrahedral arrangement gives an inverse splitting pattern in the lower and higher energy levels. This splitting also depends on the strength of the covalent bond between the transition metal and oxygen atoms. The covalency depends on several factors such as the length of the bond, the overlap between the d-orbitals of the TM atom and the p-orbitals of the oxygen atoms, and the electronegativity of the TM and O atoms. The crystal field splitting depends on several other things such as the oxidation state of the metal ions, the presence of other ligands with oxygen can also modify the crystal field effects.

In TMOs, the electronic configuration of the TM sites plays an important role in determining their properties. Coulomb repulsion tries to localize the TM d electrons at the lattice sites, while hybridization between TM d and oxygen p states tries to delocalize them. In 3d TMOs the direct overlap between TM d orbitals is very small as shown in Figure 1.7, resulting in a small bandwidth, so the d electrons move only by hybridization with oxygen 2p bands. The physics is primarily governed by three different energy scales: the charge transfer energy (Δ), which is the energy difference between TM d and O p states, the electron-electron correlation (U_{dd}) within the TM d manifold, and the hopping parameter (t_{pd}) connecting the metal and oxygen sites. For 4d and 5d TMOs the situation is different. The band widths of the TM d states in the case of 4d and 5d TMOs are much wider compared to that of 3d TMOs as shown in Figure 1.7. In addition, 4d and 5d TMOs exhibit significant spin-orbit coupling (SOC), which is defined as the coupling between the intrinsic spin of the electron and its orbital angular momentum. While SOC is considered a weak perturbation in 3d TMOs, it becomes important for heavy elements. Therefore, 4d

and 5d TMOs are good candidates to show a larger SOC effect than 3d TMOs. The SOC becomes comparable to other energy scales such as the electron-electron correlation (U_{dd}). As a result, there is a competition between the two, leading to new emergent properties in 4d and 5d TMOs.

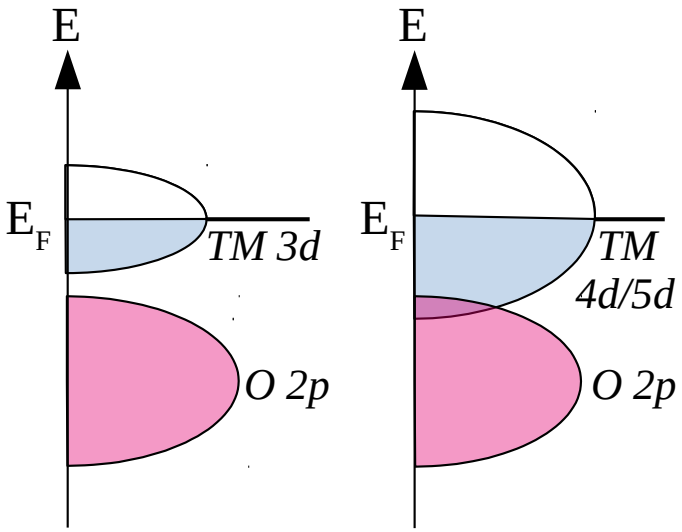

Figure 1.7: *Schematic diagram comparing the shapes of 3d and 4d/5d states in transition metal oxides. The TM 3d states form narrow bands, whereas the TM 4d/5d states form wider bands in TMOs*

This competition also affects the spin states of the TM ions. TM ions can exhibit high spin (HS), intermediate spin (IS) and low spin (LS) states, depending on the balance between the crystal field splitting (Δ) and Hund's coupling energy (J_H). The 3d TMOs generally favour the HS state due to significant electron-electron correlation, although there are many examples of LS states, especially in the case of late 3d TMOs. In contrast, the 4d and 5d TMOs are generally found in the LS state due to the significant crystal field splitting (Δ) and substantial SOC compared to 3d TMOs. For example, in $SrIrO_3$, Ir^{4+} (d^5) stabilizes in the LS state.

Perovskite Oxide-Based Heterostructures

Oxide interfaces have attracted considerable attention due to their novel properties such as ferromagnetism, large negative magnetoresistance, giant photoconductivity, electrical conductivity, superconductivity and topological phenomena that are absent in their bulk parent compounds. These properties suggest potential applications in oxide-based electronics and spintronic devices. Advances in experimental techniques such as molecular beam epitaxy (MBE) and pulsed laser deposition (PLD) have enabled the precise layer-by-layer growth of perovskite oxides, leading to the creation of oxide heterostructures. In particular, the $LaAlO_3$ (LAO) / $SrTiO_3$ (STO) heterostructure has emerged as a model system, exhibiting

unexpected properties such as conductivity, magnetism and superconductivity. The pioneering work of Ohtomo and Hwang revealed the formation of a high carrier density and high mobility electron gas (2DEG) at the interface of these two non-magnetic band insulators.

Two distinct interfaces can form in the [001] direction between the polar $LaAlO_3$ (LAO), composed of alternating $(LaO)^{+1}$ and $(AlO_2)^{-1}$ layers, and the nonpolar $SrTiO_3$ (STO), composed of $(SrO)^0$ and $(TiO_2)^0$ layers. These interfaces are classified as n-type (LaO/TiO_2) and p-type (AlO_2/SrO). Conductivity is only observed at n-type interfaces when the LAO thickness exceeds three unit cells (uc). In contrast, magnetism is found both at n-type interfaces with LAO thicknesses greater than 3 uc and at insulating p-type interfaces. There is currently no single mechanism that fully explains these phenomena for the LAO/STO system, which has led to extensive research. Four main mechanisms have been proposed to explain the formation of the two-dimensional electron gas (2DEG) at the n-type interface. The most widely accepted is intrinsic electronic reconstruction, also known as polar catastrophe as shown in Figure 1.8, which involves the ionization of the host valence band of LAO at abrupt, defect-free interfaces. The other three mechanisms involve various types of defects: oxygen vacancies at the interface and at the LAO overlayer surface, and intermixing of cations, specifically La-on-Sr antisite donor defects.

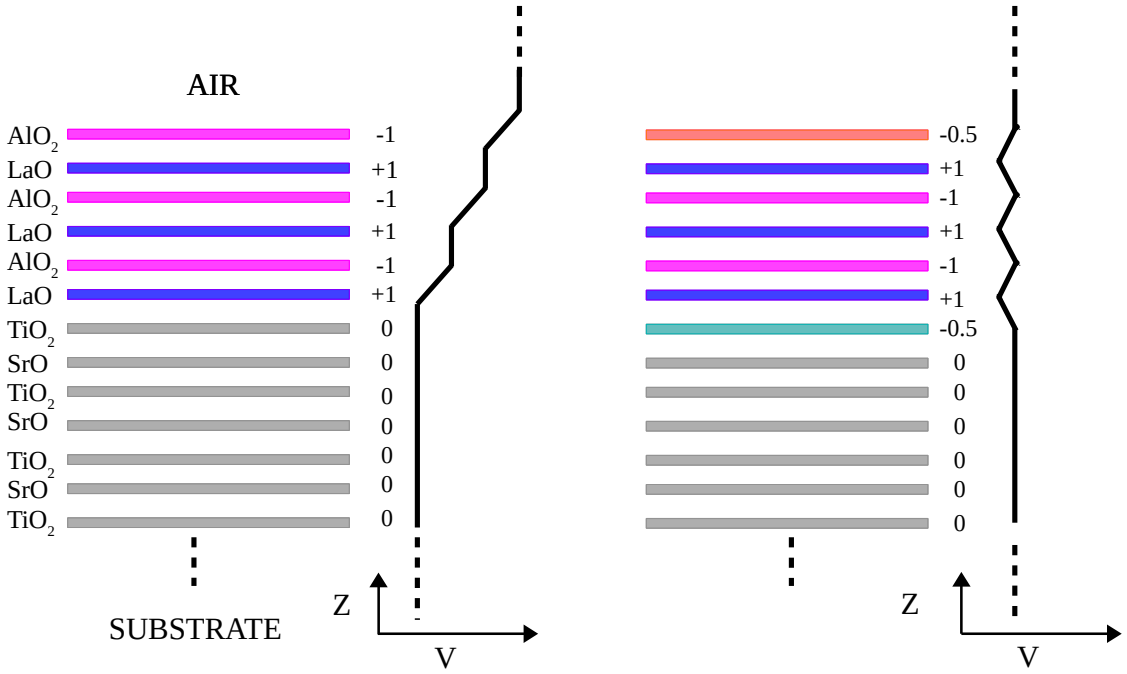

Figure 1.8: *Electrostatic model showing the polar catastrophe with atomic layers as charged planes based on ionic formal charges (e/θ). The z-axis is along the [001] direction, perpendicular to the surface. The left panel shows a pristine interface and its increasing electrostatic potential, V, with LAO film thickness. The right panel depicts the stabilized system with a transfer of $-0.5e/\theta$ from the surface to the interface.*

Various interfaces between Mott insulators and band insulators, or between Jahn-Teller

insulators and band insulators can be explored to see how the properties of these interfaces change. Sevaral interfaces exhibiting either conducting or insulating behaviour have been identified. Some of the conducting interfaces include $LaTiO_3$ (LTO) / STO, $LaGaO_3$ (LGO) / STO, $LaVO_3$ (LVO) / STO, $GdTiO_3$ (GTO) / STO, $GdAlO_3$ (GAO) / STO, $NdGaO_3$ (NGO) / STO, $NdAlO_3$ (NAO) / STO, Al_2O_3 / STO, $DyScO_3$ (DSO) / STO, $KTaO_3$ (KTO) / STO. On the other hand, insulating interfaces include $LaMnO_3$ (LMO) / $SrTiO_3$ (STO), $LaYO_3$ (LYO) / STO, $LaCrO_3$ (LCO) / STO, $EuAlO_3$ (EAO) / STO etc.

A key challenge in understanding the phenomena in oxide heterostructures is uncovering how they deal with the polar discontinuity at the interface. Unlike polar semiconductor interfaces, transition metal oxides (TMOs) offer more complex methods to compensate for valence mismatches, such as electronic reconstruction seen in the LAO/STO interface. Ab initio calculations, particularly density functional theory (DFT), have significantly enhanced our understanding of these phenomena by addressing the electronic structure and compensation mechanisms in these heterostructures.

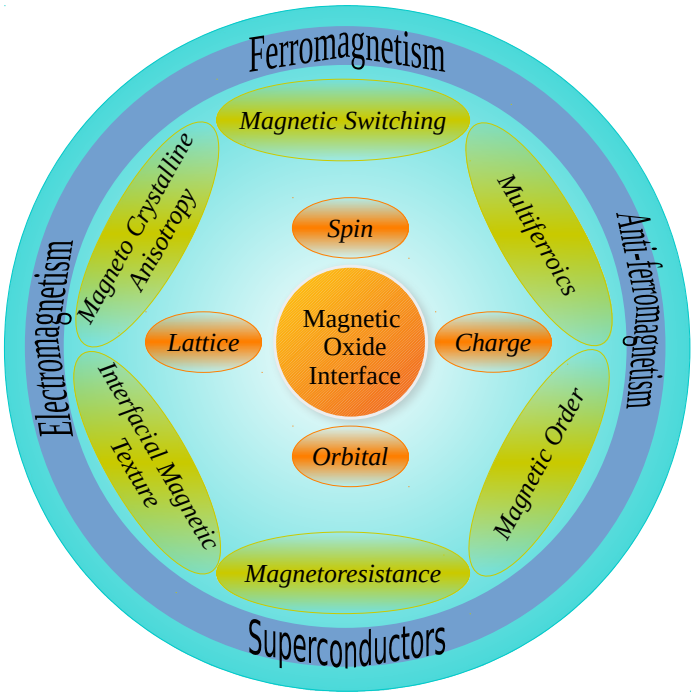

Figure 1.9: *Summary of research advancements in magnetic oxide interfaces. The unique properties of these interfaces stem from the complex interplay between spin, charge, orbital, and lattice dynamics, as well as other interactions like exchange interactions and charge carriers. This interplay leads to phenomena such as magnetic switching, multiferroicity, magnetic order, magnetoresistance, interfacial magnetic texture, and magnetocrystalline anisotropy.*

Since the 2016 Nobel Prize in Physics, the concept of 'topology' has gained considerable attention in the study of correlated electron systems. Topology describes the electronic or magnetic states with invariants preserved under the continuous transformations in a given

space, providing robustness against any perturbations, making it ideal for data storage and processing. The interplay between charge, spin, orbital and lattice degrees of freedom greatly enhances the representation of quantum phenomena at oxide interfaces. This has led to the exploration of diverse features such as Hall effect, multiferroicity, magnetoresistance, magnetocrystalline anisotropy, magnetic switching, magnetic order, interfacial magnetic texture as shown in Figure 1.9. In particular, the interfacial magnetic textures and topological properties remain underexplored. Another phenomenon based on topology and geometry is the Anomalous Hall Effect (AHE). AHE occurs in solids with broken time-reversal symmetry, such as ferromagnets, due to spin-orbit coupling (SOC). This effect is of significant technological interest for potential applications in spintronics, including magnetic sensors and memory devices. An example of engineered electronic and magnetic properties at 3d-5d interfaces is the interface between the 3d antiferromagnetic insulator $SrMnO_3$ (SMO) and the 5d paramagnetic metal $SrIrO_3$ (SIO). Charge transfer from SIO to SMO leads to strong ferromagnetism at the interface. This ferromagnetism gives rise to AHE in the SIO/SMO superlattice. Density functional calculation of the anomalous Hall conductivity (AHC) in the SIO/LMO interface supports the experimental results.

In this section of the thesis, we have explored the 3d-5d transition metal perovskite oxide heterostructures: $SrIrO_3$ (SIO) / $LaBO_3$ (LBO) (where B=Mn, Fe, Co, Ni), mainly focusing on their electronic, magnetic, and topological properties. We try to explore the intriguing features and properties of these interfaces, which will be discussed in detail in subsequent chapters.

1.1.3 Low-Dimensional Materials: Electronic and Structural Transformations

When materials are reduced from bulk structures to nanostructures, their electronic, optical, and mechanical properties can change dramatically, often influenced by quantum mechanical effects and many-body interactions due to strong spatial confinement of electrons. Restricting electrons to nanoscale objects, such as two-dimensional (2D) layers or one-dimensional (1D) chains, enhances the Coulomb interaction between electrons because of decreased electronic screening. Consequently, the intricate interaction between electronic, lattice, and spin degrees of freedom in low-dimensional materials can give rise to fascinating emergent behaviors, including high-temperature superconductivity and giant magnetoresistance, which were recognized with Nobel Prizes in 1987 and 2007 respectively.

For a long time, scientists and engineers have primarily focused on bulk materials (3D), as the microscopic details of matter are often negligible in everyday applications. Metals, for example, are typically viewed as homogeneous solids with consistent electronic prop-

erties determined by their conductivity. This allows electronic devices to be modeled using simple equations like Ohm's and Kirchhoff's laws. The fundamental atomic structure is considered uniform for practical purposes. The accurate prediction of material properties from atomic structure represents a significant achievement in the field of condensed matter physics and the ab initio community.

However, the advent of the transistor led to a renewed interest in the physics of interfaces (2D) due to the novel phenomena they exhibited. The advancement of semiconductor technology has prompted industries to pursue the reduction of device feature sizes, necessitating a shift from bulk property descriptions to methods incorporating atomic-scale features. This transition could potentially result in the emergence of new device types that may require materials distinct from those currently employed in semiconductor technology. Rather than relying on the adaptation of existing materials to align with technology, the intrinsic properties of new materials may be harnessed to achieve desired outcomes.

The discovery of carbon nanotubes (1D) in the 1990s generated significant research interest due to their unique properties, such as high tensile strength and tunable electronic properties ranging from metallic to insulating. Despite their potential, widespread technological adoption has been hindered by challenges in scaling up controlled growth and fabrication methods. Carbon nanotubes are made by rolling single or few layers of graphite into a tube, but single layers of graphite were initially thought to be thermodynamically unstable [22]. However, in 2004, Geim and Novoselov demonstrated the isolation of single stable layers of graphite, called graphene, which exhibited extremely high charge carrier mobility [23]. Despite its extraordinary properties, graphene's lack of a band gap limits its use in high-frequency electronics.

As researchers sought to engineer graphene, attention shifted to other two-dimensional materials with intrinsic band gaps. One such material is hexagonal boron nitride (h-BN), which, unlike graphene, has a diatomic unit cell that opens a large band gap, making it an insulator [24]. h-BN is effective for protecting other single-layer materials from environmental degradation. Additionally, it was discovered that other layered materials, like MoS_2, can also be exfoliated into single layers. MoS_2, part of the transition-metal dichalcogenides family, has a honeycomb-like crystal structure with a three-atom unit cell and exhibits properties like large spin-orbit splittings and high exciton binding energies [24–27]. This has spurred extensive research into these materials, though many properties remain unexplored, and more interesting materials may still be discovered.

The other form of low-dimensional materials are the quasi-1D materials. Quasi-1D materials differ from "true 1D" materials due to weak couplings with higher-dimensional environments, such as inter-chain interactions or coupling to a 3D substrate. In reality, purely 1D systems are theoretical constructs, and these couplings are always present to

some degree. Studying quasi-1D materials involves investigating these couplings, which is essential for understanding the origins of broken symmetry phases in real 1D systems and low-dimensional materials in general. According to the Mermin-Wagner theorem, long-range ordered phases are unstable in purely 1D systems due to quantum and thermal fluctuations [28]. Therefore, a dimensional crossover is necessary for a 1D system to achieve an ordered phase, as seen in many quasi-1D materials exhibiting charge and spin density waves [29, 30].

Quasi-One-Dimensional Materials (Q1D)

All materials occupy a finite volume in three-dimensional space. However, the electronic band structure in 3D crystals can be 1D if the atomic orbitals that form the conduction band overlap strongly in one direction and much less strongly in the other. Such crystals are essentially composed of parallel metallic chains with weak interactions between them, embedded in a matrix of non-metallic atoms. This ensures chemical bonding in all three directions. These Q1D crystals are therefore three dimensional in terms of their phonon interactions, while exhibiting one-dimensional electronic properties. Most of these crystals are observed as very thin needles or very narrow hair-like strands.

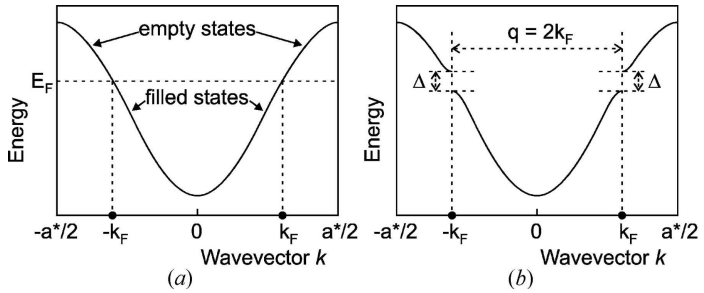

Figure 1.10: *(a) Conduction band of a one-dimensional crystal where one-electron states with energy $E_k < E_{k_F}$ are filled and those with $E_k > E_{k_F}$ are empty. The boundaries of the first Brillouin zone are given by $\pm a^*/2$. (b) A 1D crystal exhibiting Peierls lattice distortion (PLD) with a period $q = 2k_F$, showing an energy gap (Δ) in the dispersion at $k = \pm k_F$. The figure is taken from [31].*

Fifty years ago, Peierls (1955) predicted that 1D metals are unstable due to periodic lattice distortion (PLD) with a period twice the Fermi wavevector (K_F), leading to a metal-to-insulator transition. This PLD reduces the energy of filled electron states in the conduction band while increasing the energy of empty states [see Figure 1.10], resulting in a charge-density wave (CDW) driven by electron-phonon interactions. Consequently, crystals undergoing Peierls transition enter a CDW state, opening a gap at the Fermi level and transforming the material from a metal to an insulator. In a half-filled band, the CDW state creates a periodic structure with a lattice constant double that of the basic structure. If

the filling does not match the crystal's lattice periodicity, K_F can take any fraction of the reciprocal lattice's basis vector, resulting in an incommensurate CDW state.

Q1D materials attracted considerable attention when W. A. Little [32] proposed a model of superconducting organic macromolecules. However, no real compound has yet been discovered that fulfils the prediction of the model. Q1D materials exhibit interesting properties such as Peierls transition, charge density waves, open Fermi surfaces, strong electron-lattice coupling, Tomanago-Luttinger liquid behaviour, etc [33]. The Q1D materials studied include transition metal halides, transition metal chalcogenides, transition metal tetrachalcogenides, A15 compounds, Krogmann salts and others [33]. And most of these are Q1D metals, so the Q1D semiconductors and insulators are relatively less explored. Reducing the effective dimensionality from 3D to 2D and then to 1D increases the anisotropy of their physical properties. These properties include for example the exotic magnetic states in KMn_6Bi_5 [34], topological properties in β-Bi_4I_4 [35], significant optical anisotropy in $BaTiS_3$ [36], unconventional superconductivity in $K_2Cr_3As_3$ [37]. Recent studies have shown that TiS_3 crystals can be exfoliated into narrow ribbons with smooth and straight edges [38]. Furthermore, the energy required to break the weak bonds between 1D chains is similar to that required to separate 2D layers [39]. It is therefore possible to fabricate transistors with channel widths below 10 nm using Q1D materials [40]. Consequently, there is a growing interest in exploring the electrical, magnetic and optical properties of Q1D materials [41].

Quasi-One-Dimensional Transition Metal Chalcogenides (Q1DMCs)

Metal chalcogenides (MCs) are composed of at least one metal and one chalcogen (mainly S, Se and Te) atom. Quasi-one-dimensional metal chalcogenides (Q1DMCs) are a subset of MCs with a quasi-one-dimensional structure. Typically, their structures consist of infinite chains of interconnected metal chalcogen polyhedra. They are known for their structural and compositional diversity and are capable of forming binary, ternary and quaternary compounds [42]. Interest in Q1DMCs arose in 1970 with the discovery of one-dimensional electrical conduction, charge density waves (CDWs) and high-pressure superconductivity in $NbSe_3$ [43, 44]. Due to their quasi-one-dimensional nature and reduced crystal symmetry, they often have a needle-like appearance, indicating weaker interactions between adjacent chains. The reduced symmetry leads to strong anisotropies in their magnetic, electrical and optical properties.

According to the Mermin-Wagner theorem, there can be no ferromagnetic or antiferromagnetic order in ideal 1D systems at finite temperature with an isotropic Heisenberg model. However, this theorem does not hold if the magnetism is anisotropic. This makes Q1DMCs particularly interesting for the study of magnetism. Several Q1DMCs exhibit

magnetic properties. For example, $BaVS_3$ shows antiferromagnetic behaviour when it is stoichiometric, but becomes ferromagnetic when it is sulphur deficient [45]. $AFeS_2$ (where A can be K, Rb or Cs) and $BaFe_2S_4$ are antiferromagnetic semiconductors [46]. Ba_2MX_3 (where M can be Mn, Fe or Co and X can be S or Se) also exhibit antiferromagnetic properties [47]. These materials are promising for use in the next generation of magnetic storage devices.

Several Q1DMC superconductors have been identified, such as $Tl_2Mo_6Se_6$, $TaSe_3$ and $NbSe_3$ [48]. High pressure induced superconductivity has also been observed in the newly synthesised compound $Ba3TiTe_5$ [49]. Q1DMC materials with large band gaps, such as $AZrPSe_6$ (where A = K, Tb, Cs), $Cs_2CuP_3S_9$, $K_2P_2Se_6$, $AAsX_2$ (where A = Li, Na, and X = S, Se), show great promise for nonlinear optical (NLO) applications [50]. Metal chalcogenides have also attracted considerable attention as high performance thermoelectric materials, especially after the discovery of high thermoelectric figure of merit and extremely low thermal conductivity in SnSe. Nevertheless, many physical properties of Q1DMCs remain largely unexplored and provide opportunities for theoretical studies using ab-initio methods.

In this section of the thesis we have studied a newly synthesized quasi-one-dimensional transition metal tetrachalcogenide compound $(TaSe_4)_3I$, focusing on its phase transition from centrosymmetric to non-centrosymmetric structure, vacancy-induced ferromagnetism and possible superconductivity using first-principles calculations and experimental methods.

1.2 Overview of present thesis

This thesis explores a range of physical phenomena in complex materials, integrating experimental observations and first-principles calculations to investigate electronic, magnetic, topological properties, superconductivity, and structural phase transitions. These studies reveal underlying mechanisms and offer insights into designing materials with novel functionalities. The contents of different chapters discussed in this thesis can be summarized as follows:

Chapter 2 : This chapter presents the theoretical and computational methods used in this thesis to study electronic, magnetic, and topological properties of materials. It covers Density Functional Theory (DFT) and its extensions, such as DFT+U for strongly correlated systems, and outlines DFT-based techniques like the plane wave pseudopotential method, Linearized Muffin-Tin Orbital (LMTO) method, Linearized Augmented Plane Wave (LAPW) method, and Projector Augmented Wave (PAW) method. The construction of Wannier functions for detailed electronic structure analysis is also discussed. Addition-

ally, the integration of machine learning with DFT is introduced, focusing on data preparation and the use of algorithms such as Ridge Regression, Kernel Ridge Regression, Support Vector Regression, Random Forest, and Neural Networks to predict material properties.

Chapter 3 : In this chapter, we focus on predicting the properties of rare-earth lean magnets, specifically $Ce_2Fe_{17-x}Co_xCN$, using a combination of machine learning and first-principles calculations. The goal is to design affordable permanent magnets with performance comparable to high-end materials. Machine learning models predict a Curie temperature (T_c) above 600 K, magnetic moment ($\mu_0 M_s$) greater than 1 T, and positive anisotropy constant (K_u), indicating their potential as cost-effective magnets.

First-principles calculations confirm that for $x = 1$ to $x = 7$, these compounds exhibit $\mu_0 M_s$ values above 1.65 T and K_u values exceeding 1 MJ/m^3, comparable to state-of-the-art $Nd_2Fe_{14}B$ magnets. The best-performing compositions include $Ce_2Fe_{15}Co_2CN$, $Ce_2Fe_{12}Co_5CN$, $Ce_2Fe_{11}Co_6CN$, and $Ce_2Fe_{10}Co_7CN$.

A significant challenge for these magnets is the formation of nitrogen and carbon vacancies at high temperatures, which can reduce their stability. Our study shows that carbon-nitrogen codoping significantly increases vacancy formation energy, improving thermal stability by 35–40% compared to single doping.

Finally, a cost-performance analysis highlights their economic advantage, with a price-to-performance ratio between 0.03 and 0.22 USD/J. These findings underscore the potential of $Ce_2Fe_{17-x}Co_xCN$ as high-performance, affordable magnets, encouraging experimental efforts to synthesize these materials using low-cost elements like Ce, Fe, C, and N.

Chapter 4 : In this chapter, we investigate the $LaCoO_3/SrIrO_3$ (LCO/SIO) heterostructure using first-principles calculations to explain its unexpected ferromagnetic properties and explore its topological features. Our study reveals that interfacial charge transfer reduces the valence of Co ions in LCO from 3+ to 2+, leading to the stabilization of an intermediate spin (IS) state. This is notable because Co typically exists in a non-magnetic low-spin (LS) state in its bulk form.

The IS state of Co induces strong ferromagnetic exchange interactions between Co ions. These interactions extend into the $SrIrO_3$ (SIO) layer through interfacial Co–Ir coupling, stabilizing ferromagnetic order across the heterostructure. We also find that the tetragonal symmetry of SIO, constrained by the $SrTiO_3$ (STO) substrate, gives rise to charge-2 Dirac points due to the system's orbital degeneracy.

Our results explain the observed anomalous Hall effect (AHE) in the LCO/SIO system and suggest the potential for new quasiparticles associated with charge-2 Dirac points.

Chapter 5 : In this chapter, we extend our study of the $LaCoO_3/SrIrO_3$ (LCO/SIO) heterostructure to explore systematic trends in 3d, 5d superlattices, $LaBO_3/SrIrO_3$ (B = Mn, Fe, Co, Ni). These superlattices are analyzed for both *n*-type and *p*-type interfaces

to understand how interface polarity and the chemistry of the B-site cation influence their electronic, magnetic, and topological properties.

Our findings show consistent interfacial charge transfer trends. For *p*-type interfaces, charge transfer direction is uniform across all systems, while for *n*-type interfaces, it depends on the *d*-orbital occupancy of the B-site cation relative to Ir^{4+} in $SrIrO_3$. Specifically, in *n*-type interfaces, charge moves to $LaBO_3$ for B = Co and Ni, but flows to $SrIrO_3$ for B = Mn and Fe. These charge transfer effects strongly affect the magnetism of the $SrIrO_3$ block, which becomes ferromagnetic in *n*- and *p*-type LCO/SIO, LNO/SIO, and *p*-type LMO/SIO, but weakly ferromagnetic or nearly non-magnetic in LFO/SIO.

We predict insulating behavior at the *n*-type LFO/SIO interface due to charge transfer. Topologically, the magnetic $SrIrO_3$ block exhibits $C = \pm 2$ double Weyl crossings, driving an intrinsic anomalous Hall conductivity (AHC) of 7–8 Ω^{-1} cm^{-1} in *n*-type and *p*-type LCO/SIO, LNO/SIO, and *p*-type LMO/SIO. However, weakened ferromagnetic interactions in LFO/SIO suppress its AHC, making LCO/SIO and LNO/SIO the most promising candidates for robust intrinsic AHC. LMO/SIO shows moderate potential, while LFO/SIO is less favorable.

These findings align with experimental observations and provide theoretical insights to guide future studies, highlighting the potential of these superlattices for applications in spintronics and topological materials.

Chapter 6 : In this chapter, we study the structural phase transition in the quasi-one-dimensional compound $(TaSe_4)_3I$, focusing on the change from a centrosymmetric to a noncentrosymmetric structure. Experimental techniques, including single crystal X-ray diffraction (XRD), resistivity, specific heat, and Raman scattering, reveal a transition at $T_s \sim 145\ K$. This transition lowers the symmetry of the Ta chains, changing from a high-temperature (HT) centrosymmetric phase with L-L-S Ta-Ta bonds to a low-temperature (LT) noncentrosymmetric phase with L-M-S Ta-Ta bonds, while maintaining the overall tetragonal symmetry. The key aspect is the breaking of inversion symmetry at the short Ta-Ta bond.

To understand this transition, we performed first-principles density functional theory (DFT) calculations and tight-binding modeling for the HT and LT structures. Both phases show semi-metallic behavior, consistent with experiments. The phase transition is driven by a balance between hybridization energy gain and elastic energy loss. At low temperatures, the hybridization energy gain becomes dominant, stabilizing the off-centric structure. The temperature scale predicted by our model matches well with the observed transition temperature.

This study identifies a unique type of structural phase transition, different from the usual charge-density-wave transitions seen in chain compounds.

Chapter 7 : Building on the findings from Chapter 6 about the structural phase transition in the quasi-one-dimensional compound $(TaSe_4)_3I$ (*n*-TSI), this chapter explores the presence of superconductivity and weak ferromagnetism in this material at ambient pressure. Experiments, including electrical resistivity and magnetization measurements, show that *n*-TSI behaves as a metal, exhibits weak ferromagnetism below 9 K, and becomes superconducting below 2.5 K. Interestingly, first-principles calculations predict *n*-TSI to be a semiconductor, indicating that defects play a key role in its observed properties.

Our density functional theory (DFT) calculations reveal that Se_2 dimer vacancies induce metallic behavior and create localized magnetic moments. These moments lead to weak ferromagnetism via the Ruderman–Kittel–Kasuya–Yosida (RKKY) interaction, mediated by itinerant electrons. This defect-driven phase separation results in vacancy-free chains remaining metallic and nonmagnetic, supporting phonon-mediated superconductivity, while vacancy-bearing chains exhibit magnetism. The interplay between defects, low dimensionality, and electronic structure creates a complex ground state, with the calculated ferromagnetic and superconducting transition temperatures aligning well with experimental results for a vacancy concentration of 1.38%.

These findings emphasize the importance of defects in shaping the unique properties of *n*-TSI and provide a framework for studying the interaction between magnetism and superconductivity in low-dimensional materials.

Chapter 8 : In this chapter, we summarize the key findings of our study and outline potential directions for future research.

Bibliography

[1] Oliver Gutfleisch, Matthew A. Willard, Ekkes Brück, Christina H. Chen, S. G. Sankar, and J. Ping Liu. Magnetic materials and devices for the 21st century: Stronger, lighter, and more energy efficient. *Advanced Materials*, 23(7):821–842, 2011.

[2] Herbert Kroemer. Nobel lecture: Quasielectric fields and band offsets: teaching electrons new tricks. *Rev. Mod. Phys.*, 73:783–793, Oct 2001.

[3] Rainer Waser and Masakazu Aono. Nanoionics-based resistive switching memories. *Nature Materials*, 6(11):833–840, November 2007.

[4] Ji ří Chaloupka and Giniyat Khaliullin. Orbital order and possible superconductivity in $\mathrm{lanio_3/lamo_3}$ superlattices. *Phys. Rev. Lett.*, 100:016404, Jan 2008.

[5] P. Hansmann, Xiaoping Yang, A. Toschi, G. Khaliullin, O. K. Andersen, and K. Held. Turning a nickelate fermi surface into a cupratelike one through heterostructuring. *Phys. Rev. Lett.*, 103:016401, Jun 2009.

[6] B. J. Kim, Hosub Jin, S. J. Moon, J.-Y. Kim, B.-G. Park, C. S. Leem, Jaejun Yu, T. W. Noh, C. Kim, S.-J. Oh, J.-H. Park, V. Durairaj, G. Cao, and E. Rotenberg. Novel $J_{\mathrm{eff}} = 1/2$ mott state induced by relativistic spin-orbit coupling in $\mathrm{sr_2iro_4}$. *Phys. Rev. Lett.*, 101:076402, Aug 2008.

[7] Supriyo Datta and Biswajit Das. Electronic analog of the electro-optic modulator. *Applied Physics Letters*, 56(7):665–667, February 1990.

[8] Alexandr Chernyshov, Mason Overby, Xinyu Liu, Jacek K. Furdyna, Yuli Lyanda-Geller, and Leonid P. Rokhinson. . *Nature Physics*, 5(9):656–659, September 2009.

[9] Ioan Mihai Miron, Gilles Gaudin, Stéphane Auffret, Bernard Rodmacq, Alain Schuhl, Stefania Pizzini, Jan Vogel, and Pietro Gambardella. Current-driven spin torque induced by the rashba effect in a ferromagnetic metal layer. *Nature Materials*, 9(3):230–234, March 2010.

[10] Masaru Onoda and Naoto Nagaosa. Quantized anomalous hall effect in two-dimensional ferromagnets: Quantum hall effect in metals. *Phys. Rev. Lett.*, 90:206601, May 2003.

[11] M. Z. Hasan and C. L. Kane. Colloquium: Topological insulators. *Rev. Mod. Phys.*, 82:3045–3067, Nov 2010.

[12] Xiao-Liang Qi and Shou-Cheng Zhang. Topological insulators and superconductors. *Rev. Mod. Phys.*, 83:1057–1110, Oct 2011.

[13] Wikipedia contributors. Alnico. `https://en.wikipedia.org/wiki/Alnico`, 2024. Accessed: 2024-06-28.

[14] J.M.D. Coey. Permanent magnets: Plugging the gap. *Scripta Materialia*, 67(6):524–529, 2012. Viewpoint Set No. 51: Magnetic Materials for Energy.

[15] Magnet Source. Ceramic magnets. `https://www.magnetsource.com/pages/ceramic-magnets`, 2024. Accessed: 2024-06-28.

[16] J. M. D. Coey. *Permanent Magnetism*. Routledge, 1st edition, 1999.

[17] J. M. D. Coey. *Magnetism and Magnetic Materials*. Cambridge University Press, 2010.

[18] R. A. Mccurrie. Chapter 3 the structure and properties of alnico permanent magnet alloys. *Handbook of Ferromagnetic Materials*, 3:107–188, 1982.

[19] K A Gschneidner, V K Pecharsky, and A O Tsokol. Recent developments in magnetocaloric materials. *Reports on Progress in Physics*, 68(6):1479, may 2005.

[20] K.H.J. Buschow. Magnetic interactions in intermetallic compounds. *Journal of the Less Common Metals*, 43(1):55–67, 1975.

[21] K.H.J. Buschow and F.R. de Boer. *Physics of Magnetism and Magnetic Materials*. Focus on biotechnology. Springer US, 2007.

[22] L.D. Landau and E.M. Lifshitz. *Statistical Physics: Volume 5*. Number v. 5. Elsevier Science, 2013.

[23] K. S. Novoselov, A. K. Geim, S. V. Morozov, D. Jiang, Y. Zhang, S. V. Dubonos, I. V. Grigorieva, and A. A. Firsov. Electric field effect in atomically thin carbon films. *Science*, 306(5696):666–669, Oct 22 2004.

[24] K. S. Novoselov et al. Two-dimensional atomic crystals. *Proceedings of the National Academy of Sciences of the United States of America*, 102(30):10451–10453, July 2005.

[25] Ashwin Ramasubramaniam. Large excitonic effects in monolayers of molybdenum and tungsten dichalcogenides. *Phys. Rev. B*, 86:115409, Sep 2012.

[26] Z. Y. Zhu, Y. C. Cheng, and U. Schwingenschlögl. Giant spin-orbit-induced spin splitting in two-dimensional transition-metal dichalcogenide semiconductors. *Phys. Rev. B*, 84:153402, Oct 2011.

[27] Coleman et. al. Two-dimensional nanosheets produced by liquid exfoliation of layered materials. *Science*, 331(6017):568–571, February 2011.

[28] N. D. Mermin and H. Wagner. Absence of ferromagnetism or antiferromagnetism in one- or two-dimensional isotropic heisenberg models. *Phys. Rev. Lett.*, 17:1133–1136, Nov 1966.

[29] G. Grüner. The dynamics of charge-density waves. *Rev. Mod. Phys.*, pages 1129–1181, Oct 1988.

[30] G. Grüner. The dynamics of spin-density waves. *Rev. Mod. Phys.*, 66:1–24, Jan 1994.

[31] Sander van Smaalen. The peierls transition in low-dimensional electronic crystals. *Acta Crystallographica Section A*, 61(1):51–61, Jan 2005.

[32] W. A. Little. Possibility of synthesizing an organic superconductor. *Phys. Rev.*, 134:A1416–A1424, Jun 1964.

[33] Siegmar Roth and David Carroll, editors. *One-Dimensional Metals*. Wiley-VCH Verlag GmbH & Co. KGaA, Weinheim, 3rd edition, September 2015. 360 Pages, Hardcover, 8 tables, Monograph.

[34] Jin-Ke Bao, Zhang-Tu Tang, Hee Joon Jung, Ji-Yong Liu, Yi Liu, Lin Li, Yu-Ke Li, Zhu-An Xu, Chun-Mu Feng, Haijie Chen, Duck Young Chung, Vinayak P. Dravid, Guang-Han Cao, and Mercouri G. Kanatzidis. Unique $[Mn_6Bi_5]$-nanowires in KMn_6Bi_5: A quasi-one-dimensional antiferromagnetic metal. *Journal of the American Chemical Society*, 140(12):4391–4400, March 2018.

[35] Autès et. al. A novel quasi-one-dimensional topological insulator in bismuth iodide -bi4i4. *Nature materials*, 15(2):154—158, February 2016.

[36] Niu et. al. Giant optical anisotropy in a quasi-one-dimensional crystal. *Nature Photonics*, 12(7):392–396, July 2018.

[37] Jin-Ke Bao, Ji-Yong Liu, Cong-Wei Ma, Zhi-Hao Meng, Zhang-Tu Tang, Yun-Lei Sun, Hui-Fei Zhai, Hao Jiang, Hua Bai, Chun-Mu Feng, Zhu-An Xu, and Guang-Han Cao. Superconductivity in quasi-one-dimensional $k_2cr_3as_3$ with significant electron correlations. *Phys. Rev. X*, 5:011013, Feb 2015.

[38] Alexey Lipatov, Peter M. Wilson, Mikhail Shekhirev, Jacob D. Teeter, Ross Netusil, and Alexander Sinitskii. Few-layered titanium trisulfide (tis3) field-effect transistors. *Nanoscale*, 7:12291–12296, 2015.

[39] Alexey Lipatov, Mark J. Loes, Haidong Lu, Jixiang Dai, Piotr Patoka, Natalia S. Vorobeva, Dmitry S. Muratov, Greta Ulrich, Bernd Kästner, Arne Hoehl, Gerhard Ulm, Xiao Cheng Zeng, Eckart Rühl, Alexei Gruverman, Peter A. Dowben, and Alexander Sinitskii. Quasi-1d tis3 nanoribbons: Mechanical exfoliation and thickness-dependent raman spectroscopy. *ACS Nano*, 12(12):12713–12720, December 2018.

[40] Pavlo V. Galiy, Michael Randle, Alexey Lipatov, Lu Wang, Simeon Gilbert, Nataliia Vorobeva, Avinash Kumar, Chun-Pui Kwan, Jubin Nathawat, Bilal Barut, Shenchu Yin, Nargess Arabchigavkani, Taras M. Nenchuk, Takashi Komesu, Keke He, Andrew Yost, Uttam Singisetti, Wai-Ning Mei, Alexander Sinitskii, Jonathan P. Bird, and Peter A. Dowben. Building the quasi one dimensional transistor from 2d materials. In *2019 IEEE 2nd Ukraine Conference on Electrical and Computer Engineering (UKRCON)*. IEEE, July 2019.

[41] Jian Wang and Kirill Kovnir. Giant anisotropy detected. *Nature Photonics*, 12(7):382–383, June 2018.

[42] Volodymyr Smetana, Marta Wilk-Kozubek, and Anja-Verena Mudring. Review of active-transition-metal tellurides: Through crystal structures to physical properties. *Crystal Growth & Design*, 19(9):5429–5440, 2019.

[43] N. P. Ong and Pierre Monceau. Anomalous transport properties of a linear-chain metal: $Nbse_3$. *Phys. Rev. B*, 16:3443–3455, Oct 1977.

[44] P. Monceau, J. Peyrard, J. Richard, and P. Molinié. Superconductivity of the linear trichalcogenide $nbse_3$ under pressure. *Phys. Rev. Lett.*, 39:161–164, Jul 1977.

[45] O. Massenet, R. Buder, J. J. Since, C. Schlenker, J. Mercier, J. Kelber, and D. G. Stucky. Bavs3, a quasi one dimensional ferromagnet or antiferromagnet depending on stoichiometry. *Materials Research Bulletin*, 13(3):187–195, March 1978.

[46] Satish K. Tiwary and Sukumaran Vasudevan. Regular versus alternating $(fes_4)_n$ chains: Magnetism in $kfes_2$ and $csfes_2$. *Phys. Rev. B*, 56:7812–7814, Oct 1997.

[47] N. Nakayama, K. Kosuge, S. Kachi, T. Shinjo, and T. Takada. Studies on the compounds in bafes system. i. linear chain antiferromagnetism of ba2fes3 and related

compounds ba2cos3 and ba2mns3. *Journal of Solid State Chemistry*, 33(3):351–356, July 1980.

[48] J.C. Armici, M. Decroux, Ø. Fischer, M. Potel, R. Chevrel, and M. Sergent. A new pseudo-one-dimensional superconductor: T2mo6se6. *Solid State Communications*, 33(6):607–611, 1980.

[49] Jun Zhang, Yating Jia, Xiancheng Wang, Zhi Li, Lei Duan, Wenmin Li, Jianfa Zhao, Lipeng Cao, Guangyang Dai, Zheng Deng, Sijia Zhang, Shaomin Feng, Runze Yu, Qingqing Liu, Jiangping Hu, Jinlong Zhu, and Changqing Jin. A new quasi-one-dimensional compound Ba_3TiTe_5 and superconductivity induced by pressure. *NPG Asia Materials*, 11:60, October 2019.

[50] Fei Liang, Lei Kang, Zheshuai Lin, and Yicheng Wu. Mid-infrared nonlinear optical materials based on metal chalcogenides: Structure–property relationship. *Crystal Growth & Design*, 17(4):2254–2289, 2017.

2

Methodology

2.1 Introduction

This chapter outlines the theoretical methodologies used to calculate and predict the electronic, magnetic, and topological properties of the compounds under study. The specific approaches and techniques employed in this thesis are as follows:

- **Ab Initio Technique**: We have used conventional T=0 K ab initio techniques, mainly Density Functional Theory (DFT), to perform most of the theoretical calculations. To deal with strong electronic correlations, we used DFT with Hubbard U calculations within the framework of static mean field theory.
- **Machine Learning Technique**: In addition, we have integrated machine learning (ML) techniques with DFT in one of the problems for data-driven prediction of new compounds with targeted properties. The ML techniques include data processing, model selection, validation, optimization and then prediction.

The following sections provide a brief summary of the methods.

2.2 The Many Electron Hamiltonian

A real physical system can be visualized as a collection of atoms and molecules that interact with one another. The atoms and molecules in real physical systems can exist in different states. They can be found in the gas phase as isolated entities or clusters, or in the solid or condensed phase as bulk solids or surfaces. Irrespective of their state, these systems are typically composed of heavy, positively charged nuclei and lighter, negatively charged

electrons, with interactions governed by electrostatic Coulomb forces. In order to describe such a system, one needs to write a many-body Hamiltonian that takes into account the interactions between all the particles. Such a Hamiltonian includes terms for the kinetic energy of the electrons and nuclei, the potential energy arising from electron-nucleus interactions, and the potential energy due to electron-electron and nucleus-nucleus interactions. The general form of this many-body Hamiltonian is as follows,

$$H = -\sum_{I=1}^{P} \frac{\hbar^2}{2M_I}\nabla_I^2 - \sum_{i=1}^{N} \frac{\hbar^2}{2m_i}\nabla_i^2 + \frac{e^2}{2}\sum_{I=1}^{P}\sum_{J\neq I}^{P} \frac{Z_I Z_J}{|\boldsymbol{R}_I - \boldsymbol{R}_J|} + \frac{e^2}{2}\sum_{i=1}^{N}\sum_{j\neq i}^{N} \frac{1}{|\boldsymbol{r}_i - \boldsymbol{r}_j|} - e^2\sum_{I=1}^{P}\sum_{i=1}^{N} \frac{Z_I}{|\boldsymbol{R}_I - \boldsymbol{r}_i|} \tag{2.2.1}$$

where the ions are represented by charge Z_I and mass M_I and the electrons by charge e and mass m_i. The first and second terms of the Hamiltonian represent the kinetic energies of the ions (T_n) and electrons (T_e) respectively. The remaining terms represent the Coulomb interactions: ion-ion (V_{nn}), electron-electron (V_{ee}) and electron-ion (V_{ne}). Now we have to solve the time-independent Schrödinger equation to find the many-body wave function $\Psi_i(r,R)$.

$$H\Psi_i(\boldsymbol{r},\boldsymbol{R}) = E_i\Psi_i(\boldsymbol{r},\boldsymbol{R}). \tag{2.2.2}$$

It is a challenging task to find an exact analytical solution for Equation (2.2.2) within a complete quantum mechanical framework, even for a small molecule. For systems with many interacting particles, the equation becomes non-separable due to the many-body nature of Coulomb interactions. Thus, solving this Hamiltonian in practical scenarios requires approximation, such as variational principles or perturbative treatments. In principle, one may also attempt an alternate approach such as a numerical solution. However, the problem arises from the inclusion of a large number of variables (3N) in the wavefunction, as D. R. Hartree's statement: "The tabulation of a function of one variable requires a page, of two variables a volume, and of three variables a library; but the full specification of a single wave function of neutral Fe is a function of seventy-eight variables. It would be rather crude to restrict to ten the number of values of each variable at which to tabulate this function, but even so, full tabulation of it would require 10^{78} entries, and even if this number could be reduced somewhat from considerations of symmetry, there would still not be enough atoms in the whole solar system to provide the material for printing such a table." On top of this, there are challenges with interpretation as expressed by R. P. Feynman, "The trouble with quantum mechanics is not only in solving the equations, but in understanding what the solutions mean." The main challenges in solving the Schrödinger equation stem from the large number of variables involved, the complexity in interpretation, and the intricate electron-electron correlations.

The first significant approximation is the *Born-Oppenheimer Approximation* in 1927

[1]. This approximation states that electrons are much lighter than nuclei, which means that the timescale for electron motion is much shorter than the motion of nuclei. As a result, nuclei can be treated as stationary relative to the movement of electrons. Therefore, the electronic part of the Hamiltonian can be expressed for a fixed nuclear configuration as follows:

$$H_e = T_e + V_{ee} + V_{ne} + V_{nn}, \tag{2.2.3}$$

The last term, V_{nn}, represents a constant arising from the ion-ion interaction, known as Madelung energy. This can be determined classically. This approximation simplifies the many-body Hamiltonian to a many-electron Hamiltonian. However, even with this simplification, further approximations are required to accurately solve Equation (2.2.3) due to the complex interactions among the electrons.

The *Independent Electron Approximation* further simplifies the problem by converting a system where electrons interact with each other into one where they are treated as if they do not interact, thus approximating the original system.

These approximations can be approached in two main ways: (a). the wavefunction-based method, which includes Hartree [2], Hartree-Fock [3] and configuration interaction [4] techniques, etc., and (b). the density-based approach implemented by density functional theory (DFT) [5–7]. Wave-function-based methods, while accurate, are computationally expensive and scale exponentially with system size, making them impractical for larger systems. In contrast, DFT is more computationally efficient and less expensive. In this thesis, the theoretical calculations are carried out using Density Functional Theory (DFT).

2.3 Density Functional Theory

Before the theories of Hartee (1928) and Hartee-Fock (1930), Thomas and Fermi (TF) (1927) [12S-13S] proposed the concept of solving many-body problems using the density functional method. In this method, the electron density of a non-interacting homogeneous electron gas is considered as the primary variable. This approach is advantageous because a system with N electrons has a many-body wave function with $3N$ variables, $\Psi(\mathbf{r}_1, \mathbf{r}_2, \ldots, \mathbf{r}_N)$, while the corresponding electron density is given by:

$$\rho(r) = N \int \Psi^*(r, r_2, \ldots, r_N)\Psi(r_1, r_2, \ldots, r_N)\, dr_2\, dr_3 \ldots dr_N, \tag{2.3.1}$$

where r_i is the position vector of the i-th electron. Thus, working with the electron density is more computationally efficient than working with the wave function based method due to the reduction in the number of variables.

However, the TF model has several limitations. The expression for kinetic energy

was approximate and the model completely neglected electron-electron correlation. It also fails to capture the bonding between atoms. Although the TF model had certain limitations, it provided the basis for the development of Density Functional Theory (DFT). DFT effectively addresses many-electron problems with greater efficiency and has become the preferred method for electronic structure calculations in condensed matter physics.

2.3.1 Reduced Density Matrices

The mathematical framework of the density functional approach is described as follows. The electron density in the ground state is given by

$$\rho(\boldsymbol{r}_1) = N \int \Psi^*(\boldsymbol{r}_1, \boldsymbol{r}_2, ..., \boldsymbol{r}_N)\Psi(\boldsymbol{r}_1, \boldsymbol{r}_2, ..., \boldsymbol{r}_N) d\boldsymbol{r}_2 d\boldsymbol{r}_3 ... d\boldsymbol{r}_N. \tag{2.3.2}$$

where $\Psi(r_1, r_2, ..., r_N)$ represents a many-particle wave function. The single-particle electron-ion interaction can be expressed as follows:

$$\langle V_{ne} \rangle = \langle \Psi | \sum_i v(\mathbf{r}_i) | \Psi \rangle = \int d\mathbf{r}\, v(\mathbf{r})\rho(\mathbf{r}), \tag{2.3.3}$$

where the integration encompasses all space. Similarly, the two-particle electron-electron repulsion can be formulated as:

$$\langle V_{ee} \rangle = \langle \Psi | \frac{1}{2} \sum_{i,j} \frac{1}{\mathbf{r}_{ij}} | \Psi \rangle = \frac{1}{2} \int d\mathbf{r}_1\, d\mathbf{r}_2\, \frac{\Gamma_2(\mathbf{r}_1, \mathbf{r}_2)}{\mathbf{r}_{12}}, \tag{2.3.4}$$

where $\Gamma_2(\mathbf{r}_1, \mathbf{r}_2)$ represents the two-particle density indicating the joint probability of finding an electron in the volume $d\mathbf{r}_1$ at $\mathbf{r}_1$ and another electron in the volume $d\mathbf{r}_2$ at $\mathbf{r}_2$. This can be described by:

$$\Gamma_2(\mathbf{r}_1, \mathbf{r}_2) = N(N-1) \int \Psi^*(\mathbf{r}_1, \mathbf{r}_2, \ldots, \mathbf{r}_N)\Psi(\mathbf{r}_1, \mathbf{r}_2, \ldots, \mathbf{r}_N)\, d\mathbf{r}_3\, d\mathbf{r}_4 \ldots d\mathbf{r}_N. \tag{2.3.5}$$

The kinetic energy term, incorporating differential operators, is represented as:

$$T = -\langle \Psi | \frac{1}{2} \sum_i \nabla_i^2 | \Psi \rangle = -\frac{1}{2} N \int \Psi^*(\mathbf{r}_1, \mathbf{r}_2, \ldots, \mathbf{r}_N) \nabla_1^2 \Psi(\mathbf{r}_1, \mathbf{r}_2, \ldots, \mathbf{r}_N)\, d\mathbf{r}_1\, d\mathbf{r}_2 \ldots d\mathbf{r}_N, \tag{2.3.6}$$

$$= -\frac{1}{2} N \int \left[\nabla_1^2 \Psi^*(\mathbf{r}_1', \mathbf{r}_2, \ldots, \mathbf{r}_N)\Psi(\mathbf{r}_1, \mathbf{r}_2, \ldots, \mathbf{r}_N) \right]_{\mathbf{r}_1 = \mathbf{r}_1'} d\mathbf{r}_1\, d\mathbf{r}_2 \ldots d\mathbf{r}_N, \tag{2.3.7}$$

$$= -\frac{1}{2} \int d\mathbf{r}_1 \left[\nabla_1^2 \gamma(\mathbf{r}_1, \mathbf{r}_1') \right]_{\mathbf{r}_1 = \mathbf{r}_1'}, \tag{2.3.8}$$

where $\gamma(\mathbf{r}_1, \mathbf{r}_1')$ is the first-order reduced density matrix, defined as:

$$\gamma(\mathbf{r}_1, \mathbf{r}_1') = N \int \Psi^*(\mathbf{r}_1', \mathbf{r}_2, \ldots, \mathbf{r}_N)\Psi(\mathbf{r}_1, \mathbf{r}_2, \ldots, \mathbf{r}_N)\, d\mathbf{r}_2\, d\mathbf{r}_3 \ldots d\mathbf{r}_N. \tag{2.3.9}$$

Using the density matrix formalism, the total energy of the system can be represented in terms of Reduced Density Matrices (RDMs):

$$E[\rho, \gamma, \Gamma_2] = T[\gamma(\mathbf{r}_1, \mathbf{r}_1')] + V_{ne}[\rho(\mathbf{r})] + V_{ee}[\Gamma_2(\mathbf{r}_1, \mathbf{r}_2)], \tag{2.3.10}$$

This formulation allowed the development of a quantum mechanical framework for many-electron systems in reduced space, bypassing the wave function formalism. An important requirement of this approach is to find the Reduced Density Matrices (RDMs) by minimizing the energy while obeying the Pauli exclusion principle. We must also confirm the presence of an anti-symmetric wave function Ψ that can generate these RDMs. The problem of N representability involves establishing necessary and sufficient conditions for $\gamma(\mathbf{r}_1, \mathbf{r}_1')$ and $\Gamma_2(\mathbf{r}_1, \mathbf{r}_2)$, which are not yet fully known. The condition for N representability of $\rho(\mathbf{r})$ is given by

$$\int \rho(\mathbf{r})\, d\mathbf{r} = N, \quad \rho(\mathbf{r}) \geq 0. \tag{2.3.11}$$

One of the most straightforward reduced quantities is the single-particle density, which has the potential to facilitate the development of quantum mechanics within a simplified framework.

2.3.2 The Hohenberg-Kohn (HK) Theorems

Density functional theory (DFT) is based on the theorems introduced by Hohenberg and Kohn in 1964 [6S].

Hohenberg-Kohn Theorem I: A one-to-one correspondence exists between the ground state electron density $\rho(\mathbf{r})$ of a system with N electrons and the external potential $v_{\text{ext}}(\mathbf{r})$ acting on it. This implies that the electron density $\rho(\mathbf{r})$ is uniquely determined for any system of interacting particles under an external potential $v_{\text{ext}}(\mathbf{r})$.

Hohenberg-Kohn Theorem II: There exists a universal functional $E[\rho]$ for the energy, expressed in terms of the electron density $\rho(\mathbf{r})$, which is valid for any external potential. The exact ground state energy of the system, for a given external potential, is obtained as the global minimum of this functional. The electron density that minimizes the functional corresponds to the true ground state density.

Proof of Theorem I

Suppose there are two external potentials, $v_1(\mathbf{r})$ and $v_2(\mathbf{r})$, which differ only by an additive constant but give the same ground state density $\rho(\mathbf{r})$. Since these potentials are different,

they correspond to different Hamiltonians, H_1 and H_2, with corresponding wavefunctions Ψ_1 and Ψ_2. According to the variational principle, no wave function can give an energy lower than that obtained from Ψ_1 for H_1. Thus,

$$E_1 = \langle \Psi_1 | H_1 | \Psi_1 \rangle < \langle \Psi_2 | H_1 | \Psi_2 \rangle.$$

Assuming a non-degenerate ground state, and given that both Hamiltonians have the same ground state density, we can rewrite the equation as

$$E_1 < \langle \Psi_2 | H_1 | \Psi_2 \rangle = \langle \Psi_2 | H_2 | \Psi_2 \rangle + \langle \Psi_2 | H_1 - H_2 | \Psi_2 \rangle = E_2 + \int d\mathbf{r}\, \rho(\mathbf{r})[v_1(\mathbf{r}) - v_2(\mathbf{r})].$$

Thus,

$$E_1 < E_2 + \int d\mathbf{r}\, \rho(\mathbf{r})[v_1(\mathbf{r}) - v_2(\mathbf{r})].$$

By swapping the indices, we get:

$$E_2 < E_1 + \int d\mathbf{r}\, \rho(\mathbf{r})[v_2(\mathbf{r}) - v_1(\mathbf{r})].$$

The addition of these inequalities results in the following:

$$E_1 + E_2 < E_2 + E_1,$$

which is a contradiction. Therefore, our first assumption must be false, which means that a given $\rho(\mathbf{r})$ corresponds to a unique external potential $v(\mathbf{r})$. Consequently, $v(\mathbf{r})$ is determined by $\rho(\mathbf{r})$, which fixes both the Hamiltonian and the wave function. This conclusion proves Hohenberg-Kohn's first theorem.

Proof of Theorem II

Given that the wave function depends on the density, we can express the total energy functional $E_v[\rho]$ for a given external potential $v(\mathbf{r})$ as follows,

$$E_v[\rho] = F[\rho] + \int \rho(\mathbf{r}) v(\mathbf{r})\, d\mathbf{r}, \tag{2.3.12}$$

where,

$$H = T_e + U_{ee} + V_{ne}, \tag{2.3.13}$$

and,

$$F[\rho] = \langle \Psi[\rho] | T_e + U_{ee} | \Psi[\rho] \rangle \tag{2.3.14}$$

It represents a universal functional whose exact form is unknown and is independent of the external potential. The ground state energy is uniquely defined by the ground state density

$\tilde{\rho}$. Thus,

$$E_v[\tilde{\rho}] = \langle \Psi[\tilde{\rho}]|H|\Psi[\tilde{\rho}]\rangle. \tag{2.3.15}$$

By application of the variational principle, any alternative density, ρ, results in a higher energy.

$$E_v[\tilde{\rho}] = \langle \Psi[\tilde{\rho}]|H|\Psi[\tilde{\rho}]\rangle < \langle \Psi[\rho]|H|\Psi[\rho]\rangle. \tag{2.3.16}$$

This indicates that by minimizing the total energy functional with respect to the density $\rho(\mathbf{r})$ we can obtain the ground state energy. The density that achieves this minimum is the ground state density. While the Hohenberg-Kohn theorem provides an "exact theory" for determining the ground state properties of any system, its main limitation is the unknown exact form of the universal functional $F[\rho]$. If the form of $F[\rho]$ were known, it would allow exact solution of the electronic problems.

2.3.3 Kohn-Sham Formulation

In the energy functional, the main unknown component is the universal functional $F[\rho]$, which captures all the many-body interactions. In 1965 Kohn and Sham [6] made a significant advance in this concept by mapping the electron density $\rho(\mathbf{r})$ of an interacting N electron system into a system of non-interacting electrons. This mapping ensured that the density of the actual interacting system remained unchanged compared to that of the non-interacting system. With this formalism, the universal functional $F[\rho]$ can be expressed as,

$$F[\rho(\mathbf{r})] = T_0[\rho(\mathbf{r})] + \frac{e^2}{2}\int\int \frac{\rho(\mathbf{r}_1)\rho(\mathbf{r}_2)}{r_{12}} d\mathbf{r}_1 d\mathbf{r}_2 + E_{\mathrm{XC}}[\rho(\mathbf{r})], \tag{2.3.17}$$

The kinetic energy functional of the interacting electrons is replaced by the kinetic energy of the non-interacting particle system $T_0[\rho]$. The following term represents the classical electrostatic contribution, commonly referred to as the Hartree term, while $E_{XC}[\rho]$, referred to as the exchange-correlation (XC) energy, includes all contributions arising from many-body effects, such as exchange effects, which capture the Pauli exclusion principle, and correlation effects, which capture the correlation of electrons within the many-body wavefunction. The energy functional can be expressed as follows,

$$E[\rho] = T_0[\rho(\mathbf{r})] + \int v(\mathbf{r})\rho(\mathbf{r}) d\mathbf{r} + \frac{e^2}{2}\int\int \frac{\rho(\mathbf{r}_1)\rho(\mathbf{r}_2)}{r_{12}} d\mathbf{r}_1 d\mathbf{r}_2 + E_{\mathrm{XC}}[\rho(\mathbf{r})]. \tag{2.3.18}$$

Here, $T_0[\rho]$ denotes the non-interacting kinetic energy functional for a given density $\rho(r)$. To determine $T_0[\rho]$, it is necessary to find the solution of the single-particle Schrödinger equation,

$$\left[-\frac{1}{2}\nabla^2 + \lambda(\mathbf{r})\right]\psi_i = \varepsilon_i \psi_i, \tag{2.3.19}$$

By selecting a suitable function $\lambda(r)$, the orbitals obtained from that selection give the desired density.

$$\rho(\mathbf{r}) = \sum_i |\psi_i|^2. \tag{2.3.20}$$

Subsequently, the functional is then evaluated as follows,

$$T_0[\rho] = \sum_i \varepsilon_i - \int d\mathbf{r}\lambda(\mathbf{r})\rho(\mathbf{r}). \tag{2.3.21}$$

The energy functional that is used to find the equilibrium density is then formulated as follows,

$$E[\rho] = \sum_i \varepsilon_i - \int d\mathbf{r}\lambda(\mathbf{r})\rho(\mathbf{r}) + \int v(\mathbf{r})\rho(\mathbf{r})d\mathbf{r} + E_{\text{coul}}[\rho] + E_{\text{XC}}[\rho]. \tag{2.3.22}$$

Minimizing the functional results in,

$$\lambda(\mathbf{r}) = v(\mathbf{r}) + \frac{\delta E_{\text{coul}}[\rho]}{\delta\rho(\mathbf{r})} + \frac{\delta E_{\text{XC}}[\rho]}{\delta\rho(\mathbf{r})}, \tag{2.3.23}$$

This shows that selecting $\lambda(r)$ according to the above expression leads to the correct density derived from the single-particle Schrödinger equation. This leads to a set of N nonlinear integro-differential equations known as the Kohn-Sham (KS) equations. These equations need be solved in place of the many-body Schrödinger equation as follows,

$$\left[-\frac{1}{2}\nabla^2 + v_{\text{eff}}(\mathbf{r};\rho)\right]\psi_i = \varepsilon_i\psi_i, \tag{2.3.24}$$

in which case the effective potential can be written as follows

$$v_{\text{eff}}(\mathbf{r}) = v(\mathbf{r}) + \int \frac{\rho(\mathbf{r}')}{|\mathbf{r}-\mathbf{r}'|}d\mathbf{r}' + \frac{\delta E_{\text{XC}}}{\delta\rho(\mathbf{r})} = v(\mathbf{r}) + v_{\text{Hartree}}[\rho(\mathbf{r})] + v_{\text{XC}}[\rho(\mathbf{r})]. \tag{2.3.25}$$

The Kohn-Sham equations require an iterative solution until self-consistency is achieved. Here's a summary of the procedure: Start with an initial guess ρ_0 to construct the initial Kohn-Sham equation. After solving the eigenvalue problem, a new density is obtained. If the new density differs from the previous one beyond a certain threshold, the next step is to generate a new density by mixing these two densities. In the next iteration, the Hamiltonian is determined by this density, which in turn produces the new density for that iteration, and so on. This process continues until the densities from two successive steps converge to the same solution within a specified margin of error. The process is illustrated in Figure 2.1.

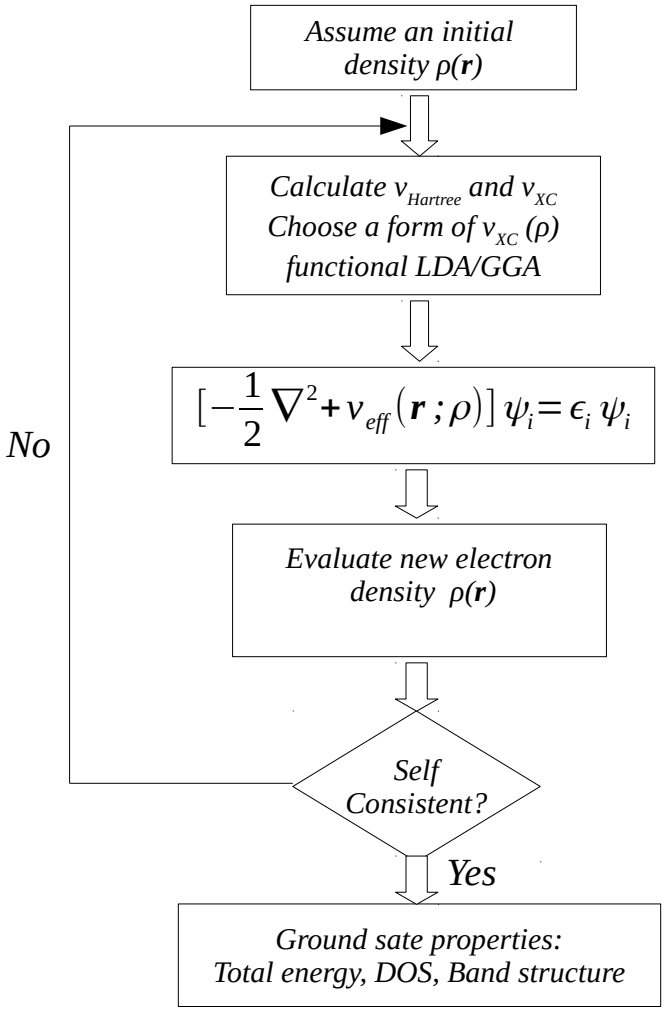

Figure 2.1: *The iterative process in Density Functional Theory (DFT) to achieve self-consistency.*

Extension to Spin-Polarized Systems

In the case of spin polarization, the electron density consists of two independent spin densities. It can be represented as follows,

$$\rho(\mathbf{r}) = \rho_{\uparrow}(\mathbf{r}) + \rho_{\downarrow}(\mathbf{r}). \tag{2.3.26}$$

Subsequently, the universal energy functional $F[\rho_{\uparrow}, \rho_{\downarrow}]$ accounts for contributions from both spin densities and can be formulated as:

$$F[\rho_{\uparrow}(\mathbf{r}), \rho_{\downarrow}(\mathbf{r})] = T_0[\rho_{\uparrow}, \rho_{\downarrow}] + \frac{e^2}{2} \int\int \frac{\rho(\mathbf{r}_1)\rho(\mathbf{r}_2)}{r_{12}} \, d\mathbf{r}_1 \, d\mathbf{r}_2 + E_{\mathrm{XC}}[\rho_{\uparrow}, \rho_{\downarrow}], \tag{2.3.27}$$

where $T_0[\rho_{\uparrow}, \rho_{\downarrow}]$ is the kinetic energy of the non-interacting spin-polarized electrons, and $E_{\mathrm{XC}}[\rho_{\uparrow}, \rho_{\downarrow}]$ is the exchange-correlation energy functional, now dependent on both spin

densities.

The total energy functional for the system is then given by,

$$E[\rho_\uparrow,\rho_\downarrow] = T_0[\rho_\uparrow,\rho_\downarrow] + \int v(\mathbf{r})\rho(\mathbf{r})\,d\mathbf{r} + \frac{e^2}{2}\int\int \frac{\rho(\mathbf{r}_1)\rho(\mathbf{r}_2)}{r_{12}}\,d\mathbf{r}_1\,d\mathbf{r}_2 + E_{\mathrm{XC}}[\rho_\uparrow,\rho_\downarrow]. \tag{2.3.28}$$

The spin-polarized Kohn-sham equations are:

$$\left[-\frac{1}{2}\nabla^2 + \lambda_\uparrow(\mathbf{r})\right]\psi_{i\uparrow} = \varepsilon_{i\uparrow}\psi_{i\uparrow}, \tag{2.3.29}$$

$$\left[-\frac{1}{2}\nabla^2 + \lambda_\downarrow(\mathbf{r})\right]\psi_{i\downarrow} = \varepsilon_{i\downarrow}\psi_{i\downarrow}. \tag{2.3.30}$$

The spin densities are obtained from the orbitals:

$$\rho_\uparrow(\mathbf{r}) = \sum_i |\psi_{i\uparrow}|^2, \tag{2.3.31}$$

$$\rho_\downarrow(\mathbf{r}) = \sum_i |\psi_{i\downarrow}|^2. \tag{2.3.32}$$

The kinetic energy functional is then evaluated as:

$$T_0[\rho_\uparrow,\rho_\downarrow] = \sum_i \varepsilon_{i\uparrow} + \sum_i \varepsilon_{i\downarrow} - \int d\mathbf{r}\left[\lambda_\uparrow(\mathbf{r})\rho_\uparrow(\mathbf{r}) + \lambda_\downarrow(\mathbf{r})\rho_\downarrow(\mathbf{r})\right]. \tag{2.3.33}$$

The energy functional that is used to find the equilibrium densities is as follows:

$$\begin{aligned} E[\rho_\uparrow,\rho_\downarrow] = \sum_i \varepsilon_{i\uparrow} + \sum_i \varepsilon_{i\downarrow} - \int d\mathbf{r}\left[\lambda_\uparrow(\mathbf{r})\rho_\uparrow(\mathbf{r}) + \lambda_\downarrow(\mathbf{r})\rho_\downarrow(\mathbf{r})\right] \\ + \int v(\mathbf{r})\rho(\mathbf{r})\,d\mathbf{r} + E_{\mathrm{coul}}[\rho] + E_{\mathrm{XC}}[\rho_\uparrow,\rho_\downarrow]. \end{aligned}$$

Minimizing the functional leads to the spin-dependent potentials:

$$\lambda_\uparrow(\mathbf{r}) = v(\mathbf{r}) + \frac{\delta E_{\mathrm{coul}}[\rho]}{\delta\rho_\uparrow(\mathbf{r})} + \frac{\delta E_{\mathrm{XC}}[\rho_\uparrow,\rho_\downarrow]}{\delta\rho_\uparrow(\mathbf{r})}, \tag{2.3.34}$$

$$\lambda_\downarrow(\mathbf{r}) = v(\mathbf{r}) + \frac{\delta E_{\mathrm{coul}}[\rho]}{\delta\rho_\downarrow(\mathbf{r})} + \frac{\delta E_{\mathrm{XC}}[\rho_\uparrow,\rho_\downarrow]}{\delta\rho_\downarrow(\mathbf{r})}. \tag{2.3.35}$$

This results in the spin-polarized Kohn-Sham equations:

$$\left[-\frac{1}{2}\nabla^2 + v_{\mathrm{eff},\uparrow}(\mathbf{r};\rho_\uparrow,\rho_\downarrow)\right]\psi_{i\uparrow} = \varepsilon_{i\uparrow}\psi_{i\uparrow}, \tag{2.3.36}$$

$$\left[-\frac{1}{2}\nabla^2 + v_{\text{eff},\downarrow}(\mathbf{r};\rho_\uparrow,\rho_\downarrow)\right]\psi_{i\downarrow} = \varepsilon_{i\downarrow}\psi_{i\downarrow}. \tag{2.3.37}$$

Here, the effective potentials are:

$$v_{\text{eff},\uparrow}(\mathbf{r}) = v(\mathbf{r}) + \int \frac{\rho(\mathbf{r}')}{|\mathbf{r}-\mathbf{r}'|}\,d\mathbf{r}' + \frac{\delta E_{\text{XC}}}{\delta\rho_\uparrow(\mathbf{r})} = v(\mathbf{r}) + v_{\text{Hartree}}[\rho(\mathbf{r})] + v_{\text{XC},\uparrow}[\rho_\uparrow(\mathbf{r}),\rho_\downarrow(\mathbf{r})], \tag{2.3.38}$$

$$v_{\text{eff},\downarrow}(\mathbf{r}) = v(\mathbf{r}) + \int \frac{\rho(\mathbf{r}')}{|\mathbf{r}-\mathbf{r}'|}\,d\mathbf{r}' + \frac{\delta E_{\text{XC}}}{\delta\rho_\downarrow(\mathbf{r})} = v(\mathbf{r}) + v_{\text{Hartree}}[\rho(\mathbf{r})] + v_{\text{XC},\downarrow}[\rho_\uparrow(\mathbf{r}),\rho_\downarrow(\mathbf{r})]. \tag{2.3.39}$$

The self-consistency procedure for the spin-polarized Kohn-Sham equations is similar to that for the non-spin-polarized case, except that spin-up and spin-down densities are treated separately. Initial estimates for $\rho_\uparrow$ and $\rho_\downarrow$ are used to construct the Kohn-Sham equations. These equations are solved iteratively until convergence is achieved within the predefined margin of error.

2.3.4 Exchange-Correlation Functional

So far, Kohn-Sham theory does not require any approximations, so in principle it is exact. However, the challenge arises with the term $E_{XC}[\rho]$, as the exact expression for this is unknown, requiring approximations. The Local Density Approximation (LDA) and the Generalized Gradient Approximation (GGA) are widely used and successful as approximate methods.

Local Density Approximation (LDA)

This approximation, first introduced by Kohn and Sham [6], is based on the core principles of Thomas-Fermi-Dirac theory [8, 9]. The key assumption in this approach is that the exchange-correlation energy depends only on the local electron density $\rho(r)$. The form of this functional can be written as,

$$E_{\text{XC}}^{\text{LDA}} = \int \rho(\mathbf{r})\varepsilon_{\text{XC}}[\rho(\mathbf{r})]\,d\mathbf{r}, \tag{2.3.40}$$

$E_{XC}[\rho(r)]$ is the exchange-correlation energy density of a homogeneous electron gas of density $\rho(r)$. In the Local Density Approximation (LDA), E_{XC} is determined by adding the contributions from the exchange and correlation parts separately.

$$\varepsilon_{\text{XC}}^{LDA}[\rho(\mathbf{r})] = \varepsilon_{\text{X}}^{LDA}[\rho(\mathbf{r})] + \varepsilon_{\text{C}}^{LDA}[\rho(\mathbf{r})]. \tag{2.3.41}$$

The exchange part $\varepsilon_X^{\mathrm{LDA}}[\rho]$ is given by the Dirac expression in a uniform electron gas,

$$\varepsilon_X^{\mathrm{LDA}}(\rho) = -\frac{0.458}{r_s} \tag{2.3.42}$$

where r_s represents the mean interelectronic distance, defined as,

$$\frac{4\pi}{3} r_s^3 = \rho^{-1} \tag{2.3.43}$$

The correlation part is more complex. E.P. Wigner [10H] initially estimated it as,

$$\varepsilon_C^{\mathrm{LDA}} \approx \frac{0.44}{r_s + 7.8} \tag{2.3.44}$$

Later, Ceperley and Alder [10] provided a more accurate estimate using quantum Monte Carlo simulations. This correlation functional is numerically exact and has been parameterized by Perdew and Zunger [11], Vosko, Wilk, and Nusair [12] John P. Perdew and Yue Wang [13].

In spin-polarized systems, the exchange-correlation (XC) energy density depends not only on the electron density ρ but also on the magnetization density $\zeta = (\rho_\uparrow - \rho_\downarrow)/(\rho_\uparrow + \rho_\downarrow)$. Generally, this is evaluated by interpolating between the fully polarized (ε_{XC}^P) and unpolarized (ε_{XC}^U) XC energy densities using an interpolation function that depends on ζ. Excellent approximate expressions for this interpolation function are available, such as those proposed by Barth and Hedin [14] and Vosko et al. [12].

The LDA is designed to work well in systems with slowly varying electronic charge density. However, it gives unexpectedly accurate results for inhomogeneous systems, as reviewed by R.O. Jones and O. Gunnarsson [15]. The reasons for this effectiveness are suggested to be related to several factors, such as,

- Only the spherical average of the xc-hole has an influence on the energy, i.e. the xc energy is given by

$$E_{XC}[\rho] = -\frac{1}{2} \int \frac{\rho(\mathbf{r})}{R(\mathbf{r})} d\mathbf{r} \tag{2.3.45}$$

where,

$$\frac{1}{R(\mathbf{r})} = \int \frac{\tilde{\rho}_{XC}(\mathbf{r}, \mathbf{r}')}{|\mathbf{r} - \mathbf{r}'|} d\mathbf{r}' \tag{2.3.46}$$

and $\tilde{\rho}_{XC}$ is the XC-hole, expressed as the pair correlation function $\tilde{g}(\mathbf{r}, \mathbf{r}')$,

$$\tilde{\rho}_{XC}(\mathbf{r}, \mathbf{r}') = \rho(\mathbf{r}')[\tilde{g}(\mathbf{r},\ \mathbf{r}') - 1] \tag{2.3.47}$$

- LDA satisfies the sum rule that the XC-hole contains exactly one electron, i.e,

$$\int \tilde{\rho}_{XC}(\mathbf{r},\mathbf{r}')\,d\mathbf{r}' = \int \rho(\mathbf{r})\tilde{g}^{\mathrm{LDA}}(|\mathbf{r}-\mathbf{r}'|,\rho(\mathbf{r}))\,d\mathbf{r}' = -1 \tag{2.3.48}$$

The LDA is quite effective in explaining phenomena involving energies related to ion motion, typically around 1 eV. However, it fails to describe phenomena that occur on much smaller energy scales, such as superconductivity, which involves energy scales of a few degrees Kelvin.

Generalized Gradient Approximation (GGA)

The Generalized Gradient Approximation (GGA) extends the Local Density Approximation (LDA) by including not only the local electron density $\rho(\mathbf{r})$ but also its gradient $\nabla\rho(\mathbf{r})$. This approach takes into account that the exchange-correlation energy depends on the spatial variations of the electron density, which provides a more accurate description for real systems.
The exchange-correlation energy in GGA can be expressed as, The functional can be expressed as,

$$E_{\mathrm{XC}}^{GGA}[\rho] = \int \varepsilon_{\mathrm{XC}}(\rho(\mathbf{r}),|\nabla\rho(\mathbf{r})|)\rho(\mathbf{r})\,d\mathbf{r} = \int \rho(\mathbf{r})\varepsilon_{\mathrm{XC}}[\rho(\mathbf{r})]F_{\mathrm{XC}}[\rho(\mathbf{r}),\nabla\rho(\mathbf{r})]\,d\mathbf{r} \tag{2.3.49}$$

In GGA, F_{XC} is referred to as the enhancement factor, which adjusts the LDA expression. There are different versions of GGA functionals, depending on the choice of the enhancement factor. Among them, Perdew and Wang (PW91) proposed a popular form of exchange-correlation functional in 1991. Subsequently, Perdew, Burke and Ernzerhof (PBE) introduced a simpler version by modifying PW91. GGA addresses some limitations of LDA and generally offers improved descriptions of properties like binding energy, total energy, structure, and magnetic properties of materials. However, it fails to capture long-range behavior (1/ R^6) and tends to overestimate electric polarization in polar systems. Particularly, it fails in case of strongly correlated systems, highlighting the need for more accurate treatment of electron-electron correlation.

2.4 Beyond DFT Exchange-Correlation: DFT+U

"DFT+U" is a method for modelling strongly correlated systems. It goes beyond the approximation of DFT. This method essentially involves an LSDA or GGA type calculation combined with an additional orbital-dependent interaction term handled in a Hartree-Fock-like manner. It includes the strong on-site Coulomb interaction, referred to as Hubbard U,

particularly to account for strongly localized orbitals like d and f orbitals. In this method, the energy of a system with a total number of d electrons N, given by $N = \sum_i n_i$, can be expressed including Hubbard correction as follows,

$$E = E_{\mathrm{LDA}} + \frac{U}{2}\sum_{i\neq j} n_i n_j - \frac{UN(N-1)}{2}. \tag{2.4.1}$$

The second term represents the Hubbard term, and any potential double counting is prevented by subtracting the third term. Orbital energies can be written as follows,

$$\varepsilon_i = \frac{\delta E}{\delta n_i} = \varepsilon_{\mathrm{LDA}} + U(\frac{1}{2} - n_i). \tag{2.4.2}$$

As a result, occupied orbitals with $n_i = 1$ are shifted by $-\frac{U}{2}$, while unoccupied orbitals ($n_i = 0$) are shifted by $+\frac{U}{2}$, as shown in Figure 2.2. This shift causes the lower and upper Hubbard bands to be separated by the Coulomb parameter U. Therefore, this method can effectively capture the essential physics of strongly correlated systems. The two prominent approaches of DFT+U are

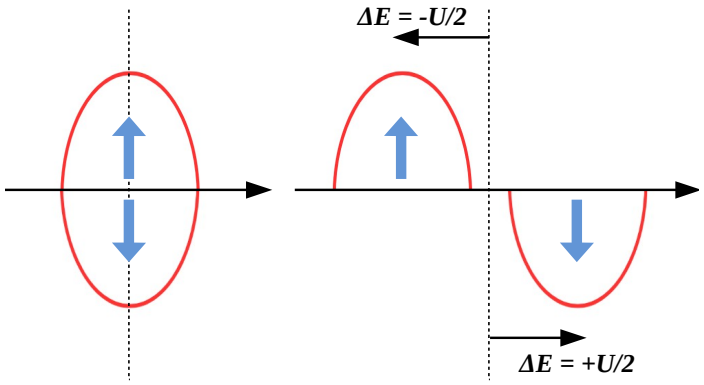

Figure 2.2: *Diagram illustrating the effect of the Hubbard U parameter on the electronic structure in LDA. The presence of U causes a relative shift between the occupied and unoccupied orbitals.*

2.4.1 Liechtenstein Method:

Liechtenstein et al. [16] introduced a generalized form of the DFT+U functional for multi-orbital correlated sites, which is outlined as follows,

$$E^{\mathrm{LDA}+U}[\rho^{\sigma}(\mathbf{r}), \{n^{\sigma}\}] = E^{\mathrm{LSDA/GGA}}[\rho(\mathbf{r})] + E^{U}[\{n_m^{I,\sigma}\}] - E_{\mathrm{dc}}[\{n^{I,\sigma}\}], \tag{2.4.3}$$

where the orbital occupancies $n_m^{I,\sigma}$ are used to describe atom I under the influence of on-site Hubbard interactions. Here, m represents the magnetic quantum number, σ denotes

the spin index, and $n^{I,\sigma}$ is the sum of these occupancies over all m. The last term accounts for correcting double-counting errors. Liechtenstein et al. have developed a rotationally invariant formulation for the Hartree-Fock-like term $E^U[n_m^{I,\sigma}]$.

$$\begin{aligned} E^U[\{n_m^{I,\sigma}\}] = \frac{1}{2}\sum_{\{m\},\sigma} & \left\langle m_1 m_3 \left| \frac{1}{\mathbf{r}-\mathbf{r}'} \right| m_2 m_4 \right\rangle n^{\sigma}_{m_1 m_2} n^{-\sigma}_{m_3 m_4} \\ & - \left\langle m_1 m_3 \left| \frac{1}{\mathbf{r}-\mathbf{r}'} \right| m_2 m_4 \right\rangle n^{\sigma}_{m_1 m_2} n^{\sigma}_{m_3 m_4} \\ & + \left\langle m_1 m_3 \left| \frac{1}{\mathbf{r}-\mathbf{r}'} \right| m_4 m_2 \right\rangle n^{\sigma}_{m_1 m_2} n^{\sigma}_{m_3 m_4} \end{aligned} \tag{2.4.4}$$

The matrix elements can be expressed as complex spherical harmonics and effective Slater integrals F^k [17] as

$$\left\langle m_1 m_3 \left| \frac{1}{\mathbf{r}-\mathbf{r}'} \right| m_2 m_4 \right\rangle = \sum_k a_k(m_1, m_2, m_3, m_4) F^k \tag{2.4.5}$$

where $0 \leq k \leq 2l$ and

$$a_k(m_1, m_2, m_3, m_4) = \frac{4\pi}{2k+1} \sum_{q=-k}^{k} \left\langle l m_1 \left| Y_{kq} \right| l m_2 \right\rangle \left\langle l m_3 \left| Y^{\dagger}_{kq} \right| l m_4 \right\rangle \tag{2.4.6}$$

For the d electrons, the required Slater integrals include F^0, F^2, and F^4, which can be characterized by two adjustable factors: the effective on-site Coulomb parameter denoted as U and the Stoner parameter denoted as J. These parameters are related as follows,

$$U = F^0 \tag{2.4.7}$$

$$J = \frac{F^2 + F^4}{14} \tag{2.4.8}$$

The expression for J for f electrons is,

$$J = \frac{286F^2 + 195F^4 + 250F^6}{6435} \tag{2.4.9}$$

In this approach, the term for correcting for double counting is expressed as follows,

$$E_{\mathrm{dc}}[n^{I,\sigma}] = \frac{U}{2} N(N-1) - \frac{J}{2}[N^{\uparrow}(N^{\uparrow}-1) + N^{\downarrow}(N^{\downarrow}-1)] \tag{2.4.10}$$

where $N^{\sigma} = \mathrm{Tr}(n^{\sigma}_{m_1 m_2})$ and $N = N^{\uparrow} + N^{\downarrow}$.

2.4.2 Dudarev Method:

The method proposed by Dudarev et al [18] offers a much simplified treatment, providing a rotationally invariant approach to DFT+U. Within this framework, the DFT+U energy functional can be expressed as,

$$E^{\text{LSDA+U}} = E^{\text{LSDA}} + \frac{U-J}{2}\sum_{\sigma}[\sum_{m_1} n^{\sigma}_{m_1,m_1} - \sum_{m_1,m_2} n^{\sigma}_{m_1,m_2} n^{\sigma}_{m_2,m_1}] \tag{2.4.11}$$

Here U and J are defined by the spherically averaged matrix elements of the screened Coulomb electron-electron interaction. The total number of electrons can be calculated from $N^{\sigma} = \sum_m n_{m,\sigma}$. In this approach, U and J are not treated separately, but their difference $U-J$ is used.

The effectiveness of the DFT+U method depends on the appropriate choice of U and J. It is possible to determine these values from first principles calculations using the constrained DFT method [19]. However, this often results in overestimated values. Therefore, the most common way is to calculate properties for a range of choice of the U values and fix the optimal one seeking agreement between calculated properties and experimental observations.

2.5 Various DFT-Based First-Principles Methods

To solve the single-particle KS equation and determine the eigenvalues and eigenfunctions, it is necessary to select a suitable basis set $\{\phi_\alpha(\mathbf{r})\}$ to expand the KS wave-functions $\Psi_i(\mathbf{r})$,

$$\Psi_i(\mathbf{r}) = \sum_{\alpha} C^i_{\alpha}\phi_\alpha(\mathbf{r}) \tag{2.5.1}$$

The choice of basis set $\{\phi_\alpha(\mathbf{r})\}$ is problem specific, such as the nature of the elements involved, the crystal structure. Over the last four decades, several basis sets have been developed and are widely used for the calculation of the band structure of solids. These methods can be broadly divided into two categories based on the choice of basis sets, fixed basis set methods and partial basis set methods.

2.5.1 Methods Using Fixed Basis Sets

This approach relies on basis sets that are not dependent on energy, such as the tight-binding method employing a linear combination of atomic orbitals (LCAO) type basis [20], and the orthogonalized plane wave (OPW) method. In the OPW method, plane waves orthogonal to the core states are used as the basis set within a pseudopotential framework [21, 22].

These methods reformulate the KS equations into an eigenvalue problem.

$$\sum_{\beta} \left(\tilde{H}_{\alpha\beta} - \varepsilon_i \tilde{O}_{\alpha\beta}\right) \tilde{C}^i_{\beta} = 0, \quad j = 1,2,\ldots,N \tag{2.5.2}$$

where,

$$\tilde{H}_{\alpha\beta} = \int d^3r\, \phi^*_{\alpha}(\mathbf{r}) \hat{H}(\mathbf{r}) \phi_{\beta}(\mathbf{r}) \tag{2.5.3}$$

$$\tilde{O}_{\alpha\beta} = \int d^3r\, \phi^*_{\alpha}(\mathbf{r}) \phi_{\beta}(\mathbf{r}) \tag{2.5.4}$$

In the following we will discuss the plane wave pseudopotential method, which is used extensively in this thesis.

Plane Wave Basis Pseudopotential Method:

Many first-principles methods based on the DFT use plane waves as basis functions to solve the KS equation. The popularity of this method is due to several factors:

- The basis is independent of atomic positions and types.
- There is no need for basis set corrections as the forces on the atoms are equivalent to the Hellmann-Feynman forces.
- It uses efficient algorithms such as Fast Fourier Transformation (FFT).

However, a significant limitation of this approach is the requirement for a large number of plane waves to accurately represent the wave function near the nucleus, referred to as the core region. In this region, electrons are tightly bound to the nucleus, leading to rapid oscillations in the wave functions due to orthogonality constraints with the valence electron wave functions. One approach to solving this problem is to replace the strong Coulomb potential of the nucleus and the effects of the tightly bound core electrons with an effective potential acting on the valence electrons, known as the pseudopotential, as described in Figure 2.3.

The process of generating pseudopotentials starts with solving the all-electron (AE) radial Schrödinger equation for a specific atomic arrangement, which defines the electron distribution in the atomic energy levels. This configuration is referred to as the reference configuration,

$$\left[\frac{1}{2}\frac{d^2}{dr^2} + \frac{l(l+1)}{2r^2} + V_{\text{eff}}[\rho]\right] r\phi^{nl}_{\text{AE}}(\mathbf{r}) = \varepsilon_{nl} r\phi^{nl}_{\text{AE}}(\mathbf{r}) \tag{2.5.5}$$

A pseudo wavefunction ϕ^{nl}_{ps} can be generated corresponding to ϕ^{nl}_{AE}, which ensures that there are no nodes inside the core of radius r_c. This pseudo wavefunction exactly matches

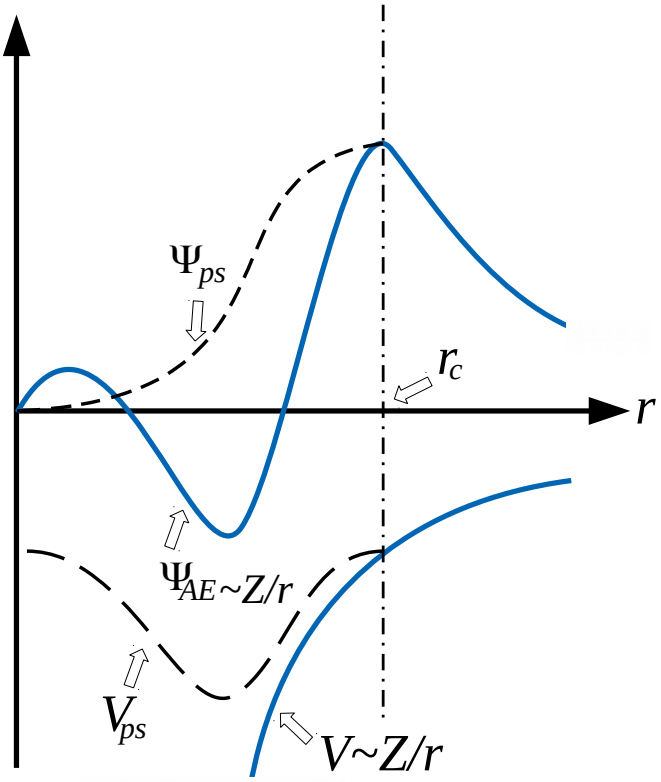

Figure 2.3: *Comparison of the all-electron (solid line) and pseudo (dashed line) wavefunctions and potentials. Beyond the cut-off radius r_c they converge and match.*

the AE wavefunction ϕ^{nl}_{AE} for $r \geq r_c$. The pseudopotential is then derived by solving the inverse Schrödinger equation.

$$V^l_{\mathrm{ps}}(r) = \varepsilon_l - \frac{l(l+1)}{2r^2} + \frac{1}{2}\frac{1}{r\phi^l_{\mathrm{ps}}}\frac{d^2}{dr^2}[r\phi^l_{\mathrm{ps}}] \tag{2.5.6}$$

Finally, the pseudopotential is obtained by subtracting the Hartree and exchange-correlation potentials, which are computed for the valence electrons.

$$V^{(ion)l}_{\mathrm{ps}} = V^l_{\mathrm{ps}} - V_{\mathrm{Hartree}}[\rho_{\mathrm{ps}}] - V_{\mathrm{xc}}[\rho_{\mathrm{ps}}] \tag{2.5.7}$$

Two main criteria are used to evaluate the quality of a pseudopotential: (i). Transferability, which measures its effectiveness in different environments. (ii). Softness, which measures the number of plane waves required.
Several approaches have been developed to fulfil these criteria. Two commonly used types of pseudopotentials are norm-conserving pseudopotentials and ultrasoft pseudopotentials.

- ⋆ **Norm-conserving pseudopotential**: Norm-conserving pseudopotentials (NCPP) [23] are formulated with an additional condition: the pseudo wavefunction must ensure that the charge within the core radius is the same for both the pseudo and all-electron

wavefunctions. This is represented as:

$$\int |\phi_{\mathrm{AE}}^{nl}(r)|^2\, dr = \int |\phi_{\mathrm{ps}}^{nl}(r)|^2\, dr \tag{2.5.8}$$

NCPPs generally perform satisfactorily for most elements, although exceptions exist, particularly for first-period 2p and 3d elements where the pseudo and all-electron wavefunctions are nearly indistinguishable.

⋆ **Ultrasoft pseudopotential**: Ultrasoft pseudopotentials, introduced by Vanderbilt [24], where he discards the norm-conservation requirement to achieve greater softness. This approach reduces the number of plane waves needed to represent the pseudo-wave functions at the cost of a more complex algorithmic formulation. Relaxing the norm-conservation condition allows for the independent formation of smooth pseudo-wavefunctions, ensuring that they match the wavefunctions at radius r_c. This flexibility allows the use of larger r_c values compared to norm-conserving pseudopotentials, with additional auxiliary functions and overlap operators ensuring the desired accuracy. The Vanderbilt pseudopotentials are implemented in several DFT software packages such as VASP [25, 26] and Quantum Espresso [27].

2.5.2 Methods Using Partial Basis Sets and Muffin-Tin Approximation

The key approximation in these methods is the Muffin-Tin (MT) approximation. In this approach, the potential is assumed to be spherically symmetric around each atom within a radius S_R, and a constant potential is assumed between the MT spheres, known as the interstitial region (as shown in Figure 2.4). A single MT potential can be described as,

$$v_{\mathrm{ext}}(r_R) = \begin{cases} v(\mathbf{r}_R) & \text{for } r_R \leq S_R, \\ -v_0 & \text{for } r_R > S_R, \end{cases} \tag{2.5.9}$$

where $r_R = |\mathbf{r} - \mathbf{R}|$. The basis set comprises two components:

(i) The rapidly varying part of the wavefunctions within the MT region, where the potential is spherically symmetric, is represented by the radial solution of the Schrödinger equation ($\phi_{Rl}(\varepsilon)$) at energy ε multiplied by spherical harmonics, known as partial waves.

(ii) In contrast, the smoothly varying part of the wave functions in the interstitial region, where the potential is constant, is represented by plane waves or other smoothly varying functions. Suitable boundary conditions at the sphere boundary are crucial for generating a well-behaved basis set in space. Various energy-dependent first-principles

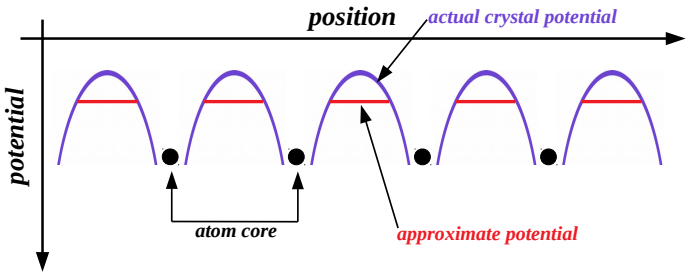

Figure 2.4: *Schematic representation of the Muffin-Tin (MT) potential, characterized by a spherically symmetric potential inside the MT radius and a constant potential outside.*

DFT-based methods have been developed based on the choice of interstitial representation and boundary conditions, such as the cellular method [28], the Korringa-Kohn-Rostocker (KKR) Green's function method [29], and the augmented plane wave (APW) method [30], etc.

The dependence of the partial waves on the energy leads to a secular equation of the following form:

$$\mathbf{M}(\varepsilon_i) \cdot \mathbf{C}^i = 0 \tag{2.5.10}$$

While this approach is highly accurate for band structure calculations, the energy dependence of the secular equations requires significant computational resources. In the early 1970s, Andersen [31] introduced a breakthrough by linearizing the energy-dependent partial waves, significantly reducing the computational requirements. The linear method employs a set of reference energies ε_ν. The solution of the radial Schrödinger equation (at these specific energies) and its first energy derivative are used to construct the radial basis functions:

$$\phi_{Rl}(\varepsilon) = \phi_{Rl}(\varepsilon_\nu) + (\varepsilon - \varepsilon_\nu)\dot{\phi}_{Rl}(\varepsilon_\nu) \tag{2.5.11}$$

This approach leads to a set of eigenvalue problems similar to those of fixed basis sets, but without the energy dependence of the Hamiltonian. In the following, we will describe two linearized methods that have been proposed based on partial waves.

Linearized Muffin-Tin Orbital Method (LMTO)

In the construction of Muffin-Tin Orbitals (MTO), the plane wave solutions in the interstitial region are expanded at a constant potential using spherical Neumann functions $\eta_l(\kappa, r_R)$ and Bessel functions $j_l(\kappa, r_R)$, where $\kappa^2 = \varepsilon - v_0$. These solutions smoothly connect with the partial waves at the boundary of the MT sphere to form MTOs. A simplified version of MTOs is achieved by the Atomic Sphere Approximation (ASA) [31], where the constant

κ is set to $\kappa = 0$. In this approximation, muffin-tin spheres, also known as Wigner-Seitz spheres, are replaced by space-filling atomic spheres. As $\kappa \to 0$, $\eta_l \to (r_R/S_R)^{-l-1}$ with a logarithmic derivative $D = -l-1$, and $j_l \to (r_R/S_R)^l$ with $D = l$. Under this approximation, a single MTO can be expressed as,

$$\chi^{\alpha}_{RL}(r_R,\varepsilon) = \phi_{RL}(r_R,\varepsilon)N^{\alpha}_{Rl}(\varepsilon) + \sum_{R'L'} j^{\alpha}_{l'}(r_{R'})[P^{\alpha}_{R'L'}(\varepsilon)\delta_{R'L',RL} - S^{\alpha}_{R'L',RL}] \tag{2.5.12}$$

where N^{α}_{Rl} represents the normalization factor, P^{α}_{Rl} denotes the potential function, and α is the screening constant regulating the range of MTOs. The connection between the potential function P^{α}_{Rl}, the parameter α, and the logarithmic derivative D_{Rl} is expressed as,

$$[P^{\alpha}_{Rl}]^{-1} = \left[2(2l+1)\frac{D_l + l + 1}{D_l - 1}\right]^{-1} - \alpha \tag{2.5.13}$$

The last term in equation (2.5.12) describes the tail of the MTO centered on the sphere of radius $S_{R'}$. This term is solely dependent on the structure and positions of the atoms, represented by the structure matrix S^{α}, and does not rely on the type of atoms at the sites. In terms of the canonical structure constant S^0, S^{α} is expressed as,

$$S^{\alpha} = S^0(1 - \alpha S^0)^{-1} \tag{2.5.14}$$

The energy dependence of the MTO basis gives rise to the general secular equations of the ASA-KKR type,

$$\det|P^{\alpha}_{R'L'}(\varepsilon)\delta_{R'L',RL} - S^{\alpha}_{R'L',RL}| = 0 \tag{2.5.15}$$

The LMTO basis functions can be written according to Andersen's linearization [31] approach as,

$$\chi^{\alpha}_{RL} = \phi_{RL}(r_R) + \sum_{R'L'} \dot{\phi}^{\alpha}_{R'L'}(r_{R'})h^{\alpha}_{R'L',RL} \tag{2.5.16}$$

The functions $\dot{\phi}^{\alpha}_{R'L'}(r_{R'})$ are expressed as linear combinations of ϕ and $\dot{\phi}$, given by:

$$\dot{\phi}^{\alpha}_{R'L'} = \dot{\phi}_{R'L'} + \phi_{R'L'}o^{\alpha} \tag{2.5.17}$$

Here, o^{α} represents the non-diagonal overlap matrix. The matrix h^{α} is defined as,

$$h^{\alpha} = C^{\alpha} - \varepsilon_{\nu} + (\Delta^{\alpha})^{1/2}S^{\alpha}(\Delta^{\alpha})^{1/2} \tag{2.5.18}$$

The diagonal potential matrices are denoted by C^{α} and Δ^{α}. These matrices rely on the potential inside the sphere, the selected screening parameter α, and the sphere radii. The

band center parameter, represented by C^{α}, is expressed as,

$$C^{\alpha} = \varepsilon_{\nu} - \frac{P^{\alpha}(\varepsilon_{\nu})}{\dot{P}^{\alpha}(\varepsilon_{\nu})} \tag{2.5.19}$$

and the band width is given by,

$$\sqrt{(\Delta^{\alpha})} = \frac{1}{\dot{P}^{\alpha}(\varepsilon_{\nu})} \tag{2.5.20}$$

Each set of screened LMTOs is characterized by the set of screening constants α_{Rl}, which can be chosen to ensure the LMTO set has a short range. The site-independent set of screening constants,

$$\alpha = \begin{cases} 0.3485 & \text{for } l = 0\,(s) \\ 0.05303 & \text{for } l = 1\,(p) \\ 0.010714 & \text{for } l = 2\,(d) \end{cases} \tag{2.5.21}$$

For *spd* orbitals, screening has been determined numerically [32] to yield short-ranged envelope functions suitable for all reasonably homogeneous three-dimensional structures. These corresponding LMTO sets are commonly known as tight-binding (TB) sets. The two-center nearly orthogonal TB-Hamiltonian is defined as follows,

$$H^{(1)}_{RL,R'L'} = \varepsilon_{\nu Rl}\delta_{RR'}\delta_{LL'} + h^{\alpha}_{RL,R'L'} \tag{2.5.22}$$

To achieve self-consistency, especially in open structures, it is often required to go beyond the limits of the ASA to achieve the desired level of accuracy. This is accomplished by introducing a correction term, referred to as the combined correction. The corrected Hamiltonian is defined as follows,

$$H^{(2)} = \varepsilon_{\nu} + h^{\alpha} - (\kappa^2_{\nu} + v_0)\partial_{\kappa^2}h^{\alpha} = C^{\alpha} + (\Delta^{\alpha})^{1/2}S^{\alpha}(\Delta^{\alpha})^{1/2} - (\kappa^2_{\nu} + v_0)\partial_{\kappa^2}h^{\alpha} \tag{2.5.23}$$

The Linearized Augmented Plane Wave Method (LAPW)

The Augmented Plane Wave (APW) basis set is particularly advantageous for capturing information localized in proximity to the nucleus, in comparison to pseudopotential methods. The behaviour of electrons near the nucleus can be accurately described by atomic-like wave functions, while electrons are delocalized in regions distant from the nucleus and can be described by plane waves. In a manner similar to the approach described in the LMTO method, the space is divided into muffin tin spheres and the interstitial region.

The linearized version of the augmented plane wave (LAPW) basis, inspired by Andersen's

linearization approach [31], is expressed as follows:

$$\chi_q(\mathbf{r},\varepsilon) = \begin{cases} \sum_{l,m} \left({A^q}_{lm,R} \Phi_{LR}(\mathbf{r}_R, \varepsilon_v) + {B^q}_{lm,R} \dot{\Phi}_{LR}(\mathbf{r}_R, \varepsilon_v) \right) & \text{for } r_R \leq S_R, \\ e^{i\mathbf{q}\cdot\mathbf{r}} & \text{for } r_R > S_R, \end{cases} \tag{2.5.24}$$

where the coefficients $A^q_{lm;R}$ and $B^q_{lm;R}$ are determined by matching boundary conditions. This is achieved by expanding the plane wave solution in the interstitial region using Bessel functions, specifically the Bessel function of the first kind, $j_l(r_R;q)$. While exact matching can be achieved by considering a large number of values of the index l, to maintain a manageable problem size, truncation at a certain value $l_{\max}$ is necessary. Consequently, the value of $l_{\max}$ assumes a primary role in LAPW basis set calculations for band structures, and a suitable selection is of greatest importance. The criterion is as follows,

$$R_i K_{\max} = l_{\max} \tag{2.5.25}$$

In LAPW, the cutoff for plane waves is determined by $K_{\max}$, where R_i is the radius of the i^{th} MT sphere. The term $R_i^{\min} K_{\max}$ controls the basis accuracy, where $R_i^{\min}$ is the smallest MT sphere radius in the unit cell.

Core states, which do not contribute significantly to chemical bonding, are treated similarly to free atoms. However, they are influenced by the potential due to valence states. The challenge arises in handling semi-core states, which lie between core and valence states. To address this issue, an additional set of basis functions, known as "local orbitals" can be introduced into the model. These are composed of a linear combination of two radial functions at two different energies and one energy derivative at one of these energies.

$$\phi^{LO}_{lm} = A_{lm,R}\phi_{LR}(r_R;\varepsilon_{v1}) + B_{lm,R}\dot{\phi}_{LR}(r_R;\varepsilon_{v1}) + C_{lm,R}\phi_{LR}(r_R;\varepsilon_{v2}). \tag{2.5.26}$$

The coefficients are chosen to ensure that ϕ^{LO} is normalized and has zero value and slope at the sphere boundary. Although incorporating local orbitals enlarges the size of the LAPW basis set, the number of functions remains relatively small compared to the typical LAPW basis set size of a few hundred functions.

The issue of energy dependence in the APW method is resolved in the LAPW+LO method, resulting in a slightly larger basis set size. Sjöstedt, Nordstrom, and Singh [33] introduced the APW+lo method, which maintains an energy-independent basis set of a similar size to that of the APW method. This approach combines the beneficial aspects of both the APW and LAPW+LO methods, thereby creating a new approach that is superior to either of the two original methods. The APW+lo basis set combines two types of functions. The first type is the standard APW basis function, where the partial wave is evaluated at a fixed

energy ε_v. The second type consists of local orbitals, denoted as "lo" to distinguish them from the "LO" functions used in the LAPW method. The local orbitals are defined as follows:

$$\phi_{lm}^{\mathrm{lo}} = A_{lm,R}^{lo}\phi_{LR}(r_R,\varepsilon_{v1}) + B_{lm,R}^{lo}\dot{\phi}_{LR}(r_R,\varepsilon_{v1}) \tag{2.5.27}$$

The coefficients $A_{lm,R}^{lo}$ and $B_{lm,R}^{lo}$ are determined by normalization and ensuring that the local orbital is zero at the MT boundary with a non-zero slope. Consequently, both the APW and local orbital functions are continuous at the sphere boundary, although their first derivatives are discontinuous. This approach converges to results nearly identical to those of the LAPW method [34], while significantly reducing $R_i^{\min}K_{\max}$ and consequently the computational time.

2.5.3 The Projector Augmented Wave (PAW) Method

The Projector Augmented Wave (PAW) method, introduced by Blöchl [35], is a general approach to the all-electron solution. It combines the simplicity of the plane wave pseudopotential method with the flexibility of the LAPW method.
In this method, a transformation τ is employed to map the true wave function ψ onto a smooth auxiliary wave function $\tilde{\psi}$. An augmentation region Ω_R is defined such that outside this region, the true wave function coincides with the auxiliary wave function. Inside the augmentation region, the true wave function is represented as $\psi = \tau\tilde{\psi}$. The transformation τ is defined as an identity plus a localized, atom-centered contribution $\hat{\tau}_R$,

$$\tau = 1 + \hat{\tau}_R \tag{2.5.28}$$

Within each augmentation region, each valence wave function ψ can be decomposed into the sum of atomic partial waves $\phi_m(r)$,

$$\psi(r) = \sum_m c_m\phi_m(r) \tag{2.5.29}$$

Here the atomic partial waves consist only of the valence states orthogonal to the core wave functions of the atom. Each partial wave corresponds to an auxiliary partial wave $\tilde{\phi}_m$,

$$\phi_m = \tau\tilde{\phi}_m \tag{2.5.30}$$

All auxiliary waves should match ϕ_m beyond a certain radius because the transformation operates locally in the core region. By ensuring that the transformation applies to any auxiliary wave function, the auxiliary wave function can be expanded into the auxiliary

partial waves with the same coefficients c_m,

$$\tilde{\psi} = \sum_m c_m \tilde{\phi}_m \tag{2.5.31}$$

Starting from Eqn. (2.3.90), the all-electron wave function can be expressed as,

$$\psi = \tilde{\psi} + \sum_m c_m(\phi_m - \tilde{\phi}_m) \tag{2.5.32}$$

The projection operator $\tilde{P}_m$ is then defined as,

$$c_m = \langle \tilde{P}_m | \tilde{\psi} \rangle \tag{2.5.33}$$

The projection operator explores the local character of the auxiliary wave function in the atomic domain. From the above equation, we can derive,

$$\sum_m |\tilde{\psi}\rangle\langle \tilde{P}_m| = 1 \tag{2.5.34}$$

which is valid within the augmentation range. To fully determine the projector operator, another condition is added,

$$\langle \tilde{P}_m | \tilde{\phi}_{m'} \rangle = \delta_{mm'} \tag{2.5.35}$$

The transformation is expressed in terms of projector operators as,

$$\tau = 1 + \sum_m (|\phi_m\rangle + |\tilde{\phi}_m\rangle)\langle \tilde{p}_m| \tag{2.5.36}$$

The true wave function can be expressed as,

$$\psi = \tilde{\psi} + \sum_m (\phi_m - \tilde{\phi}_m)\langle \tilde{p}_m | \tilde{\psi} \rangle \tag{2.5.37}$$

Any operator A in the original all-electron space can be represented as $\tilde{A}$ using the transformation τ,

$$\tilde{A} = \tau^* A \tau \tag{2.5.38}$$

The KS equation is transformed in a similar way to,

$$(\tilde{H} - \varepsilon \tilde{S})|\tilde{\psi}_i\rangle = 0 \tag{2.5.39}$$

where $\tilde{H} = \tau^* H \tau$ is the pseudopotential Hamiltonian and $\tilde{S} = \tau^* \tau$ is the pseudopotential overlap operator.

The PAW method, as implemented in VASP [25, 26], was used in this study.

2.6 Wannier Functions

In the tight-binding method, the Bloch wave functions can be extended by various local orbitals beyond the atomic orbitals. One such type of local orbitals are the Wannier functions, first proposed by G. Wannier [36].

2.6.1 NMTO based Wannier functions

To compute the single-electron components, such as orbitals, hopping integrals, and on-site terms of a correlated Hamiltonian, deriving a low-energy few-band Hamiltonian from the complete all-band Hamiltonian is essential. This process is accomplished using the downfolding technique. It involves partitioning the basis set space into two subsets: the lower subset $|l\rangle$ and the higher subset $|s\rangle$, and then reducing the full Hamiltonian H to the lower subset Hamiltonian $\tilde{H}_{ll}$. This reduction ensures that the lowest l eigenvalues of H are identical to the eigenvalues of $\tilde{H}_{ll}$. The formation of $\tilde{H}_{ll}$ introduces an additional energy dependence as follows,

$$\tilde{H}_{ll}(\varepsilon) = H_{ll} - H_{lh}(H_{hh} - \varepsilon)^{-1} H_{hl} \tag{2.6.1}$$

In the LMTO method, this procedure is carried out within the KKR equation by transforming the structure matrix S^{α} to β,

$$S^{\beta}_{ll} = S^{\alpha}_{li} + S^{\alpha}_{li}(P^{\alpha}_{ii} - S^{\alpha}_{ii})^{-1} S^{\alpha}_{il} \tag{2.6.2}$$

The additional energy dependence is managed through the linearization procedure in the LMTO construction. Although this approach addresses the issue of ghost bands, it lacks accuracy for extensive downfolds where downfolded bands occupy a narrow energy window. Limitations of the LMTO method include:

- The basis is complete up to $(\varepsilon - \varepsilon_{\nu})$ (i.e. first order) inside the sphere but only complete up to $(\varepsilon - \varepsilon_{\nu})^0 = 1$ (zeroth order) in the interstitial region, causing an inconsistency. This is corrected by eliminating the interstitial region using ASA.
- For open systems, non-ASA corrections (combined corrections) are included in the Hamiltonian matrix and the overlap matrix, which:
  1. Increases computational cost.
  2. Often requires expanding the basis through multi-panel calculation.

- The expansion of the Hamiltonian H in the orthogonal representation as a power series in the two-centered tight-binding Hamiltonian h,

$$\langle\chi|(H-\varepsilon_\nu)|\chi\rangle = h - h_0 h + \ldots \tag{2.6.3}$$

  is only achieved within ASA, excluding downfolding.

A more advanced method, based on the N^{th}-order muffin-tin orbital (NMTO), has been developed to address these limitations, providing an accurate description of the downfolded band structure within a chosen energy window. This method utilizes partial waves $\phi_{RL}(\varepsilon, r_R)$ within the atomic sphere and screened spherical waves (SSWs) instead of Neumann functions for the tail. The screening technique employed is as follows:

- Introduces a hard sphere of radius a and a phase-shifted partial wave solution $\phi^{\alpha 0}_{Rl}(\varepsilon, r_R)$ that matches the value and slope of ϕ at S_R, but their curvatures differ. For the hard sphere, $\phi^{\alpha 0}_{Rl}(\varepsilon, r_R)$ is continuous but with a kink to the SSW, $\phi^{\alpha}_{RL}(\varepsilon, r)$.

The combined form of these contributions, called the Kink Partial Wave (KPW), is given by

$$\psi^{\alpha}_{RL}(\varepsilon, r_R) = [\phi^{\alpha}_{RL}(\varepsilon, r_R) - \phi^{\alpha 0}_{RL}(\varepsilon, r_R)]Y_L(\hat{r}_R) + \phi^{\alpha}_{RL}(\varepsilon, r) \tag{2.6.4}$$

The members of the NMTO basis set $\chi^{(N)}_{R'L'}$ are constructed by Lagrange interpolation of $\psi^{\alpha}_{RL}(\varepsilon, r_R)$ evaluated at the energy points $\varepsilon_0, \ldots, \varepsilon_N$:

$$\chi^{(N)}_{R'L'} = \sum_{n=0}^{N} \sum_{RL \in A} \psi^{\alpha}_{RL}(\varepsilon_n, r_R) L^{N}_{RL,R'L'} \tag{2.6.5}$$

This basis set is energy selective and localized in nature. The energy-selective property allows the accurate selection of a narrow energy window from the full LDA band structure, with the accuracy tunable by the number of energy points (N). The NMTO downfolding technique also provides the underlying Wannier or Wannier-like basis, which are the effective orbitals that define the low-energy Hamiltonian. When the selected bands are isolated from other bands, the orthonormalized NMTOs are the Wannier functions. For strongly hybridized bands, however, the NMTOs define a Wannier-like basis.

2.6.2 Maximally localized Wannier functions

Although Wannier functions are sometimes delocalized at large bandwidths, they are typically Fourier transforms of the Bloch wave functions $\psi_{n\mathbf{k}}(\mathbf{r})$. Given the periodicity of $\psi_{n\mathbf{k}}(\mathbf{r})$ in the reciprocal lattice, expressed as $\psi_{n\mathbf{k}+\mathbf{G}}(\mathbf{r}) = \psi_{n\mathbf{k}}(\mathbf{r})$, where $\mathbf{G}$ is a reciprocal

lattice vector, $\psi_{n\mathbf{k}}(\mathbf{r})$ can be expanded in plane waves as,

$$\psi_{n\mathbf{k}}(\mathbf{r}) = \sum_{\mathbf{R}} w_n(\mathbf{r}-\mathbf{R}) e^{i\mathbf{k}\cdot\mathbf{R}} \tag{2.6.6}$$

where $w_n(\mathbf{r}-\mathbf{R})$ are the Wannier functions, which by Bloch's theorem depend only on $\mathbf{r}-\mathbf{R}$. The Wannier functions can be derived from inverse transformations such as

$$w_n(\mathbf{r}-\mathbf{R}) = \frac{\Omega_{\text{cell}}}{(2\pi)^3} \int_{\text{BZ}} e^{-i\mathbf{k}\cdot\mathbf{R}} \psi_{n\mathbf{k}}(\mathbf{r})\, d\mathbf{k} \tag{2.6.7}$$

where Ω_{cell} is the volume of the real-space primitive cell of the crystal. Due to the phase factor $\phi_n(\mathbf{k})$, these Wannier functions are not unique:

$$\psi_{n\mathbf{k}}(\mathbf{r}) \rightarrow \tilde{\psi}_{n\mathbf{k}}(\mathbf{r}) = e^{i\phi_n(\mathbf{k})} \psi_{n\mathbf{k}}(\mathbf{r}) \tag{2.6.8}$$

A more general form of Wannier functions is given by,

$$w_n(\mathbf{r}-\mathbf{R}) = \frac{\Omega_{\text{cell}}}{(2\pi)^3} \int_{\text{BZ}} e^{i\phi_n(\mathbf{k})} e^{-i\mathbf{k}\cdot\mathbf{R}} \psi_{n\mathbf{k}}(\mathbf{r})\, d\mathbf{k} \tag{2.6.9}$$

Moreover, there is flexibility in selecting a unitary matrix $U^{\mathbf{k}}_{nm}$ that transforms the N Bloch wave functions $\psi_{n\mathbf{k}}(\mathbf{r})$ at each wave vector $\mathbf{k}$ without altering the electronic energy functional in an insulator. This results in the most general construction of Wannier functions.

$$w_n(\mathbf{r}-\mathbf{R}) = \frac{\Omega_{\text{cell}}}{(2\pi)^3} \int_{\text{BZ}} \sum_{m=1}^{N} U^{\mathbf{k}}_{nm} e^{-i\mathbf{k}\cdot\mathbf{R}} \psi_{m\mathbf{k}}(\mathbf{r})\, d\mathbf{k} \tag{2.6.10}$$

where $U^{\mathbf{k}}$ is a $M \times N$ unitary matrix with $M \leq N$. This matrix is not necessarily square and can be chosen to construct M Wannier functions from N bands. The choice of $U^{\mathbf{k}}$ allows the construction of Wannier functions with desirable properties such as maximum localization. The widely used maximally localized Wannier functions proposed by Vanderbilt and coworkers [37, 38] minimize the quantity,

$$\Omega = \sum_{n=1}^{N} \left(\langle r^2 \rangle_n - \langle \mathbf{r} \rangle_n^2 \right) \tag{2.6.11}$$

where $\langle \cdots \rangle_n$ denotes the expectation value over the n-th Wannier function in the unit cell. Other Wannier functions are constructed to emphasize symmetries by projections onto local orbitals. The Wannier functions $w_n(\mathbf{r}-\mathbf{R})$ for all band n and lattice vector $\mathbf{R}$ form a

complete orthogonal set,

$$\int w_m(\mathbf{r}-\mathbf{R}_i)w_n(\mathbf{r}-\mathbf{R}_j)\,d\mathbf{r} = \delta_{m,n}\delta_{i,j} \tag{2.6.12}$$

The use of Wannier functions in the tight binding approach simplifies the overlap matrix $s_{m,n}(\mathbf{R})$,

$$s_{m,n}(\mathbf{R}) = \delta_{m,n}\delta_{\mathbf{0},\mathbf{R}} \tag{2.6.13}$$

which leads to,

$$S_{m,n}(\mathbf{k}) = \sum_{\mathbf{R}} e^{i\mathbf{k}\cdot\mathbf{R}} s_{m,n}(\mathbf{R}) = \delta_{m,n} \tag{2.6.14}$$

Consequently, the Hamiltonian equation simplifies to,

$$\sum_n H_{m,n}(\mathbf{k})b_n(\mathbf{k}) = \varepsilon_{\mathbf{k}} b_m(\mathbf{k}) \tag{2.6.15}$$

Wannier functions are typically derived from DFT calculations and serve as local orbitals in the tight-binding method. The hopping parameters $t_{m,n}(\mathbf{R})$,and on-site energy (ε_n) are obtained by fitting $\varepsilon_n(\mathbf{k})$ from tight-binding to DFT band structures. These parameters are then used to construct model Hamiltonians for the study of many-body effects. This approach works best for narrow-band systems where Wannier functions are more localized.

In this context, we have used Wannier90 [39] to generate maximally localized Wannier functions (MLWFs) from Bloch states. This is a very powerful and widely used band structure interpolation technique because of its ability to transform complex high-dimensional electronic structure calculations into more manageable low-dimensional problems by focusing on the low-energy physics of the system. In this thesis, three different basis sets were used, as follows:

- Muffin tin orbital (MTO)-based methods:
  - Linear MTO (LMTO) [31, 32]
  - Nth-order MTO (NMTO) [40]
- Plane wave-based method:
  - Used Vienna ab initio simulation package (VASP) for this purpose [26]
- Full-potential linear augmented plane wave (LAPW) method:
  - Used Wien2k for this purpose [41, 42]

2.7 Machine Learning

In recent years, machine learning (ML) has become an invaluable asset in the field of information technology, and its application has expanded to the discovery of new functional compounds. In order to explore the vast search space for materials with specific electronic and magnetic properties, here we used data-driven machine learning approaches. ML works by analyzing patterns from existing data (such as the available literature) and using them to make future predictions (material discovery). ML can be seen as a set of tools designed to uncover hidden patterns within the data, providing valuable information for predicting desired outcomes. In essence, it is a process of discovery using databases. The discovery of knowledge from databases can be broken down into the following key steps:

- Identify the target and gather the necessary prior knowledge about the domain, followed by the construction of an appropriate data set for knowledge extraction.
- Data preprocessing involves removing noise, handling missing attributes, and identifying relevant features to efficiently represent the data.
- Model selection involves choosing a machine learning algorithm based on prediction quality, applying it to the preprocessed dataset to extract knowledge, and analyzing the model to interpret discovered patterns.
- Validating the interpreted results on previously unseen data, that is, the prediction.

This thesis adopts a four-step ML process, which is schematically represented in Figure 2.5. Each step is briefly described in the following sections.

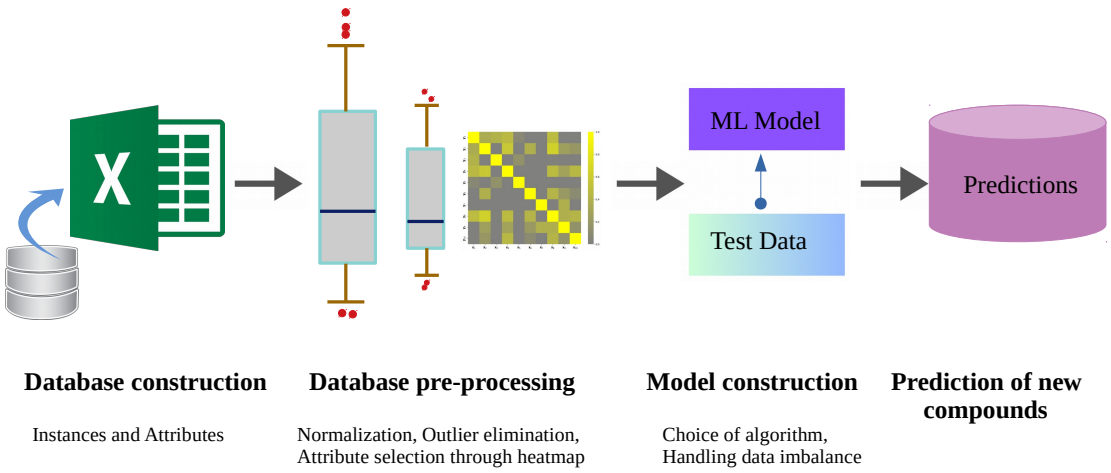

Figure 2.5: *Schematic representation of the steps that are used in the machine learning algorithm for the screening of stable compounds.*

2.7.1 Database Construction

The database includes two main components:

Instances: These are individual, independent examples that are used to develop the concept of the model. Instances are collected from existing literature and categorized or grouped according to certain characteristics.

Attributes: These are the specific features or characteristics that define the uniqueness of each instance. Selecting the appropriate set of attributes is a critical aspect of machine learning. In this work, attributes are selected based on either chemical or structural properties of the instances. This selection simplifies database construction as these attributes can be obtained without computational analysis.

2.7.2 Data Pre-processing

Data pre-processing is crucial in machine learning to improve the quality of raw data by converting it into a meaningful format. It also helps to understand the underlying trends in the dataset. In this study, data preprocessing included normalization using the bootstrapped sampling technique as shown in Figure 2.6, outlier removal and the elimination of correlated attributes using a heat map. This process can be summarized as follows:

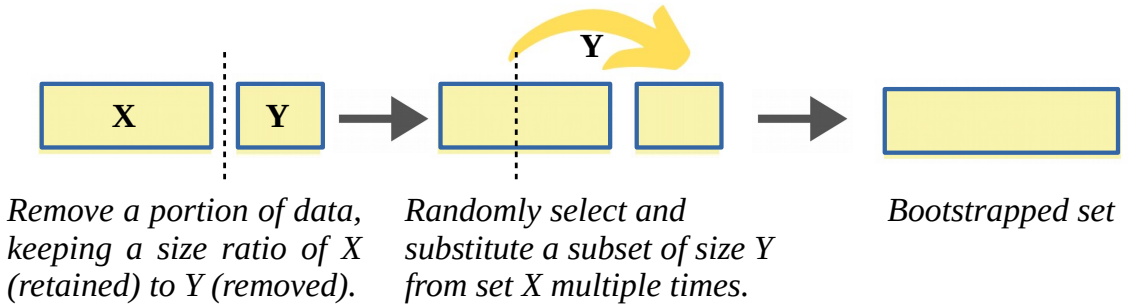

Figure 2.6: *Generation of a bootstrapped dataset through random re-sampling with replacement from the original dataset.*

Bootstrapping and Z-Score Renormalization

Given the wide range of numerical values in the dataset attributes, normalization is essential to standardize these values while preserving their relative differences. This was achieved using the Z-score normalization method, which can be described as follows,

$$\tilde{X} = \frac{X - \mu_X}{\sigma_X} \tag{2.7.1}$$

Where $\tilde{X}$ is the normalised attribute set, X is the original attribute set, and μ_X and σ_X are the population mean and standard deviation. As the actual population mean and standard deviation cannot be calculated directly due to the unavailability of the full distribution, these values are estimated from the dataset. A naive bootstrapping method is used, in which several subsets of the original dataset are created by resampling with random replacement. The bootstrapped datasets are created by replacing a quarter of the original dataset with randomly selected values from the rest of the dataset. This process is repeated until the averaged μ_X and σ_X of two consecutive steps differ by less than a specified threshold. The final averaged μ_X and σ_X are then used for normalization. A schematic diagram of the bootstrapping method is shown in Figure 2.7.

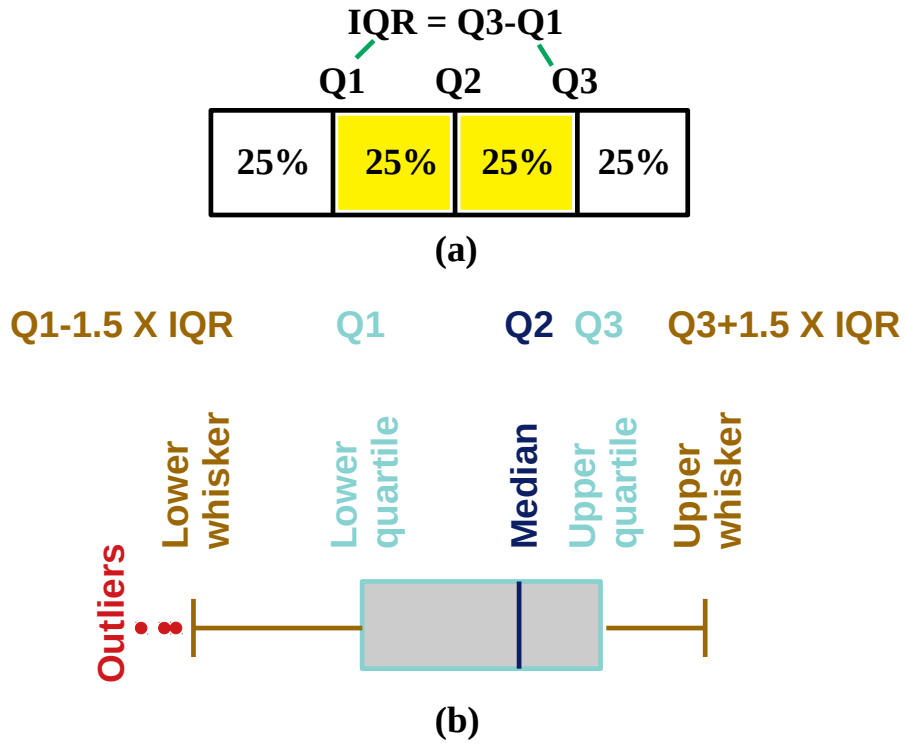

Figure 2.7: *Identification of outliers using a box plot. (a) The interquartile range (IQR) contains 50% of the data and Q2, the median, divides the distribution into two equal halves. (b) The lower and upper whiskers are defined by Q1-1.5×IQR and Q3+1.5×IQR respectively. In a Gaussian distribution, 99.3% of the values fall within this range, leaving only 0.7% as outliers.*

Outlier Elimination

The next step in data pre-processing involves identifying and removing outliers from the normalized dataset. The entire normalized dataset is ranked and divided into four equal parts known as quartiles: Q1, Q2, and Q3. The interquartile range (IQR), which is the difference between Q1 and Q3, provides a measure of the data spread. A box plot is commonly

used to visualize the data distribution in terms of quartiles. A data point is considered an outlier if it falls below $Q1 - 1.5 \times \text{IQR}$ or above $Q3 + 1.5 \times \text{IQR}$.

Attribute Selection

The final step is the evaluation of the correlation between pairs of attributes by means of the Pearson correlation coefficient, which is defined as follows,

$$r = \frac{\sum_{i=1}^{n}(x_i - \bar{x})(y_i - \bar{y})}{\sqrt{\sum_{i=1}^{n}(x_i - \bar{x})^2}\sqrt{\sum_{i=1}^{n}(y_i - \bar{y})^2}} \tag{2.7.2}$$

In this equation, n is the sample size, x_i and y_i are the sample points, and $\bar{x}$ and $\bar{y}$ are the sample means. The absolute value of r lies between 0 and 1, with values close to 1 indicating a high correlation between the corresponding attributes. To avoid bias in the machine learning model, such correlations need to be addressed and one of the correlated attributes should be removed. Figure 2.8 shows a heatmap illustrating the correlations between different attributes using the Pearson correlation coefficient.

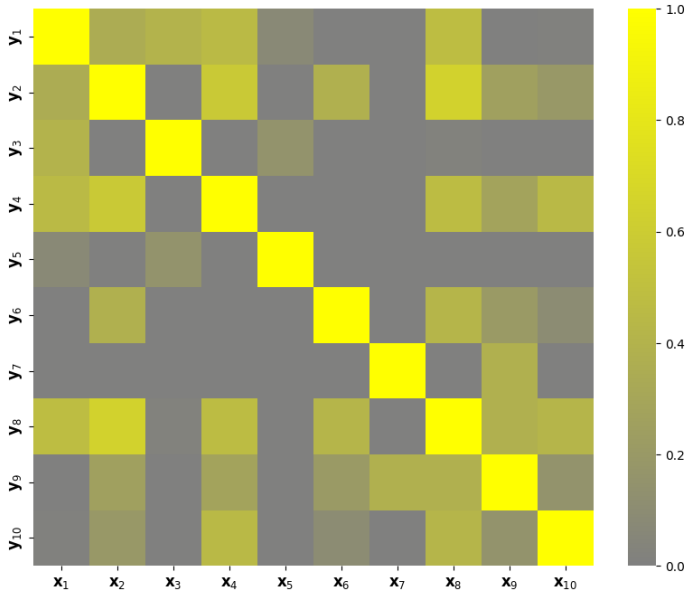

Figure 2.8: *Heatmap showing the correlation between different attributes. The colour intensity indicates the strength of the correlation, with grey boxes indicating weak or no correlation and yellow boxes indicating strong correlation.*

2.7.3 Model Construction

The final and most important step is to select an appropriate machine learning algorithm that can effectively identify the underlying patterns in the data set.

Supervised Learning: Supervised learning is a machine learning approach where the

model is trained on labelled data, meaning that each input is associated with a known output. The goal is to learn a function that can accurately map new inputs to their corresponding outputs. This technique is widely used for tasks such as classification, where the model predicts categorical labels, and regression, where the model predicts continuous values.

Unsupervised Learning: Unsupervised learning, on the other hand, deals with unlabelled data, where the model aims to identify hidden patterns or structures without predefined outputs. It is used for tasks such as clustering, where similar items are grouped together, and dimensionality reduction, which simplifies the data while retaining essential features.

In our thesis, we have focused exclusively on supervised learning algorithms for both regression and classification tasks, with the aim of using the known input-output pairs to build predictive models. Although a detailed analysis of each algorithm is beyond the scope of this thesis, we aim to provide an intuitive understanding of how each algorithm constructs a model. Many algorithms have both classification and regression versions, and we will discuss both types. Several supervised algorithms such as Ridge Regression (RR), Kernel Ridge Regression (KRR), Support Vector Regression (SVR), Random Forest (RF) and also Artificial Neural Networks (ANN) have been used for the regression problems and Random Forest (RF) has been used for the classification problem as discussed in the following section.

Ridge Regression (RR)

Ridge regression (RR) is an extension of linear regression that incorporates a regularization term to reduce overfitting and handle multicollinearity in data sets. Traditional linear regression attempts to minimize the sum of squared residuals between predicted and actual values, which can lead to overfitting, especially when the model is complex or the data are noisy. RR overcomes this problem by adding a penalty term to the loss function, which shrinks the regression coefficients towards zero. The regularization term in RR is the L2 norm of the coefficients, which is the sum of the squared values of the coefficients. Mathematically, the RR loss function can be expressed as,

$$\text{minimize } \|\mathbf{y} - X\beta\|_2^2 + \lambda\|\beta\|_2^2 \tag{2.7.3}$$

where $\mathbf{y}$ ($\in \mathbb{R}^n$) is the vector of target values, X ($\in \mathbb{R}^{n\times p}$) is the matrix of input features, where n is the number of samples and p is the number of features, β ($\in \mathbb{R}^p$) is the vector of coefficients, and λ (≥ 0) is the regularization parameter, which controls the trade-off between fitting the data and keeping the coefficients small to avoid overfitting. Some of the key aspects of RR are:

- **Regularization Parameter (λ)**: The value of λ determines the amount of regularization. A higher value of λ increases the penalty, resulting in smaller coefficients, which can reduce the variance, but may introduce bias. In contrast, a lower value of λ reduces the penalty, making the model more like an ordinary linear regression.

- **Bias-Variance Trade-off**: By including the penalty term, RR manages the bias-variance trade-off. It reduces variance (overfitting) by introducing some bias (underfitting), resulting in a model that generalizes better to new, unseen data.

- **Multicollinearity Handling**: In cases where the predictor variables are highly correlated (multicollinearity), RR can stabilize the estimation of the coefficients. It does this by shrinking correlated coefficients together, which ordinary least squares regression may not do well.

Kernel Ridge Regression (KRR)

Kernel Ridge Regression (KRR) extends the traditional Ridge Regression by using kernel functions to capture nonlinear relationships in the data. Whereas Ridge Regression considers a linear relationship between the input features and the target variable, KRR operates in a higher-dimensional space induced by the kernel function. In KRR, the regularization parameter λ controls the trade-off between fitting the training data and reducing the complexity of the model. The kernel function plays a crucial role in KRR by mapping the input features into a higher-dimensional space, where the relationship between the features and the target variable may become linearly separable. Mathematically, the objective function of KRR can be expressed as follows,

$$\text{minimize } \|\mathbf{y} - K\alpha\|_2^2 + \lambda \alpha^T K \alpha \tag{2.7.4}$$

where K ($\in \mathbb{R}^{n \times n}$) is the kernel matrix where $K = k(\mathbf{x}_i, \mathbf{x}_j)$, α ($\in \mathbb{R}^n$) is the vector of dual coefficients, λ (≥ 0) is the regularization parameter, and k $(\mathbf{x}_i, \mathbf{x}_j)$ is the kernel function. Some of the key aspects of KRR are,

- **Nonlinear Modeling**: KRR can capture nonlinear relationships between input features and a target variable. This flexibility allows KRR to model complex patterns in the data that may not be linearly separable.

- **Regularization**: Similar to RR, KRR incorporates regularization in order to prevent overfitting. The regularization parameter λ, controls the magnitude of the penalty term. This parameter is used to balance the complexity of the model and its performance in generalizing to new data.

- **Kernel Selection**: The selection of the kernel function is of crucial importance in KRR, as it determines the mapping of the input features into the higher-dimensional space. The most common kernel functions include linear, polynomial, radial basis function (RBF), and sigmoid kernels, which are suitable for different types of data and relationships.

Support Vector Regression (SVR)

Support Vector Regression (SVR) is a type of regression algorithm based on the principles of Support Vector Machines (SVM). Similar to SVM for classification, SVR aims to identify a hyperplane in a high-dimensional space that has the maximum margin and simultaneously minimizes the error for the data points that lie within a specified margin. The fundamental concept underlying SVR is the transformation of the original feature space into a higher-dimensional space through the application of a kernel function. In this higher-dimensional space, SVR seeks to identify a hyperplane that optimally fits the training data while maintaining a maximum margin. In contrast to traditional regression techniques, which aim to minimize prediction errors for all data points, SVR focuses on minimizing the error for data points within a margin, known as the epsilon-insensitive tube.

The objective function of SVR can be formulated mathematically as follows,

$$minimize \frac{1}{2}\|w\|_2^2 + C\sum_{i=1}^{n}(\xi_i + \xi_i^*) \tag{2.7.5}$$

subject to,

$$\begin{aligned} y_i - \langle w, \mathbf{x}_i\rangle - b &\leq \varepsilon + \xi_i \\ \langle w, \mathbf{x}_i\rangle + b - y_i &\leq \varepsilon + \xi_i^* \\ \xi_i, \xi_i^* &\geq 0 \end{aligned} \tag{2.7.6}$$

where $\mathbf{x}_i$ is the input feature vector, w and b are the coefficients of the hyperplane, ε is the margin of tolerance, ξ_i, ξ_i^* are slack variables for error terms, and C is the regularization parameter balancing margin width and error tolerance. The key aspects of support vector regression include,

- **Kernel Trick**: The SVR algorithm employs the kernel trick to map the input features into a higher-dimensional space, thereby enabling it to capture nonlinear relationships between the features and the target variable.

- **Epsilon-Insensitive Tube**: SVR introduces an epsilon-insensitive tube around the regression line, within which errors are not penalized. This allows SVR to focus on modeling the data points within the margin, while ignoring outliers outside the margin.

- **Regularization Parameter** (C): The regularization parameter C controls the trade-off between fitting the training data and maintaining a smooth regression function. A higher value of C allows for more flexible models that fit the training data closely, but may lead to overfitting.

Random Forest (RF)

Random Forest (RF) is a widely-used ensemble learning technique utilized for both classification and regression tasks. This approach involves building numerous decision trees during training and aggregating the results to make predictions. For classification tasks, RF outputs the mode of the classes predicted by individual trees, while for regression tasks, it provides the average prediction of the trees. The main features of Random Forest are as follows:

- **Bootstrap Aggregating (Bagging)**: RF uses a technique called bagging, where multiple decision trees are trained on different parts of the training data. Bootstrapping helps introduce diversity and reduce overfitting.
- **Random Feature Selection**: At each node, RF selects a random subset of features for splitting. This randomness makes the trees more diverse and improves the ensemble's performance.
- **Voting or Averaging**: RF combines the predictions of all individual trees for classification tasks, while for regression tasks, it averages them to obtain the final prediction.
- **Tuning Parameters**: RF offers several hyperparameters that can be tuned to optimize its performance, such as the number of trees in the forest, the maximum depth of the trees, and the minimum number of samples required to split a node.

Random Forest is good at handling lots of data. It is less likely to overfit than individual decision trees and often works well with little tuning.

In our thesis, we chose Random Forest for both classification and regression tasks because it is versatile and performs well. We used the ensemble nature of Random Forest to build accurate and robust models that can handle complex datasets.

Artificial Neural Networks (ANN)

Artificial Neural Networks (ANN) are computational models inspired by the organization and behavior of biological neural networks found in the human brain. ANNs comprise interconnected nodes, or neurons, arranged in layers: an input layer, one or more hidden layers, and an output layer. Each neuron processes inputs, performs computations, and

transmits the results to neurons in the subsequent layer. The fundamental components and characteristics of ANNs include:

- **Activation Functions**: In artificial neural networks (ANNs), neurons usually apply an activation function to the weighted sum of their inputs to introduce nonlinearity. The commonly used activation functions include sigmoid, hyperbolic tangent (tanh), and rectified linear unit (ReLU), each offering unique advantages and applications.

- **Learning Algorithms**: Artificial Neural Networks (ANNs) learn from data by a process known as training, during which the weights of connections between neurons are iteratively adjusted to minimize a loss function. Backpropagation, along with optimization algorithms like stochastic gradient descent (SGD), Adam, or RMSprop, is commonly employed for training ANNs.

- **Deep Learning**: Artificial Neural Networks (ANNs) with multiple hidden layers, also known as deep neural networks (DNNs), have become popular for their capability to learn intricate patterns from extensive datasets. Deep learning models have demonstrated state-of-the-art performance across various domains, such as image recognition, natural language processing, and speech recognition.

- **Hyperparameters**: Artificial Neural Networks (ANNs) have various hyperparameters that require tuning to optimize their performance, including the number of hidden layers, the number of neurons in each layer, the learning rate, and the strength of regularization. Hyperparameter tuning is typically performed using methods like grid search or random search.

2.7.4 Prediction of New Compounds

Finally, the machine learning model that has been developed is deployed in order to classify new instances. In order to achieve this, a dataset comprising the aforementioned new instances and the relevant attributes considered during the algorithm's training phase must be created. Subsequently, the trained algorithm predicts the class of each instance, typically providing a probability score. Instances with a high degree of confidence in the prediction are typically given priority for further investigation. In our study, these cases correspond to unknown compounds. Their treatment is described in detail in Chapter 3.

Bibliography

[1] M. Born and R. Oppenheimer. Zur quantentheorie der molekeln. *Annalen der Physik*, 389(20):457–484, 1927.

[2] D. R. Hartree. The wave mechanics of an atom with a non-coulomb central field. part i. theory and methods. *Mathematical Proceedings of the Cambridge Philosophical Society*, 24(1):89–110, 1928.

[3] C. C. J. Roothaan. New developments in molecular orbital theory. *Rev. Mod. Phys.*, 23:69–89, Apr 1951.

[4] C. David Sherrill. *An Introduction to Configuration Interaction Theory*. University Science Books, 1995.

[5] P. Hohenberg and W. Kohn. Inhomogeneous electron gas. *Phys. Rev.*, 136:B864–B871, Nov 1964.

[6] W. Kohn and L. J. Sham. Self-consistent equations including exchange and correlation effects. *Phys. Rev.*, 140:A1133–A1138, Nov 1965.

[7] W. Kohn. Nobel lecture: Electronic structure of matter—wave functions and density functionals. *Rev. Mod. Phys.*, 71:1253–1266, Oct 1999.

[8] L. H. Thomas. The calculation of atomic fields. *Mathematical Proceedings of the Cambridge Philosophical Society*, 23(5):542–548, 1927.

[9] Enrico Fermi. Un metodo statistico per la determinazione di alcune proprietà dell'atomo. *Rend. Accad. Naz. Lincei*, 6:602–607, 1927.

[10] D. M. Ceperley and B. J. Alder. Ground state of the electron gas by a stochastic method. *Phys. Rev. Lett.*, 45:566–569, Aug 1980.

[11] J. P. Perdew and Alex Zunger. Self-interaction correction to density-functional approximations for many-electron systems. *Phys. Rev. B*, 23:5048–5079, May 1981.

[12] S. H. Vosko, L. Wilk, and M. Nusair. Accurate spin-dependent electron liquid correlation energies for local spin density calculations: a critical analysis. *Canadian Journal of Physics*, 59:1200, August 1980.

[13] John P. Perdew and Yue Wang. Accurate and simple analytic representation of the electron-gas correlation energy. *Phys. Rev. B*, 45:13244–13249, Jun 1992.

[14] U. von Barth and L. Hedin. A local exchange-correlation potential for the spin polarized case. i. *Journal of Physics C Solid State Physics*, 5(13):1629–1642, July 1972.

[15] R. O. Jones and O. Gunnarsson. The density functional formalism, its applications and prospects. *Rev. Mod. Phys.*, 61:689–746, Jul 1989.

[16] A. I. Liechtenstein, V. I. Anisimov, and J. Zaanen. Density-functional theory and strong interactions: Orbital ordering in mott-hubbard insulators. *Phys. Rev. B*, 52:R5467–R5470, Aug 1995.

[17] B. R. Judd. *Operator Techniques in Atomic Spectroscopy*. McGraw-Hill, New York, 1963.

[18] S. L. Dudarev, G. A. Botton, S. Y. Savrasov, C. J. Humphreys, and A. P. Sutton. Electron-energy-loss spectra and the structural stability of nickel oxide: An lsda+u study. *Phys. Rev. B*, 57:1505–1509, Jan 1998.

[19] Pui-Wai Ma and S. L. Dudarev. Constrained density functional for noncollinear magnetism. *Phys. Rev. B*, 91:054420, Feb 2015.

[20] J. C. Slater and G. F. Koster. Simplified lcao method for the periodic potential problem. *Phys. Rev.*, 94:1498–1524, Jun 1954.

[21] Conyers Herring. Some theorems on the free energies of crystal surfaces. *Phys. Rev.*, 82:87–93, Apr 1951.

[22] James C. Phillips and Leonard Kleinman. New method for calculating wave functions in crystals and molecules. *Phys. Rev.*, 116:287–294, Oct 1959.

[23] D. R. Hamann, M. Schlüter, and C. Chiang. Norm-conserving pseudopotentials. *Phys. Rev. Lett.*, 43:1494–1497, Nov 1979.

[24] David Vanderbilt. Soft self-consistent pseudopotentials in a generalized eigenvalue formalism. *Phys. Rev. B*, 41:7892–7895, Apr 1990.

[25] G. Kresse and J. Hafner. Ab initio molecular dynamics for liquid metals. *Phys. Rev. B*, 47:558–561, Jan 1993.

[26] G. Kresse and J. Furthmüller. Efficient iterative schemes for ab initio total-energy calculations using a plane-wave basis set. *Phys. Rev. B*, 54:11169–11186, Oct 1996.

[27] Stefano Baroni, Stefano de Gironcoli, Andrea Dal Corso, and Paolo Giannozzi. Phonons and related crystal properties from density-functional perturbation theory. *Rev. Mod. Phys.*, 73:515–562, Jul 2001.

[28] E. Wigner and F. Seitz. On the constitution of metallic sodium. ii. *Phys. Rev.*, 46:509–524, Sep 1934.

[29] J. Korringa. Early history of multiple scattering theory for ordered systems. *Physics Reports*, 238(6):341–360, 1994.

[30] T. L. Loucks. *Augmented Plane Wave Method; a Guide to Performing Electronic Structure Calculations*. W. A. Benjamin, 1967.

[31] O. Krogh Andersen. Linear methods in band theory. *Phys. Rev. B*, 12:3060–3083, Oct 1975.

[32] O. K. Andersen and O. Jepsen. Explicit, first-principles tight-binding theory. *Phys. Rev. Lett.*, 53:2571–2574, Dec 1984.

[33] E Sjöstedt, L Nordström, and D.J Singh. An alternative way of linearizing the augmented plane-wave method. *Solid State Communications*, 114(1):15–20, 2000.

[34] Georg K. H. Madsen, Peter Blaha, Karlheinz Schwarz, Elisabeth Sjöstedt, and Lars Nordström. Efficient linearization of the augmented plane-wave method. *Phys. Rev. B*, 64:195134, Oct 2001.

[35] P. E. Blöchl. Projector augmented-wave method. *Phys. Rev. B*, 50:17953–17979, Dec 1994.

[36] Gregory H. Wannier. The structure of electronic excitation levels in insulating crystals. *Phys. Rev.*, 52:191–197, Aug 1937.

[37] Nicola Marzari and David Vanderbilt. Maximally localized generalized wannier functions for composite energy bands. *Phys. Rev. B*, 56:12847–12865, Nov 1997.

[38] Ivo Souza, Nicola Marzari, and David Vanderbilt. Maximally localized wannier functions for entangled energy bands. *Phys. Rev. B*, 65:035109, Dec 2001.

[39] Arash A. Mostofi, Jonathan R. Yates, Giovanni Pizzi, Young-Su Lee, Ivo Souza, David Vanderbilt, and Nicola Marzari. An updated version of wannier90: A tool for obtaining maximally-localised wannier functions. *Computer Physics Communications*, 185(8):2309–2310, 2014.

[40] O. K. Andersen and T. Saha-Dasgupta. Muffin-tin orbitals of arbitrary order. *Phys. Rev. B*, 62:R16219–R16222, Dec 2000.

[41] O. Jepsen, J. Madsen, and O. K. Andersen. Band structure of thin films by the linear augmented-plane-wave method. *Phys. Rev. B*, 18:605–615, Jul 1978.

[42] Peter Blaha, Karlheinz Schwarz, Georg K H Madsen, Dieter Kvasnicka, Joachim Luitz, Robert Laskowsk, Fabien Tran, Laurence Marks, and Laurence Marks. *WIEN2k: An Augmented Plane Wave Plus Local Orbitals Program for Calculating Crystal Properties*. Techn. Universitat, 2019.

3

Prediction of the Properties of the Rare-Earth Magnets $Ce_2Fe_{17-x}Co_xCN$: A Combined Machine-Learning and Ab Initio Study*

3.1 Introduction and Motivation

Permanent magnets are a part of almost all technologies, starting from acoustic transducers, motors and generators, magnetic field and imaging systems to more recent technologies, such as computer hard-disk drives, medical equipment, magnetomechanics, etc. [1]. The search for efficient permanent magnets is thus everlasting. In this connection, the family of rare-earth (RE) and 3d transition metal (TM)-based intermetallics has evolved over the last 50 years or so and has transformed the landscape of permanent magnets [2, 3]. Two of the most prominent examples of RE-TM permanent magnets that are currently in commercial production, together with hard magnetic ferrites, are $SmCo_5$ and $Nd_2Fe_{14}B$. While $SmCo_5$ and $Nd_2Fe_{14}B$ provide reasonably good solutions, keeping in mind the resource criticality of RE elements like Nd and Sm, a significant amount of effort has been directed towards the search for permanent magnets without, or with less content of, critical RE elements. The idea is to optimize the price-to-performance ratio [2]. This has led to two routes: (a) the search for potential magnets devoid of rare-earth elements [4] and (b) the design of rare-earth lean intermetallics using abundant RE elements such as La and Ce instead of Sm

*This chapter is based on publication: Anita Halder, **Samir Rom**, Aishwaryo Ghosh, and Tanusri Saha-Dasgupta, Phys. Rev. Applied 14, 034024 (2020).

and Nd [5–7]. As stressed by Coey [8], seeking low-cost magnets with a maximum Energy product to bridge ferrites and the presently used RE magnets is needed. Following route (b), cheap ternary and quaternary RE lean RE-TM intermetallics need to be investigated, since binaries have already been well explored. In parallel, due to Co being expensive, it may be worthwhile to focus on intermetallic compounds containing Fe.

Starting from the simplest binary RE-TM structure of $CaCu_5$, by replacing n out of m RE (R) sites with a pair of TM (M) sites, $R_{m-n}M_{5m+2n}$ structures are obtained. This can give rise to several possible binary structures of different chemical compositions, listed in order of RE leanness: RM_{13} (7.1%), RM_{12} (7.7%), R_2M_{17} (10.5%), R_2M_{14} (12.5%), RM_5 (16.7%), R_6M_{23} (20.7%), R_2M_7 (22.2%), RM_3 (25%), RM_2 (33%), etc. Judging by the rare-earth content, 1:13, 1:12, 2:17, 2:14 compounds may form examples of rare-earth lean materials. It is desirable to modify the known binary compounds containing low-cost REs belonging to these families to achieve the best possible intrinsic magnetic properties, namely (i) high spontaneous or saturation magnetization ($\mu_0 M_s$), at least around 1 T, (ii) a Curie temperature (T_c) high enough for the contemplated device use, 600 K or above, and (iii) a mechanism for creating sufficiently high easy-axis coercivity (K_u). The synthesis and optimization of properties of real materials in experiments is both time-consuming and costly and is mostly based on trial and error. A computational approach in this connection is of natural interest to screen compounds before they can be suggested and tested in the laboratory. Typical computational approaches in this regard are based on density-functional-theory (DFT) calculations. A detailed calculation estimating all required magnetic properties, i.e., M_s, T_c, K_u from first principles is expensive and also not devoid of shortcomings. For example, estimation of T_c relies on parametrization of DFT or supplemented U-corrected theory of DFT+U total energies to construct a spin Hamiltonian and a solution of the spin Hamiltonian by the mean field or Monte Carlo method. While this approach works for localized insulators, its application to metallic systems with itinerant magnetism is questionable, as it fails even for elemental metals, such as Fe, Co, and Ni [9]. A more reasonable approach of DFT+dynamical mean field (DMFT) [10] is significantly more expensive. An alternative approach is to use a machine-learning (ML) technique based on a suitable training dataset. This approach has been used for RE-TM permanent magnets based on a DFT-calculated magnetic properties database of M_s and K_u [5, 11]. Creation of a database based on calculations, even with high-throughput calculations, is expensive and relies on the approximations of the theory. It is far more desirable to build a dataset based on experimental results, and then train the ML algorithm based on that. However, the size and availability of the experimental data in the required format can be a concern. Focusing on the available experimental data on RE lean intermetallics, the set of T_c is largest, followed by that for K_u and M_s. While the quantitative values of T_c in

kelvins or degrees Celsius are available in the literature, for magnetocrystalline anisotropy often only the information about whether they are easy axis or easy plane is available. Similarly, the $\mu_0 M_s$ values are reported either in μ_B/f.u. or in emu/gm or in tesla; conversion from μ_B/f.u. and emu/gm to tesla requires information of the volume and density, which may introduce inaccuracies up to one decimal point. Restricting experimental data to those containing values of K_u and $\mu_0 M_s$ in the same format (either tesla or μ_B/f.u. or emu/gm) reduces the dataset of K_u and M_s significantly, making the application of ML questionable. We thus use a two-pronged approach, as illustrated in Figure 3.1. We first create a database

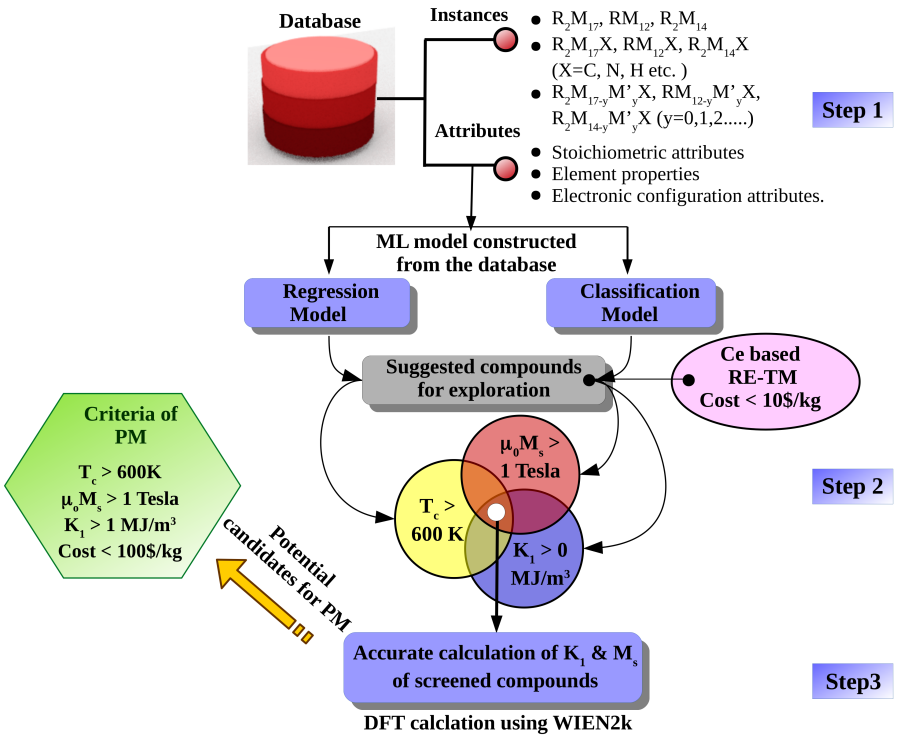

Figure 3.1: *Steps of a Machine-Learning-Combined DFT Approach for Predictions of Properties in $Ce_2Fe_{17-x}Co_xCN$ Permanent Magnets.*

of T_c, M_s, and K_u from the available experimental data on RE lean intermetallics, and use ML for prediction of T_c values, for estimating whether $\mu_0 M_s$ satisfies the criteria of being larger than 1 T, and for predicting the sign of K_u. For M_s and K_u, ML thus serves the purpose of initial screening. We next evaluate M_s and the magnetic anisotropy properties based on elaborate DFT calculations. Calculation of the magnetic anisotropy energy (MAE) is challenging due to its extremely small value. However, since the pioneering work of Brooks [12], several studies [6, 13–15] have shown that U-corrected DFT generally reproduces the orientation and the right order of magnitude of the MAE.

We demonstrate the applicability of our proposed approach on Ce- and Fe-based 2:17 RE-TM intermetallics, $Ce_2Fe_{17-x}Co_xCN$ compounds ($x = 1, \ldots, 7$). Our choice is based on the following criteria: (a) the compounds contain rare-earth Ce, which is the cheapest

within the RE family with a market price of approximately 5 USD/kg [16]. The cost of other components Fe, C, and N are all < 1 USD/kg. The price of Co is higher than Fe [16], being the less abundant metal. The Co:Fe ratio is thus restricted within 0.4. (b) Co substitution in place of Fe has been reported [17, 18] to be efficient in simultaneous enhancements of K_u as well as T_c in several TM magnets. This is in sharp contrast to other TM substitutes, such as Ti, Mo, Cr, and V, where magnetic anisotropy as well as T_c are generally suppressed. (c) The search space belongs to the 2:17 family, which is the family in which most of the instances in our training set belong to. (d) This class of compounds is found to be more stable than the well-explored 1:12 compounds. (e) For large saturation magnetization, it is desirable to use Fe-rich compounds, which are also less expensive compared to Co. (f) Although Ce has a negative second-order Stefan factor, which favors in-plane MAE, experimental findings support that nitrogenation and carbonation can switch the MAE from easy plane to easy axis [19]. (g) Although R_2Fe_{17} compounds display a large magnetization value due to high Fe content, these compounds are disadvantageous as they exhibit low Curie temperature [20]. The presence of Co, as well as C/N interstitials, help in increasing T_c. (h) While magnetic properties of carbonitrides are expected to be similar to those of nitrides for sufficiently high concentration of N, carbonitride compounds have been proven to show better thermal stability [21].

Our study suggests that Fe-rich $Ce_2Fe_{17-x}Co_xCN$ compounds may form potential candidate materials for low-cost permanent magnets, satisfying the necessary requirements of a permanent magnet with $T_c > 600$ K, $\mu_0 M_s > 1$ T, and easy axis $K_u > 1$ MJ/m^3. The calculated maximal energy product and estimated anisotropy field, which are technologically interesting figures of merit for hard-magnetic materials, turn out to be within the reasonable range. Some of the studied compounds may possibly bridge the gap between the low maximal energy product and high anisotropy field for $SmCo_5$ and vice versa for $Nd_2Fe_{14}B$.

3.2 Machine Learning Approach

3.2.1 Database construction and training of the model

Aiming to search not-yet-explored candidates for permanent magnets, we use a supervised machine-learning (ML) algorithm, which helps us to screen compounds with high T_c ($T_c > 600$ K), high M_s ($\mu_0 M_s > 1$ T), and easy-axis anisotropy ($K_u > 0$) among the huge number of possible candidates of unexplored RE-TM intermetallics. The first step of any ML algorithm is to construct a dataset. We construct three datasets of existing RE-TM compounds for T_c, M_s, and K_u separately using the following sources: ICSD [22], the handbook of magnetic materials [23], the book of magnetism and magnetic materials [24], and other

relevant references [11, 19, 21, 25–59, 59–75]. To construct the database of rare-earth lean compounds, the RE percentage in the intermetallic compounds is restricted to 14%, which includes the four different binary RE-TM combinations namely RM_{12}, RM_{13}, R_2M_{17}, and R_2M_{14} along with their interstitial and derived compounds. We discard RM_{13} from the dataset as only a few candidates are available from this series with known experimental T_c, M_s, and K_u.

We list a total of 565 compounds with reported experimental T_c, among which the majority of compounds (about 55%) belong to the R_2M_{17} series. The minimum contribution to the dataset comes from the R_2M_{14} (about 10%) family. The highest T_c in the dataset belongs to the R_2M_{17} class of compounds namely Lu_2Co_{17} [25] with $T_c \sim 1203$ K and the compound with the lowest T_c is $NdCo_{7.2}Mn_{4.8}$ (approximately 120 K) [23], a member from the RM_{12} family. In the dataset, all three compositions with RE to TM ratio 2:17, 2:14, and 1:12 show a large variation in T_c, having the difference between maximum and minimum values as 1051, 775, and 991 K, respectively. There exist a few compounds in the dataset with more than one reported value of T_c. For example, T_c of $SmFe_{10}Mo_2$ has been reported with two different values of 421 K [76] and 483 K [77]. There are other examples of such multiple T_c [78–82]. The quality of the sample, their growth conditions, coexistence of compounds in two or multiple phases, and accuracy of the measurements may lead to the multiple values of T_c reported for a particular compound. In such cases, we consistently consider the largest among the reported values of T_c. Notably, in the majority of cases, we find little variation in the reported values of T_c (approximately 20–50 K).

The dataset of M_s is relatively smaller than T_c, containing only 195 entries. The majority of compounds in this dataset belong to the 2:17 composition similar to the database of T_c. The relatively smaller dimension of the M_s dataset is primarily due to the fact that experimental reports available for M_s are much less than for T_c. Secondly, M_s has mostly been reported at room temperature, but in some cases at low temperature. To maintain uniformity of the dataset, we consider M_s reported at room temperature, resulting in a lesser number of compounds in the M_s dataset.

Reports with quoted values of anisotropy constant are even more rare. Our exhaustive search resulted in only 73 data points. This pushes the dataset size to the limit of ML algorithms, for which predictive capability becomes questionable due to large bias masking the small variance [83]. On the other hand, if we also allow for experimental data only reporting the sign of K_u, this dataset gets expanded to a reasonable size of 258.

After constructing the dataset, we carry out preprocessing of the data, as outlined in Ref. [84]. It comprises the removal of noisy data, outliers, and correlated attributes. While constructing the database, we avoid inclusion of noisy data. We perform bootstrapping to normalize the data, followed by the removal of outliers with the help of a violin plot.

Data is removed if it lies outside of $Q1 - 1.5 \times \text{IQR}$ or $Q3 + 1.5 \times \text{IQR}$, where IQR is the interquartile range and $Q1$, $Q2$, and $Q3$ are the lower, median, and upper quartiles, respectively. In the next step, we identify correlated attributes using Pearson's correlation coefficient, which can be defined as:

$$r = \frac{\sum_{i=1}^{n}(x_i - \bar{x})(y_i - \bar{y})}{\sqrt{\sum_{i=1}^{n}(x_i - \bar{x})^2 \sum_{i=1}^{n}(y_i - \bar{y})^2}}$$

where n is the sample size, x_i and y_i are sample points, and $\bar{x}$ and $\bar{y}$ are the sample means.

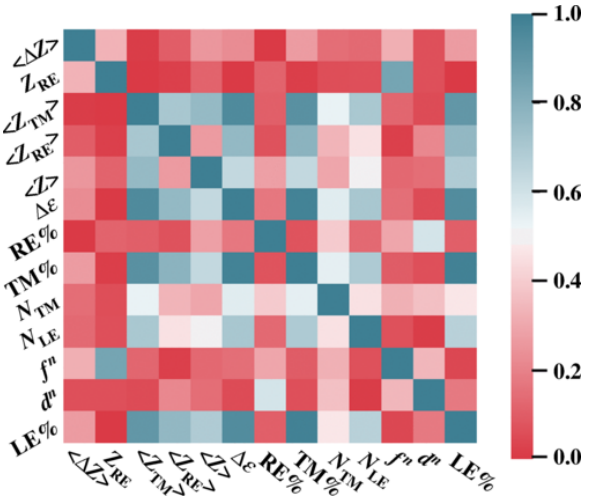

Figure 3.2: *Heatmap indicating the correlation between different attributes considered to built ML algorithm. The color code is shown in the side panel. The boxes with red represent weak or no correlation, whereas blue boxes represent strong correlation between the attributes.*

The heatmap obtained using the above-mentioned correlation is shown in Figure 3.2. The correlation between the attributes is mapped between 0 and 1, considering the absolute values. The highly correlated attributes with correlation greater than 0.75 are as follows:

1. Electronegativity difference between RE and TM ($\Delta\varepsilon$) and CW average of atomic number of TM ($\langle Z_{\text{TM}} \rangle$).
2. CW TM percentage (TM%) and CW average of atomic number of TM ($\langle Z_{\text{TM}} \rangle$).
3. CW TM percentage (TM%) and electronegativity difference between RE and TM ($\Delta\varepsilon$).
4. Total number of f electrons (f^n) and atomic number of RE (Z_{RE}).
5. LE percentage (LE%) and CW average of atomic number of TM ($\langle Z_{\text{TM}} \rangle$).
6. LE percentage (LE%) and electronegativity difference between RE and TM ($\Delta\varepsilon$).

7. LE percentage (LE%) and CW TM percentage (TM%).

We thus discard $\Delta\varepsilon$, LE%, Z_{RE}, and $\langle Z_{\mathrm{TM}} \rangle$ from the list of attributes.

The next and most crucial step is to construct a set of simple attributes, which are capable of describing the instances (in this case, RE-TM compounds) and then deploy the ML algorithm to map them to a target (in this case, T_c, M_s, and K_u). The attributes considered in this study are summarized in Table 3.1, which can be divided into three broad categories, namely, stoichiometric attributes, element properties, and electronic configuration attributes. The stoichiometric attributes may contain information of both elemental and compositional properties as suggested by Ward et al. [85]. This is based on taking compositional weights (CW) of elemental properties.

Table 3.1: *List of 13 different attributes with description, notation, and range used in the ML algorithm. Here "CW" stands for "composition-weighted."*

Attribute type	Attribute	Notation	Value range
Stoichiometric	CW absolute deviation of atomic no.	$< \Delta Z >$	1.70-16.74
	CW av. of atomic no. of TM	$< Z_{TM} >$	10–33.30
	CW av. of atomic no. of LE	$< Z_{LE} >$	0–9.79
	CW av. Z	$< Z >$	21.08–37.71
	CW electronegativity diff. of RE and TM	$\Delta\varepsilon$	0.61–1.84
	CW RE percentage	RE%	4.76–14.29
	CW TM percentage	TM%	38.46–95.24
	CW LE percentage	LE%	0–53.85
Element	Atomic no. of RE	Z_{RE}	58–71
	Presence of more than one TM	N_{TM}	yes/no
	Presence of LE	N_{LE}	yes/no
Electronic	Total no. of f electrons	f_n	1-28
	Total no. of d electrons	d_n	30-136

In the third step, we train different popular machine-learning (ML) algorithms with the constructed dataset for prediction. We use the ML algorithm in three different problems: (a) to predict the compounds with T_c more than 600 K, (b) compounds with $\mu_0 M_s > 1$ T, and (c) compounds with easy-axis anisotropy. Regression is used in the former case, whereas the latter two cases are treated as classification problems. We use five different ML algorithms for regression in the case of T_c, namely ridge regression (RR) [86], kernel ridge regression (KRR) [87], random forest (RF) [88, 89], support vector regression (SVR) [90],

and artificial neural network (ANN) [91]. The performance of a model can be quantified in terms of the coefficient of determination, which can be expressed as follows [92]:

$$R^2 = 1 - \frac{\sum_{i=1}^{N}[y_i - f(x_i)]^2}{\sum_{i=1}^{N}[y_i - \mu]^2}$$

for predictions $f(x_i)$ and a set of actual values y_i with mean μ. If the algorithm performs perfectly, the R^2 score is 1. Figure 3.3 shows the R^2 score for five different algorithms.

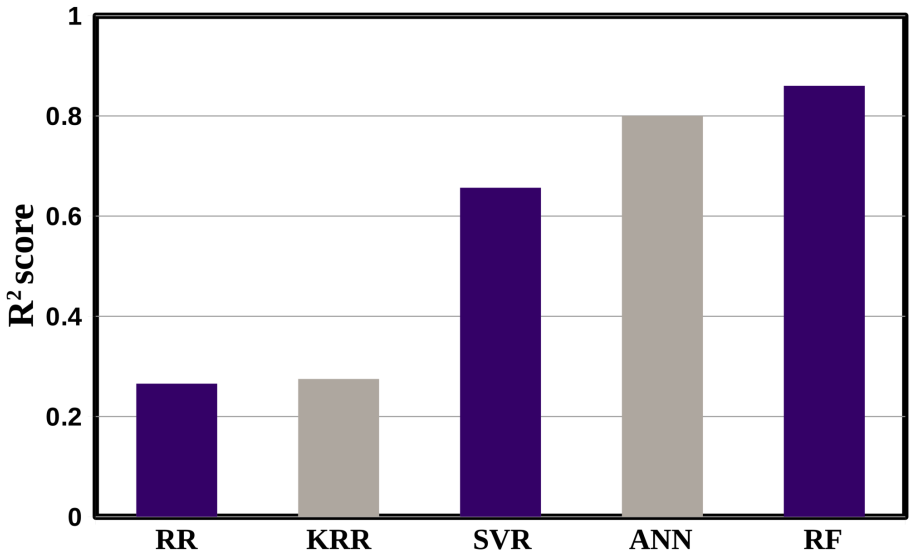

Figure 3.3: *Coefficient of determination R^2 score of five different ML algorithms applied to the T_c dataset.*

The RR algorithm circumvents issues in ordinary linear regression like overfitting or failure in finding a unique solution due to multicollinearity. It develops on least-squares error by adding an extra penalty and regularization term to the loss function of ordinary linear regression. KRR builds on the ridge-regression technique by using a kernel trick [93] so that it can capture the nonlinearity present in the feature space. It can fit a nonlinear function by learning from a linear function spanned by a kernel, which in turn mimics a nonlinear function in the original space. SVR originated from support vector machines, which are mainly popular in the classification problem. It is based on the idea to search a hyperplane [94] by minimizing the error that is able to separate two different classes. SVR also uses the kernel trick to map the data into a high-dimensional feature space and then performs linear regression to fit the data. These three models are based on the same principle of linear regression and SVR is the best form according to our result. The R^2 score is 0.66 for SVR whereas it is found to be poor (approximately 0.25) for the other two algorithms.

Apart from these, we use two other algorithms, ANN and RF. The model performance

scores are satisfactory for both of them. A simple ANN architecture called perceptron implements a processing element or artificial neuron called threshold logic unit (TLU), which can have one or more inputs and one output. Each input is related to a weight. The TLU calculates the weighted sum of its inputs, applies a step function (generally Heaviside or sign function) to it, and outputs the result. A perceptron [95] is simply a layer of TLUs operating in parallel and connected to all the inputs. Training an ANN model is equivalent to learning each weight factor in an iterative cycle. A more complex system (multilayer perceptron) can be built by associating additional interconnected layers to the architecture. A well-functioning system consists of an input layer, several hidden layers, and an output layer. In our case, we have one input layer, two hidden layers where rectified linear unit (ReLU) [96] is used as the activation function along with L2 regularization in the kernel, and an output layer. The constructed ANN model shows 0.80 as R^2 score.

Random forest is an ensemble method, which consists of multiple decision trees. Each tree is built on a portion of the entire training data with a subset of the total number of attributes. The tree algorithm is based on a "top to bottom" approach, starting from a root node, it consists of many intermediate nodes and ends at leaf nodes. At each node of a tree, a particular attribute classifies the data and helps to grow the tree. The prediction is based on accumulating the results from all such trees, taking ensemble average in the case of regression or considering votes from majority trees in the case of classification. Such an algorithm can capture the complex and nonlinear interaction between different attributes and can build a robust and sophisticated model. Our random forest consists of 100 trees built by bootstrapped [97] sampling of the training set. Each tree allows checking a maximum of $\log_2$ (number of features) while detecting the best split node. The quality of such a split is measured by using mean squared error (Gini index) in regression (classification). The model efficiency is calculated by running out-of-bag samples down each of the trees. We use tenfold cross-validation to extract the hyperparameter and to construct the best model.

Figure 3.4 shows the result of the best regression model using the RF algorithm in the case of T_c. The plot in the left panel shows the predicted T_c versus T_c obtained from experiments. The determination score R^2 is high enough (0.86), indicating a good agreement between the predicted T_c and experimentally reported T_c. The mean absolute error in this model is 60 K. Additionally, we evaluate absolute error and relative error for the compounds with $T_c > 600$ K (cf. Figure 3.4, right panel). This analysis helps to determine the model performance for the compounds with $T_c > 600$ K as we are interested to predict RE-TM intermetallics with high T_c. The distribution of absolute error shows that for most of the compounds (approximately 85%) the absolute error is less than 100 K. For 65% of the predicted cases, the absolute error is less than 50 K. We also check the absolute error for the compounds with $T_c < 300$ K (not included in the figure). In this case, our model

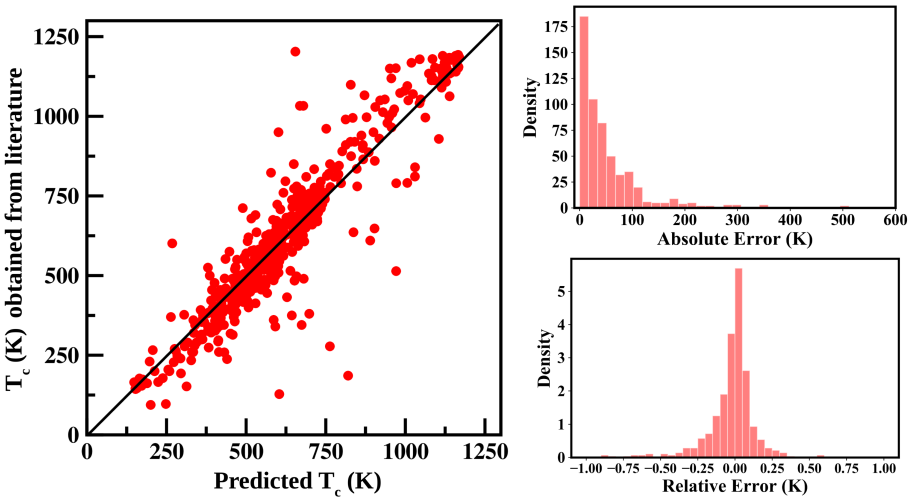

Figure 3.4: *Model output from RF algorithm for T_c of RE-TM intermetallics. The left panel shows the comparison of T_c obtained from the literature and predicted T_c. The distribution of absolute error between predicted T_c and actual T_c is shown in the upper right panel, while the lower right panel presents the distribution of relative error for the compounds with $T_c > 600$ K.*

predicts approximately 76% of compounds with an absolute error less than 100 K and 50% of instances are predicted with an absolute error of 50 K. This observation prompts us to conclude that though the model prediction is in general good, it is less accurate for low T_c compounds compared to high T_c compounds. The distribution of relative error, expressed as $\varepsilon_{\text{rel}} = \frac{T_c^{\text{exp}} - T_c^{\text{predicted}}}{T_c^{\text{exp}}}$, provides further support to this statement, which is shown in the bottom, right panel of Figure 3.4. The relative error distribution appears Gaussian-like with slight asymmetry about the mean position. The relative error is less on the right side of the mean position than on the left side suggesting the prediction of T_c suffers less overestimation than underestimation. As found, only 1% of the instances are having $\varepsilon_{\text{rel}} > 50\%$, 3% of the instances have $50\% > \varepsilon_{\text{rel}} > 30\%$, and 2% of instances have $30\% > \varepsilon_{\text{rel}} > 25\%$, most cases having tiny values of ε_{rel}. This gives us confidence in the accuracy of the predicted T_c for compounds with T_cs exceeding 600 K.

Turning to M_s, we use the random-forest algorithm to classify high M_s from low M_s compounds. The best model by performing tenfold cross-validation is built up with 81.53% accuracy. The resultant confusion matrix is shown in Figure 3.5. For classification problems, the F1 score determines the balance between precision and recall. In this case, the F1 score of 82.2% indicates good anticipation with slight favor towards the prediction of compounds with high M_s ($\mu_0 M_s > 1$) (83.8%) compared to the compounds with low M_s ($\mu_0 M_s < 1$) (79.2%).

Similar to M_s, we use the random-forest algorithm for K_u, to classify positive K_u from negative K_u compounds. The best model by performing tenfold cross-validation, in this

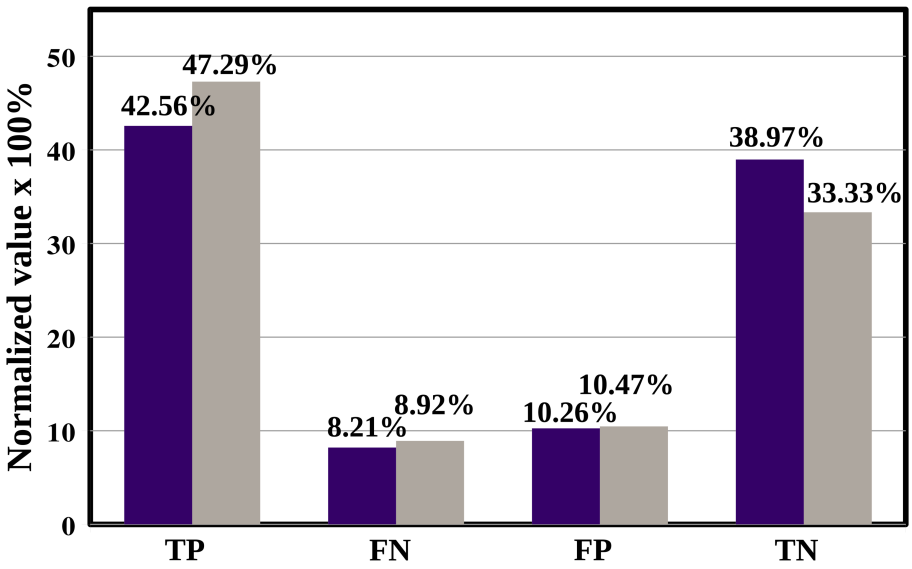

Figure 3.5: *Normalized confusion matrix for $\mu_0 M_s$ (violet) and K_u (gray) classification using tenfold cross-validation. Here positive (negative) class represents either compounds with $\mu_0 M_s > (<)$ 1 T, or compounds with uniaxial anisotropy, i.e., $K_u > (<)$ 0 MJ/m^3. True positive and negative or TP and TN are the compounds where their classes are predicted correctly. Whereas false positive (FP) and false negative (FN) are the off-diagonal terms of the matrix where the classes are incorrectly classified.*

case, is built up with 80.62% accuracy. Like M_s, in this case, the F1 score for positive K_u is 83% and for negative K_u is 77.5% suggesting a slight preference of classification towards positive K_u, which is also captured in the plot of the confusion matrix as shown in Figure 3.5.

Out of the five different ML algorithms, it is seen that random forest performs best, which has also been successfully used for prediction of Heusler compounds [98], half-Heusler compounds [99], double perovskite compounds [84], half-Heusler semiconductors with low thermal conductivity [100], zeolite crystal-structure classification [101], etc. Results presented in the following are based on the random-forest method.

3.2.2 Model evaluation

The final step is to employ the trained algorithm on yet-to-be synthesized RE-TM compounds, and thus to explore unexplored compositions with targeted properties. We choose $Ce_2Fe_{17-x}Co_xC_yN_z$ ($y,z = 0/1$; $x = 0\ldots8$) as the exploration set for application of the trained ML algorithm. This results in a set of 36 compounds among which eight compositions ($Ce_2Fe_{17-x}Co_xCN$, $x = 1,\ldots,8$) have not been reported experimentally or theoretically. We apply our trained ML algorithms on all of these 36 compounds and the results are summarized in Figure 3.6. The top panel of Figure 3.6 shows the predicted T_c of all the compounds. It is seen that the nitrogenation or carbonation increases the T_c with respect to

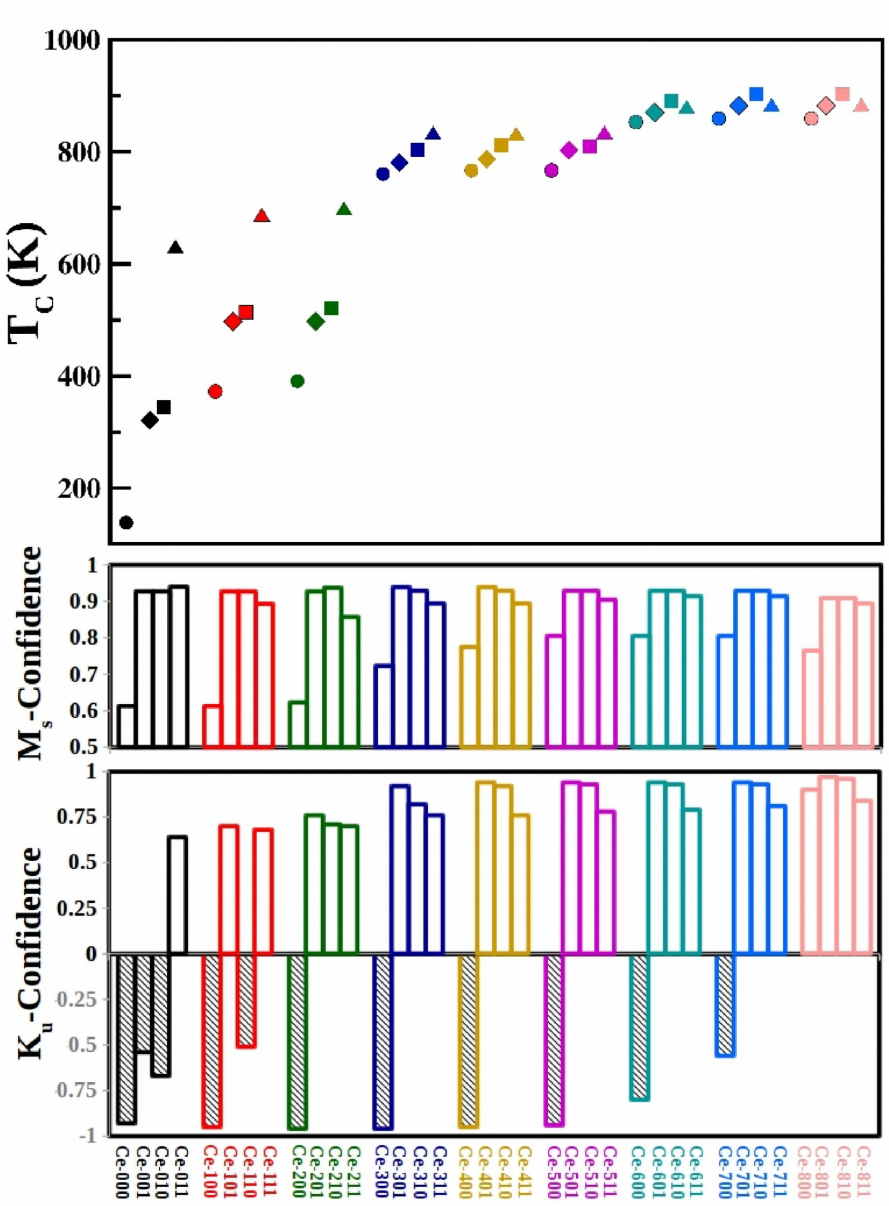

Figure 3.6: *ML predictions of Curie temperature (T_c) from regression model, and saturation magnetization (M_s) and anisotropy constant (K_u) from classification model. The upper (middle/lower) panel shows the results of T_c (M_s/K_u). The exploration set is $Ce_2Fe_{17-x}Co_xC_yN_z$ where y and z can have values either 0 or 1, and $x = 0 \ldots 8$, acronymed as xyz. In the top panel, noninterstitial compounds, carbonated, nitrogenated, and carbonitrogenated compounds are symbolized by circle, diamond, square, and upper triangle. Different colors specify compounds with different x values. The middle panel shows the ML prediction confidence for M_s. In the lower panel, ML prediction confidence for K_u is illustrated. Here the upper (lower) half having bars with no-fill (shaded) shows the confidence for the compounds with positive (negative) K_u.*

their respective parent compound $Ce_2Fe_{17-x}Co_x$. Our ML model predicts that the nitrides have higher T_c than that of the carbides. For $x \leq 5$, the enhancement of T_c is maximum for the compounds where both carbon and nitrogen are present. For $x > 5$, T_c shows a slight

decrease compared to only the nitrogenated case. It is also noted that the relative rise in T_c in interstitial compounds compared to parent compounds decays gradually with Co concentration. The increase in T_c varies from approximately 200 to 10 K as x varies from 0 to 8 for carbides and nitrides, whereas introduction of both nitrogen and carbon shows the variation from approximately 310 to 30 K. Our result reproduces the trend of experimental findings in a qualitative manner. The experimental results for $x = 0$ (Ce_2Fe_{17}) [102, 103] concluded that the enhancement in T_c is highest in the presence of both carbon and nitrogen [104, 105] ($T_c \sim 721$ K), followed by the nitrogenated compound [106, 107] ($T_c \sim 700$ K) and lowest for the carbonated compound [104, 105] ($T_c \sim 589$ K). Though it is not possible to compare the results quantitatively as the stoichiometry of the experimentally studied carbonated and nitrogenated compounds are not the same as in our exploration dataset, the overall trend is similar. We also find that our ML model underestimates the T_c of the pure binary compound Ce_2Fe_{17} [20]. This is expected, as already discussed, our model is less precise for the prediction of low T_c compounds.

Switching to the M_s part, the middle panel of Figure 3.6 shows the confidence of classification of compounds with $\mu_0 M_s$ more than 1 T. The confidence value closer to 1 implies that the prediction is viable to be more accurate. All the compounds are classified in favor of forming permanent magnets with $\mu_0 M_s > 1$ T. For compounds like $Ce_2Fe_{17-x}Co_x$, the prediction confidence varies from 0.6 to 0.8 with increasing Co concentration, whereas the carbon and nitride compounds are always classified with high prediction confidence.

The predictions from the classification model on K_u are shown in the bottom panel of Figure 3.6. We find that while the anisotropy of $Fe_{17-x}Co_x$ compounds without interstitial C/N ($x = 2, \ldots, 7$) atoms are predicted to be easy plane, their carbonated or nitrogenated or carbonitrogenated counterparts show easy-axis anisotropy. For pure Fe compounds, apart from the carbonitrogenated compound, all are predicted to be easy plane, while for $Fe_{16}Co$ compounds, carbonated as well as carbonitrogenated compounds are predicted to be easy axis. This in turn highlights the effectiveness of Co substitution on making K_u positive. We note the prediction confidence of the carbonitrogenated compounds is around 0.75.

On the basis of the above ML analysis, we pick seven yet-to-be synthesized compounds, $Ce_2Fe_{17-x}Co_xCN$, $x = 1, \ldots, 7$. This choice is guided by the compounds satisfying $T_c > 600$ K from the regression model, and $\mu_0 M_s > 1$ T with easy-axis anisotropy from classification models, and being Fe rich. In the following, we describe their crystal structure, and present results of DFT-calculated electronic structure, anisotropy properties, and stability properties.

3.3 DFT details

DFT calculations for electronic structure and magnetocrystalline anisotropy are performed using the all-electron density-functional-theory code in full-potential linear-augmented-plane-wave (FP LAPW) basis, as implemented in the WIEN2K code [108]. For expensive structural optimization calculations, the plane-wave-based calculations, as implemented in the Vienna ab initio simulation package (VASP) [109, 110], are carried out. The exchange-correlation functional is chosen to be the generalized-gradient approximation of Perdew, Burke, and Ernzerhof [111]. The localized nature of 4f states of Ce is captured through GGA+U calculations [112], with the choice of $U = 6$ eV and $J_H = 0.8$ eV. For light rare earths like Ce, the U value is shown to range from 4 to 7 eV, without affecting the physical properties much [113]. The spin-orbit coupling effect at Ce, and TM sites is captured through GGA+U+SOC calculations.

For FP LAPW calculations, APW + lo is used as the basis set, and the spherical harmonics are expanded up to $l = 10$ and the charge density and potentials are represented up to $l = 6$. The sphere radii are set at 2.5, 1.9, 2.34, 1.56, and 1.51 bohr for Ce, Fe, Co, N, and C. For good convergence, an $RK_{\max}$ value (the product of the smallest sphere radius and the largest plane-wave expansion wave vector) of 7.0 is used. We set the cutoff between core and valence states at -8.0 Ry. The k-space integrations are performed with 112 k points in the irreducible Brillouin zone (BZ), following the report of the use of 80 k points in the irreducible BZ in the case of $SmCo_5$ to provide a good estimate of MAE [114]. Nevertheless, the convergence of results on the k-space mesh is checked by carrying out calculations with 260 k points.

The structural optimization in the plane-wave basis is carried out starting with the experimental structure of $Sm_2Fe_{17}CN$ [115], replacing Sm with Ce, and relaxing all the internal coordinates until the forces on all atoms become less than 0.001 eV/Å. Upon moving from Sm 2:17 carbide and nitride interstitial compounds to the Ce counterpart, the cell volume changes only nominally by 0.2% to 0.4% [106]. For the plane-wave calculations, an energy cutoff of 600 eV and Monkhorst-Pack k-point mesh of $8 \times 8 \times 8$ are used.

All the calculations are performed by considering a collinear spin arrangement. The MAE is obtained by calculating the GGA+U+SOC total energies of the system, in FP LAPW basis as $K_u = E_a - E_c$, where E_a and E_c are the energies for the magnetization oriented along the crystallographic a and c directions, respectively. For accurate estimates of vacancy formation energy, we also use the FP LAPW basis.

3.4 Properties of Predicted Compounds

3.4.1 Crystal structure

The Ce_2Fe_{17} compounds crystallize in the rhombohedral Th_2Zn_{17}-type structure (space group $R\bar{3}m$), derived from the $CaCu_5$-type structure with a pair (dumbbell) of Fe atoms for each third rare-earth atom in the basal plane and the substituted layers stacked in the sequence ABCABC.... As shown in Figure 3.7, the transition metal atoms are divided

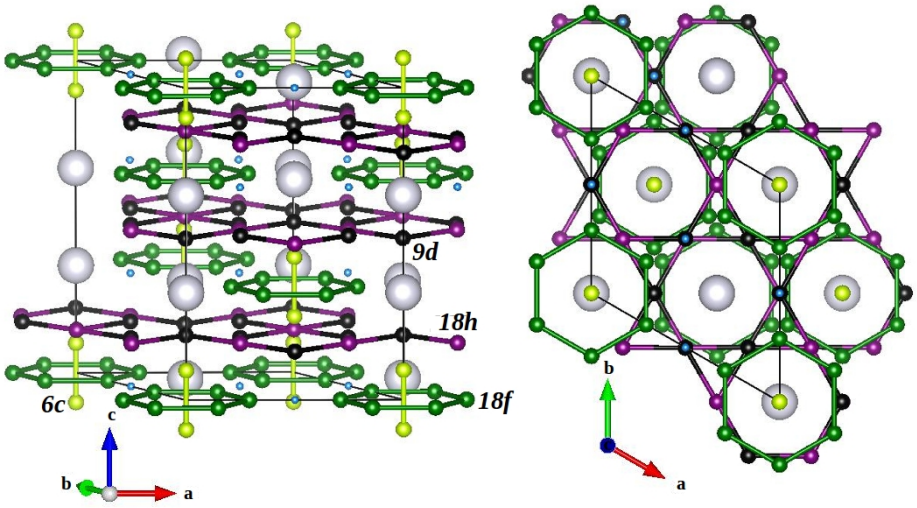

Figure 3.7: *Crystal structure of $Ce_2Fe_{17-x}Co_xCN$ magnets. The Ce, Fe/Co, and C/N atoms are shown with large, medium, and small balls, respectively. Four transition metal sublattices 9d, 18f, 18h, and 6c are shown in black, green, magenta, and yellow colored balls, respectively. The left panel shows the crystal structure viewed with the c-axis pointed vertically up, and the right panel shows the crystal structure viewed along the c-axis.*

into four sublattices, 9d, 18f, 18h, and 6c, having 3 (9), 6 (18), 6 (18), and 2 (6) multiplicity in the one (three) formula unit primitive-rhombohedral (hexagonal) unit cell. The TM atoms occupying the 6c sites, referred to as dumbbell sites, form the ...-TM-TM-RE-RE-... chains running along the c axis of the hexagonal cell. The 18f TM atoms form a hexagonal layer, which alternates with the hexagonal layer formed by 9d and 18h TM atoms. The 6c TM-TM dumbbells pass through the hexagons formed by 18f TMs. For the interstitial C and N atoms, neutron powder diffraction [116, 117], EXAFS experiments confirmed that they fill voids of nearly octahedral shape formed by a rectangle of 18f and 18h TM atoms and two RE atoms at opposite corners, which are the 9e sites of Th_2Zn_{17}-type structure, and having the shortest distance from the RE atoms. Sites among all available interstitial

sites. All our calculations are thus carried out with C/N atoms in 9e positions. The RE atoms in 6c position as well as light elements C/N in 9e interstitial sites belong to the same layer as 18f TMs. As the 9e sites are in the same c plane as the RE sites, having RE atoms as neighbors, introduction of interstitials like C and N is expected to have a profound influence on the electronic environment of RE atoms, thereby altering the magnetocrystalline anisotropy.

Although the $R\bar{3}m$ symmetry is lowered upon Co substitution and the spin-orbit coupling (SOC) in the anisotropy calculation, for the ease of identification, we still use the notations 9d, 18f, 18h, and 6c. Our total energy calculations show that Co preferentially occupy sites in the sequence 9d $>$ 18h $>$ 6c $>$ 18f. Out of the available 17 TM sites we consider Co substitution up to seven sites, which result in Fe-rich phases of compositions $Ce_2Fe_{17-x}Co_xCN$ with $x = 1, 2, \ldots, 7$. Following the site preference we consider Co atoms in 9d and 18h sites.

We expect the lattice parameters not to change much upon Co substitution, as Fe and Co, being neighboring elements in the periodic table, have similar atomic radii. Nevertheless, to check the influence of Co substitution on lattice structure, we optimize the lattice constant and the volume for all x values. Following our expectation, the results only show a marginal decrease in lattice parameter and volume (with a maximum deviation of 1%) upon increasing Co content, in line with the findings by Odkhuu et al. [18] for 1:12 compounds, and the experimental findings by Xu and Shaheen on 2:17 compounds [19]. This minimal change is found to have no appreciable effect on magnetic properties, as explicitly checked on representative compounds with $x = 1, 4$, and 7. We thus choose the lattice structure as the optimized lattice structure of $x = 0$, with lattice constant = 6.59 Å and angle $\beta = 83.3^\circ$ of the rhombohedral unit cell [115] in subsequent calculations.

3.4.2 Magnetic moment and electronic structure

In the following we present the DFT results for the magnetic moments and density of states (DOS), as given in generalized-gradient approximation (GGA)+U+SOC calculations. The importance of the application of supplemented Hubbard U on RE sites within LDA or GGA+U formalism is considered as one of the possible means to deal with localized f orbitals of RE ions, and has shown to provide reasonable description [13, 14]. Previous calculations in compounds containing Ce, showing variations of U within 3 to 6 eV, keeps the results qualitatively the same [6, 113]. In the following, we present results for U applied on Ce atoms chosen to be 6 eV. Figure 3.8 shows the calculated total magnetic moments of the seven mixed Fe-Co compounds, $Ce_2Fe_{17-x}Co_xCN$ (x = 1, 2, . . . 7). The total magnetic moment shows a decreasing trend with an increase of Co concentration, arising from the fact that Co moment is smaller than that of Fe. However, it is reassuring to note that even for

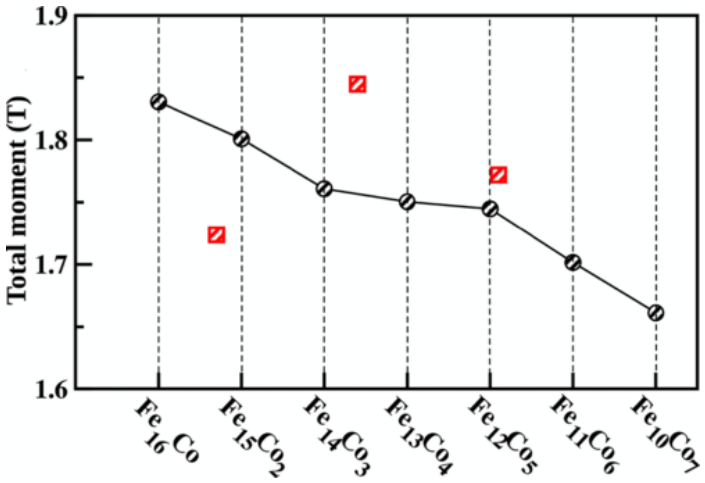

Figure 3.8: *Calculated total moment (black circles), $\mu_0 M$ in T plotted for increasing Co concentrations of $Ce_2Fe_{17-x}Co_xCN$ compounds. Experimental results are also shown [19] (red, square) for $Ce_2Fe_{17-x}Co_xN_y$ compounds measured at room temperature. For comparison between $T = 0$ K calculated moments and experimental data measured at room temperature, the experimental data has been scaled by a factor of 1.3.*

the compound with the largest Co concentration, $Ce_2Fe_{10}Co_7CN$, the calculated moment is more than 1.65 T. This is in agreement with ML prediction, which predicts $\mu_0 M_s$ of all the considered compounds to be larger than 1 T, though it is to be noted the ML predictions are made for room-temperature moments while the DFT-calculated moments are at T = 0 K. The measured values of total moment in corresponding nitrogenated compounds show good comparison (cf. Figure 3.8) with our calculated moments. In particular, barring the data on $x \approx 2$, the other two data points show good matching with the trend of theoretical results. We note that the experimentally determined moments are for $Ce_2Fe_{17-x}Co_xN_y$ compounds, which only contain N as an interstitial atom, and the value of y is not mentioned, which may even vary depending on the value of x.

Figure 3.9 shows the spin and orbital moments projected to Ce, Fe(9d), Fe(18f), Fe(18h), Fe(6c), and Co atoms for the representative case of the $Ce_2Fe_{15}Co_2CN$ compound. The results for other Co concentrations are similar. In the presence of large SOC at the Ce site, a substantial orbital moment develops, which is oppositely aligned to its spin moment following Hund's rule. Considering 3+ nominal valence of Ce, it would be in $4f^1$ state, with S = 1/2 and L = 3. While the calculated value of the Ce spin moment is close to 1 μ_B (approximately equal to 0.95 μ_B) in accordance with nominal S = 1/2 state, the orbital moment shows significant quenching with a calculated value of about 0.5 μ_B. This value of orbital moment is in agreement with DFT-calculated values of other Ce containing RE-TM magnets [6, 118]. The 4f electrons are coupled to 5d electrons at the Ce site by intra-atomic exchange interaction, following which their spin moments are aligned in parallel direction. The delocalized 5d electrons at the Ce site, hybridize with Fe or Co 3d electrons, favoring

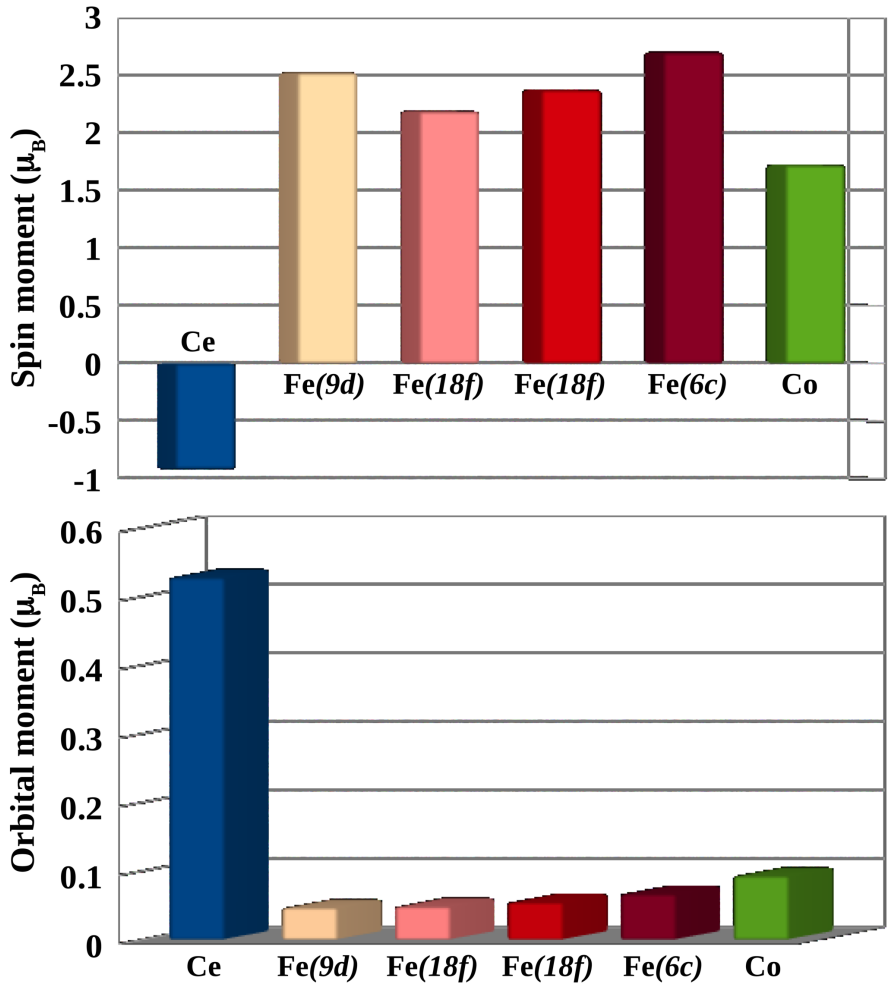

Figure 3.9: *Calculated spin (top) and orbital (bottom) moments at Ce, Fe(9d), Fe(18f), Fe(18h), Fe(6c), and Co sites in the representative case of $Ce_2Fe_{15}Co_2CN$ compound.*

antiparallel alignment of Ce and Fe or Co spins, as found in Figure 3.9. The spin magnetic moment at Fe sites shows a distribution, with Fe at the 6c site having the largest moment, followed by Fe at 9d and 18h sites while Fe at the 18f site shows the lowest moment. We notice that Fe (6c) atoms occupying the dumbbell sites, have less connectivity compared to Fe(9d), Fe (18f), and Fe (18h), and thus possess the largest moment, being of most localized character. Among Fe (9d), Fe(18f), Fe(18h) sites Fe (18f) has the smallest moment, driven by the fact that interstitial C and N atoms are in same plane as Fe (18f) causing enhanced d-p hybridization, and reduction in moment. These spin moments though are larger than that of bulk Fe (approximately equal to 2.2 μ_B). The orbital moment at Fe sites are tiny (approximately equal to 0.05 μ_B). In comparison, Co shows significantly smaller spin moment (approximately equal to 1.7 μ_B) and somewhat larger orbital moment (approximately equal to 0.1 μ_B), justifying the fall in total moment with increasing concentration of Co.

Figure 3.10 shows the density of states of $Ce_2Fe_{15}Co_2CN$, projected to various orbital characters. The Ce 4f states are all unoccupied in the majority spin channel, partly occupied

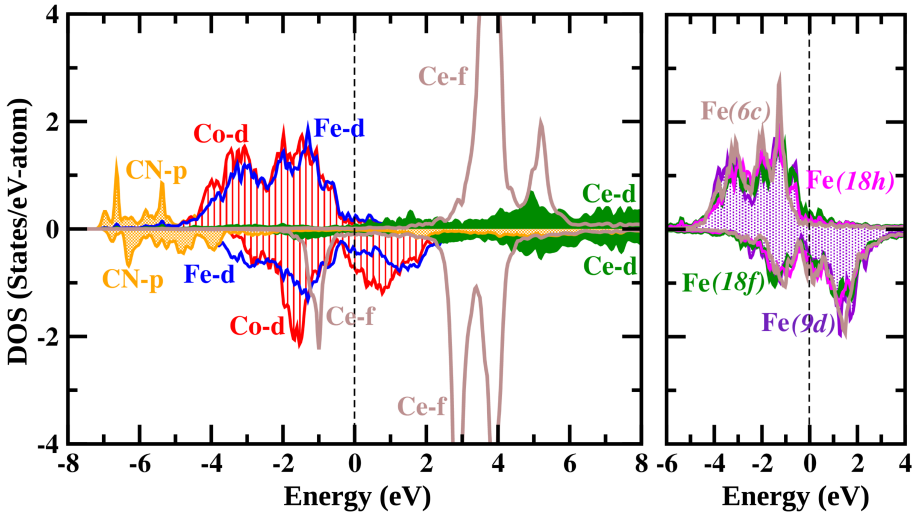

Figure 3.10: *Left: density of states of the $Ce_2Fe_{15}Co_2CN$ compound, projected onto Ce f (brown), Ce d (shaded green), Fe d (blue), Co d (shaded red), and CN p (shaded orange) characters. Right: density of states of the $Ce_2Fe_{15}Co_2CN$ compound projected onto different Fe d's: Fe(9d) (shaded indigo), Fe(18h) (magenta), Fe(18f) (green), and Fe(6c) (brown). The zero of the energy is set at Fermi energy.*

in the minority spin channel, in accordance with nominal f^1 occupancy. The RE 4f-TM 3d hybridization through empty RE 5d states is visible, making the spin splitting at Fe and Co sites antiparallel to that of Ce. The C/N p states mostly spanning the energy range -7 to -4 eV, show nonnegligible mixing with Fe d, Co d, and Ce f characters, justifying their role in influencing the magnetic properties. Fe d and Co d states span about the same energy range from -4 to 2 eV, with states mostly occupied in the majority spin channel and partially occupied in the minority spin channel, largely accounting for the metallicity of the compound. Spin splitting of Fe d is larger than that of Co, being consistent with the larger magnetic moment of Fe compared to Co. Projection to different inequivalent Fe sites (cf. the right panel of Figure 3.10), Fe(9d), Fe(18h), Fe(18f), and Fe(6c) show that Fe(6c) belonging to the dumbbell pair is distinct from the other Fe sites, which also exhibit the largest magnetic moment among all Fe's.

3.4.3 Magnetocrystalline anisotropy

Having an understanding of the basic electronic structure, in terms of magnetic moments and density of states, we next focus on calculation of magnetocrystalline anisotropy constant, K_u, which is a crucial quantity responsible for coercivity in a permanent magnet. MAE defines the energy required for turning the orientation of the magnetic moment under applied field, expressed as $E(\theta) \approx K_1 \sin^2\theta + K_2 \sin^4\theta + K_3 \sin^4\theta \cos^4\phi$, where K_1, K_2, and K_3 are the magnetic anisotropy constants, θ is the polar angle between the magnetization vector and the easy axis (c axis), and ϕ is the azimuthal angle between the magneti-

zation component projected onto the *a*-*b* plane and the *a* axis. In most cases, the higher-order term K_3 is relatively small compared with K_1 and K_2. For $\theta = \pi/2$, one may thus write $K_u \approx K_1 + K_2$. Its positive and negative values indicate the easy-axis and easy-plane anisotropy, respectively. To satisfy the criteria of a good permanent magnet, it should have easy-axis anisotropy with a value larger than 1 MJ/m^3 [2, 8]. The MAE in RE-TM arises from two contributions: (i) MAE of the RE sublattice due to strong spin-orbit coupling and crystal-field effect and (ii) MAE of the TM sublattice. The interplay of the two decides the net sign and magnitude. In particular, in the proposed compounds, the presence of Co with a significant value of orbital moment makes the contribution of the TM sublattice noteworthy. While 2:17 compounds, primarily show easy-plane anisotropy, switching to easy-axis anisotropy for interstitial compounds has been reported. In particular, upon nitrogenation, easy-plane anisotropy has been reported for Ce containing mixed Fe-Co compounds [19]. As mentioned already, the interstitial atoms occupy the same plane as the RE atoms, significantly influencing their properties. With predicted high T_c and large saturation moment of our proposed compounds with carbonation and nitrogenation, it remains to be seen whether they exhibit easy-axis anisotropy of reasonable values, as required for a legitimate candidate for permanent magnet. For this purpose, we carry out calculations within GGA+U+SOC with the magnetization axis pointing along the crystallographic *c* axis and perpendicular to it. The significance of the application of U on the proper description of MAE in terms of its sign and order of magnitude has been stressed upon by several authors [6, 13]. In order to establish our method on the calculation of MAE involving a small energy difference, we first apply our method to the known and well-studied case of $SmCo_5$, with choice of $U = 6$ eV on Sm, and obtain a MAE value of 24.4 meV/f.u., which agrees well with the GGA+U+SOC-calculated value of 21.6 meV/f.u., reported in the literature [13] as well as experimentally measured values of 13–16 meV/f.u. [114, 119]. The calculated results for the proposed $Ce_2Fe_{17-x}Co_xCN$ are shown in the top panel of Figure 3.11. We find that MAE shows site dependence on the Co substitution. We consider configurations with Co atoms substituting Fe(9d) and Fe(18h) sites, configurations involving other substituting sites being energetically much higher. We consider configurations that are energetically close (within 600 K) and calculate the Co-composition-dependent MAE using the virtual crystal approximation. Specifically, for $x = 1$ we consider configurations Co@Fe(9d) and Co@Fe(18h), the latter being 3.58 meV higher compared to the former. Similarly for $x = 2$, we consider Co@2×Fe(9d) and Co@2×Fe(18h), the latter being 4.43 meV higher compared to the former. For $x = 3$, the configurations considered are Co@2×Fe(9d)+Fe(18h); Co@3×Fe(9d); Co@Fe(9d)+2×Fe(18h), the energies being 0 meV (set as zero of energy), 12.37 meV and 47.66 meV, respectively. For $x = 4$, the configurations considered are Co@2×Fe(9d)+2×Fe(18h); Co@3×Fe(9d)+Fe(18h), the ener-

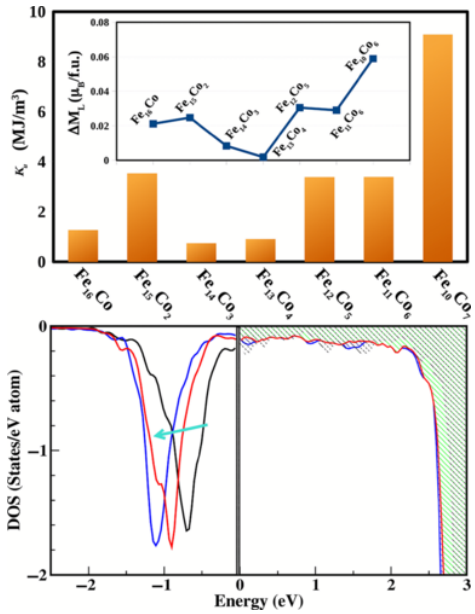

Figure 3.11: *Top: calculated magnetocrystalline anisotropy constant in MJ/m^3 plotted for increasing Co concentrations of $Ce_2Fe_{17-x}Co_xCN$ compounds. The inset shows the anisotropy in orbital moment (see text for details). Bottom: the GGA+U+SOC DOS projected to Ce f energy states with magnetization axis pointed along easy axis, for Ce_2Fe_{17} (black), $Ce_2Fe_{17}CN$ (red), and $Ce_2Fe_{16}CoCN$ (blue). The zero of the energy is set at Fermi energy, with the unoccupied part shown as shaded. The arrow indicates the shift in the occupied part.*

gies being 0 meV (set as zero of energy) and 36.5 meV, respectively. For $x = 5$, 6, and 7, only one configuration is considered, others being energetically much higher, namely, Co@3×Fe(9d)+2×Fe(18h), Co@3×Fe(9d)+3×Fe(18h), and Co@3×Fe(9d)+4×Fe(18h), respectively.

Considering the spin-orbit effect only on the Ce atom, it is found to account for about 60% of the calculated MAE. We find all the calculated MAE is positive, in good agreement with ML prediction on mixed Fe-Co carbonitride compounds. Further, MAE values show non-monotonic dependence on Co concentration. Such a non-monotonic trend upon varying TM content has also been reported in the context of R$(Fe_{1-x}Co_x)_{11}$TiZ (R = Y and Ce; Z = H, C, and N) [7] and RE-TM systems in general [120]. In the inset of the top panel of Figure 3.11, we show the calculated orbital magnetic anisotropy (ΔM_L) defined as $\Delta M_L = M_L(a) - M_L(c)$, as employed in Ref. [18], $M_L(c)$ and $M_L(a)$ being the orbital moment along the c axis and a axis, respectively. We find a correlation between ΔM_L and K_u, qualitatively satisfying Bruno's expression [121] for itinerant ferromagnets given as $K_u =) \frac{\xi}{4\mu_B}) \Delta M_L$, where ξ is the strength of SOC.

Most of the easy-axis K_u values are found to be larger than 1 MJ/m^3, except $Fe_{14}Co_3$ and $Fe_{13}Co_4$ for which it is found to be 0.74 and 0.91 MJ/m^3, respectively. Few of the concentrations exhibit easy-axis K_u values larger than 2 MJ/m^3, e.g., $Fe_{15}Co_2$ (3.54 MJ/m^3),

$Fe_{12}Co_5$ (3.39 MJ/m^3), $Fe_{11}Co_6$ (3.39 MJ/m^3), $Fe_{10}Co_7$ (9.10 MJ/m^3), being comparable to $Nd_2Fe_{14}B$ (4.9 MJ/m^3) [122].

To obtain microscopic understanding of the role of Co substitution and doping by C, N on magnetocrystalline anisotropy, we further calculate the magnetocrystalline anisotropy of Fe-only compounds Ce_2Fe_{17}, $Ce_2Fe_{17}C$, $Ce_2Fe_{17}N$, and $Ce_2Fe_{17}CN$. This results in negative K_u values for Ce_2Fe_{17} and $Ce_2Fe_{17}C$ (-2.12 MJ/m^3 and -1.35 MJ/m^3), a tiny positive value for $Ce_2Fe_{17}N$ (0.26 MJ/m^3) and a positive value for the codoped compound $Ce_2Fe_{17}CN$ (1.27 MJ/m^3). We further plot the GGA+U+SOC density of states (cf. bottom panel, Figure 3.11) with the magnetization axis along the c axis projected to Ce f states for Ce_2Fe_{17}, $Ce_2Fe_{17}CN$, and $Ce_2Fe_{16}CoCN$, which is expected to reveal the mechanism of uniaxial anisotropy. We find that a lowering of occupied Ce f energy states and increase in bandwidth occur upon introduction of light elements C and N. This gets further helped by substitution of Co, caused by hybridization between Ce f states and Co d and C, N p states. This gain in hybridization energy stabilizes easy-axis magnetization (cf. Ref. [123]) as observed experimentally [19].

3.4.4 Maximal energy product and anisotropy field

While the estimates of K_u and $\mu_0 M_s$ are useful information to assess the effectiveness of the suggested materials as permanent magnets, technologically interesting figures of merit of hard magnetic materials are the maximal energy product $(BH)_{\max}$ and anisotropy field H_a. These can be estimated from the knowledge of $\mu_0 M_s$ and K_u as follows:

$$(BH)_{\max} = \frac{(0.9\mu_0 M_s)^2}{4\mu_0}$$

$$H_a = \frac{2K_u}{\mu_0 M_s}$$

The factor 0.9 in the expression for $(BH)_{\max}$ implies the common assumption that ideally 10% of a processed bulk hard magnet consists of nonmagnetic phases [124]. The estimated $(BH)_{\max}$ and H_a are shown in Figure 3.12. The $(BH)_{\max}$ value is found to range from 444 to 540 kJ/m^3, in comparison to experimentally measured values 516 kJ/m^3 and 219 kJ/m^3 for $Nd_2Fe_{14}B$ [125] and $SmCo_5$ [125], respectively. The H_a shows a strong variation with Co concentration, ranging from approximately 1 to 14 T [126]. We further note that the hardness parameter, defined as $\kappa = \sqrt{\frac{K_u}{\mu_0 M_s^2}}$, turns out to be greater than 1 for $Ce_2Fe_{15}Co_2CN$, $Ce_2Fe_{12}Co_5CN$, $Ce_2Fe_{11}Co_6CN$, and $Ce_2Fe_{10}Co_7CN$ compounds, employing the calculated $T = 0$ K values of K_u and M_s.

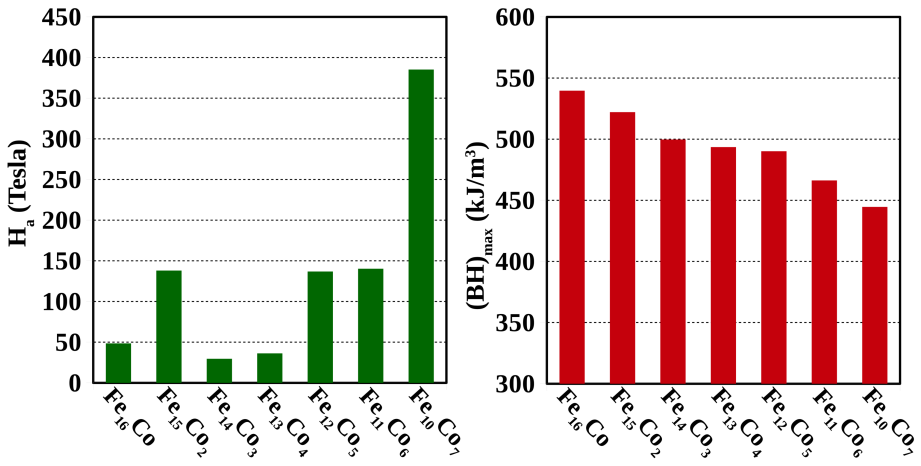

Figure 3.12: *Calculated anisotropy field in tesla (left) and maximal energy product in kJ/m^3 (right) plotted for increasing Co concentrations of $Ce_2Fe_{17-x}Co_xCN$ compounds.*

3.4.5 Stability

Unlike the other RE-TM magnets like 1:12 compounds, one of the advantages of 2:17 compounds is their stability. Both the stable form of Ce_2Fe_{17} and its Co-substituted form have been reported in the literature [19]. Calculation of formation enthalpies [18], as given by $E_{\text{form}} = \frac{E_{\text{compound}} - \sum_k N_k E_k}{\sum_k N_k}$, where N_k indicates the number of different atoms (Ce, Fe, Co, N, and C) in the cell, and E_k denotes the energy and atom of bulk Ce in fcc structure, α-Fe, Co in HCP structure, molecular nitrogen, and C in graphite structure, gives values of -0.61 to -0.59 eV/atom for the studied $Ce_2Fe_{17-x}Co_xCN$ compounds.

A major challenge with interstitial compounds, though, is nitrogen diffusion [21]. It has been further suggested that the blockage of nitrogen diffusion by a carbon layer is useful in reducing nitrogen outgassing in carbonitrides. In particular, heating up Sm_2Fe_{17} carbonitrides at a constant rate in a differential scanning calorimeter, the onset temperature of nitrogen outgassing is found to be higher by more than 40 K, as compared to the nitride counterpart [21]. This justifies the choice of carbonitrides as our exploration set.

To this end, we calculate the vacancy formation energy of the interstitial atoms in our chosen compounds. For this purpose, we calculate the formation energy of the N and/or C vacancy (ΔE_f) defined as

$$\Delta E_f = E^{N(\text{C})_{vac}} - E^{\text{pristine}} + E_{\text{N(C)}}$$

where $E^{N(\text{C})_{vac}}$ and E^{pristine} denote the optimized total energies of the compound containing N and/or C vacancies, and the vacancy-free compound, respectively. The internal positions for the defect-free pristine structure and structures containing nitrogen and/or carbon vacancies are performed while keeping the lattice parameters fixed. $E_{\text{N(C)}}$ is the energy per

N or C atom, which is obtained from the calculation of N_2 molecule or graphite. The obtained results for $Ce_2Fe_{17-x}Co_xCN$ compounds in the minimum energy configuration of Co are shown in Table 3.2. The vacancy formation energies show hardly any variation on the chosen configuration for a given Co concentration.

Table 3.2: *Vacancy formation energy for carbon [E_f(C)], nitrogen [E_f(N)], and nitrogen-carbon [E_f(CN)] in eV in $Ce_2Fe_{17-x}Co_xCN$ compounds.*

	E_f(CN)	E_f(N)	E_f(C)
x=1	4.32	2.10	0.97
x=2	3.99	2.09	0.85
x=3	4.16	2.09	0.88
x=4	3.98	2.10	0.79
x=5	3.82	2.07	0.70
x=6	3.91	2.05	0.72
x=7	3.78	2.01	0.69

The vacancy formation energies, listed in Table 3.2, show only small variation between compounds of varying Co concentration, with the general trend $\Delta E_f(\mathrm{CN}) > [\Delta E_f(\mathrm{N}) + \Delta E_f(\mathrm{C})]$. The individual nitrogen-vacancy formation energy and carbon-vacancy formation energy are in overall agreement with that found for the related compound, $SmCaFe_{17}C(N)_3$ [6]. The vacancy formation energy for codoped carbon-nitrogen compounds is found to be enhanced by about 35–40% compared to the sum of the individual C and N vacancy formation energies, proving that carbon-nitrogen codoping provides better thermal stability. We also check our results by repeating vacancy formation energy calculations for $x = 0$ compounds, which, however, do not show significant differences, suggesting that Co doping does not have a major role in stability, as also indicated by no significant variation of results between $x = 1, 2, 3, 4, 5, 6$, and 7.

3.5 Summary and Discussion

Designing alternative solutions for permanent magnets, satisfying the criteria of low cost while keeping the magnetic properties comparable to those of permanent magnets in use, is key for cost-effective technology. Towards this goal, we use a combined route of machine learning, based on experimental data, and first-principles calculations.

While machine learning has been applied to the problem of rare-earth magnets [5], those studies have been based on datasets created from high-throughput calculations. Being dependent on calculation-based inputs, the creation of such a database is not only computationally expensive but also not devoid of approximations in theory. Our study, on the other hand, is based on an exhaustive search of experimental data.

While a large volume of experimental data is available with numerical values of T_c, the corresponding dataset with numerical values of M_s and K_u is small. On the other hand, there exists a sizable dataset with information on K_u being positive (easy axis) or negative (easy plane), and $\mu_0 M_s$ being larger or smaller than 1 T. We thus employ a regression model for machine-learning training to make predictions on numerical values of T_c, and a classification model to make predictions on the sign of K_u, and $\mu_0 M_s$ being larger or smaller than 1 T. We apply the trained machine learning to 2:17 rare-earth transition-metal compounds with carbon and nitrogen in interstitials. We choose the compounds to contain abundant rare-earth Ce and to be Fe-rich to make them cost-effective. Although the nitrogenated version of this series has been investigated [19], a systematic study of the carbonitride family is not available.

The machine learning predicts T_c of the chosen carbonitride family to be larger than 600 K, $\mu_0 M_s > 1$ T, and $K_u > 0$, thereby indicating the possibility of them becoming good solutions for cost-effective permanent magnets. Subsequent first-principles calculations show $T = 0$ K, $\mu_0 M_s$ to be larger than 1.65 T, and $K_u \geq 1$ MJ/m^3 for the entire family, $Ce_2Fe_{17-x}Co_xCN$ ($x = 1, \ldots, 7$). Calculated K_u values are found to be comparable to the state-of-the-art permanent magnet $Nd_2Fe_{14}B$ for $Ce_2Fe_{15}Co_2CN$, $Ce_2Fe_{12}Co_5CN$, $Ce_2Fe_{11}Co_6CN$, and $Ce_2Fe_{10}Co_7CN$. This results in two figures of merit for hard magnets, $(BH)_{\max}$ and H_a, in the range of 444–540 kJ/m^3 and approximately 1–14 T, respectively.

In spite of good magnetic properties, one of the limitations of practical applications of interstitial 2:17 magnets is the formation of nitrogen and carbon vacancies at high temperatures. By calculating the N-(C)-vacancy formation energy, we show that carbon-nitrogen codoping enhances the vacancy formation energy significantly, by 35–40% compared to the sum of individual doping. This is likely to improve the thermal stability at high-temperature conditions.

Our computational exercise, based on an exhaustive search of the experimental database, should motivate future experimental processes in making high-performance 2:17 interstitial magnets, with the cheapest rare-earth element Ce, the most abundant 3d metal Fe, and cheap nonmetal interstitial dopings like C and N. The estimated price-to-performance ratio, based on the calculated energy product and available market prices [16], turns out to be 0.03–0.22 USD/J. The enhanced thermal stability of the carbonitride compounds against the vacancy formation of the light elements further boosts the promise of the suggested compounds.

Bibliography

[1] K. H. J. Buschow. New developments in hard magnetic materials. *Reports on Progress in Physics*, 54:1123–1178, 1991.

[2] J. M. D. Coey. Hard magnetic materials: A perspective. *IEEE Transactions on Magnetics*, 47:4671–4681, 2011.

[3] Hong Sun, Y. Otani, and J. M. D. Coey. Gas-phase carbonation of r_2fe_{17}. *Journal of Magnetism and Magnetic Materials*, 104–107:1439–1440, 1992.

[4] A. Vishina, O. Y. Vekilova, T. Björkman, A. Bergman, H. C. Herper, and O. Eriksson. High-throughput and data-mining approach to predict new rare-earth free permanent magnets. *Physical Review B*, 101:094407, 2020.

[5] J. J. Möller, W. Körner, G. Krugel, D. F. Urban, and Christian Elsässer. Compositional optimization of hard-magnetic phases with machine-learning models. *Acta Materialia*, 153:53–60, 2018.

[6] T. Pandey, M.-H. Du, and D. S. Parker. Tuning the magnetic properties and structural stabilities of the 2-17-3 magnets $sm_2fe_{17}x_3$ (x = c, n) by substituting la or ce for sm. *Physical Review Applied*, 9:034002, 2018.

[7] L. Ke and D. D. Johnson. Intrinsic magnetic properties in $r(fe_{1-x}co_x)_{11}tiz$ (r = y and ce; z = h, c, and n). *Physical Review B*, 94:024423, 2016.

[8] J. M. D. Coey. Permanent magnets: Plugging the gap. *Scripta Materialia*, 67:524–525, 2012.

[9] S. V. Halilov, H. Eschrig, A. Y. Perlov, and P. M. Oppeneer. Adiabatic spin dynamics from spin-density-functional theory: Application to fe, co, and ni. *Physical Review B*, 58:293–299, 1998.

[10] A. Georges, G. Kotliar, W. Krauth, and M. J. Rozenberg. Dynamical mean-field theory of strongly correlated fermion systems and the limit of infinite dimensions. *Reviews of Modern Physics*, 68:13–125, 1996.

[11] W. Körner, G. Krugel, and C. Elsässer. Theoretical screening of intermetallic $thmn_{12}$-type phases for new hard-magnetic compounds with low rare earth content. *Scientific Reports*, 6:24686, 2016.

[12] H. Brooks. Ferromagnetic anisotropy and the itinerant electron model. *Physical Review*, 58:909–919, 1940.

[13] P. Larson, I. I. Mazin, and D. A. Papaconstantopoulos. Calculation of magnetic anisotropy energy in $smco_5$. *Physical Review B*, 67:214405, 2003.

[14] S. Yehia, S. H. Aly, and A. E. Aly. Electronic band structure and spin-density maps of $smco_5$. *Computational Materials Science*, 41:482–489, 2008.

[15] H. Ucar, R. Choudhary, and D. Paudyal. An overview of the first principles studies of doped re-tm_5 systems for the development of hard magnetic properties. *Journal of Magnetism and Magnetic Materials*, 496:165902, 2020.

[16] J. M. D. Coey. Perspective and prospects for rare earth permanent magnets. *Engineering*, 6:119–122, 2020.

[17] D. Odkhuu and S. C. Hong. First-principles prediction of possible rare-earth free permanent magnet of tetragonal feco with enhanced magnetic anisotropy and energy product through interstitial nitrogen. *Physical Review Applied*, 11:054085, 2019.

[18] D. Odkhuu, T. Ochirkhuyag, and S. C. Hong. Enhancing energy product and thermal stability of $smfe_{12}$ by interstitial doping. *Physical Review Applied*, 13:054076, 2020.

[19] X. Xu and S. A. Shaheen. Structural and magnetic properties of rare-earth iron nitride $ce_2(fe_{1-x}co_x)_{17}n_y$ series. *Journal of Applied Physics*, 73:5896–5902, 1993.

[20] H. Fujii and H. Sun. Handbook of magnetic materials. In *Handbook of Magnetic Materials*, pages 303–308. Elsevier, Amsterdam, 1995.

[21] X. Chen, Z. Altounian, and D. H. Ryan. Carbonitrides of r_2fe_{17} prepared by gas-solid reaction. *Journal of Magnetism and Magnetic Materials*, 125:169–174, 1993.

[22] Inorganic crystal structure database. `https://icsd.nist.gov/guide.html`.

[23] K. H. J. Buschow. *Handbook of Magnetic Materials*, volume 6 & 9. Elsevier, Amsterdam, 1991.

[24] J. M. D. Coey. *Magnetism and Magnetic Materials*. Cambridge University Press, Cambridge, 2010.

[25] Shiqiang Liu. Sm–co high-temperature permanent magnet materials. *Chinese Physics B*, 28:017501, 2019.

[26] S. R. Mishra, Gary J. Long, O. A. Pringle, D. P. Middleton, Z. Hu, W. B. Yelon, F. Grandjean, and K. H. J. Buschow. A magnetic neutron diffraction, and mössbauer spectral study of the $ce_2fe_{17-x}al_x$ solid solutions. *Journal of Applied Physics*, 79:3145–3150, 1996.

[27] H. Klesnar, K. Hiebl, and P. Rogl. Magnetic behaviour of $re_2ti_{15}ga_2$; re mischmetal mm, y, ce, pr, nd, sm; t fe, co and $re_2fe_{15-x}co_xga_2$; re y, nd. *Journal of the Less Common Metals*, 154:217–223, 1989.

[28] Y. Otani, D. P. F. Hurley, Hong Sun, and J. M. D. Coey. Magnetic properties of a new family of ternary rare-earth iron nitrides $r_2fe_{17}n_{3-\delta}$. *Journal of Applied Physics*, 69:5584–5587, 1991.

[29] M. Merches, W. E. Wallace, and R. S. Craig. Magnetic and structural characteristics of some 2:17 rare earth-cobalt systems. *Journal of Magnetism and Magnetic Materials*, 24:97–103, 1981.

[30] F. Pourarian, R. Obermyer, Y. Zheng, S. G. Sankar, and W. E. Wallace. Crystal structure and magnetic characteristics of alloys based on r - fe - si (r = y, nd, gd, dy, ho, er). *Journal of Applied Physics*, 73:6272–6278, 1993.

[31] F. Weitzer, H. Klesnar, K. Hiebl, and P. Rogl. Magnetism of $pr_2(fe_{1-x-y}co_xal_y)_{17}$ alloys with a th_2zn_{17}-type structure. *Journal of Applied Physics*, 67:2544–2548, 1990.

[32] X. P. Zhong, R. J. Radwanski, F. R. de Boer, T. H. Jacobs, and K. H. J. Buschow. Magnetic and crystallographic characteristics of rare-earth ternary carbides derived from r_2fe_{17} compounds. *Journal of Magnetism and Magnetic Materials*, 86:333–338, 1990.

[33] A. T. Pedziwiatr and W. E. Wallace. Magnetism of $r_2co_{14-x}si_xb$ systems (r = y, pr, and nd). *Journal of Applied Physics*, 61:3439–3441, 1987.

[34] R. van Mens. Ternary phase studies of nd - fe - x where x = c, si, pb, sn. *Journal of Magnetism and Magnetic Materials*, 61:24–28, 1986.

[35] Bo-Ping Hu and J. M. D. Coey. Effect of hydrogen on the curie temperature of $nd_2(fe_{15}m_2)$; m ai, si, co. *Journal of the Less Common Metals*, 142:295–299, 1988.

[36] H. Y. Chen, S. G. Sankar, and W. E. Wallace. Spin reorientation in substituted nd_2co_{17} compounds. *Journal of Applied Physics*, 63:3969–3972, 1988.

[37] M. Juczyk and W. E. Wallace. Magnetic behavior of $r_{1.9}zr_{0.1}fe_{14}b$ and $r_{1.9}zr_{0.1}fe_{12}co_2b$ compounds. *Journal of Magnetism and Magnetic Materials*, 59:L182–184, 1986.

[38] Y. G. Xiao, G. H. Rao, Q. Zhang, G. Y. Liu, Y. Zhang, and J. K. Liang. Crystallographic and magnetic studies on iron-rich mixed rare-earth intermetallics $(nd/tb)_2(fe/al)_{17}$. *Journal of Alloys and Compounds*, 407:1–8, 2006.

[39] E. Girt, M. Guillot, I. P. Swainson, Kannan M. Krishnan, Z. Altounian, and G. Thomas. Structural and magnetic properties of $nd_2fe_{17-\delta}ga_\delta$ ($\delta \leq 2$). *Journal of Applied Physics*, 87:5323–5327, 2000.

[40] A. M. Schönhöbel, R. Madugundo, O. Yu. Vekilova, O. Eriksson, H. C. Herper, J. M. Barandiaran, and G. C. Hadjipanayis. Intrinsic magnetic properties of $smfe_{12-x}v_x$ alloys with reduced v-concentration. *Journal of Alloys and Compounds*, 786:969–976, 2019.

[41] Y. Z. Wang, G. C. Hadjipanayis, A. Kim, D. J. Sellmyer, and W. B. Yelon. Structure and magnetic properties of $rfe_{10}v_2n_x$ compounds. *Journal of Magnetism and Magnetic Materials*, 104–107:1132–1133, 1992.

[42] E. P. Wohlfarth and K. H. J. Buschow. *Handbook of Magnetic Materials*, volume 4. Elsevier, Amsterdam, 1988.

[43] Y. Z. Wang, B. P. Hu, X. L. Rao, G. C. Liu, L. Yin, W. Y. Lai, W. Gong, and G. C. Hadjipanayis. Structural and magnetic properties of $ndfe_{12-x}mo_xn_{1-\delta}$ compounds. *Journal of Applied Physics*, 73:6251–6256, 1993.

[44] D. P. F. Hurley and J. M. D. Coey. Gas-phase interstitially modified intermetallics $r(fe_{11}ti)z_{1-\delta}$: I. magnetic properties of the series $r(fe_{11}ti)c_{1-\delta}$: R = y, nd, sm, gd, tb, dy, ho, er, tm, lu. *Journal of Physics: Condensed Matter*, 4:5573–5580, 1992.

[45] Yosuke Harashima, Kiyoyuki Terakura, Hiori Kino, Shoji Ishibashi, and Takashi Miyake. Nitrogen as the best interstitial dopant among x = b, c, n, o, and f for strong permanent magnet $ndfe_{11}tix$: First-principles study. *Physical Review B*, 92(18):184426, 2015.

[46] Y. G. Xiao, G. H. Rao, Q. Zhang, J. Luo, G. Y. Liu, Y. Zhang, and J. K. Liang. Formation, structure and magnetic properties of $tbfe_{12-x}mo_x$ (x = 0.5–3.0) compounds. *Physica B: Condensed Matter*, 369(1):56, 2005.

[47] V. K. Sinha, S. F. Cheng, W. E. Wallace, and S. G. Sankar. Magnetic behavior of heavy rare earth $rtife_{11-x}co_x$ alloys. *Journal of Magnetism and Magnetic Materials*, 81(1):227, 1989.

[48] M. Jurczyk. Magnetic properties of $rfe_{10.8}re_{1.2}$ compounds (r = y, tb and ho). *Journal of Magnetism and Magnetic Materials*, 89(1):L5, 1990.

[49] M. Katter, J. Wecker, C. Kuhrt, L. Schultz, X. C. Kou, and R. Grössinger. Structural and intrinsic magnetic properties of $(sm_{1-x}nd_x)_2fe_{17}n$ 2.7 and $(sm_{1-x}nd_x)_2(fe_{1-z}co_z)_{17}n$ 2.7. *Journal of Magnetism and Magnetic Materials*, 111:293, 1992.

[50] M. Jurczyk and W. E. Wallace. Magnetic behavior of $r_{1.9}zr_{0.1}fe_{14}b$ and $r_{1.9}zr_{0.1}fe_{12}co_2b$ compounds. *Journal of Magnetism and Magnetic Materials*, 59(1):L182, 1986.

[51] Yang Fu-ming, Qing-an Li, Ru-wen Zhao, Jianping Kuang, F. R. de Boer, J. P. Liu, K. V. Rao, G. Nicolaides, and K. H. J. Buschow. Magnetic behaviour of heavy rare earth compounds of the type $rfe_{10}cr_2$. *Journal of Alloys and Compounds*, 177:93, 1991.

[52] Bao-gen Shen, Fang-wei Wang, Lin-shu Kong, Lei Cao, and Hui-qun Guo. Formation and magnetic properties of $r_2fe_{17-x}ga_xc_2$ compounds prepared by arc-melting. *Journal of Magnetism and Magnetic Materials*, 127(1):L267, 1993.

[53] X. C. Kou, T. S. Zhao, R. Grössinger, and F. R. de Boer. Ac-susceptibility anomaly and magnetic anisotropy of r_2co_{17} compounds, with r = y, ce, pr, nd, sm, gd, tb, dy, ho, er, tm, and lu. *Physical Review B*, 46(12):6225, 1992.

[54] Zhi-gang Sun, Shao-ying Zhang, Hong-wei Zhang, Jing-yun Wang, and Bao-gen Shen. The effect of manganese substitution on the magnetic properties of ce_2co_{17} compounds. *Journal of Physics: Condensed Matter*, 12(14):2495, 2000.

[55] Z. X. Tang, E. W. Singleton, and G. C. Hadjipanayis. Rare-earth transition metal carbides. *IEEE Transactions on Magnetics*, 28(5):2572, 1992.

[56] C. H. de Groot, K. H. J. Buschow, and F. R. de Boer. Magnetic properties of $r_2co_{17-x}al_x$ compounds (r = ho, dy, y). *Physica B: Condensed Matter*, 229(1-3):213, 1997.

[57] L. Zhang, D. C. Zeng, Y. N. Liang, J. C. P. Klaasse, E. Bruck, Z. Y. Liu, F. R. de Boer, and K. H. J. Buschow. Magnetic properties of $er_2co_{17-x}si_x$ compounds. *Journal of Magnetism and Magnetic Materials*, 214(1):31, 2000.

[58] Bing Liang, Bao-gen Shen, Fang-wei Wang, Tong-yun Zhao, Zhao-hua Cheng, Shao-ying Zhang, Hua-yang Gong, and Wen-shan Zhan. The magnetic properties of $gd_2co_{17-x}ga_x$ compounds. *Journal of Applied Physics*, 82(6):3452, 1997.

[59] Zhi-gang Sun, Shao-ying Zhang, Hong-wei Zhang, and Bao-gen Shen. The structure and magnetic properties of $gd_2co_{17-x}mn_x$ (x = 0–4) compounds. *Journal of Alloys and Compounds*, 322:69, 2001.

[60] Lin Qin, Yunxi Sun, Jian Lan, Shizhong Lu, and Hongwei Jiang. Crystallographic and magnetic properties of $r_2fe_{17}c_x$ with r = y, pr, nd, sm, gd, dy, and er. *Chinese Physics Letters*, 8:267, 1991.

[61] Shao-Ying Zhang Wen Shan Zhan Jing-Yun Wang, Bao-Gen Shen and Li-Gang Zhang. Structure, exchange interactions and magnetic anisotropy of $ho_2co_{17-x}si_x$ compounds. *Journal of Applied Physics*, 87:427, 2000.

[62] O. Isnard and M. Guillot. Investigation of the magnetic properties of nd_2fe_{17} and $nd_2fe_{17}h_x$ (x = 3, 4.9) in high magnetic field. *Journal of Applied Physics*, 87:5326, 2000.

[63] M. V. Satyanarayana, H. Fujii, and W. E. Wallace. Magnetic and structural investigations on substituted $pr_2co_{17-x}t_x$ systems (t = fe, mn, cr, cu and al). *Journal of Magnetism and Magnetic Materials*, 40:241, 1984.

[64] Zhi-gang Sun, Hong-wei Zhang, Shao-ying Zhang, Jing-yun Wang, and Bao-gen Shen. Structure and magnetic properties of $sm_2fe_{17-x}mn_x$ compounds. *Journal of Physics D: Applied Physics*, 33:485, 2000.

[65] Zhi-gang Sun, Hong-wei Zhang, Shao-ying Zhang, Jing-yun Wang, and Bao-gen Shen. Structure and magnetic properties of $tb_2co_{17-x}mn_x$ compounds. *Journal of Applied Physics*, 87:8666, 2000.

[66] E. A. Tereshina, H. Drulis, Y. Skourski, and I. S. Tereshina. Strong room-temperature easy-axis anisotropy in $tb_2fe_{17}h_3$: An exception among r_2fe_{17} hydrides. *Physical Review B*, 87:214425, 2013.

[67] Yingchang Yang, Qi Pan, Xiaodong Zhang, and Senlin Ge. Magnetic properties of $r_2fe_{17}cn_x$. *Journal of Applied Physics*, 72:2989, 1992.

[68] Z. Altounian, Xu Bo Liu, and Er Girt. Formation, structure and hard magnetic properties of $sm_2fe_{17-x}co_xc_y$ compounds. *Journal of Physics: Condensed Matter*, 15:3315, 2003.

[69] Linshu Kong, Jiabin Yao, Minghou Zhang, and Yingchang Yang. Magnetic properties of sm_2 $(fe_{1-x}co_x)_{17}c$ and y_2 $(fe_{1-x}co_x)_{17}c$. *Journal of Applied Physics*, 70:6154, 1991.

[70] O. Isnard, S. Miraglia, J. L. Soubeyroux, D. Fruchart, and P. L'Heritier. A structural analysis and some magnetic properties of the $r_2fe_{17}h_x$ series. *Journal of Magnetism and Magnetic Materials*, 137:151, 1994.

[71] D. P. Middleton, S. R. Mishra, Gary J. Long, O. A. Pringle, Z. Hu, W. B. Yelon, F. Grandjean, and K. H. J. Buschow. A magnetic, neutron–diffraction, and mössbauer spectral study of the $ce_2fe_{17-x}si_x$ solid solutions. *Journal of Applied Physics*, 78:5568, 1995.

[72] T. Pandey and David S. Parker. Magnetic properties and magnetocrystalline anisotropy of nd_2fe_{17}, $nd_2fe_{17}x_3$, and related compounds. *Scientific Reports*, 8:3601, 2018.

[73] H. Luo, Z. Hu, W. B. Yelon, S. R. Mishra, G. J. Long, O. A. Pringle, and K. H. J. Buschow. Neutron diffraction structural study of $ce_2fe_{17-x}ga_x$. *Journal of Applied Physics*, 79:6318, 1996.

[74] O. Isnard, S. Miraglia, D. Fruchart, J. Deportes, and P. L'Heritier. Magnetic properties of fully nitrogenated, $r_2fe_{17}n_3$ (r = ce, nd, pr). *Journal of Magnetism and Magnetic Materials*, 131:76, 1994.

[75] A. V. Andreev, D. Rafaja, J. Kamarad, Z. Arnold, Y. Homma, and Y. Shiokawa. Magnetic properties of the $lu_2fe_{17-x}si_x$ single crystals. *Journal of Alloys and Compounds*, 383:40, 2004.

[76] V. Psycharis, M. Anagnostou, C. Christides, and D. Niarchos. Rietveld analysis of x-ray powder diffraction patterns for the new $smfe_{10}mo_2n_x$ nitride compound. *Journal of Applied Physics*, 70:6122, 1991.

[77] K. Ohashi, Y. Tawara, R. Osugi, and M. Shimao. Magnetic properties of fe-rich rare-earth intermetallic compounds with a $thmn_{12}$ structure. *Journal of Applied Physics*, 64:2338, 1988.

[78] Satoshi Hirosawa, Yutaka Matsuura, Hitoshi Yamamoto, Setsuo Fujimura, and Masato Sagawa. Magnetization and magnetic anisotropy of $r_2fe_{14}b$ measured on single crystals. *J. Appl. Phys.*, 59:873, 1986.

[79] C. Abache and H. Oesterreicher. Magnetic properties of compounds $r_2fe_{14}b$. *J. Appl. Phys.*, 57:4112, 1985.

[80] Z. X. Tang, G. C. Hadjipanayis, and V. Papaefthymiou. Intrinsic and hard magnetic properties of rapidly quenched $ndfe_{10}mo_2n_x$ ribbons. *J. Alloys Compd.*, 194:87, 1993.

[81] Y. Z. Wang, B. P. Hu, X. L. Rao, G. C. Liu, L. Yin, W. Y. Lai, W. Gong, and G. C. Hadjipanayis. Structural and magnetic properties of ndfe$_{12-x}$mo$_x$n$_{1-\delta}$ compounds. *J. Appl. Phys.*, 73:6251, 1993.

[82] M. Anagnostou, C. Christides, and D. Niarchos. Nitrogenation of the rfe$_{10}$mo$_2$ (r = rare earth) compounds with thmn$_{12}$ type structure. *Solid State Commun.*, 78:681, 1991.

[83] Y. Zhang and C. Ling. A strategy to apply machine learning to small datasets in materials science. *npj Comput. Mater.*, 4:25, 2018.

[84] Anita Halder, Aishwaryo Ghosh, and Tanusri Saha Dasgupta. Machine-learning-assisted prediction of magnetic double perovskites. *Phys. Rev. Mater.*, 3:084418, 2019.

[85] L. Ward, A. Agrawal, A. Choudhary, and C. Wolverton. A general-purpose machine learning framework for predicting properties of inorganic materials. *npj Comput. Mat.*, 2:16028, 2016.

[86] Wessel N. van Wieringen. Lecture notes on ridge regression, 2020.

[87] Vladimir Vovk. *Empirical Inference*. Springer, Berlin, Heidelberg, 2013.

[88] Leo Breiman. Random forests. *Mach. Learn.*, 45:5, 2001.

[89] Andy Liaw and Matthew Wiener. Classification and regression by randomforest. *R News*, 2:18, 2002.

[90] Harris Drucker, C. J. C Burges, Linda Kaufman, Alex J. Smola, and Vladimir Vapnik. Support vector regression machines. In Michael Mozer, Michael I. Jordan, and Thomas Petsche, editors, *Proceedings of the International Conference on Advances in Neural Information Processing Systems*, page 155, Denver, CO, USA, 1997. MIT Press.

[91] Mohamad Hassoun. *Fundamentals of Artificial Neural Networks*. MIT Press, Cambridge, 1995.

[92] Nico J. D. Nagelkerke. A note on a general definition of the coefficient of determination. *Biometrika*, 78:691, 1991.

[93] Bernhard Schölkopf. The kernel trick for distances. In *Advances in Neural Information Processing Systems*, page 301, Cambridge, 2001. MIT Press.

[94] Support vector regression(svr). `http://lasa.epfl.ch/teaching/lectures/ML_Phd/Notes/nu-SVM-SVR.pdf`.

[95] I. Stephen. Perceptron-based learning algorithms. *IEEE Trans. Neural Netw.*, 50:179, 1990.

[96] Di Wei, Anurag Bhardwaj, and Jianing Wei. *Deep Learning Essentials*. Packt Publishing, Birmingham, 2018.

[97] Bradley Efron and Robert J. Tibshirani. *An Introduction to the Bootstrap*. CRC Press, Washington, D.C, 1994.

[98] Anton O. Oliynyk, Erin Antono, Taylor D. Sparks, Leila Ghadbeigi, Michael W. Gaultois, Bryce Meredig, and Arthur Mar. High-throughput machine-learning-driven synthesis of full-heusler compounds. *Chem. Mater.*, 28:7324, 2016.

[99] Fleur Legrain, Jesús Carrete, Ambroise van Roekeghem, Georg K. H. Madsen, and Natalio Mingo. Materials screening for the discovery of new half-heuslers: Machine learning versus ab initio methods. *J. Phys. Chem. B*, 122:625, 2018.

[100] Jesús Carrete, Wu Li, Natalio Mingo, Shidong Wang, and Stefano Curtarolo. Finding unprecedentedly low-thermal-conductivity half-heusler semiconductors via high-throughput materials modeling. *Phys. Rev. X*, 4:011019, 2014.

[101] D. Andrew Carr, Mohammed Lach-hab, Shujiang Yang, Iosif I. Vaisman, and Estela Blaisten-Barojas. Machine learning approach for structure-based zeolite classification. *Microporous Mesoporous Mater.*, 117:339, 2009.

[102] H. Fujii, K. Tatami, M. Akayama, and K. Yamamoto. Proc. 6th int. conf. on ferrites, icf6. In *Proceedings of the 6th International Conference on Ferrites*, page 1081, Tokyo, Japan, 1992. The Japan Society of Powder and Powder Metallurgy.

[103] H. Fujii, M. Akayama, K. Nakao, and K. Tatami. Effect of interstitial hydrogen and nitrogen on magnetic and structural properties of r_2t_{17} (r = y, ce and sm; t = fe, co and ni). *J. Alloys Comp.*, 219:10, 1995.

[104] Z. Altounian, X. Chen, L. X. Liao, D. H. Ryan, and J. O. Ström-Olsen. Structure and magnetic properties of rare-earth iron nitrides, carbides and carbonitrides. *J. Appl. Phys.*, 73:6017, 1993.

[105] X. Chen, Z. Altounian, and D. H. Ryan. Carbonitrides of r_2fe_{17} prepared by gas-solid reaction. *J. Magn. Magn. Mater.*, 125:169, 1993.

[106] K. H. J. Buschow, T. H. Jacobs, and W. Coene. Structure and properties of novel ternary fe-rich rare earth-carbides. *IEEE Trans. Magn.*, MAG-26:1364, 1990.

[107] J. P. Liu, K. Bakker, E. R. de Boer, T. H. Jacobs, D. B. de Mooij, and K. H. J. Buschow. Magnetic properties of $r_2fe_{17}n_{2.7}$ compounds. *J. Less-Common Met.*, 170:109, 1991.

[108] P. Blaha, K. Schwarz, G. K. H. Madsen, D. Kvasnicka, and J. Luitz. *WIEN2K, An Augmented Plane Wave + Local Orbitals Program for Calculating Crystal Properties*. Technische Universität Wien, Vienna, 2001.

[109] G. Kresse and J. Hafner. Ab initio molecular dynamics for liquid metals. *Phys. Rev. B*, 47:R558, 1993.

[110] G. Kresse and J. Furthmueller. Efficient iterative schemes for ab initio total-energy calculations using a plane-wave basis set. *Phys. Rev. B*, 54:11169, 1996.

[111] J. P. Perdew, K. Burke, and M. Ernzerhof. Generalized gradient approximation made simple. *Phys. Rev. Lett.*, 77:3865, 1996. Erratum: 78, 1396(E) (1997).

[112] A. I. Liechtenstein, V. I. Anisimov, and J. Zaanen. Density-functional theory and strong interactions: Orbital ordering in mott-hubbard insulators. *Phys. Rev. B*, 52:R5467, 1995.

[113] I. L. M. Locht, Y. O. Kvashnin, D. C. M. Rodrigues, M. Pereiro, A. Bergman, L. Bergqvist, A. I. Lichtenstein, M. I. Katsnelson, A. Delin, A. B. Klautau, B. Johansson, I. Di Marco, and O. Eriksson. Standard model of the rare earths analyzed from the hubbard i approximation. *Phys. Rev. B*, 94:085137, 2016.

[114] T. S. Zhao, H.-M. Jin, R. Grossinger, X.-C. Kou, and H. R. Kirchmayr. Analysis of the magnetic anisotropy in $smco_5$ and $gdco_5$. *J. Appl. Phys.*, 70:6134, 1991.

[115] X. C. Kou, R. Grossinger, M. Katter, J. Wecker, L. Schultz, T. H. Jacobs, and K. H. J. Buschow. Intrinsic magnetic properties of $r_2fe_{17}c_yn_x$ compounds: (r = y, sm, er, and tm). *J. Appl. Phys.*, 70:2272, 1991.

[116] W. G. Haije, T. H. Jacobs, and K. H. J. Buschow. Magnetic structure of ternary rare earth carbides of the type $r_2fe_{17}c$. *J. Less-Common Met.*, 163:353, 1990.

[117] T. W. Capehart, R. K. Misra, and F. E. Pickerton. $Sm_2fe_{17}n_x$: Site and valence of the interstitial nitrogen. *Appl. Phys. Lett.*, 58:1395, 1991.

[118] R. K. Chouhan, A. K. Pathak, D. Paudyal, and V. K. Pecharsky. High performance magnetic material with ce and la: An alternative to nd-fe-b magnet, smco-a case of strong j-mixing, 2024.

[119] B. Szpunar. Magnetic anisotropy of smco-a case of strong j-mixing. *Acta Phys. Pol. A*, 60:791, 1981.

[120] N. Thuy, J. Franse, N. Hong, and T. Hien. 3d anisotropy in r-3d intermetallics. *J. Phys. Colloques*, 49:499, 1988.

[121] P. Bruno. Tight-binding approach to the orbital magnetic moment and magnetocrystalline anisotropy of transition-metal monolayers. *Phys. Rev. B*, 39:865, 1989.

[122] J. Herbst. $R_2fe_{14}b$ materials: Intrinsic properties and technological aspects. *Rev. Mod. Phys.*, 63:819, 1991.

[123] T. Miyake and H. Akai. Quantum theory of rare-earth magnets. *J. Phys. Soc. Jpn*, 87:041009, 2018.

[124] Y. Hirayama, Y. Takahashi, S. Hirosawa, and K. Hono. $Ndfe_{12}n_x$ hard-magnetic compound with high magnetization and anisotropy field. *Scr. Mater.*, 95:70, 2015.

[125] K. H. J. Buschow. *Concise Encyclopedia of Magnetic and Superconducting Materials*. Elsevier, Amsterdam, 2005.

[126] J. M. D. Coey. *Magnetism and Magnetic Materials*. Cambridge University Press, Cambridge, 2010.

4

Magnetism and Unconventional Topology in $LaCoO_3/SrIrO_3$ Heterostructure*

4.1 Introduction and Motivation

Oxide heterostructures have emerged as a focal point of intense scientific inquiry in recent years, driven by the discovery of unique phenomena at interfaces between perovskite oxides. These interfaces exhibit unexpected electronic, magnetic, and transport properties that are often absent in the bulk forms of the constituent materials [1–5]. The emergence of such novel behaviors at oxide interfaces has opened up new avenues for exploring fundamental physics and developing potential applications in advanced electronics and materials science.

The creation of heterostructures with optimized properties, however, remains a complex challenge. This complexity arises from the intricate interactions occurring at the interface, which involve a delicate interplay of structural, electronic, and magnetic degrees of freedom. Understanding and controlling these interactions is crucial for harnessing the full potential of oxide heterostructures in both fundamental research and technological applications.

Among the various systems studied, the $LaAlO_3$ (LAO)/$SrTiO_3$ (STO) interface stands out as a paradigmatic example. This interface exhibits conductivity between two otherwise insulating materials, a phenomenon attributed to the polarity mismatch at the atomic

*This chapter is based on publication: **Samir Rom**, Santu Baidya, Subhro Bhattacharjee, and Tanusri Saha-Dasgupta, Appl. Phys. Lett. 122, 021602 (2023).

level [3]. The LAO/STO system has become a cornerstone in the field, demonstrating how controlled termination of atomic layers can introduce additional charge, resulting in unusual electronic states. Moreover, it has shown the possibility of tuning material properties through precise interface engineering.

Expanding on the findings derived from the LAO/STO system, our investigation primarily addresses the relatively unexplored $LaCoO_3$ (LCO)/$SrIrO_3$ (SIO) interface. This system serves as a compelling example where polarity discontinuities and charge transfer are anticipated to significantly influence interfacial properties. Among the materials under consideration, 5d TMOs have been identified as promising candidates for manifesting noteworthy quantum phenomena. These phenomena stem from the interaction between pronounced spin-orbit coupling (SOC) and electron-electron correlation. Specifically, iridium-based TMOs from the Ruddlesden-Popper series, represented as $Sr_{n+1}Ir_nO_{3n+1}$, have garnered substantial research interest [6]. For instance, the $n = 1$ member, Sr_2IrO_4, is recognized as a SOC-driven magnetic insulator [7] with a half-filled doublet $J_{\text{eff}} = 1/2$ state. Conversely, the $n = \infty$ member, $SrIrO_3$ (SIO), demonstrates paramagnetic semimetallic behavior attributed to the increased covalency between Ir 5d and O 2p orbitals [8]. The SOC in SIO further leads to the emergence of a Dirac-nodal line semimetallic state [9]. Despite its semimetallic nature, theoretical calculations indicate that SIO is close to a magnetic instability [10], prompting significant interest in SIO-based heterostructures, particularly when paired with magnetically active layers such as $SrRuO_3$ [11] or manganites [12].

Building upon these investigations, a heterostructure consisting of SIO and LCO has been successfully synthesized [13]. This specific combination has exhibited remarkable properties, notably a pronounced anomalous Hall effect (AHE) and anomalous magnetoresistance. These observations are particularly surprising given that bulk LCO is known to be a diamagnetic insulator at low temperatures [14], unlike the magnetic nature of $SrRuO_3$ or manganites typically used in other SIO-based heterostructures. An important aspect of the experimental setup is that the heterostructure is formed on a $SrTiO_3$ (STO) substrate. The substrate imposes a pseudo-tetragonal symmetry on both SIO and LCO layers. Although the strained tetragonal structure of SIO supports a canted antiferromagnetic state [15], the emergence of ferromagnetism (FM) in SIO, as observed in the LCO/SIO heterostructure, suggests a significant role played by LCO. This underscores the importance of a thorough theoretical investigation to unravel the microscopic mechanisms underpinning these observations and to understand the contribution of LCO to the induced FM in SIO [13].

Given these considerations, detailed theoretical studies are necessary to achieve a comprehensive understanding of the microscopic processes in these heterostructures. Such investigations may provide insights that enable the design of new materials with tailored properties.

4.2 Computational Methodology

In this work, we employed first-principles calculations using the PAW potentials, as implemented in VASP package [16, 17]. The generalized gradient approximation (GGA) was chosen to describe the exchange-correlation functional, while the effect of spin-orbit coupling (SOC), which is particularly significant at the Ir sites, was incorporated through GGA+SOC calculations.

A crucial aspect of studying correlated oxides is the treatment of electron-electron interactions, particularly via the Hubbard U parameter and Hund's coupling J_H. These parameters are essential for capturing the localized nature of d-electrons in transition metal oxides. To account for the strong electron-electron correlation beyond GGA, we employed +U calculations within the rotationally invariant formulation [18]. Specifically, the U and J_H values at the Ir site were set to 2 and 0.5 eV, respectively, in accordance with the literature [19].

While U and J_H are often treated as adjustable parameters that can be varied within a reasonable range, a more rigorous approach involves determining these parameters from first principles. In our study, we utilized the constrained density functional theory (DFT) method [20, 21] to compute these values. This method involves constraining the d-orbital occupancy during DFT calculations and determining U as the numerical derivative of the d-orbital energy with respect to its occupancy. Consequently, we obtained U and J_H values of 2.2 and 0.45 eV, respectively, for the Ir site, which are close to the values used in the present calculations.

To ensure reliable convergence of the ground-state properties, a Monkhorst-Pack k-point mesh of $7 \times 7 \times 1$ and a plane-wave energy cutoff of 600 eV were employed. These computational parameters were carefully selected based on convergence tests that confirmed their adequacy for accurately describing the system's properties.

This methodology was applied to investigate the electronic and magnetic properties of LCO/SIO heterostructures. The atomic positions were relaxed to their equilibrium configurations until the Hellmann-Feynman forces on each ion were reduced to below 0.001 eV/Å, ensuring precise structural optimization.

The topological properties were analyzed using the WANNIER90 code [22]. Initially, we computed the maximally-localized Wannier functions (MLWFs) to derive a tight-binding model from the ab-initio DFT calculations, with Sr-s, Ir-d, and O-p orbitals as the basis set. We then calculated the Berry flux through a closed surface enclosing a node using the WannierTools software [23].

In the clean limit, we used the Kubo formalism [24] to calculate the Berry curvature, given by:

$$\Omega_n^z(k) = -2\,\mathrm{Im} \sum_{m \neq n} \frac{\langle n|\hat{v}_x|m\rangle \langle m|\hat{v}_y|n\rangle}{(\varepsilon_m - \varepsilon_n)^2}$$

where ε_m and $|m\rangle$ are the m-th energy eigenvalue and eigenvector of the Hamiltonian, and $\hat{v}_x$ and $\hat{v}_y$ are the velocity operators along the x and y directions, respectively.

The Chern numbers were derived by integrating the Berry curvatures over the first Brillouin zone:

$$C_N = \frac{1}{2\pi} \sum_n \int_{BZ} \Omega_n(k)\, d^2k$$

where $\Omega_n(k)$ represents the Berry curvature of the n-th band at a specified k point.

We then calculated the intrinsic anomalous Hall conductivity, originating from the Berry curvature effect, using:

$$\sigma_{xy} = -\frac{e^2}{\hbar} \sum_n \int_{BZ} \frac{d^3k}{(2\pi)^3} \Omega_n^z(k) f_n$$

where f_n is the Fermi-Dirac distribution function.

4.3 Results

4.3.1 Heterostructure in superlattice geometries and interface characteristics

To theoretically explore the physical properties of LCO/SIO heterostructures, we consider a superlattice geometry denoted as $[(\mathrm{LCO})_{m.5}/(\mathrm{SIO})_{n.5}]$. In this configuration, the IrO_2 layer of SIO is adjacent to the LaO layer of LCO. The in-plane lattice constants are fixed at 3.905 Å to simulate the effect of the STO substrate. This imposition induces strain in both materials: SIO experiences a compressive strain of approximately 1.1%, while LCO undergoes an expansive strain of around 1.5%. While the in-plane lattice constant is held fixed, the out-of-plane lattice constant is allowed to relax, including adjustments to the z-coordinates of the atoms. The calculations are conducted within the framework of DFT using the plane wave-based pseudopotential method, as implemented in the VASP Package [25, 26].

The top panel of Figure 4.1 illustrates the schematic representation of the $[(\mathrm{LCO})_{m.5}/(\mathrm{SIO})_{n.5}]$ superlattice structure, constrained by the in-plane lattice constants of the STO substrate. Notably, the A+/B+ cations in SIO are in 2+/4+ valence states, resulting in neutral SrO and IrO_2 layers. In contrast, in LCO, the cations are in 3+/3+ valence states, yielding a positively charged LaO layer with a charge of +1 and a negatively charged CoO_2 layer with

a charge of -1. Consequently, the neutral IrO_2 layer of SIO, facing the positively charged LaO layer of LCO, creates an n-type interface (IF).

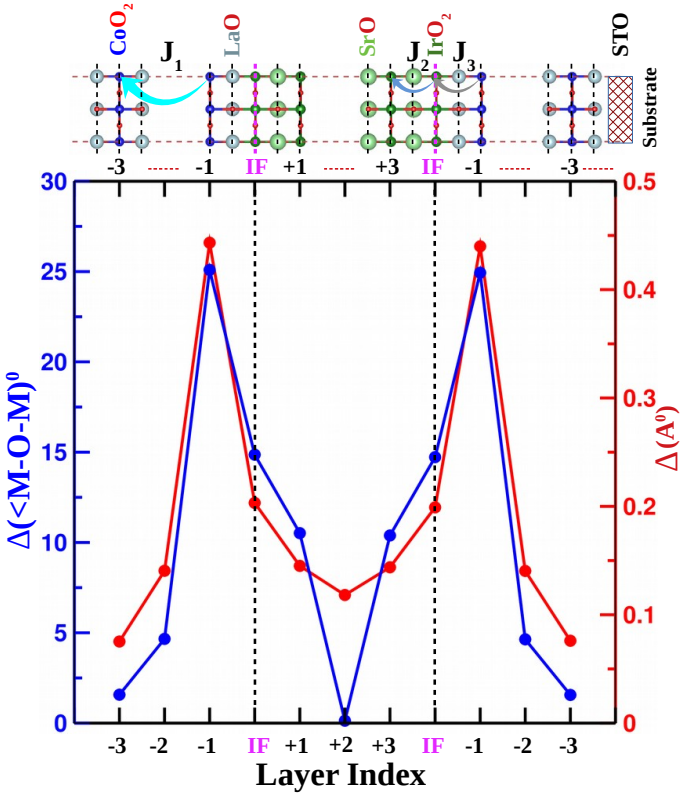

Figure 4.1: *Top: Schematic representation of the LCO/SIO superlattice structure on an STO substrate. The n-type interface (IF) formed between the IrO_2 layer of SIO and the LaO layer of LCO is marked, along with the different transition metal-oxygen (TM-O) layers and the magnetic exchanges J_1, J_2, and J_3. Bottom: The distortion of the CoO_6 and IrO_6 octahedra plotted as a function of the layer index for the $m = 4$ superlattice. Distortion is measured in terms of the tilt angle (left axis), representing the deviation of the TM–O–TM bond angle from 180°, and the tetragonal bond distortion (right axis).*

In the superlattice geometry, we consider two symmetric n-type interfaces within the periodic cell, leading to nonstoichiometric supercells characterized by an extra IrO_2 layer in SIO and an additional LaO layer in LCO. The parameter n is fixed at 4, while m varies from 4 to 6. The bottom panel of Figure 4.1 depicts the tilt and distortion of the CoO_6 and IrO_6 octahedra, measured by the variation in metal-oxygen bond lengths, as a function of the layer number. The layers are numbered relative to the interface (IF), with IF + l and IF - l referring to the transition metal (TM) layers in the SIO and LCO blocks, respectively. As expected, the maximum tilt and distortion of the octahedra occur at the IF, with tilt angles reaching up to 15° for IrO_6 and 25° for CoO_6, and bond distortions of approximately 0.2 Å and 0.45 Å, respectively. These structural deviations diminish progressively toward the center of each block, becoming negligible at the block's center.

The polar discontinuity at the IF, arising from the interface between the neutral layers

of SIO and the charged layers of LCO, results in a diverging electrostatic potential. This potential can be mitigated by interfacial polar charge transfer, a process that significantly influences the properties of the heterostructure. The direction and magnitude of this charge transfer are critical factors that will be discussed in detail in subsequent sections.

4.3.2 Valence and spin states of transition metal ions in superlattice structures

The compound $LaCoO_3$ (LCO) is widely studied for its temperature-induced spin state transition and the ongoing debate surrounding the nature of the spin state. The calculated spin state of the Co ion in bulk LCO is highly sensitive to the choice of the Hubbard U and Hund's coupling J_H parameters, as reported in previous studies [14]. In our current investigation, we varied the U and J_H values for Co over a wide range to examine their impact on the structural, electronic, and magnetic properties of the heterostructure. The trends observed in these properties were consistent across the studied systems with $m = 4, 5,$ and 6.

Figure 4.2 presents the layer-resolved and atom-projected GGA+U density of states for the $(LCO)_{4.5}/(SIO)_{4.5}$ heterostructure. The contributions from the four distinct CoO_2 layers [(IF-1), (IF-2), (IF-3), and (IF-4) from top to bottom] within the LCO block are displayed in the left panel. Meanwhile, the contributions from the five distinct IrO_2 layers [(IF), (IF+1), (IF+2), (IF+3), and IF from top to bottom] are depicted in the right panel.

In SIO, the crystal field split and spin split Ir t_{2g} states, which are strongly mixed with O p states, cross the Fermi level (E_F) while the e_g states remain unoccupied. This electronic structure characterizes the SIO as a ferromagnetic metal within the heterostructure. The calculated magnetic moment at the Ir site is approximately 0.5 μ_B, which includes an orbital moment of around 0.1 μ_B. Additionally, a significant magnetic moment of approximately 0.1 μ_B is observed at the O sites within the IrO_2 layers.

Focusing on the Co electronic structure, in the majority spin channel, the Co t_{2g} states are fully occupied, while the broad Co e_g states partially cross E_F, showing a low density of states at E_F. In the minority spin channel, the Co e_g states are completely empty, while the Co t_{2g} states are largely filled, with a partial gap arising from the combined effects of crystal field splitting and the Hubbard U. The low density of states at E_F in the majority spin channel may be susceptible to localization effects, which could explain certain experimental observations [13].

Figure 4.3 illustrates the computed magnetic moments and Bader charges for the Co and Ir sites across different layers. The top panel shows the magnetic moments at CoO_2 layers adjacent to the interface (IF-1) and the next layer (IF-2) for various U and J_H values.

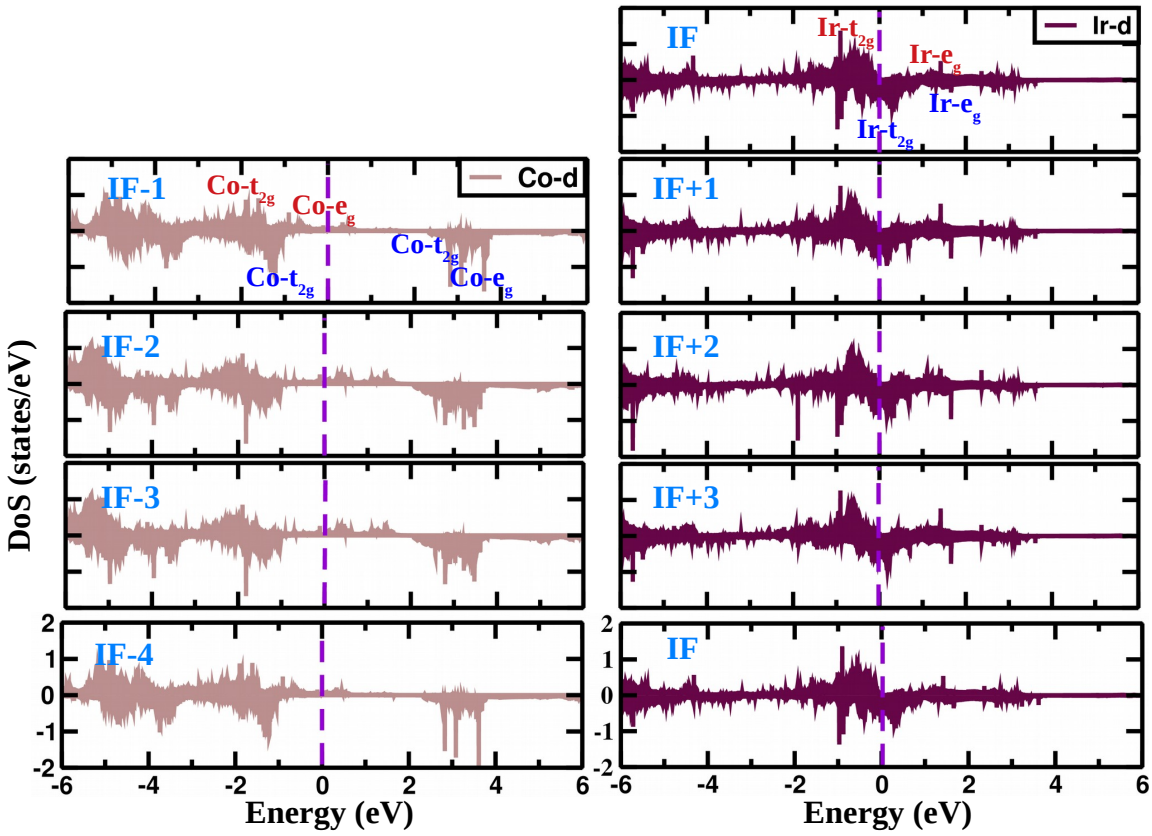

Figure 4.2: *(Color Online) The layer-resolved density of states projected onto Co d (left) and Ir d (right) orbitals in the (IF-l) and (IF+l) layers of CoO_2 and IrO_2 in the LCO and SIO blocks of the $(LCO)_{4.5}/(SIO)_{4.5}$ superlattice. The energy zero point is set at the Fermi energy. The octahedral crystal field split t_{2g} and e_g contributions of Co d and Ir d orbitals are marked.*

The bottom panel depicts the variation in magnetic moments and Bader charges at these sites as a function of the layer index.

The Co d states exhibit layer-dependent behavior; the electronic structure near E_F for Co atoms in layers closer to the interface differs from those in more distant layers. The partially filled Co e_g states in the majority spin channel are notably more pronounced for layers adjacent to the interface compared to those further away. This difference is also evident in the magnetic moment calculations, with layers close to the interface showing approximately 0.3 μ_B higher magnetic moments than those farther from the interface. Bader charge analysis [27] corroborates this finding, revealing that Co sites near the interface have approximately 0.2 e^- more charge than those away from it.

The calculated magnetic moments for the Co ions, including contributions from oxygen atoms, range between 2 and 3 μ_B, depending on the chosen U and J_H values. In the fully polarized limit, the nominal Co^{3+} valence in a $3d^6$ configuration can exhibit magnetic moments of 0, 2, and 4 μ_B corresponding to low-spin (LS), intermediate-spin (IS) and high-spin (HS) states, respectively [14]. Thus, our results indicate a reduction in the Co valence

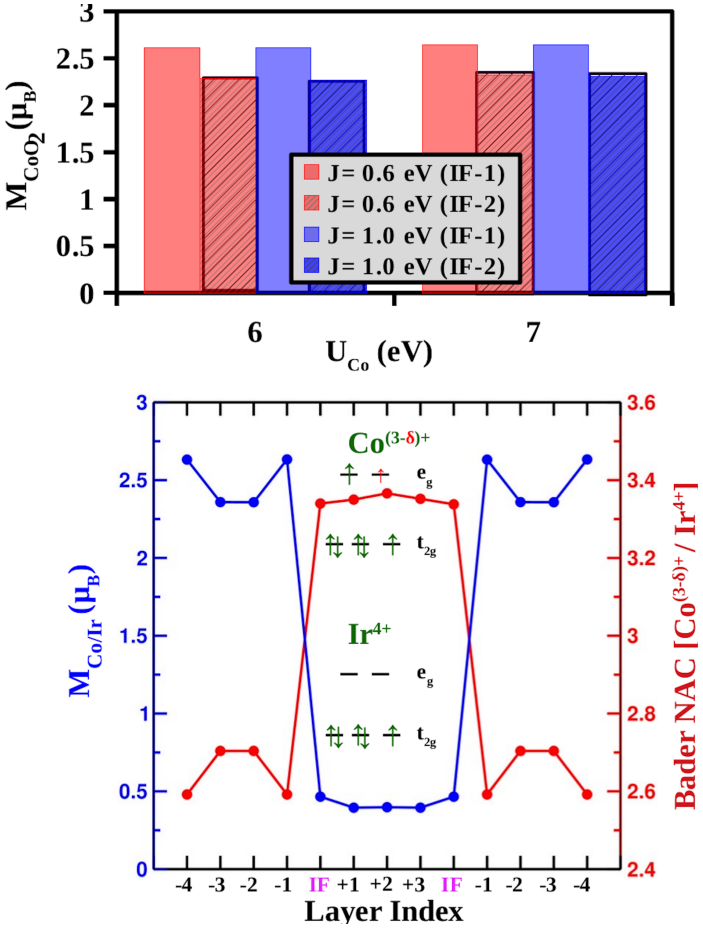

Figure 4.3: *Top: Computed magnetic moment in the CoO_2 layers adjacent to the interface (IF), labeled as IF-1, and the subsequent layer, labeled as IF-2, for various U and J_H values at the Co site. Bottom: Magnetic moment (left axis) and Bader charge (right axis) at the Co and Ir sites, plotted as a function of the layer index for the m = 4 LCO/SIO superlattice. The inset shows the electron occupancy of the Ir and Co d levels split by the octahedral crystal field.*

.

state from 3+ in the bulk structure towards 2+ in the heterostructure, leading to a (3-δ)+ valence state, where δ is larger for Co atoms near the interface compared to those farther away. This corresponds to an intermediate-spin state for Co.

To verify the dependence of the charge and spin state of Co on the choice of Coulomb parameters, we varied the value of U over a broad range (4–7 eV) and the value of J_H over 0.6–1.0 eV. As shown in Figure 4.4, the calculated magnetic moments consistently fall within 2–3 μ_B for all cases, with larger moments observed in layers close to the interface compared to those farther away. This robustness in the magnetic moment suggests a consistent interfacial charge flow towards the LCO block, in alignment with experimental findings [13] as observed through energy loss spectroscopy. The stabilization of the intermediate spin state of Co observed in this study warrants further experimental investigation to confirm these theoretical predictions.

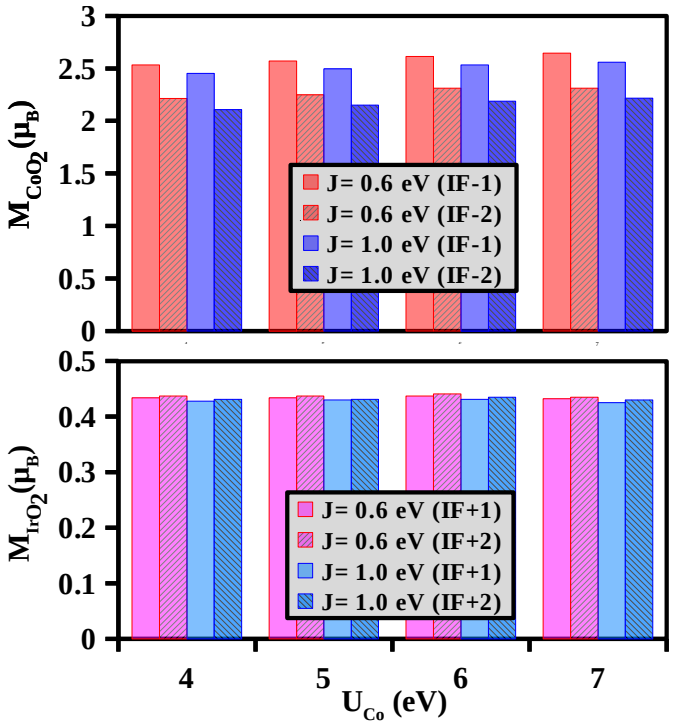

Figure 4.4: *(Color Online) Top: Computed magnetic moment in the CoO_2 layers adjacent to the interface (IF-1) and the next layer (IF-2). Bottom: Computed magnetic moment in the IrO_2 layers adjacent to the interface (IF+1) and the next layer (IF + 2) for various values U and J_H at the Co site.*

4.3.3 Magnetic exchange interactions and interface magnetism

To fully comprehend the magnetic ground state of the system, it is essential to investigate the magnetic exchange interactions in addition to the magnetic states of the transition-metal ions established earlier. As depicted in Figure 4.1, the primary magnetic interactions include the nearest neighbor (NN) Co–Co interactions within the LCO block, the Co–Ir interactions across the interface and the Ir–Ir interactions within the SIO block.

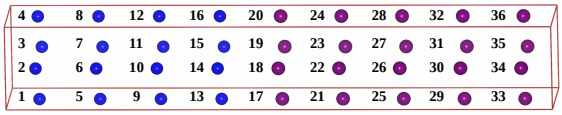

	1-4	5-8	9-12	13-16	17-20	21-24	25-28	29-32	33-36	ΔE
FM.	u	u	u	u	u	u	u	u	u	0
FiM1.	u	u	u	u	d	d	d	d	d	-31.98
FiM2.	u	u	u	u	d	u	u	u	d	-1.86
FiM3.	u	d	d	u	d	d	d	d	d	-767.6
FiM4.	u	d	d	u	u	u	u	u	u	-613.57

Figure 4.5: *(Color Online) The five different spin configurations considered to estimate the magnetic exchanges. The top panel diagram illustrates the numbering of the Co (blue) and Ir (violet) atoms. The table in the bottom panel presents the energies (in meV) of each configuration, measured relative to the energy of the ferromagnetic configuration.*

To estimate these interactions, we examined five different spin configurations with various possible alignments of the Co and Ir spins, as shown in Figure 4.5. The Co and Ir atoms in four distinct layers of CoO_2 and five layers of IrO_2 are numbered, with their spin orientations indicated. In shorthand notation, up and down spins are represented by the letters "u" and "d," respectively.

We calculated the total energy for these five spin configurations and mapped them onto the spin Hamiltonian $H_{\text{magnetic}} = -J_{ij}\mathbf{S}_i \cdot \mathbf{S}_j$, where $\mathbf{S}_i$ and $\mathbf{S}_j$ represent the spins of two atoms separated by a distance r, and J_{ij} is the exchange constant. A positive J_{ij} indicates a ferromagnetic (FM) interaction, while a negative J_{ij} indicates an antiferromagnetic (AFM) interaction. Our results show that the total energy of each spin configuration is highly dependent on the structural relaxation of atomic positions induced by the magnetic order, indicating a strong magnetostructural coupling in the heterostructure.

Interestingly, among all the spin configurations studied, the parallel alignment of Co and Ir spins within the LCO and SIO blocks is the most energetically favorable. By mapping the computed total energies to an NN spin model, we determined the exchange constants J_1, J_2, and J_3 to be $+8.8$, $+0.6$, and $+1.6$ meV, respectively. The positive values indicate ferromagnetic interactions, highlighting that strong FM within the LCO block induces FM within the SIO block via Co–Ir magnetic coupling.

Further analysis of magnetocrystalline anisotropy revealed a pronounced preference for an in-plane spin orientation, with an energy gain of approximately 4 meV per Ir atom over the out-of-plane orientation. This result is consistent with experimental findings [13] and underscores the significance of in-plane magnetic anisotropy in this heterostructure system.

4.3.4 Topology in strained tetragonal ferromagnetic $SrIrO_3$

As discussed previously, the potential topological properties of bulk $SrIrO_3$ (SIO) have been extensively explored both theoretically and experimentally [9, 28]. Theoretical calculations revealed the presence of a line node composed of $J_{\text{eff}} = 1/2$ bands below the Fermi level [9]. Angle-resolved photoemission spectroscopy (ARPES) studies on strained SIO grown on substrates such as $SrTiO_3$ (STO) and $(LaAlO_3)_{0.3}(Sr_2TaAlO_6)_{0.7}$ (LSAT) indicated the existence of Dirac line nodes, which were observed to be gapped [28]. Furthermore, the experimental observation of a large anomalous Hall effect (AHE) in the LCO/SIO heterostructure [13] points to an intriguing interplay between magnetism and topology when SIO is in contact with LCO.

In the heterostructure configuration, the interaction between Co and Ir at the interface induces ferromagnetism (FM) in SIO, which contrasts with its bulk paramagnetic, monoclinic symmetry. Moreover, the pseudo-tetragonal symmetry of the heterostructure, imposed by the substrate, further modifies the electronic structure of the SIO. Consequently,

it is essential to investigate the topological properties of FM and tetragonal SIO under these conditions.

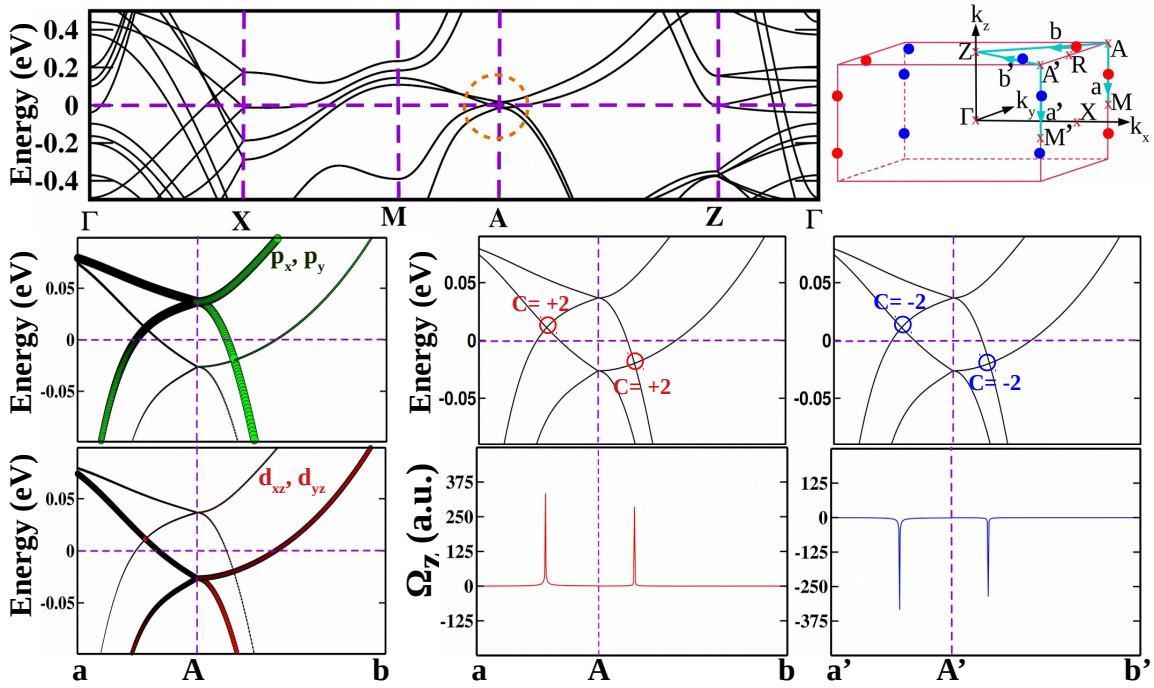

Figure 4.6: *Top: The GGA + SOC + U band structure of ferromagnetic (FM), tetragonal $SrIrO_3$ (SIO), with in-plane lattice parameters constrained to those of $SrTiO_3$ (STO) (left), plotted along the high-symmetry directions of the tetragonal Brillouin zone (BZ) (right). Bottom: Left—band structure zoomed along $a = (\pi/a, \pi/a, 0.126\pi/c)$, $A = (\pi/a, \pi/a, \pi/c)$, $b = (0.224\pi/a, 0.224\pi/a, \pi/c)$, and the symmetry-related path $a' = (\pi/a, \pi/a, 0.126\pi/c)$, $A' = (\pi/a, \pi/a, \pi/c)$, $b' = (0.224\pi/a, 0.224\pi/a, \pi/c)$, projected onto the Ir d_{xz}/d_{yz} and the O p_x/p_y orbitals. Middle—calculated Chern numbers and Berry curvatures of the two crossings above and below E_F along a–A–b. Right—the same along a'–A'–b'. See the top right panel for the positioning of a, a', b, and b' in the BZ, with Weyl points of positive and negative chirality colored red and blue, respectively.*

The top panel of Figure 4.6 illustrates the GGA + SOC + U band structure of FM, tetragonal SIO, confirming its metallic nature and showing several band crossings near the Fermi level (E_F). The pseudo-tetragonal symmetry leads to orbital degeneracies among the orbitals Ir d_{yz} and d_{xz}, as well as the O p_x and p_y. Recent studies have sought to identify topological semimetals beyond the conventional Dirac and Weyl types, focusing on those characterized by higher topological charges. In this context, the concept of double Weyl points has been explored and is illustrated schematically in Figure 4.7 [29]. These can manifest as three-fold degenerate spin-1 Weyl points with linear band crossings and a Chern number $C = 2$ along with an additional flat band [30], four-fold degenerate charge-2 Dirac points [29], or two-fold degenerate charge-2 Weyl points with quadratic dispersion [31].

The FM SIO's orbital degeneracy offers the potential for realizing such double Weyl

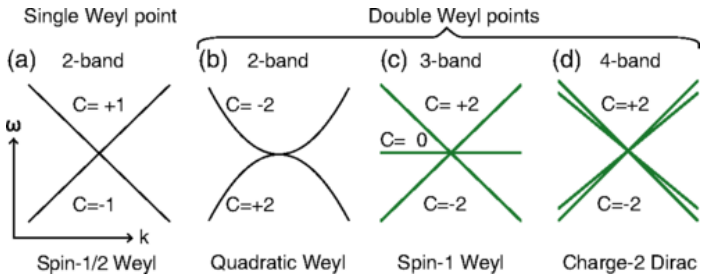

Figure 4.7: *Illustrations of various Weyl points with different Chern numbers. (a) A conventional spin-*$1/2$ *Weyl point characterized by a Chern number of* ± 1*. (b) A quadratic Weyl point, which involves 2 bands and exhibits Chern numbers of* ± 2*. (c) A spin-1 Weyl point, consisting of 3 bands with Chern numbers of 0 and* ± 2*. (d) A charge-2 Dirac point involving 4 bands, characterized by Chern numbers of* ± 2*. In this context, the quadratic Weyl point, spin-1 Weyl point, and charge-2 Dirac point are categorized as double Weyl points. The figure is adapted from [29].*

points. Analyzing the band structure near the A point (π/a, π/a, π/c) along the M(π/a, π/a, 0) – A – Z(0, 0, π/c) path reveals two linear band crossings: one at approximately 0.01 eV above E_F and another at approximately 0.02 eV below E_F (see the encircled regions in the bottom panels of Figure 4.6). Furthermore, two semi-Dirac crossings are observed at high-symmetry A (A$'$) points. These crossings result from the intersection of two doubly degenerate bands, arising from the degenerate orbitals Ir d_{xz}/d_{yz} and O p_x/p_y, as shown in the left panels of the bottom row in Figure 4.6.

Focusing on linear crossings away from the high-symmetry A point, the degenerate orbitals undergo transformations under symmetry operations, leading to two degenerate Weyl points at the same momenta, K. These linear crossings can be described by the low-energy Hamiltonian $H = H \otimes \sigma_0$, where H is the Hamiltonian for each Weyl point and σ_0 is the identity matrix in orbital space. This results in double Weyl points that are locally stable unless perturbed by mixing with Weyl points of opposite chirality or lifting of orbital degeneracy. These points are characterized by a topological charge of $C = \pm 2$, which meets the criteria for charge-2 Dirac points.

The calculated Chern number for the crossing at $K = (\pi/a, \pi/a, 0.339)$ above E_F is $+2$, while the symmetry-related crossing at $K = (\pi/a, -\pi/a, 0.339)$ exhibits a Chern number of -2. Similarly, the crossing at $K = (0.446\ \pi/a, 0.446\ \pi/a, \pi/a)$ above E_F has a Chern number of $+2$, whereas the symmetry-related crossing at $K = (0.446\ \pi/a, -0.446\ \pi/a, \pi/a)$ shows a Chern number of -2, as illustrated in the bottom, middle and right panels of Figure 4.6. These opposite chiralities of Weyl points above and below E_F are corroborated by the opposite signs of the calculated Berry curvatures (cf. Figure 4.6). The calculated intrinsic anomalous Hall conductivity (AHC), arising from the Berry curvature effect, is found to be positive and substantial, with a value of 7.5 Ω^{-1} cm^{-1}, in good agreement with the experimental measurements. An adaptively refined [32] k grid of $16 \times 16 \times 16$ was

sufficient to achieve convergence for the AHC value.

4.4 Summary and Discussion

In summary, our first-principles investigation of the $LaCoO_3/SrIrO_3$ (LCO/SIO) heterostructure provides a detailed microscopic understanding of the observed counterintuitive ferromagnetism and reveals intriguing topological properties of the system. Our study corroborates the experimental findings of interfacial charge transfer to the LCO layer, leading to a reduction in the nominal valence of Co from $3+$ towards $2+$. Furthermore, we predict the presence of an intermediate spin (IS) state for Co, which generates robust ferromagnetic exchange interactions between Co sites. This is noteworthy since, in the bulk ground state, Co stabilizes in a non-magnetic low-spin (LS) state.

The strong ferromagnetic exchange between Co ions is found to induce a long-range ferromagnetic order within the SIO block through interfacial Co–Ir ferromagnetic interactions. This elucidates the critical role of LCO in stabilizing the magnetism within the LCO/SIO heterostructure. Additionally, the ferromagnetic, tetragonal SIO, constrained by the STO substrate, is shown to host charge-2 Dirac points, driven by the inherent orbital degeneracy.

Our findings not only offer a microscopic explanation for the observed anomalous Hall effect (AHE) in the LCO/SIO heterostructure [13], but also pave the way for the exploration of novel quasiparticles. The realization of charge-2 Dirac points suggests the potential for discovering new material phases beyond the conventional Dirac and Weyl points, thereby expanding the scope of topological materials research.

Bibliography

[1] R. Ramesh and V. G. Keramidas. Metal-oxide heterostructures. *Annual Review of Materials Science*, 25:647–672, 1995.

[2] Zhen Huang, Ariando, Xiao Renshaw Wang, Andrivo Rusydi, Jingsheng Chen, Hyunsoo Yang, and Thirumalai Venkatesan. Interface engineering and emergent phenomena in oxide heterostructures. *Advanced Materials*, aug 2018.

[3] Akira Ohtomo and Harold Y. Hwang. A high-mobility electron gas at the laalo3/srtio3 heterointerface. *Nature*, 427(6973):423–426, 2004. Erratum in: Nature. 2006 May 4;441(7089):120.

[4] Yin-Long Han, Sheng-Chun Shen, Jie You, Hai-Ou Li, Zhong-Zhong Luo, Cheng-Jian Li, Guo-Liang Qu, Chang-Min Xiong, Rui-Fen Dou, Lin He, Don Naugle, Guo-Ping Guo, and Jia-Cai Nie. Two-dimensional superconductivity at (110) LaAlO3/SrTiO3 interfaces. *Applied Physics Letters*, 105(19):192603, 11 2014.

[5] M. Ye. Zhuravlev, R. F. Sabirianov, S. S. Jaswal, and E. Y. Tsymbal. Giant electroresistance in ferroelectric tunnel junctions. *Phys. Rev. Lett.*, 94:246802, Jun 2005.

[6] W. Witczak-Krempa, G. Chen, Y. B. Kim, and L. Balents. Correlated quantum phenomena in the strong spin-orbit regime. *Annual Review of Condensed Matter Physics*, 5:57–82, 2014.

[7] B. J. Kim, Hosub Jin, S. J. Moon, J.-Y. Kim, B.-G. Park, C. S. Leem, Jaejun Yu, T. W. Noh, C. Kim, S.-J. Oh, J.-H. Park, V. Durairaj, G. Cao, and E. Rotenberg. Novel $J_{\text{eff}} = 1/2$ mott state induced by relativistic spin-orbit coupling in sr_2iro_4. *Phys. Rev. Lett.*, 101:076402, Aug 2008.

[8] Z. T. Liu, M. Y. Li, Q. F. Li, J. S. Liu, W. Li, H. F. Yang, Q. Yao, C. C. Fan, X. G. Wan, Z. Wang, and D. W. Shen. Direct observation of the dirac nodes lifting in semimetallic perovskite sriro3 thin films. *Scientific Reports*, 6(1):30309, 2016.

[9] M. Ahsan Zeb and Hae-Young Kee. Interplay between spin-orbit coupling and hubbard interaction in $sriro_3$ and related *Pbnm* perovskite oxides. *Phys. Rev. B*, 86:085149, Aug 2012.

[10] Jean-Michel Carter, V. Vijay Shankar, M. Ahsan Zeb, and Hae-Young Kee. Semimetal and topological insulator in perovskite iridates. *Phys. Rev. B*, 85:115105, Mar 2012.

[11] Jun-ichiro Matsuno, Naoya Ogawa, Kenji Yasuda, Fumiyuki Kagawa, Wataru Koshibae, Naoto Nagaosa, Yoshinori Tokura, and Masashi Kawasaki. Interface-driven topological hall effect in srruo3-sriro3 bilayer. *Science Advances*, 2(7):e1600304, 2016.

[12] G. A. Ovsyannikov, T. A. Shaikhulov, K. L. Stankevich, Yu. Khaydukov, and N. V. Andreev. Magnetism at an iridate/manganite interface: Influence of strong spin-orbit interaction. *Phys. Rev. B*, 102:144401, Oct 2020.

[13] A. Kumar Jaiswal, D. Wang, V. Wollersen, R. Schneider, M. Le Tacon, and D. Fuchs. Direct observation of strong anomalous hall effect and proximity-induced ferromagnetic state in sriro3. *Advanced Materials*, 34:2109163, 2022.

[14] M. A. Korotin, S. Yu. Ezhov, I. V. Solovyev, V. I. Anisimov, D. I. Khomskii, and G. A. Sawatzky. Intermediate-spin state and properties of $lacoo_3$. *Phys. Rev. B*, 54:5309–5316, Aug 1996.

[15] T. R. Dasa, L. Hao, J. Yang, J. Liu, and H. Xu. Designing iridate-based superlattice with large magnetoelectric coupling. *Materials Today Physics*, 4:43–48, 2018.

[16] G. Kresse and J. Hafner. Ab initio molecular dynamics for liquid metals. *Physical Review B*, 47(1):558–561, 1993.

[17] G. Kresse and J. Furthmüller. Efficient iterative schemes for ab initio total-energy calculations using a plane-wave basis set. *Physical Review B*, 54(16):11169–11186, 1996.

[18] A. I. Liechtenstein, V. I. Anisimov, and J. Zaanen. Density-functional theory and strong interactions: Orbital ordering in mott-hubbard insulators. *Phys. Rev. B*, 52:R5467–R5470, Aug 1995.

[19] Tamene R. Dasa, Lin Hao, Jian Liu, and Haixuan Xu. Designing iridate-based superlattice with large magnetoelectric coupling. *J. Mater. Chem. C*, 7:13294–13300, 2019.

[20] V. I. Anisimov and O. Gunnarsson. Density-functional calculation of effective coulomb interactions in metals. *Physical Review B*, 43(10):7570–7574, Apr 1991.

[21] P. H. Dederichs, S. Blügel, R. Zeller, and H. Akai. Ground states of constrained systems: Application to cerium impurities. *Physical Review Letters*, 53(26):2512–2515, Dec 1984.

[22] A. A. Mostofi, J. R. Yates, G. Pizzi, Y. S. Lee, I. Souza, D. Vanderbilt, and N. Marzari. An updated version of wannier90: A tool for obtaining maximally-localised wannier functions. *Computer Physics Communications*, 185(8):2309–2310, 2014.

[23] Q. Wu, S. Zhang, H. F. Song, M. Troyer, and A. A. Soluyanov. Wanniertools: An open-source software package for novel topological materials. *Computer Physics Communications*, 224:405–416, 2018.

[24] M. Gradhand, D. V. Fedorov, F. Pientka, P. Zahn, I. Mertig, and B. L. Györffy. First-principle calculations of the berry curvature of bloch states for charge and spin transport of electrons. *Journal of Physics: Condensed Matter*, 24(21):213202, 2012.

[25] G. Kresse and J. Hafner. Ab initio molecular dynamics for liquid metals. *Phys. Rev. B*, 47:558–561, Jan 1993.

[26] G. Kresse and J. Furthmüller. Efficient iterative schemes for ab initio total-energy calculations using a plane-wave basis set. *Phys. Rev. B*, 54:11169–11186, Oct 1996.

[27] E. Sanville, S. D. Kenny, R. Smith, and G. Henkelman. Improved grid-based algorithm for bader charge allocation. *Journal of Computational Chemistry*, 28(5):899–908, 2007.

[28] Y. F. Nie, P. D. C. King, C. H. Kim, M. Uchida, H. I. Wei, B. D. Faeth, J. P. Ruf, J. P. C. Ruff, L. Xie, X. Pan, C. J. Fennie, D. G. Schlom, and K. M. Shen. Interplay of spin-orbit interactions, dimensionality, and octahedral rotations in semimetallic $sriro_3$. *Phys. Rev. Lett.*, 114:016401, Jan 2015.

[29] Tiantian Zhang, Zhida Song, A. Alexandradinata, Hongming Weng, Chen Fang, Ling Lu, and Zhong Fang. Double-weyl phonons in transition-metal monosilicides. *Phys. Rev. Lett.*, 120:016401, Jan 2018.

[30] Barry Bradlyn, Jennifer Cano, Zhijun Wang, M. G. Vergniory, C. Felser, R. J. Cava, and B. Andrei Bernevig. Beyond dirac and weyl fermions: Unconventional quasiparticles in conventional crystals. *Science*, 353(6299):aaf5037, 2016.

[31] H. He, C. Qiu, X. Cai, et al. Observation of quadratic weyl points and double-helicoid arcs. *Nature Communications*, 11:1820, 2020.

[32] Yugui Yao, Leonard Kleinman, A. H. MacDonald, Jairo Sinova, T. Jungwirth, Dingsheng Wang, Enge Wang, and Qian Niu. First principles calculation of anomalous hall conductivity in ferromagnetic bcc fe. *Phys. Rev. Lett.*, 92:037204, Jan 2004.

5

Trend in Interfacial Charge Transfer, Emergent Electronic and Magnetic Structure and Topological Properties in the 3d, 5d Superlattices $LaBO_3/SrIrO_3$ (B = Mn, Fe, Co, Ni)*

5.1 Introduction and Motivation

The investigation of transition-metal oxides (TMOs), especially at the interface between 3d and 5d TMOs, has opened new avenues in understanding the interplay of electron-electron correlations and spin-orbit coupling (SOC). This interaction forms the basis of several emergent phenomena in condensed matter systems [1]. In particular, the combination of 3d TMOs, where strong electron correlations dominate, with 5d TMOs, which exhibit significant SOC, is a promising approach for discovering exotic properties. This study extends the detailed investigation of the $LaCoO_3$(LCO)/$SrIrO_3$(SIO) system presented in the previous chapter. It examines heterostructures consisting of $LaBO_3$ (B = Mn, Fe, Co, Ni) and $SrIrO_3$ (SIO), where the variation of the transition metal at the B-site offers novel pathways to modulate the complex interplay between electron correlation and spin-orbit coupling (SOC).

The spatial separation between 3d ions, characterized by pronounced electronic correlations, and 5d ions, which exhibit significant spin-orbit coupling (SOC), minimizes the

*This chapter is based on the article: **Samir Rom** and Tanusri Saha-Dasgupta, (Under Review).

complexities that often arise due to the interaction between correlation effects and SOC at the same site. Furthermore, as mentioned in Ref.[2], the stabilization of 5d ions in low-spin states with t_{2g} occupancy within the octahedral crystal field splitting *d* levels, coupled with robust oxygen covalency, prevents Jahn-Teller distortion, thus supporting the potential emergence of nontrivial topological phases. Investigations into such bi-component perovskite systems have been carried out both in the form of naturally occurring double perovskite compounds with the general formula $AA'BB'O_6$ or in the form of artificial superlattices, realized through the epitaxial deposition of a perovskite layer with the formula ABO_3 atop another layer characterized by the formula $A'B'O_3$.[3] The alternating deposition of chemically distinct ABO_3 perovskites not only combines the intrinsic properties of each perovskite layer but also creates mutual influence through a proximity effect, leading to emergent interfacial properties.

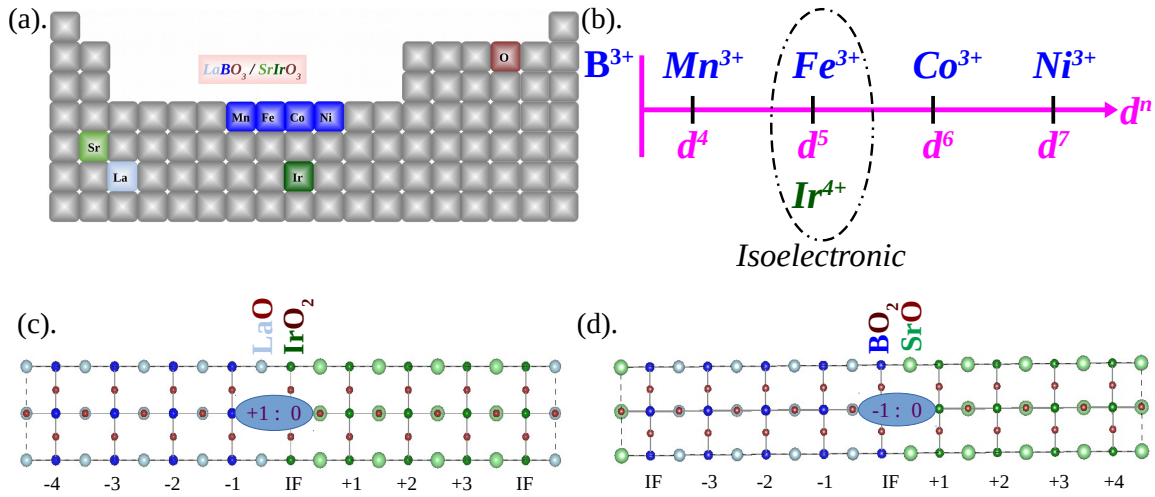

Figure 5.1: *(a) The chemical constituents of $ABO_3/A'B'O_3$ superlattices explored in this study with A and A′ chosen as lathanide series element, La and alkaline metal Sr, B chosen as 3d TM elements, Mn, Fe, Co, Ni and B′ chosen as 5d TM element, Ir. (b) The d occupancy of B^{3+} cation in LBO and $B'(Ir)^{4+}$ cation in SIO. (c) LBO/SIO superlattice with two symmetric n-type interfaces in the unit cell. (d) LBO/SIO superlattice with two symmetric p-type interfaces in the unit cell. The La, Sr, Ir, 3d TM and O atoms are shown as large-cyan, large-green, medium-dark green, medium-blue and small-brown balls, respectively.*

Recent investigations have focused extensively on the (001) heterostructure involving 3d transition metal oxides (TMO) and 5d TMO, specifically $SrIrO_3$ (SIO), which have unveiled novel phenomena at the interfaces [4–6]. Discussions around strontium iridate compounds predominantly center on the realization of the spin-orbital Mott insulating state within the J=1/2 states of Ir^{4+} in the layered perovskite Sr_2IrO_4.[7] In contrast, orthorhombic perovskite $SrIrO_3$ is characterized by semi-metallic, non-magnetic properties and the presence of protected Dirac line nodes.[8–11] Despite its non-magnetic nature, $SrIrO_3$ is predicted to be on the verge of magnetic instability.[12] Consequently, significant efforts

have been directed at stabilizing magnetic states in SIO either by exerting strain to achieve a tetragonal structure [13] or by engineering heterostructures that interface SIO with magnetically active perovskite layers such as manganites [4, 14–21], $LaCoO_3$, or ruthenates.[22] The synthesis of a heterostructure comprising SIO and $LaCoO_3$ (LCO) has revealed significant anomalous Hall effect (AHE) and anomalous magnetoresistance.[23] Theoretical investigation [24] have unraveled the underlying mechanisms of the observed AHE. Specifically, in the constructed superlattice geometry, there was a clear polar charge transfer to the LCO block, altering the nominal valence state of Co from 3+ towards 2+, which in turn stabilized the intermediate spin state of Co accompanied by robust ferromagnetic Co–Co coupling. This interaction subsequently stabilized the ferromagnetic (FM) state in the tetragonal-structured SIO within the superlattice geometry, driven by the FM influence of the LCO block. In particular, the band structure of SIO in this geometry was revealed to host non-trivial $C = 2$ double Weyl points.[24]

In this backdrop, it will be interesting to study the systematics in properties of superlattices of $LaBO_3$ (LBO) and $SrIrO_3$, where B cations are 3d TM ions (Mn, Fe, Co, and Ni), moving from left to right across the 3d TM row of the periodic table, as shown in Figure 5.1(a). While Fe^{3+} in $LaFeO_3$ (LFO) is isoelectronic to Ir^{4+} in $SrIrO_3$ (both having d^5 occupancy), Co^{3+} in LCO and Ni^{3+} in $LaNiO_3$ (LNO) have higher occupancy, and Mn^{3+} in $LaMnO_3$ (LMO) has lower occupancy compared to Ir^{4+} in SIO (cf. Figure 5.1(b)). Interestingly, all four LBO/SIO heterostructures have recently been synthesized using pulsed laser deposition (PLD) and characterized through magnetotransport measurements [15, 23, 25–27].

The bulk properties of LBO and SIO exhibit a variety of physical characteristics, which form the foundation for understanding their heterostructures. LBO compounds display diverse magnetic and electronic behaviors: LMO (d^4) and LFO (d^5) are antiferromagnetic insulators, LCO (d^6) shows spin-state transitions, and LNO (d^7) is a paramagnetic metal. Meanwhile, SIO, a 5d transition metal oxide, is a paramagnetic semimetal with strong spin-orbit coupling (SOC) and a d^5 configuration. These bulk properties are summarized in Table 5.1. In the heterostructures, where the in-plane lattice parameters are constrained to match $SrTiO_3$ (3.905 Å), the lattice mismatch leads to strain in the LBO and SIO layers. SIO experiences a 1.1% compression, while the LBO layers show varied strain: LMO is compressed by 1.3%, LFO by 0.69%, LCO is expanded by 1.5%, and LNO by 0.59%. These strain values are expected to significantly affect the electronic and magnetic properties at the interfaces.

It is important to note that the A/B cations in SIO adopt valence states of 2 + / 4 + with neutral $(SrO)^0$ and $(IrO_2)^0$, while the layers in LBO are charged, comprising $(LaO)^{+1}$ and $(BO_2)^{-1}$. This charge disparity leads to the formation of two distinct types of interfaces:

Compound	a (Å)	b (Å)	c (Å)	Crystal Symmetry	Magnetic State	Transition Temp.
SIO	3.959	3.945	3.940	Orthorhombic (Pnma)[28, 29]	Non-magnetic (Semi-metal)	–
LMO	3.915	4.064	3.846	Orthorhombic (Pnma)[30]	Antiferromagnetic (A-type, Mott-Hubbard Insulator)[31]	$T_N \sim 140$ K
LFO	3.929	3.935	3.927	Orthorhombic (Pbnm)[32]	Antiferromagnetic (G-type, Insulator)	$T_N \sim 740$ K
LCO	3.846	3.846	3.270	Rhombohedral ($R\bar{3}c$)[33]	Non-magnetic (Insulator)	$T_C \sim 150$ K
LNO	3.882	3.882	3.285	Rhombohedral ($R\bar{3}c$)[34]	Non-magnetic (Metal)	–

Table 5.1: *Structural and magnetic properties of the bulk phases of SIO, LMO, LFO, LCO, and LNO.*

n type (IrO_2 of the SIO facing LaO of LBO) and *p* type (BO_2 of LBO facing SrO of SIO) (cf. Figure 5.1(c) and Figure 5.1(d)). Since experimental setups often do not allow control or identification of *n*-type or *p*-type interface formation, we study both geometries to comprehensively analyze their electronic and magnetic structure.

Our investigation reveals a notable pattern in the interfacial charge transfer behavior when the transition from the Mn^{3+} cation to the Ni^{3+} cation at the B site in a heterostructure. The polarity of the interface (*n*-type or *p*-type) and the selection of the B cation govern whether the interfacial charge is transferred to the LBO block or the SIO block. This phenomenon either enhances or suppresses the magnetic moment of both the B site cation and the iridium (Ir) in the heterostructure setting, in comparison to their behavior in isolated components. Our calculations indicate significant ferromagnetic Ir-Ir magnetic exchanges in both *n*-type and *p*-type LCO/SIO and LNO/SIO, and in *p*-type LMO/SIO heterostructures, whereas it is significantly diminished in LFO/SIO. Consequently, we observe a substantial intrinsic anomalous Hall conductivity (AHC) in LCO/SIO, LNO/SIO, and LMO/SIO, while it is considerably reduced in LFO/SIO. These results can potentially explain recent experimental observations[27]. Our study underscores the pivotal influence of the interface polarity and the chemistry of the 3d transition metal oxide layer (TMO) in dictating the nature of charge transfer, thus modulating the complex topological properties in SIO.

5.2 Computational Details

In the superlattice geometry, we consider two symmetric *n*-type or *p*-type interfaces in the cell which result in nonstoichiometric supercells. In the case of *n*-type (*p*-type) superlattices there results in an additional IrO_2 (SrO) layer in SIO and an additional LaO (BO_2) layer in LBO. This gives rise to superlattices with the formula $(LBO)_{m.5}/(SIO)_{n.5}$. The (m,n) values are chosen to be 4 and 3 for *n*-type and 3 and 4 for *p*- type geometries. The larger superlattices with $m/n = 5, 6$ do not significantly change the result, as was found for LCO/SIO. [24]

To mimic the experimental setup where heterostructures are grown epitaxially on a $SrTiO_3$ (STO) substrate, the in-plane lattice constants in our simulations were fixed to

match the periodicity of STO. Specifically, the in-plane lattice parameters (a, b) were set to 3.905 $\AA \times \sqrt{2}$ to account for potential octahedral tilts. During structural optimization, the out-of-plane lattice parameter and the z-coordinates of the atomic positions were allowed to relax, accommodating strain perpendicular to the interface. This method enables structural changes such as octahedral tilts and tetragonal elongation or compression. As a similar procedure was detailed in chapter 4 for the LCO/SIO system, redundant figures are omitted here.

First-principles calculations were performed using DFT with a plane-wave basis set and PAW potentials, as implemented in VASP package [35, 36]. The Perdew-Burke-Ernzerhof (PBE) form of the generalized gradient approximation (GGA) was employed for the exchange-correlation functional. The valence states considered for each element were: O ($2s^2$, $2p^4$), Sr ($4s^2$, $4p^6$, $5s^2$), La ($5s^2$, $5p^6$, $5d^1$, $6s^2$), Mn ($3d^6$, $4s^1$), Fe ($3d^7$, $4s^1$), Co ($3d^8$, $4s^1$), Ni ($3d^9$, $4s^1$), and Ir ($5d^8$, $6s^1$). The ground-state properties were computed using a Monkhorst-Pack k-point grid of $7 \times 7 \times 1$ and a plane-wave energy cut-off of 600 eV. The atomic structures were optimized by minimizing the Hellmann-Feynman forces on each ion to less than 0.001 eV/Å, ensuring precise structural determination. These computational parameters were selected after thorough convergence tests to ensure their reliability for the studied systems.

To address the localized nature of the d-electrons in transition metal oxides, we employed the Hubbard U parameter and Hund's coupling J_H within a rotationally invariant formulation [37]. For Ir, the U and J_H values were set to 2 eV and 0.5 eV, respectively, based on existing literature [17, 38, 39]. For the 3d transition metals (Mn, Fe, Co, and Ni), U and J_H were fixed at 5 eV and 0.8 eV, respectively. While we used the same U and J_H values for all B elements in this study, we verified the robustness of our results by varying the U value within a range of $\pm$1–2 eV for each case. Since the J_H value is expected to show little variation across the 3d transition metal series, it was kept constant. It was observed that the qualitative trend remains unchanged, with only minor variations in the actual values. To ensure a straightforward comparison and avoid introducing additional complexity from varying U values, we decided to report all results using a fixed U value of 5 eV. This approach provides a consistent and simplified platform to understand the underlying trends in the system.

Given the significant role of spin-orbit coupling (SOC) at the iridium (Ir) sites, we performed self-consistent GGA+U+SOC calculations to account for its effects accurately. For the specific case of the LCO/SIO heterostructure, SOC effects on structural relaxation were also considered. However, the results showed only marginal differences when compared to those obtained without SOC-induced relaxation. Based on this observation, structural relaxations for all other cases were carried out using the GGA+U method alone, as the

inclusion of SOC during relaxation was considered unnecessary for these systems.

The topological properties of the band structure were studied using the WANNIER90 code[40]. In particular, the maximally localized wannier functions were derived with Sr-s, Ir-d and O-p as basis set and the Berry flux through a closed surface enclosing the node was calculated[41].

In the clean limit, the anomalous Hall conductivity (AHC) was calculated using the Kubo formalism [42], which accounts for the Berry curvature contribution. The Berry curvature for each band is determined as:

$$\Omega_n^z(k) = -2\mathrm{Im} \sum_{m \neq n} \frac{\langle n|\hat{v}_x|m\rangle \langle m|\hat{v}_y|n\rangle}{(\varepsilon_m - \varepsilon_n)^2} \tag{1}$$

where ε_m and $|m\rangle$ represent the energy eigenvalue and eigenvector of the Hamiltonian, while $\hat{v}_x$ and $\hat{v}_y$ denote the velocity operators along the x and y directions, respectively. The total AHC was then obtained by integrating the Berry curvature over the Brillouin zone, weighted by the Fermi-Dirac distribution function f_n, as follows:

$$\sigma_{xy} = -\frac{e^2}{\hbar} \sum_n \int_{\mathrm{BZ}} \frac{d^3k}{(2\pi)^3} \Omega_n^z(k) f_n \tag{2}$$

Here, f_n is the Fermi-Dirac distribution function, and the integral is performed over the entire Brillouin zone. This method effectively captures the intrinsic contribution to the AHC arising from the Berry curvature of the occupied electronic states.

5.3 Results

5.3.1 Charge Transfer in LBO/SIO Superlattices

In the well-documented instance of $LaAlO_3/SrTiO_3$ heterostructures,[43] a notable phenomenon occurs at the interface (IF) due to the polar discontinuity that arises when perovskite layers belonging to different charge families are brought into proximity. To prevent the divergence of the electrostatic potential, it is necessary to facilitate an interfacial polar charge transfer. The orientation and magnitude of this interfacial charge transfer are critical parameters that can significantly affect the overall characteristics and properties of the heterostructure.

In order to determine the direction of charge transfer, we first examine the scenario on the basis of calculated magnetic moments at the TM sites, which serve as good indicators of the nominal valences including the spin states. For this purpose, we consider different possibilities of charge and spin states, as a given charge state can appear in different spin

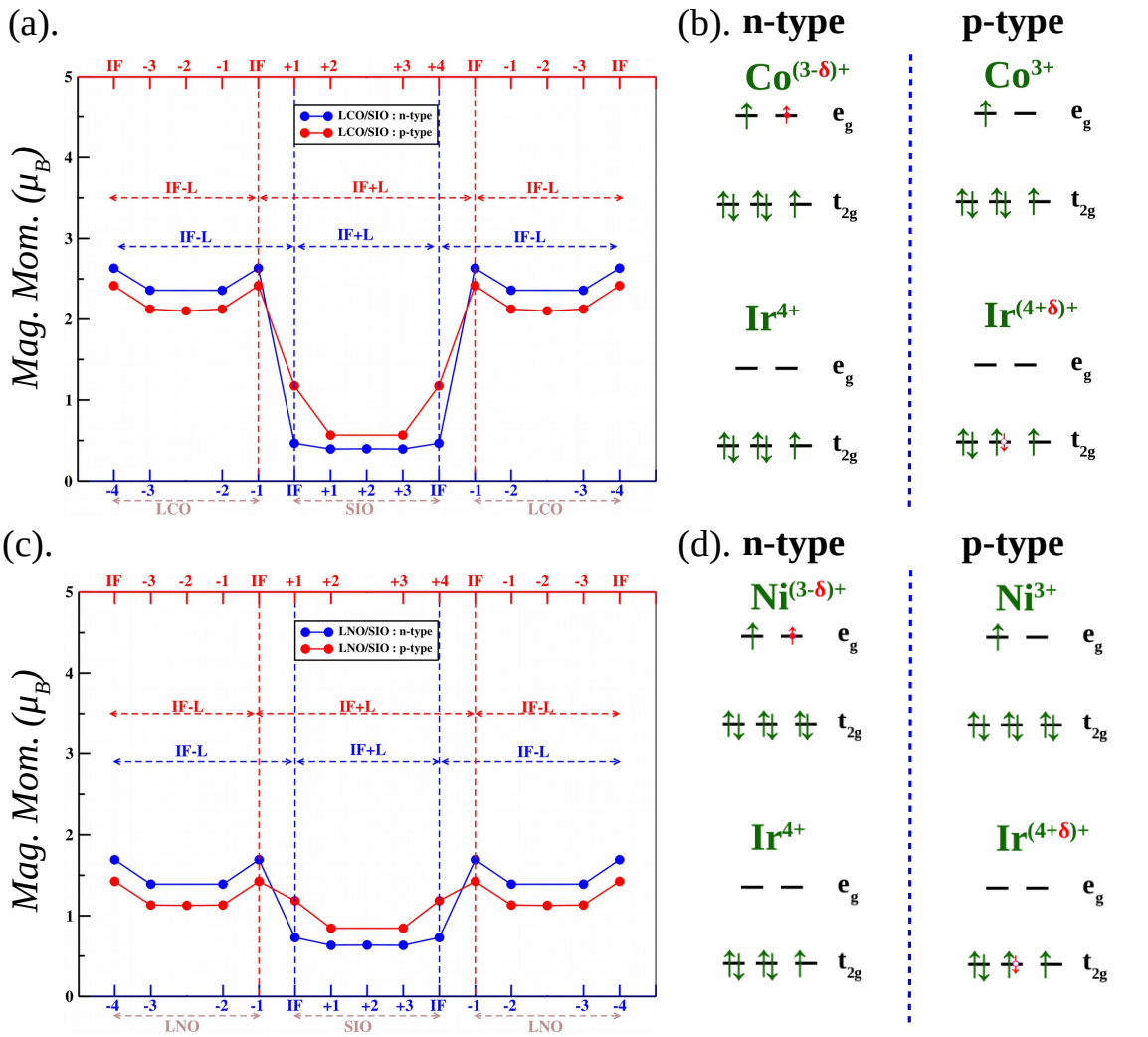

Figure 5.2: *(a) The calculated magnetic moment at Co and Ir sites at different CoO_2/IrO_2 layers of LCO/SIO superlattices with two symmetric n-type (blue symbols) and p-type (red symbols) IFs in the cell. The IF+L layers belong to the SIO block, while the IF-L layers belong to the LCO block. IF is formed in the IrO_2 (CoO_2) layer in the n-type (p-type) geometry. (b) The nominal occupancy of the octahedral crystal field split t_{2g} and e_g levels of Co and Ir in the n-type and p-type IFs after electronic reconstruction. Up and down electrons are shown as up and down arrows. The δ amount of occupancy of Co $d^{6+\delta}$ due to charge transfer in the n-type IF is shown with a red arrow and a closed symbol. The depletion of δ electrons in Ir $d^{5-\delta}$ due to charge transfer in p-type IF is shown with a red arrow and an open symbol. (c) same as (a), but shown for calculated magnetic moment at Ni and Ir sites at different NiO_2/IrO_2 layers of LNO/SIO superlattices. (d) same as (b), but shown for the d occupancy of Ni and Ir.*

states, high-spin, intermediate-spin or low-spin, thus influening the values of magnetic moments. Subsequently, we corroborate these conclusions through analysis of partial density of states.

Keeping this in mind, the magnetic moments at the B and Ir sites belonging to the BO_2 and IrO_2 layers in the LBO and SIO blocks, calculated by GGA+U, are presented in

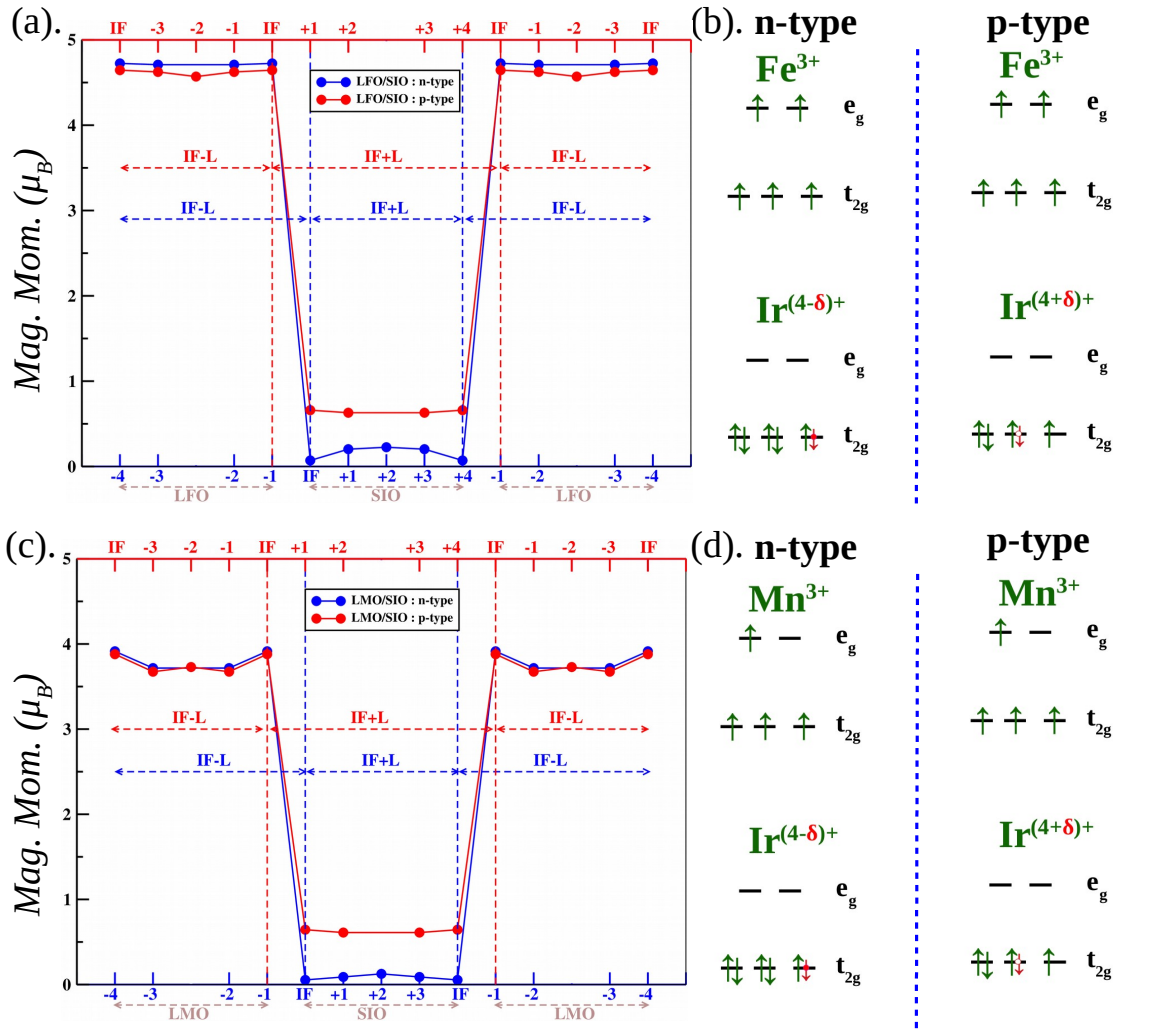

Figure 5.3: *(a) The calculated magnetic moment at Fe and Ir sites at different FeO_2/IrO_2 layers of LFO/SIO superlattices with two symmetric n-type (blue symbols) and p-type IFs in the unit cell. The color convention and illustration is same as in Fig. 5.2. (b) The nominal occupancy of Fe and Ir octahdedral crystal field split, t_{2g} and e_g states in the n-type and p-type IFs after electronic reconstruction. Conventions same as in Fig. 5.2. (c) same as (a), but shown for calculated magnetic moment at Mn and Ir sites at different MnO_2/IrO_2 layers of LMO/SIO superlattices. (d) same as (b), but shown for the d occupancy of Mn and Ir.*

Figure 5.2 and Figure 5.3 for the four systems studied. Note that because of the superlattices constructed with two symmetric IFs in the unit cell, the magnetic moments are symmetric with respect to the mid point of each block.

We first consider the Ir moment in SIO, which is common for all four superlattices. The photoemission study on $SrIrO_3$ thin films[8] show a band-width driven pronounced mixing between the J_{eff} = 1/2 and J_{eff} = 3/2 states, which causes breakdown of the J_{eff}=1/2, 3/2 picture in SIO. We thus first consider the spin only moment, and discuss the trend in magnetic moment based on the spin-only moment of Ir as given in GGA+U calculations.

Subsequently, the effect of spin-orbit is considered within GGA+U+SOC calculations. The inclusion of SOC is found to keep the discussed trend unaltered.

We note that in the bulk SIO, Ir is in low-spin (LS) 4+ (d^5) nominal valence, resulting in a spin moment of 1 μ_B in the fully polarized limit with six t_{2g} levels (including spin degeneracy) filled by five electrons. An increase in Ir valence to (4+δ)+ would cause an increase in fully polarized spin moment to (1+δ) μ_B, while a decrease in Ir valence to (4-δ)+ would cause a decrease in fully polarized spin moment to (1-δ) μ_B. Note, this description of considering the spin-only GGA+U calculated moments relies on the use of the (L,S) basis rather than the J basis. As $SrIrO_3$ exhibits significant mixing between $j_{\text{eff}} = 1/2$ and $j_{\text{eff}} = 3/2$ states,[8] the (L,S) basis provides a more suitable framework for understanding the electronic structure. Thus, the Ir moment is discussed within the (L,S) basis in this study, consistent with previous works on $SrIrO_3$.[11, 44]

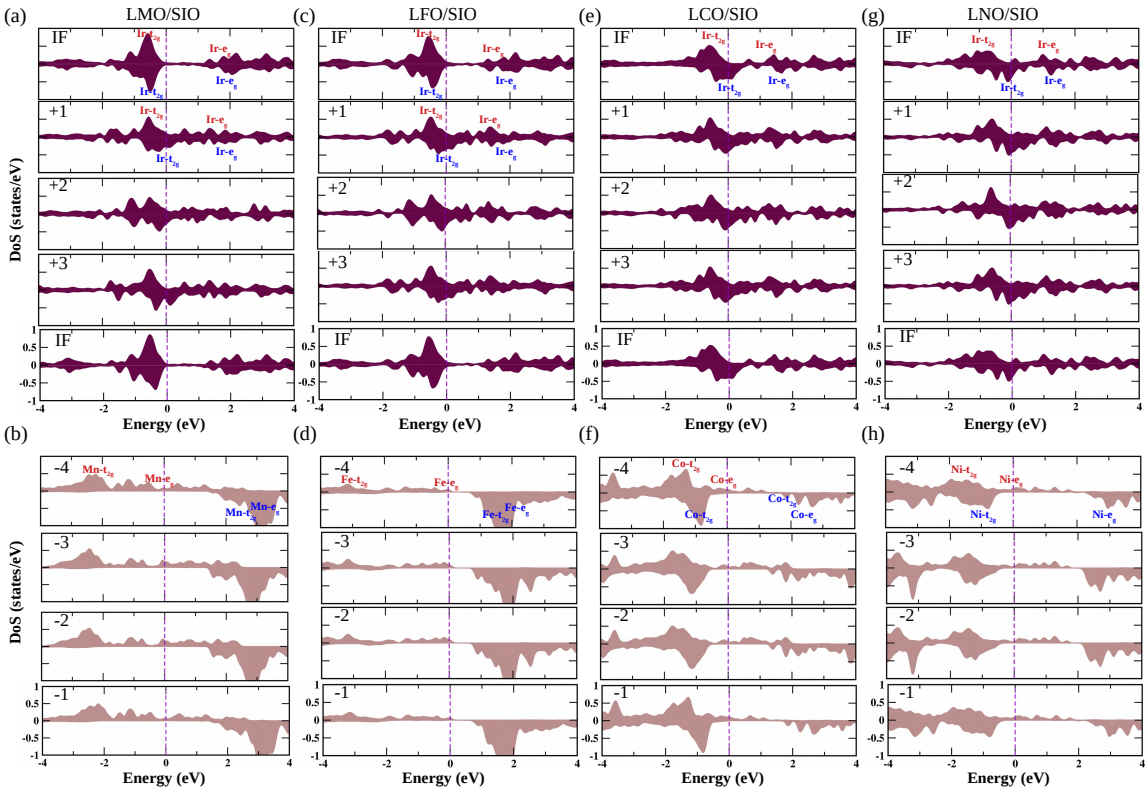

Figure 5.4: *The layer-decomposed density of states projected to Ir d (top) within SIO block and B d (bottom) states within the LBO block of LBO/SIO n-type heterostructures. The numbering of the layers is same as in Figure 5.2 and Figure 5.3. The zero of the energy is set at Fermi level. Marked are the octahedral crystal field split, t_{2g} and e_g states. Panels in (a)-(b), (c)-(d), (e)-(f), and (g)-(h) show the plots for B = Mn, Fe, Co, Ni, respectively.*

For LCO, Co^{3+} in its nominal valence of d^6, is expected to give rise to a fully polarized spin moment of 4 μ_B in its high-spin state (HS), 2 μ_B in its intermediate-spin (IS) state, and 0 μ_B in its LS state. The decrease in Co valence from 3+ to (3-δ)+ would cause an increase in the spin moment. The calculated spin magnetic moments of Co and Ir ions

at different layers of AO and BO_2 of the n-type and p-type LCO/SIO heterostructures are shown in Figure 5.2(a). In accordance with the published literature [24], for the interface of type n, the Ir moments in the SIO block show little variation among the layers with an average moment of $\sim 0.5\ \mu_B$. The moment at Co sites, on the other hand, shows a strong layer dependence with Co sites at IF having moment $\sim 2.5\ \mu_B$, suggesting stabilization of nominal $Co^{(3-\delta)+}$ valence in its IS state, with the value δ decreasing towards the middle of the LCO block. In contrast, for the p-type LCO/SIO heterostructure, the Ir moments in the SIO block show a strong layer dependence with the moment of Ir atoms close to the IF substantially enhanced to a value larger than 1 μ_B. Co moments, on the other hand, are reduced by about 0.2-0.3 μ_B. Thus for n-type heterostructure the nominal valence of Co decreases from 3+ to (3-δ)+, while for p-type interface the nominal valence of Ir increases from 4+ to (4+δ)+. The interfacial electron for n-type superlattice thus flows to the LCO block, while the interfacial hole for p-type superlattice flows to the SIO block. Figure 5.2(b) shows the suggested filling of octahedrally crystal field split Co and Ir e_g and t_{2g} states close to IF for the n-type and p-type interfaces. This scenario continues to be valid for LNO/SIO with Ni nominal valence decreasing from Ni^{3+} to $Ni^{(3-\delta)+}$ for n-type interface and nominal valence of Ir increasing from 4+ to (4+δ)+ for p-type interface (cf. Figure 5.2(c)). The corresponding filling of Ni and Ir states close to IF are shown in Figure 5.2(d).

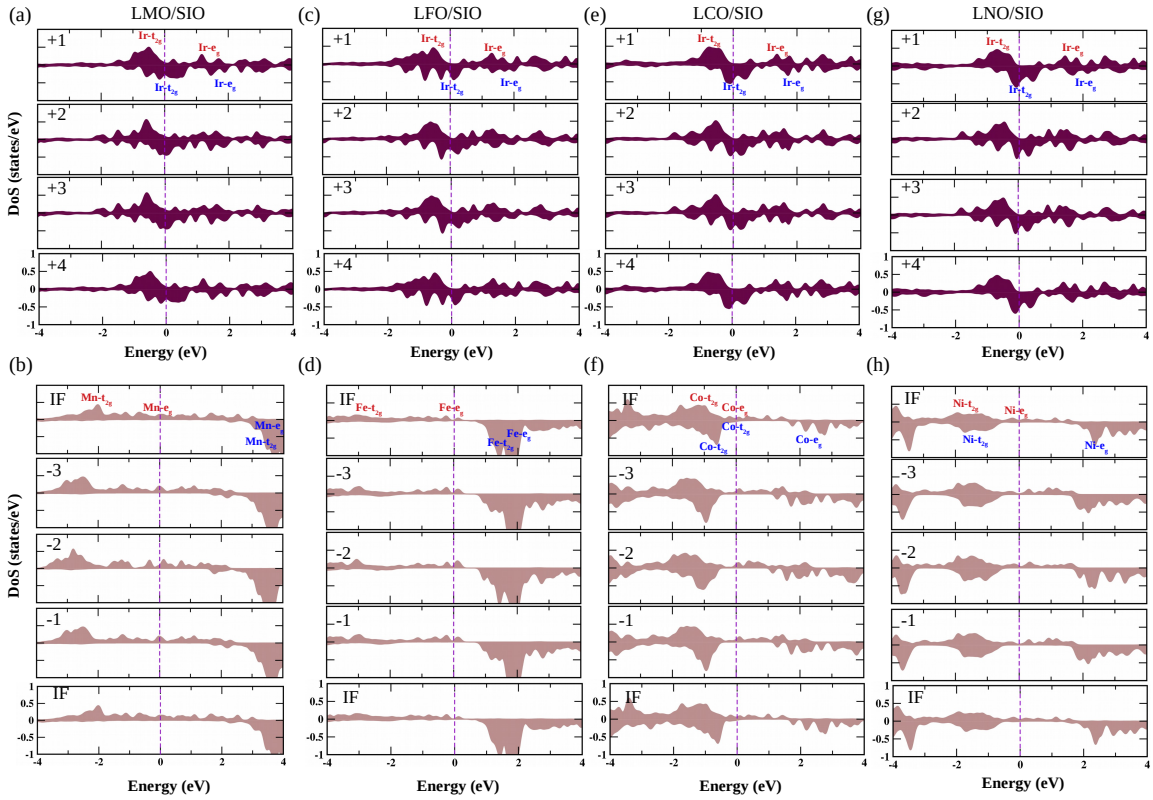

Figure 5.5: *Same as in Fig 5.4, but plotted for the LBO/SIO p-type superlattices.*

The situation for LFO/SIO is found to be remarkably different. The magnetic moments

at the Fe sites show negligibly small variation among the different FeO_2 layers in the LFO block, (cf Figure 5.3(a)) with a moment of 4.6-4.7 μ_B following the nominal d^5 valence of Fe^{3+}. On the contrary, significant variations of Ir moments are observed in the SIO block. In particular for *n*-type IF, the Ir site has a nearly vanishing moment, suggestive of close to Ir^{3+} valence with nearly filled Ir t_{2g} levels, as shown in Figure 5.3(b). On the contrary, a large increase of magnetic moment at Ir sites is witnessed for *p*-type interface, significantly larger than the moment of 0.5 μ_B observed for LS Ir^{4+}. This suggests that interfacial electron for *n*-type IF as well as interfacial hole for *p*-type IF flows towards the SIO block. A more or less similar situation is found for LMO/SIO, as demonstrated in Figure 5.3(c) and Figure 5.3(d).

To study the influence of spin-orbit coupling, we further repeated calculations within GGA+U+SOC. The 3d TM sites, Ni, Co, Fe and Mn at B sites show tiny orbital moment, while the orbital moment at the Ir site is found to be appreciable, ranging from 0.1 to 0.2 μ_B. The general trend, as discussed above, however, remains preserved, with charge transfer behavior similar for LNO/SIO and LCO/SIO superlattices, which are distinct from LFO/SIO and LMO/SIO superlattices.

The magnetocrystalline anisotropy (MAE) calculations were performed using non-collinear spin configurations with spin-orbit coupling (SOC) by evaluating the energy difference between out-of-plane (001) and in-plane (110) spin orientations. Positive $MAE = E_{001} - E_{110}$ indicates a preference for in-plane spin alignment, while negative values suggest out-of-plane alignment. For *n*-type heterostructures, such as LCO/SIO and LNO/SIO, the results reveal a strong preference for in-plane spin orientation, with energy gains ranging from moderate to high ($\sim$ 4–10 meV/Ir). On the other hand, *p*-type LCO/SIO and LNO/SIO exhibit a modest preference for out-of-plane spin alignment, with energy gains around $\sim$ 2 meV/Ir. Both *n*-type and *p*-type heterostructures of LFO/SIO and LMO/SIO show a preference for out-of-plane alignment, with energy gains varying from weak ($\sim$ 0.2 meV/Ir) to strong ($\sim$ 4.5 meV/Ir). These anisotropic spin alignments result from the interplay between SOC and structural distortions, such as octahedral tilts and rotations, which strongly influence the magnitude and direction of MAE. Our computed MAE provide predictions to be validated by experiments.

While the above analysis provides indication of charge transfer direction, and nominal valences of B and Ir, magnetic moment is related to charge in a correlated fashion, carrying information of both charge state and spin state. In following, we thus validate our findings based on magnetic moments with that obtained from analysis of partial density of states.

Figure 5.4 shows the layer resolved GGA+U partial density of states (pDOS), projected to Ir *d* in SIO block (top panels) and B *d* in LBO block (bottom panels) for LBO/SIO *n*-type superlattices. In agreement with the conclusions drawn from magnetic moments,

the Ir pDOS for LMO/SIO and LFO/SIO appear distinctly different from that of LCO/SIO and LNO/SIO. In particular, the Ir pDOS at IF is nearly nonmagnetic and insulating for LMO/SIO and LFO/SIO, as opposed to LCO/SIO and LNO/SIO for which they are strongly spin-split and metallic. The B site pDOS in the LBO block for all the systems, except LFO/SIO, on the other hand, exhibit a half-metallic behavior with B-e_g states crossing the Fermi level in the majority spin channel and no state at Fermi level in the minority spin channel. In the case of LFO/SIO due to the nominal d^5 occupancy of Fe at almost all the layers, a nearly insulating solution is obtained. Thus our calculations predict an unusual insulating IF to be created at the *n*-type junction between LFO and SIO.

Figure 5.5 shows similar plots as in Figure 5.4 but shown for *p*-type superlattices. Focusing on the Ir *d* projected states we find that distinctive features between LMO/SIO, LFO/SIO and LCO/SIO, LNO/SIO, observed in the case of *n*-type interfaces do not show up for *p*-type, supporting the similar nature of charge transfer in all four *p*-type superlattices. The B site pDOS in the LBO block for the LMO/SIO, LCO/SIO, and LNO/SIO systems remains half-metallic. The slight decrease in the magnetic moment of Fe in *p*-type superlattice compared to *n*-type makes the LFO block semi-metallic.

To estimate the charge transfer at the interfaces of LBO/SIO heterostructures from density of states, we integrated the pDOS projected to B *d* and Ir *d* up to the Fermi level at IF layer of the heterostructure as well as for the bulk systems. The bulk geometries of LBO as well as SIO were considered in tetragonal structures, with lattice parameters same as that in LBO and SIO block of the heterostructures. The difference of the integrated pDOS in heterostructure and bulk systems provide the information of charge transfer (ΔQ) due to electronic reconstruction that happens upon formation of heterostructure. The charge transfer for the B-site (ΔQ_B) and Ir (ΔQ_{Ir}) for n-type and p-type interfaces are presented in Table 5.2. Positive values of charge transfer indicate electron gain, while negative values represent electron loss. The results further confirm the conclusions drawn from magnetic moments.

Finally, we note while the direction of interfacial charge transfer is found to be the same for all four *p*-type superlattices, the strength of the charge transfer is found to be different for different superlattices, as inferred from Ir magnetic moments as well as from pDOS analysis. It is maximum for LNO, followed by LCO and significantly smaller for LFO and LMO. This may be rationalized by the fact that there exists finite covalency between 3d TM B cation and 5d TM Ir, both of direct and indirect nature via the corner shared oxygen of BO_6 and IrO_6 octahedra. The magnitude of this covalency influences the strength of charge transfer. In this context, it is to be noted that by symmetry the LS Ir t_{2g} states hybridize with t_{2g} states of B. In the case of LNO, the t_{2g} manifold of B ion being filled, the influence of covalency is minimal, thus making the strength of charge transfer maximum.

Interface Type	B-Site Element	ΔQ_B (e)	ΔQ_{Ir} (e)	Net Direction
n-type	Mn	-0.08	+0.13	B $\rightarrow$ Ir
n-type	Fe	-0.04	+0.17	B $\rightarrow$ Ir
n-type	Co	+0.95	-0.06	Ir $\rightarrow$ B
n-type	Ni	+0.26	-0.04	Ir $\rightarrow$ B
p-type	Mn	+0.04	-0.09	Ir $\rightarrow$ B
p-type	Fe	$\sim$ 0.0	-0.09	Ir $\rightarrow$ B
p-type	Co	+0.60	-0.13	Ir $\rightarrow$ B
p-type	Ni	+0.15	-0.10	Ir $\rightarrow$ B

Table 5.2: *Charge transfer (ΔQ) for B-site (ΔQ_B) and Ir (ΔQ_{Ir}) in LBO/SIO heterostructures (B = Mn, Fe, Co, Ni) with n-type and p-type interfaces. Positive values indicate electron gain, while negative values indicate electron loss.*

LCO, and LFO, LMO, on the other hand, host one half-filled t_{2g} and three half-filled t_{2g}, making the covalency effect intermediate and large for LCO/SIO and LMO/SIO, LFO/SIO, respectively, providing a tentative explanation to the trend in the strength of charge transfer.

5.3.2 Magnetic Interactions

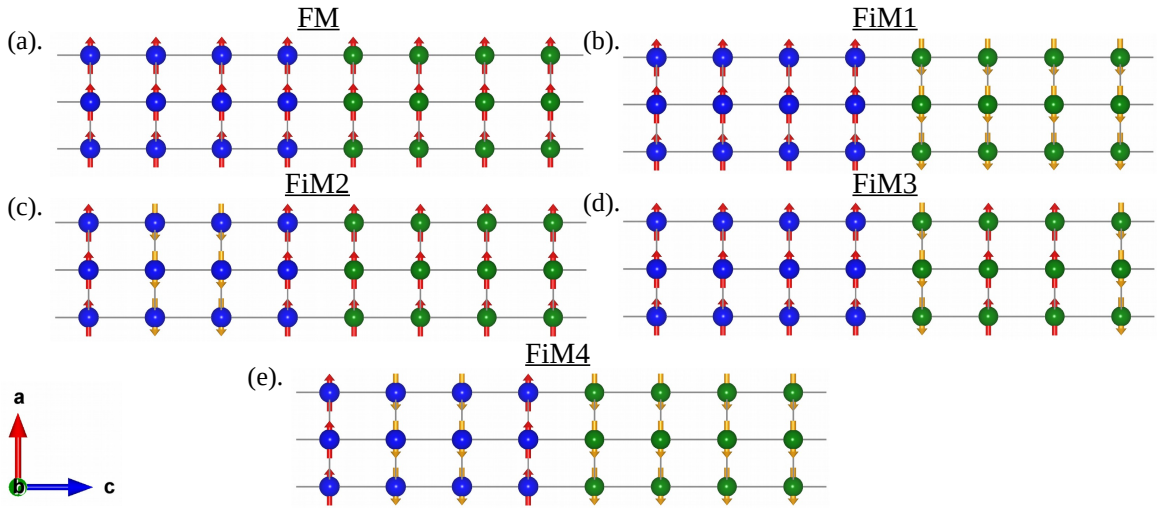

Figure 5.6: *Schematic representation of five spin configurations used in GGA+U total energy calculations. (a) Ferromagnetic (FM) state with parallel alignment of spins at B (blue) and Ir (green) sites. (b)–(e) Different antiparallel alignments (FiM1, FiM2, FiM3, FiM4) B and Ir spins in LBO/SIO. The up and down spins are marked with red and orange arrows, respectively.*

To find the ground state magnetic configuration, GGA+U total energy calculations of five different possible arrangements of B and Ir spins were carried out. In addition to FM configuration with parallel alignment of B and Ir spins, different possible antiparallel alignment of B spins in LBO block and Ir spins in SIO block, FiM1, FiM2, FiM3, FiM4 were considered. See Figure 6.6 for the considered spin arrangements. We also considered

G-type antiferromagnetic configurations for the LBO and SIO block. However, most of the calculations faced convergence issues, with the exception of LFO/SIO. For LFO/SIO, the LFO block is found to stabilize in G-AFM while maintaining a FM alignment of Ir spins in the SIO block. Thus when calculating the magnetic coupling strengths between atoms, these configurations were not considered. Mapping the differences of the total energies to the spin Hamiltonian H_{spin} = -J_{ij} S_i.S_j , where S_i and S_j are the two spins at sites i and j, and J_{ij} is the exchange constant, the B-B, Ir-Ir and B-Ir exchange couplings were extracted. Due to the nearly non-magnetic nature of Ir ions in n-type LMO/SIO and LFO/SIO, the corresponding exchanges were not considered as magnetic nature of SIO is of interest for the present study. The results are presented in Table 5.3. The Ir-Ir magnetic coupling is found to be FM with appreciable value for n-type as well as p-type LNO/SIO and also for p-type LMO/SIO. In all these cases, the B-B exchange in the LBO block is found to be strongly FM, which induces ferromagnetism through an FM B-Ir exchange. In the case of LFO, on the other hand, the Fe spins in LFO with half-filled d -shell in nominal d^5 occupancy stabilize in G-type AFM configuration, with strong AFM Fe-Fe coupling. This makes the FM Ir-Ir exchange at the SIO block extremely weak, making its manifestation in AHC also weak.

n-LCO/SIO	
J_1 (Co-Co)	-8.8
J_2 (Ir-Ir)	-0.6
J_3 (Co-Ir)	-1.6

n-LNO/SIO	
J_1 (Ni-Ni)	-5.18
J_2 (Ir-Ir)	-0.44
J_3 (Ni-Ir)	-3.11

p-LMO/SIO	
J_1 (Mn-Mn)	-2.94
J_2 (Ir-Ir)	-0.3
J_3 (Mn-Ir)	-2.71

p-LFO/SIO	
J_1 (Fe-Fe)	3.37
J_2 (Ir-Ir)	-0.05
J_3 (Fe-Ir)	-0.16

p-LCO/SIO	
J_1 (Co-Co)	-12.0
J_2 (Ir-Ir)	-0.31
J_3 (Co-Ir)	-1.85

p-LNO/SIO	
J_1 (Ni-Ni)	-1.14
J_2 (Ir-Ir)	-0.21
J_3 (Ni-Ir)	-1.78

Table 5.3: *B-B (J_1), Ir-Ir (J_2) and B-Ir (J_3) magnetic exchanges in meV for LBO/SIO superlattices. Negative values indicate ferromagnetic coupling, while positive values indicate antiferromagnetic coupling.*

5.3.3 Topological Properties of SIO

The topological properties of the SIO in contact with LCO in n-type superlattice geometry were theoretically explored [24] following the experimental observation of large AHE in LCO/SIO. [23] The contact with LCO in the heterostructure geometry, affects the SIO in two ways, a) induces ferromagnetism through the interaction with FM LCO block, and b) makes the crystal structure of SIO pseudo-tetragonal in contrast to the monoclinic structure of bulk SIO, as the heterostructures are grown on cubic $SrTiO_3$ substrates. Accordingly,

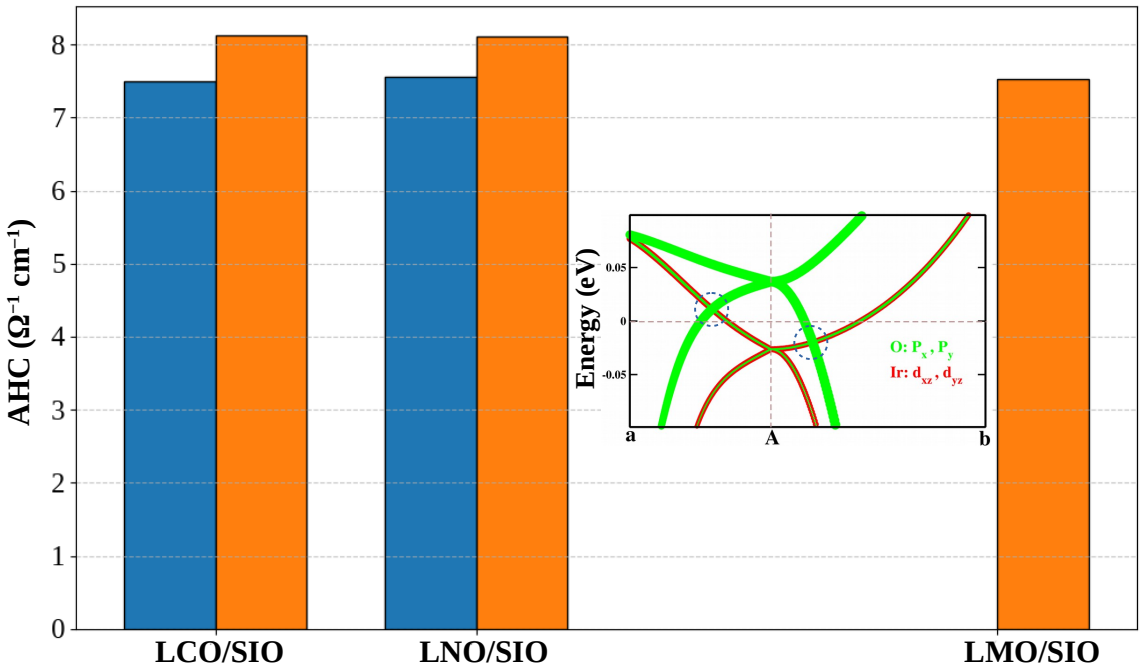

Figure 5.7: *Calculated anomalous Hall conductivity in LCO/SIO, LNO/SIO and LMO/SIO superlattices. The values for n-type and p-type are shown in blue and orange, respectively. For LMO/SIO, only p-type superlattice is considered, as for n-type the SIO block becomes essentially non-magnetic. The results are LFO/SIO are also not considered due to non-magnetic nature of SIO in n-type case, and heavily suppressed ferromagnetism in p-type case. Inset shows the representative band structure of n-type LCO/SIO projected onto the Ir d_{xz}/d_{yz} (red) and the O p_x/p_y (green) characters along the path a = (π/a, π/a, $0.126\pi/c$) - A = (π/a, π/a, π/c) - b = ($0.224\pi/a$, $0.224\pi/a$, π/c), revealing two linear band crossings (shown in dashed circles) near the high-symmetry A point.*

the GGA+U+SOC band structure of FM, tetragonal-structured SIO was studied. The band structure, as given in the inset of Figure 5.7, shows two pairs of symmetry-allowed Dirac crossings close to the high-symmetry A = (π/a, π/a, π/c) and A$'$ = (π/a, -π/a, π/c) points, (only the ones around A point are shown in the inset figure) originating from the two-fold degenerate Ir d_{xz}/d_{yz} orbitals in the tetragonal crystal structure, and the degenerate O p_x/p_y orbitals. These crossings are found to be nontrivial with a topological charge of $C = \pm 2$.[24] These non-trivial features give rise to large values of Berry curvatures with positive and negative signs corresponding to two different chirality of the two topological charges. The calculations of the tetragonal band structure of FM SIO, in contact with LCO (in *p*-type geometry), LNO (in *n*-type and *p*-type geometry), LMO (in *p*-type geometry) show that symmetry-allowed Dirac crossings close to high-symmetry A and A$'$ remain preserved. However, the energy position of crossings varies. Though the in-plane ($a = b$) lattice constant of the superlattices is kept fixed to the lattice constant of cubic STO, the *c*-axis is free to relax. Due to different out-of-plane relaxation in different superlattices, the tetragonality of the SIO block varies among different superlattices. The compressed

tetragonality is observed for n-type LCO/SIO, LNO/SIO and p-type LMO/SIO with c/a = 0.97, 0.99 and 0.93, respectively. On the contrary, elongated tetragonality is observed for p-type LCO/SIO, and p-type LNO/SIO with c/a = 1.55 and 1.56, respectively. This in turn makes the Dirac crossings move a bit closer or away from the Fermi level, influencing the marginally Berry curvature contribution to AHC at the Fermi level. The calculated values of AHC, as shown in Figure 5.7, are found to be around 7-8 Ω^{-1} cm^{-1}, in fair agreement with experimentally observed range of 3-11 Ω^{-1} cm^{-1}. The weakening of ferromagnetism in SIO block in LFO/SIO, as brought out in our study, is supported by experimental observation[27] of strong suppression of AHC to 0.2 Ω^{-1} cm^{-1} for LFO/SIO.

5.4 Summary and Discussion

Motivated by the experimental synthesis of 3d-5d superlattices, LBO/SIO with B = Mn, Fe, Co, Ni, [27] we theoretically study these systems. The choice of B site cations offers a nice platform to study the systematic trend in moving from left to right of the 3d TM row of the periodic table. Due to experimental uncertainty on the interface type, both n-type and p-type superlattices are studied. Our study highlights the polarity of the interface as well as the chemistry of the B site play a significant role in influencing the interface properties. While all four superlattices behave identically in terms of the direction of the interfacial charge transfer for p-type interfaces, the differences show up for n-type interfaces. For n-type superlattices, the interfacial charge gets transferred to the LBO block for B = Ni and Co, having d occupancy larger than that of Ir^{4+} in SIO, while the direction of charge transfer is found to be opposite for B = Fe and Mn, having d occupancy equal or smaller than that of Ir^{4+} in SIO. Thus the direction of charge transfer is dictated by the polarity of IF as well as the chemistry of B cation. This makes the tetragonal SIO block strongly FM for both n-type and p-type LCO/SIO, LNO/SIO and p-type LMO/SIO, weakly FM for p-type LFO/SIO, and nearly non-magnetic for n-type LMO/SIO, LFO/SIO, setting a trend in the magnetism of SIO block of LBO/SIO superlattices. Remarkably, we predict an insulating IF to be formed at n-type IF of LFO and SIO, driven by the charge transfer effect. Our study further reveals magnetic SIO in the LBO/SIO superlattice exhibits $C = \pm 2$ double Weyl crossings driving the intrinsic AHC of 7-8 Ω^{-1} cm^{-1} for n-type and p-type LCO/SIO, LNO/SIO and p-type LMO/SIO. The weakening of FM Ir-Ir interaction in LFO/SIO should suppress the intrinsic AHC. Thus we predict LCO/SIO and LNO/SIO to be the most suited candidates for exhibiting intrinsic AHC, having both n-type and p-type interfaces contributing, LMO/SIO to be moderately suited which may or may not exhibit intrinsic AHC depending on the choice of interface type. LFO/SIO is least suited which may exhibit none or weak intrinsic AHC. It is however to be noted that our calculation

relies only on the intrinsic AHC originating from Berry phase-driven physics, and does not consider the extrinsic origins like skew scattering and side jumps.[45]

Our findings will help in understanding some of the recently measured experimental data[27] and guidance to future experiments.

Bibliography

[1] Dmytro Pesin and Leon Balents. Mott physics and band topology in materials with strong spin–orbit interaction. *Nature Physics*, 6(5):376–381, 2010.

[2] Santu Baidya, Umesh V. Waghmare, Arun Paramekanti, and Tanusri Saha-Dasgupta. High-temperature large-gap quantum anomalous hall insulating state in ultrathin double perovskite films. *Phys. Rev. B*, 94:155405, Oct 2016.

[3] T Saha-Dasgupta. Ferroic properties in bi-component perovskites: artificial superlattices and naturally forming compounds. *Journal of Physics: Condensed Matter*, 26(19):193201, apr 2014.

[4] John Nichols, Xiang Gao, Shinbuhm Lee, Tricia L. Meyer, John W. Freeland, Valeria Lauter, Di Yi, Jian Liu, Daniel Haskel, Jonathan R. Petrie, Er-Jia Guo, Andreas Herklotz, Dongkyu Lee, Thomas Z. Ward, Gyula Eres, Michael R. Fitzsimmons, and Ho Nyung Lee. Emerging magnetism and anomalous hall effect in iridate–manganite heterostructures. *Nature Communications*, 7(1):12721, 2016.

[5] J. Matsuno, K. Ihara, S. Yamamura, H. Wadati, K. Ishii, V. V. Shankar, Hae-Young Kee, and H. Takagi. Engineering a spin-orbital magnetic insulator by tailoring superlattices. *Phys. Rev. Lett.*, 114:247209, Jun 2015.

[6] Wei Fan and Seiji Yunoki. Electronic and magnetic structure under lattice distortion in sriro3/srtio3 superlattice: A first-principles study. *Journal of Physics: Conference Series*, 592(1):012139, mar 2015.

[7] B. J. Kim, Hosub Jin, S. J. Moon, J.-Y. Kim, B.-G. Park, C. S. Leem, Jaejun Yu, T. W. Noh, C. Kim, S.-J. Oh, J.-H. Park, V. Durairaj, G. Cao, and E. Rotenberg. Novel $J_{\text{eff}} = 1/2$ mott state induced by relativistic spin-orbit coupling in sr_2iro_4. *Phys. Rev. Lett.*, 101:076402, Aug 2008.

[8] Z. T. Liu, M. Y. Li, Q. F. Li, J. S. Liu, W. Li, H. F. Yang, Q. Yao, C. C. Fan, X. G. Wan, Z. Wang, and D. W. Shen. Direct observation of the dirac nodes lifting in semimetallic perovskite sriro3 thin films. *Scientific Reports*, 6:30309, 2016.

[9] X. Zhang, H. Zhang, J. Wang, C. Felser, and S. C. Zhang. Actinide topological insulator materials with strong interaction. *Science*, 335(6075):1464–1466, Mar 2012.

[10] M. Ahsan Zeb and Hae-Young Kee. Interplay between spin-orbit coupling and hubbard interaction in $sriro_3$ and related *Pbnm* perovskite oxides. *Phys. Rev. B*, 86:085149, Aug 2012.

[11] Y. F. Nie, P. D. C. King, C. H. Kim, M. Uchida, H. I. Wei, B. D. Faeth, J. P. Ruf, J. P. C. Ruff, L. Xie, X. Pan, C. J. Fennie, D. G. Schlom, and K. M. Shen. Interplay of spin-orbit interactions, dimensionality, and octahedral rotations in semimetallic $sriro_3$. *Phys. Rev. Lett.*, 114:016401, Jan 2015.

[12] Jean-Michel Carter, V. Vijay Shankar, M. Ahsan Zeb, and Hae-Young Kee. Semimetal and topological insulator in perovskite iridates. *Phys. Rev. B*, 85:115105, Mar 2012.

[13] Haozhe Wang, Alberto de la Torre, Joseph T. Race, Qiaochu Wang, Jacob P. C. Ruff, Patrick M. Woodward, Kemp W. Plumb, David Walker, and Weiwei Xie. Pseudosymmetry in tetragonal perovskite sriro3 synthesized under high pressure. *ACS Applied Electronic Materials*, August 2024.

[14] Di Yi, Jian Liu, Shang-Lin Hsu, Lipeng Zhang, Yongseong Choi, Jong-Woo Kim, Zuhuang Chen, James D. Clarkson, Claudy R. Serrao, Elke Arenholz, Philip J. Ryan, Haixuan Xu, Robert J. Birgeneau, and Ramamoorthy Ramesh. Atomic-scale control of magnetic anisotropy via novel spin–orbit coupling effect in $la_{2/3}sr_{1/3}mno_3/sriro_3$ superlattices. *Proceedings of the National Academy of Sciences*, 113(23):6397–6402, 2016.

[15] Elizabeth Skoropata, John Nichols, Jong Mok Ok, Rajesh V. Chopdekar, Eun Sang Choi, Aniruddha Rastogi, Changhee Sohn, Xiang Gao, Suk Hyun Yoon, Thomas Farmer, Ryan D. Desautels, Yongseong Choi, Daniel Haskel, John W. Freeland, Satoshi Okamoto, Matthew Brahlek, and Ho Nyung Lee. Interfacial tuning of chiral magnetic interactions for large topological hall effects in $lamno_3/sriro_3$ heterostructures. *Science Advances*, 6(27):eaaz3902, 2020.

[16] Yujun Zhang, Yong Zheng Luo, Liang Wu, Motohiro Suzuki, Qinghua Zhang, Yasuyuki Hirata, Kohei Yamagami, Kou Takubo, Keisuke Ikeda, Kohei Yamamoto, Akira Yasui, Naomi Kawamura, Chun Lin, Keisuke Koshiishi, Xin Liu, Jinxing Zhang, Yasushi Hotta, X. Renshaw Wang, Atsushi Fujimori, Yuanhua Lin, Cewen Nan, Lei Shen, and Hiroki Wadati. Interfacial-hybridization-modified ir ferromagnetism and electronic structure in $lamno_3/sriro_3$ superlattices. *Phys. Rev. Res.*, 2:033496, Sep 2020.

[17] Sayantika Bhowal and S. Satpathy. Electronic structure and anomalous hall effect in the ferromagnetic $3d-5d$ superlattice $srmno_3/sriro_3$. *Phys. Rev. B*, 99:245145, Jun 2019.

[18] Di Yi, Charles L. Flint, Purnima P. Balakrishnan, Krishnamurthy Mahalingam, Brittany Urwin, Arturas Vailionis, Alpha T. N'Diaye, Padraic Shafer, Elke Arenholz,

Yongseong Choi, Kevin H. Stone, Jiun-Haw Chu, Brandon M. Howe, Jian Liu, Ian R. Fisher, and Yuri Suzuki. Tuning perpendicular magnetic anisotropy by oxygen octahedral rotations in $(\mathrm{la}_{1-x}\mathrm{sr}_x\mathrm{mno}_3)/(\mathrm{sriro}_3)$ superlattices. *Phys. Rev. Lett.*, 119:077201, Aug 2017.

[19] T. S. Suraj, Ganesh Ji Omar, Hariom Jani, M. M. Juvaid, Sonu Hooda, Anindita Chaudhuri, Andrivo Rusydi, K. Sethupathi, Thirumalai Venkatesan, Ariando Ariando, and M. S. Ramachandra Rao. Tunable and enhanced rashba spin-orbit coupling in iridate-manganite heterostructures. *Phys. Rev. B*, 102:125145, Sep 2020.

[20] G. A. Ovsyannikov, T. A. Shaikhulov, K. L. Stankevich, Yu. Khaydukov, and N. V. Andreev. Magnetism at an iridate/manganite interface: Influence of strong spin-orbit interaction. *Phys. Rev. B*, 102:144401, Oct 2020.

[21] Myoung-Woo Yoo, J. Tornos, A. Sander, Ling-Fang Lin, Narayan Mohanta, A. Peralta, D. Sanchez-Manzano, F. Gallego, D. Haskel, J. W. Freeland, D. J. Keavney, Y. Choi, J. Strempfer, X. Wang, M. Cabero, Hari Babu Vasili, Manuel Valvidares, G. Sanchez-Santolino, J. M. Gonzalez-Calbet, A. Rivera, C. Leon, S. Rosenkranz, M. Bibes, A. Barthelemy, A. Anane, Elbio Dagotto, S. Okamoto, S. G. E. te Velthuis, J. Santamaria, and Javier E. Villegas. Large intrinsic anomalous hall effect in sriro_3 induced by magnetic proximity effect. *Nature Communications*, 12(1):3283, 2021.

[22] J. Matsuno, N. Ogawa, K. Yasuda, F. Kagawa, W. Koshibae, N. Nagaosa, Y. Tokura, and M. Kawasaki. Interface-driven topological hall effect in srruo_3-sriro_3 bilayer. *Sci Adv*, 2(7):e1600304, 2016.

[23] Arun Kumar Jaiswal, Di Wang, Vanessa Wollersen, Rudolf Schneider, Matthieu Le Tacon, and Dirk Fuchs. Direct observation of strong anomalous hall effect and proximity-induced ferromagnetic state in sriro3. *Advanced Materials*, 34(14):2109163, 2022.

[24] Samir Rom, Santu Baidya, Subhro Bhattacharjee, and Tanusri Saha-Dasgupta. Magnetism and unconventional topology in LaCoO3/SrIrO3 heterostructure. *Applied Physics Letters*, 122(2):021602, 01 2023.

[25] A. K. Jaiswal, R. Schneider, M. Le Tacon, and D. Fuchs. Magnetotransport of SrIrO3-based heterostructures. *AIP Advances*, 12(3):035120, 03 2022.

[26] X. Liu, M. Kotiuga, H. S. Kim, A. T. N'Diaye, Y. Choi, Q. Zhang, Y. Cao, M. Kareev, F. Wen, B. Pal, J. W. Freeland, L. Gu, D. Haskel, P. Shafer, E. Arenholz, K. Haule, D. Vanderbilt, K. M. Rabe, and J. Chakhalian. Interfacial charge-transfer mott state

in iridate-nickelate superlattices. *Proceedings of the National Academy of Sciences of the United States of America*, 116(40):19863–19868, October 2019.

[27] A. K. Jaiswal and D. Fuchs. Private communication.

[28] *Physical Review*, 155:15, 1967.

[29] *Physical Review B*, 60:24.

[30] Saqib Javaid, M. Javed Akhtar, Irfan Ahmad, Muhammad Younas, Shafqat H. Shah, and Iftikhar Ahmad. Pressure driven spin crossover and isostructural phase transition in lafeo3. *Journal of Applied Physics*, 114(24):243712, 12 2013.

[31] R. Scherwitzl, S. Gariglio, M. Gabay, P. Zubko, M. Gibert, and J.-M. Triscone. Metal-insulator transition in ultrathin lanio$_3$ films. *Phys. Rev. Lett.*, 106:246403, Jun 2011.

[32] S. Acharya, J. Mondal, S. Ghosh, S.K. Roy, and P.K. Chakrabarti. Multiferroic behavior of lanthanum orthoferrite (lafeo3). *Materials Letters*, 64(3):415–418, 2010.

[33] J.M. Longo, J.A. Kafalas, and R.J. Arnott. Structure and properties of the high and low pressure forms of sriro3. *Journal of Solid State Chemistry*, 3(2):174–179, 1971.

[34] K. Sreedhar, J. M. Honig, M. Darwin, M. McElfresh, P. M. Shand, J. Xu, B. C. Crooker, and J. Spalek. Erratum: Electronic properties of the metallic perovskite lanio$_3$: Correlated behavior of 3*d* electrons. *Phys. Rev. B*, 47:5543–5544, Mar 1993.

[35] G. Kresse and J. Hafner. Ab initio molecular dynamics for liquid metals. *Phys. Rev. B*, 47:558–561, Jan 1993.

[36] G. Kresse and J. Furthmüller. Efficient iterative schemes for ab initio total-energy calculations using a plane-wave basis set. *Phys. Rev. B*, 54:11169–11186, Oct 1996.

[37] A. I. Liechtenstein, V. I. Anisimov, and J. Zaanen. Density-functional theory and strong interactions: Orbital ordering in mott-hubbard insulators. *Phys. Rev. B*, 52:R5467–R5470, Aug 1995.

[38] Tamene R. Dasa, Lin Hao, Jian Liu, and Haixuan Xu. Designing iridate-based superlattice with large magnetoelectric coupling. *J. Mater. Chem. C*, 7(42):13294–13300, 2019.

[39] D. J. Groenendijk, C. Autieri, J. Girovsky, M. Carmen Martinez-Velarte, N. Manca, G. Mattoni, A. M. R. V. L. Monteiro, N. Gauquelin, J. Verbeeck, A. F. Otte, M. Gabay, S. Picozzi, and A. D. Caviglia. Spin-orbit semimetal sriro$_3$ in the two-dimensional limit. *Phys. Rev. Lett.*, 119:256403, Dec 2017.

[40] Pizzi G Lee Y S Souza I Vanderbilt D Mostofi A A, Yates J R and Marzari N. *Comput. Phys. Commun.*, 185:2309, 2014.

[41] Song H F Troyer M Wu Q, Zhang S and Soluyanov A A. *Comput. Phys. Commun.*, 224:405, 2018.

[42] M Gradhand, D V Fedorov, F Pientka, P Zahn, I Mertig, and B L Györffy. First-principle calculations of the berry curvature of bloch states for charge and spin transport of electrons. *Journal of Physics: Condensed Matter*, 24(21):213202, may 2012.

[43] A. Ohtomo and H. Y. Hwang. A high-mobility electron gas at the laalo3/srtio3 heterointerface. *Nature*, 427(6973):423–426, 2004.

[44] Fernando Gallego, Javier Tornos, Juan Ignacio Beltran, Andrea Peralta, Javier Garcia-Barriocanal, Guichuan Yu, Geoffrey Rojas, Carmen Munuera, Mariona Cabero, David Sanchez-Manzano, Fabian Cuellar, Gabriel Sanchez-Santolino, Zouhair Sefrioui, Alberto Rivera-Calzada, Federico Jose Mompean, Mar Garcia-Hernandez, Carlos Leon, Maria del Carmen Muñoz, and Jacobo Santamaria. Reversible metal-insulator transition in sriro$_3$ ultrathin layers by field effect control of inversion symmetry breaking. *Communications Materials*, 4(1):36, May 2023.

[45] Xiaodong Zhou Yuriy Mokrousov Xiuxian Yang, Wanxiang Feng and Yugui Yao. Intrinsic and extrinsic anomalous transport properties in noncollinear antiferromagnetic mn3sn from first-principles calculations. *Physical Review B*, 109:214406, 2024.

6

Centrosymmetric-noncentrosymmetric Structural Phase Transition in the Quasi-one-dimensional Compound $(TaSe_4)_3I$*

6.1 Introduction and Motivation

Symmetry plays a crucial role in determining the properties of materials [1–4]. In particular, the symmetry of crystal structures, especially in lower dimensions, has a profound influence on their physical behavior. In low-dimensional systems, symmetry-breaking phase transitions can result in fascinating effects [5–16]. For example, the onset of ferroelectricity, driven by the breaking of inversion symmetry [17, 18], leads to spontaneous polarization. Moreover, in materials lacking inversion symmetry, spin-orbit coupling can induce novel spin textures and give rise to topological phases [19–22].

Transition metal chalcogenides such as MX_2 and MX_3, where M stands for niobium (Nb) or tantalum (Ta), and X represents sulfur (S) or selenium (Se), are noteworthy due to their reduced dimensionality characteristics. Dichalcogenides, designated as MX_2, represent two-dimensional (2D) systems, making them ideal models for studying properties unique to 2D materials. On the other hand, trichalcogenides, represented as MX_3, are characterized by quasi-one-dimensional (quasi-1D) behavior, which includes the presence of charge density wave (CDW) phenomena. In both MX_2 and MX_3 compounds, an identical

*This chapter is based on publication: Arnab Bera†, **Samir Rom**†, Suman Kalyan Pradhan, Satyabrata Bera, Sk Kalimuddin, Tanusri Saha-Dasgupta, and Mintu Mondal, Phys. Rev. B 108, 035112 (2023). († These authors contributed equally to this work)

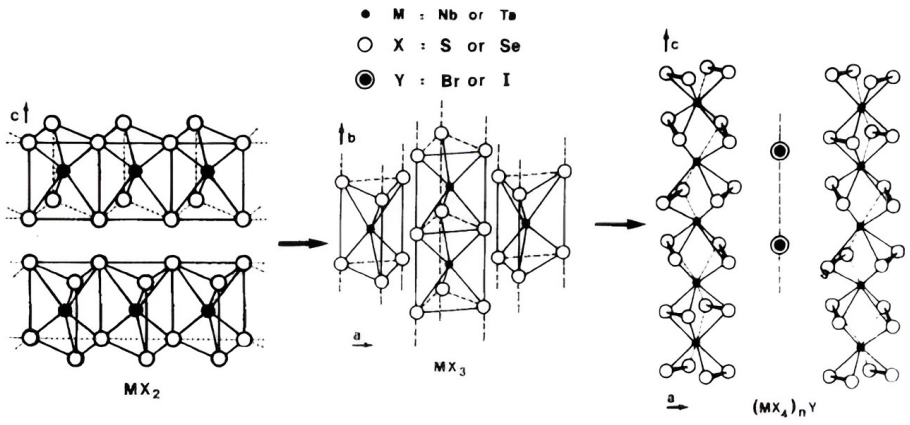

Figure 6.1: *Schematic models of MX_2, MX_3, and MX_4. The Figure is taken from Ref. [23].*

trigonal prismatic coordination surrounds the metal atom. For the MX_2 compound, these prisms are systematically arranged into $[MX_2]$ infinite layers. Conversely, in the case of MX_3, the prisms are vertically stacked to establish $[MX_3]$ infinite chains, as illustrated in Figure 6.1. The aforementioned structural arrangement imparts MX_3 compounds with a pseudo-one-dimensional characteristic, as exemplified by the notable charge density wave phenomena observed in $NbSe_3$ [24]. In these trichalcogenides, there exist anionic pairs $(X_2)^{2-}$ coupled with M^{4+} metal ions in a d^1 configuration. This structure allows for the formation of metal-metal pairs along the chains, which can lead to semiconducting properties under certain conditions, such as observed in NbS_3 type I with a bandgap (E_g) of 0.44 eV [24].

Transition metal tetrachalcogenides, represented by the general formula $(MX_4)_nY$-where M stands for niobium (Nb) or tantalum (Ta), X signifies sulfur (S) or selenium (Se), and Y comprises bromine (Br) or iodine (I), with n values of 2, 3, or approximately 10/3-serve as model quasi-one-dimensional systems for examining diverse phases and phase transitions [23, 25–39]. These compounds are characterized by "M" atoms enveloped by antiprisms of "X" atoms, forming one-dimensional chains with "Y" ions interspersed to provide cohesion, as illustrated in Figure 6.1. Although these pseudo-one-dimensional materials exhibit structural similarities to trichalcogenides, they are differentiated by the presence of halogens and variations in metal-metal bonding distances. These materials generally comprise two MX_4 chains per unit cell, displaying similar 'a' parameters but distinct 'c' parameters.

The electrical characteristics are influenced by the behavior of d^1 electrons in M^{4+} ions, which can either form localized d^1-d^1 bonds, resulting in semiconducting properties, or become more or less delocalized, potentially leading to metallic conductivity. Additionally, the presence of M^{5+} ions with a d^0 electron configuration can disrupt metallic conductivity along the chain. Furthermore, variations in the distances between metal atoms affect the activation energies of semiconducting compounds; equidistant metal-metal spacings are

associated with high room-temperature conductivity. This phenomenon aligns with the hopping mechanism [23].

These materials are susceptible to Peierls instability, and the occupancy level of the metal $d_z{}^2$ band, described by the expression $(n-1)/2n$, affects the characteristics of charge density wave (CDW) fluctuations that are driven by correlation effects [26]. Of particular interest is $(TaSe_4)_2I$, a chiral quasi-one-dimensional compound that lacks an inversion symmetry center. This compound has recently been characterized as a topological Weyl semimetal, in which its Weyl nodes interact with CDW modes, suggesting the potential formation of an axion insulator [40–45]. This discovery presents a new research direction focused on investigating the interaction between strongly correlated CDW condensates and the topology of electronic states. This could pave the way for identifying unprecedented quantum phenomena [40, 46].

Another interesting member of this family, $(TaSe_4)_3I$, has recently drawn attention due to reports suggesting the possible coexistence of ferromagnetism and superconductivity below 2.5 K [47]. A detailed discussion of this is provided in the next chapter. The initial study by C Roucau et al. in the 1980s [27] indicated that this compound stabilizes in a crystal structure with space group $P4/mnc$ at room temperature and shows weakly metallic behavior [27]. Despite its long history of synthesis, research on $(TaSe_4)_3I$ has been limited. Previous studies assumed similar behavior to $(NbSe_4)_3I$ based on their identical crystal structures [23, 26, 27]. However, recent findings [47] highlight the need for a distinct investigation into this compound to understand its proposed exotic behavior. Theoretical studies on $(TaSe_4)_3I$ [35], using a crystal structure derived from $(NbSe_4)_3I$ with Nb replaced by Ta, suggest a van-Hove singularity in the low-energy electronic structure, potentially influencing its unique electronic properties. Nonetheless, the origin of the observed ferromagnetism alongside superconductivity remains unclear. Previous work [47] concentrated on the low-temperature phase properties of $(TaSe_4)_3I$ but did not thoroughly investigate the low-temperature phase or potential structural phase transitions. To fully understand the exotic behavior reported, it is essential to examine the associated structural phase transitions and the details of the low-temperature crystal structure.

This study aims to explore the inversion symmetry-breaking structural phase transition in $(TaSe_4)_3I$ using a combination of experimental and theoretical methods. Experiments involving electronic transport, specific heat, and Raman scattering reveal a phase transition around $T_S \sim 145$ K. Temperature-dependent single-crystal X-ray diffraction (SXRD) studies indicate that the phase transition results from a temperature-induced distortion of Ta-chains, breaking inversion symmetry at low temperatures, and causing a structural transition from a high-temperature (HT) centrosymmetric ($P4/mnc$) structure to a low-temperature (LT) noncentrosymmetric structure ($P\bar{4}2_1c$). Our theoretical work, involving first-principles cal-

culations and an ab-initio derived tight-binding formulation, elucidates the microscopic origin of this inversion symmetry-breaking transition. We find that the transition occurs due to a gain in hybridization energy from the off-centric movement of Ta atoms in the chain-like structure, outweighing the elastic energy loss, similar to lattice-driven ferroelectricity mechanisms. These findings offer valuable insights into the unique symmetry-breaking structural transition in this quasi-1D system and encourage further research into how this transition affects its physical properties.

6.2 Computational Methodology

For the theoretical investigation, first-principles calculations were performed using three different basis sets: (a) VASP [48, 49], (b) LAPW [50, 51], and (c) LMTO basis [52, 53]. The consistency of the results across these basis sets was verified through comparisons of band structures and density of states. The exchange-correlation functional employed was the Perdew-Burke-Ernzerhof (PBE) implementation of the generalized gradient approximation. A Monkhorst-Pack k-point mesh of $8 \times 8 \times 4$ was used to ensure convergence of the computed ground-state properties. In the plane-wave calculations, a cutoff energy of 600 eV was applied with projected augmented wave potentials. For LAPW calculations, a criterion based on the muffin-tin radius multiplied by K_{max} for the plane wave was set to 7.0. In the LMTO calculations, the muffin-tin radii were selected as 3.06, 3.05, 3.32, and 2.50-2.60 Å for Ta (1), Ta (2), I, and Se, respectively, for the high-temperature (HT) structure at 300 K, and as 3.06, 3.06, 3.05, 3.30, and 2.55-2.70 Å for Ta (1), Ta (2), Ta (3), I, and Se for the low-temperature (LT) structure at 100 K. These methods, namely, plane wave, LAPW, and LMTO, were employed to examine the electronic structure in both HT and LT phases, confirming the robustness of the semi-metallic solution in these phases.

To evaluate the kinetic energy gain in the LT phase, a low-energy Hamiltonian was constructed in the Wannier function basis derived from first-principles calculations. This was achieved using the NMTO-downfolding technique, starting from a full density functional theory (DFT) band structure. NMTO calculations utilized potentials obtained from self-consistent LMTO calculations. The real-space representation of the NMTO-downfolded Hamiltonian, expressed as $H_{TB} = \sum_{ij} t_{ij}^{mm'} (C_{i,m}^{\dagger} C_{j,m'} + h.c)$ in the Wannier function basis, provides estimates for various hopping integrals (t), where m and m' are non-downfolded orbitals at sites i and j, and $C_{i,m}^{\dagger}$ ($C_{j,m'}$) denotes electron creation (annihilation) operators.

6.3 Observations from Experimental Studies

Our theoretical predictions are supported by experimental data*. This section summarizes the key experimental findings.

6.3.1 Structural phase transition (SPT): broken inversion symmetry

The temperature-dependent single-crystal X-ray diffraction (SXRD) studies, as shown in Figure 6.2 and detailed in Table 6.1, provide insights into the structural changes occurring across the phase transition. These studies reveal changes in the crystal structure, such as the disappearance of inversion centers and mirror planes in the low-temperature phase, consistent with theoretical predictions of symmetry breaking.

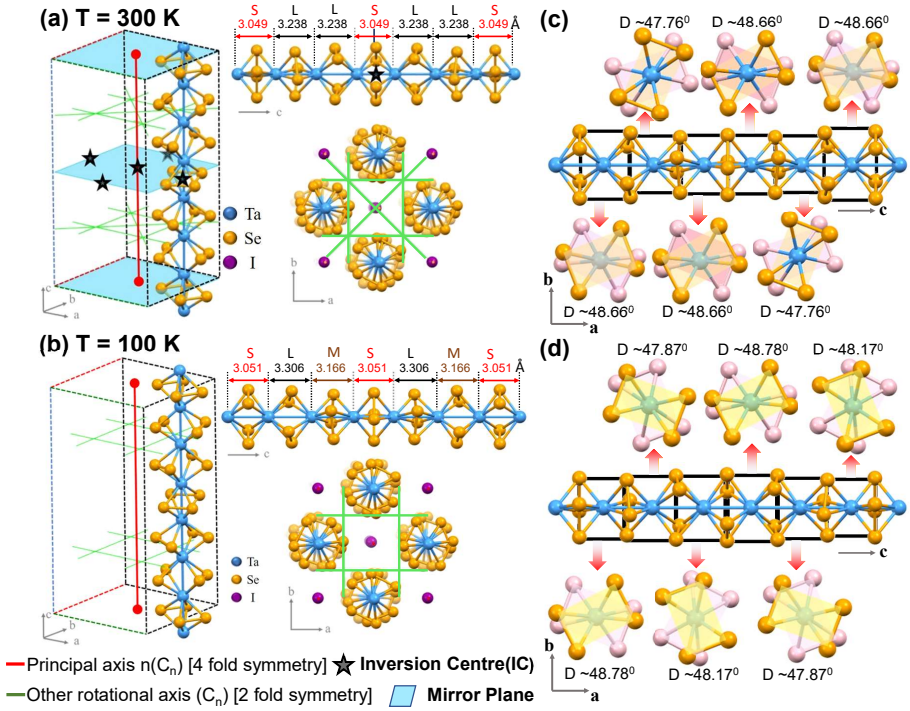

Figure 6.2: *Single crystal XRDs: Structures and Symmetries of $(TaSe_4)_3I$ single crystal. Schematics of the $(TaSe_4)_3I$ crystal structure at (a) $T = 300$ K (RT) and (b) $T = 100$ K (LT). The "Inversion Centre (IC)" points are indicated with star symbols and are present only in the RT structure. Likewise, mirror planes, depicted in light blue, are observed in the RT structure but are absent in the LT structure. For clarity, different inequivalent Ta sites (Ta(1) and Ta(2) at HT and Ta(1), Ta(2), Ta(3) at LT) are displayed in the same color. (c-d) The distribution of the dihedral angles at HT and LT (refer to text for more details). Experimental observations were conducted by Mintu Mondal's group from IACS, Kolkata.*

Crystal Structure at $T = 300$ K: At room temperature, $(TaSe_4)_3I$ adopts a tetragonal crystal structure with space group $P4/mnc$ (no. 128). The unit cell parameters are $a = b =$

*Experimental observations were conducted by Mintu Mondal's group from IACS, Kolkata

9.4696(5) Å, $c = 19.049(11)$ Å, and all angles are 90°. The RT structure is characterized by $TaSe_4$ chains separated by iodine atoms. Each Ta atom is coordinated by Se_4 units, with Ta-Ta bonds alternating between short and long. This configuration confirms the quasi-one-dimensional nature of the crystal, with strong covalent bonds along the chain and weak interactions between chains, as depicted in Figure 6.2(a).

Crystal Structure at T = 100 K: At low temperatures, the structure transitions to a tetragonal phase with space group $P\bar{4}2_1c$ (no. 114), which is noncentrosymmetric compared to the centrosymmetric RT phase. The lattice parameters remain similar, but the Ta-Ta bond sequence changes, incorporating longer and medium bonds. This change is illustrated in Figure 6.2(b), and the corresponding details are summarized in Table 6.1.

Temperature-Dependent Structural Changes: The transition to the noncentrosymmetric phase at around 145 K is marked by changes in Ta-Ta bond lengths and dihedral angles. Specifically, the bond length between Ta(2) and Ta(3) changes from long to medium, and corresponding adjustments are observed in other Ta-Ta distances. The dihedral angles also vary with temperature, reflecting structural rearrangements. These variations are shown in Figure 6.3(a-b).

Raman Spectroscopy and Structural Transition Signature:

Centrosymmetric Phase: Theoretical predictions of the vibrational modes for a tetragonal crystal structure with space group $P4/mnc$ are derived from lattice dynamics calculations. It is noteworthy that there are 64 atoms in one unit cell (n) for both structures. The vibrational modes in the centrosymmetric phase decompose into 192 ($3n$) mechanical representations and can be represented as:

$$\begin{aligned}\Gamma_{D4h} = &(A_{2u} + E_u) \\ &+ (12A_{1g} + 10A_{1u} + 13A_{2g} + 10A_{2u} \\ &+ 12B_{1g} + 10B_{1u} + 11B_{2g} + 9B_{2u} \\ &+ 27E_u + 24E_g),\end{aligned} \tag{2}$$

where the first term represents the acoustic modes and the remaining terms represent the optical modes. Among these optical modes, $(10A_{2u} + 27E_u)$ are infrared (IR) active as well as Raman (R) inactive, while $(12A_{1g} + 12B_{1g} + 11B_{2g} + 24E_g)$ are Raman active but IR inactive.

Noncentrosymmetric Phase: In the noncentrosymmetric phase, the vibrational modes decompose into 192 mechanical representations, represented as:

$$\begin{aligned}\Gamma_{D2d} = &(B_2 + E) \\ &+ (22A_1 + 22A_2 + 22B_1 + 21B_2 + 51E).\end{aligned} \tag{2}$$

Here, the first and second groups of the representation correspond to the acoustic and optical modes, respectively. Among the optical modes, the IR-active modes are $(21B_2 + 51E)$, while the Raman-active modes are $(22A_1 + 22B_1 + 21B_2 + 51E)$.

Notably, the number of Raman-active modes in the noncentrosymmetric phase (total 167 modes) is greater than that in the centrosymmetric phase (total 83 modes), even though the total number of vibrational modes in both cases is identical. This increase in Raman-active modes at low temperatures, as shown in Figure 6.4 is consistent with the group theory predictions [54]. However, experimental limitations, such as weak photon-phonon coupling and a restricted wavenumber range, result in fewer detected modes compared to theoretical expectations. This observation is consistent with similar studies on related materials.

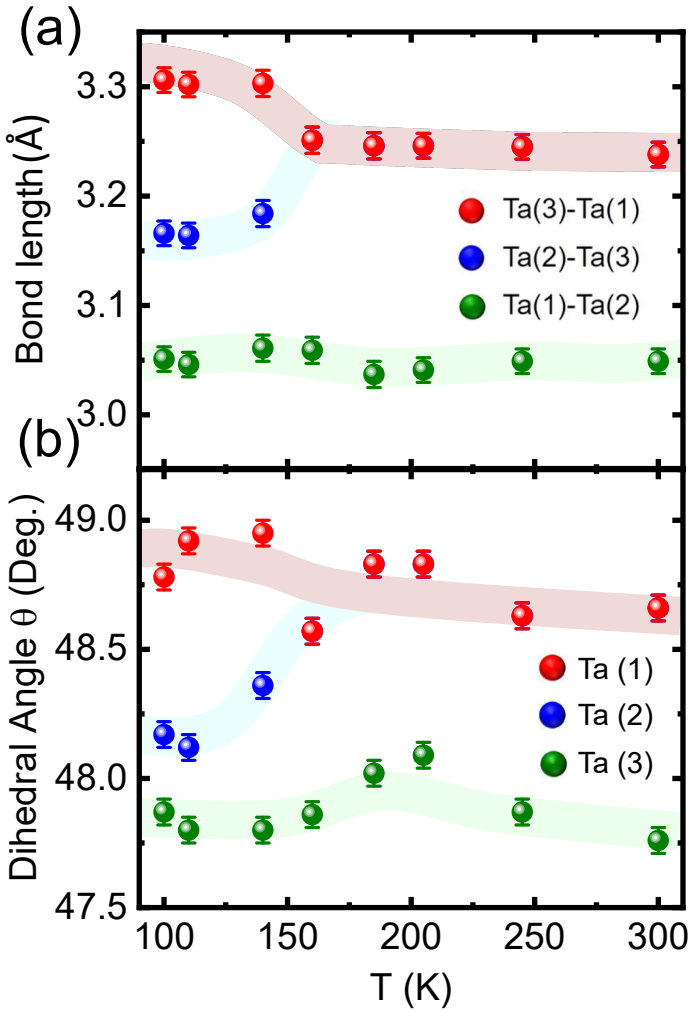

Figure 6.3: *(a) Temperature variation of bond distances among different Ta atoms and (b) dihedral angles. The solid spheres represent experimental data, while thick solid lines are guides to the eye.*

Table 6.1: *SXRD Refinement results for $(TaSe_4)_3I$ at T = 100 K, and 300 K.*

Crystallographic Information					
Temperature (T)		100 K		300 K	
	Crystal system	Tetragonal		Tetragonal	
	Space Group	$P\bar{4}2_1c$		$P4/mnc$	
	a (Å)	9.4358(5)		9.4696(5)	
	b (Å)	9.4358(5)		9.4696(5)	
	c (Å)	19.046(11)		19.049(11)	
	$\alpha = \beta = \gamma$ (°)	90		90	
	Cell Volume (Å^3)	1695.78		1708.19	
	R-factor (%)	2.27		2.75	
Atomic Coordinates					
Atom	Site	100 K Position (x, y, z)	300 K Position (x, y, z)	B_{iso} (100 K)	B_{iso} (300 K)
Ta(1)	4d	(0.500, 1.000, 0.913)	8f (0.000, 0.500, 0.580)	0.009	0.021
Ta(2)	4d	(0.500, 1.000, 0.573)	4d (0.000, 0.500, 0.750)	0.009	0.023
Ta(3)	4d	(0.500, 1.000, 0.739)	-	0.009	-
Se(1)	8e	(0.547, 0.785, 0.820)	16i (0.186, 0.375, 0.660)	0.011	0.024
Se(2)	8e	(0.313, 0.876, 0.832)	16i (-0.048, 0.280, 0.672)	0.011	0.025
Se(3)	8e	(0.283, 1.049, 0.663)	8h (0.021, 0.275, 0.500)	0.011	0.026
Se(4)	8e	(0.372, 0.814, 0.653)	8h (-0.199, 0.391, 0.500)	0.011	0.027
Se(5)	8e	(0.610, 0.800, 0.493)	-	0.012	-
Se(6)	8e	(0.725, 1.022, 0.492)	-	0.011	-
I	4c	(0.500, 0.500, 0.626)	4e (0.500, 0.500, 0.627)	0.022	0.056

6.3.2 Confirmation of phase transition at $T_S \simeq 145\ K$

The resistance (R) as a function of temperature (T) displays a near-linear decrease with decreasing temperature as shown in Figure 6.4(a), indicating semi-metallic behavior, as suggested by a residual resistance ratio (RRR) of $\frac{R_{300K}}{R_{2K}} = 30$. A distinct slope change at approximately 145 K, observed in both $R(T)$ and dR/dT vs T plots, suggests a phase transition at this temperature (T_S). The resistance shows linear temperature dependence in the range of 70–200 K, indicative of strong electron-phonon scattering. Below 15 K, a T^2 dependence points to dominant electron-electron scattering, confirming theoretical predictions about low-temperature transport behavior [55].

Specific heat measurements reveal a sharp change at $T \sim 140$ K, consistent with the transition observed in the resistance data as shown in Figure 6.4(b), although a slight difference in transition temperatures is noted due to sample geometry differences. Analysis of the low-temperature specific heat data provides a Sommerfeld coefficient of γ = 11.80 mJ/K^2-mol, indicative of significant electronic correlations [56].

Raman spectroscopy further supports the phase transition, with distinct Raman-active modes (P_2, P_6, and P_{10}) emerging at low temperatures, which are absent at room temperature as shown in Figure 6.4(c). These findings, corroborated with both powder and single-crystal samples, indicate the structural phase transition responsible for the appearance of additional peaks at low temperatures.

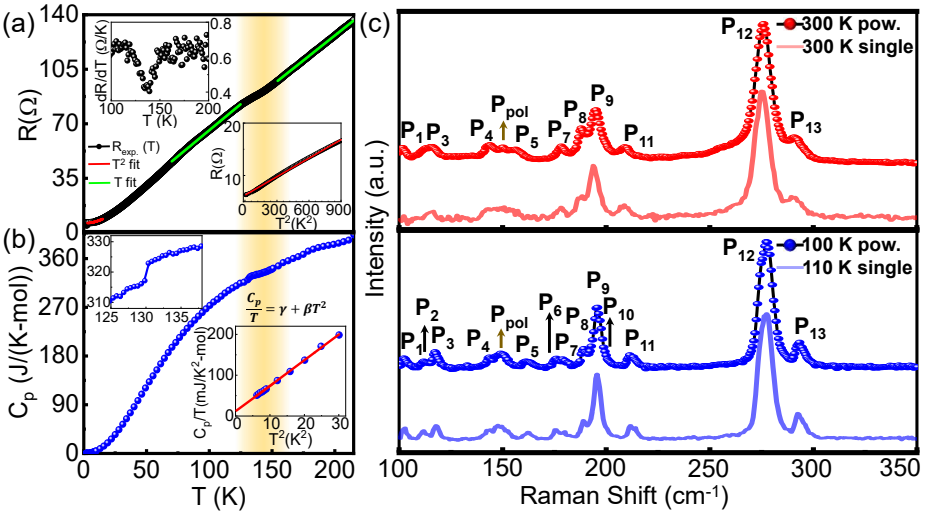

Figure 6.4: *Indicators of phase transition in $(TaSe_4)_3I$: (a) Temperature-dependent resistance measurements of wire-like $(TaSe_4)_3I$ samples down to $T \sim 2$ K. The upper inset (dR/dT vs. T plot) identifies the phase transition occurring around 145 K. The lower inset displays a R vs. T^2 plot for the temperature range of 2.5–30 K, with the red solid line representing a linear fit to the data. (b) Specific heat measurements reveal a distinct jump, highlighted in the upper inset, which indicates a phase transition at approximately $T_S \sim$ 145 K. The lower inset shows C_p/T vs. T^2 with linear behavior at low temperatures. (c) Raman spectra obtained from both powder and single-crystal samples at T = 300 K (for both powder and single-crystal samples), T = 100 K (for powder sample), and T = 110 K (for single-crystal sample). The arrows denote the Raman-active modes P_2, P_6, and P_{10} that emerge in the low-temperature samples below the transition. Experimental observations were conducted by Mintu Mondal's group from IACS, Kolkata.*

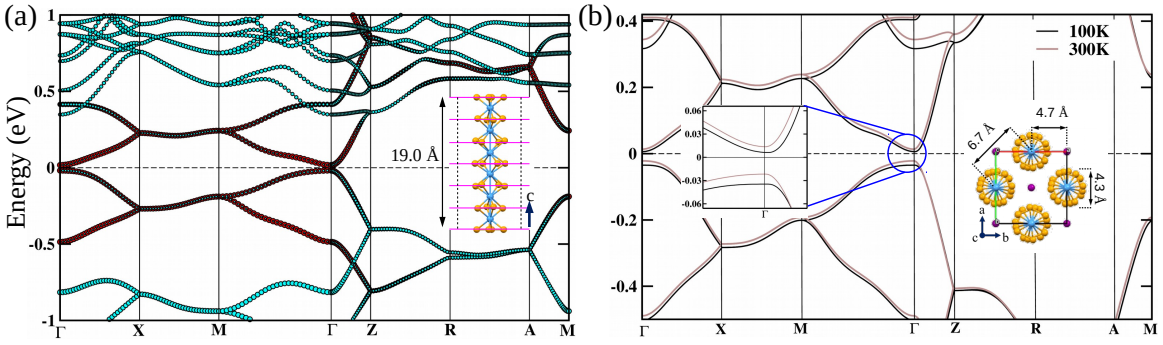

Figure 6.5: *(a) The band structure of $(TaSe_4)_3I$ at high temperature (T=300 K), plotted along the high symmetry k-points in the tetragonal Brillouin zone (BZ). The zero of the energy is set at the Fermi energy. The band "fatness" indicates the orbital characters (red for Ta-d, cyan for Se-p). The inset shows the $TaSe_4$ chain running along the crystallographic c-axis. (b) Comparison of the band structure for low temperature (T=100 K) with that at room temperature (T=300 K). The change in the band gap between the two temperatures is highlighted in the zoomed-in plot. The inset shows the $TaSe_4$ chains, separated by iodine atoms, in the $(TaSe_4)_3I$ structure, projected in the ab plane.*

6.4 Theoretical Caculation

To investigate the origin of the structural transition in $(TaSe_4)_3I$, we performed first-principles electronic structure calculations for both the high-temperature (HT, T=300 K) and low-temperature (LT, T=100 K) crystal structures. Our theoretical work aimed to elucidate the changes in electronic properties associated with the phase transition.

The left panel of Figure 6.5 shows the band structure of $(TaSe_4)_3I$ at 300 K, plotted along the high symmetry k-points in the tetragonal Brillouin zone (BZ) and projected onto Ta-d and Se-p states. Each Se_4 rectangle in the structure is composed of two Se_2^{2-} dimers. In this configuration, the Ta atoms within the $TaSe_4$ chains, which are embedded in a rectangular antiprism Se environment, are in a nominal 4+ or d^1 charge state. The presence of iodine atoms between the chains withdraws electrons, reducing the nominal valence of Ta from 4+ to approximately 4.333+ or $d^{2/3}$.

As a result of this fractional occupancy, a Peierls distortion is observed at 300 K, resulting in trimerization with two inequivalent Ta atoms (Ta(1) and Ta(2)) and alternating long (L) and short (S) Ta-Ta bonds with a sequence of ... L-L-S ..., consistent with experimental observations. This Peierls distortion induces a small gap at the Fermi level, with a calculated value of 0.02 eV, rendering the electronic structure almost semimetallic. The low-energy band structure is predominantly influenced by Ta-d orbitals with some contribution from Se-p orbitals. The rectangular antiprism coordination of Se atoms surrounding Ta positions the Ta $3z^2$-r^2 orbital as the lowest energy state, approximately half-filled for Ta(1) and nearly empty for Ta(2). The unit cell contains 12 Ta atoms: 8 Ta(1) and 4 Ta(2). This results in eight Ta(1)-$3z^2$-r^2-dominated bands and four Ta(2)-$3z^2$-r^2 bands. Overlap between Ta(1)-$3z^2$-r^2 and Ta(1)/Ta(2)-$3z^2$-r^2 splits the eight Ta(1)-$3z^2$-r^2-dominated bands into four occupied and four unoccupied bands, while the four Ta(2)-$3z^2$-r^2 bands remain predominantly unoccupied. The bands are nearly flat along the X-M direction (b-direction), where the chains are separated by approximately 9.5 $\AA$ with intervening I^{-1} ions, which remain isolated (see insets). The occupied bands along M-Γ (moving along the diagonal in the ab-plane) further split due to Ta-Ta interactions via the intervening Se atoms in adjacent chains. The trimerization along the chain direction (c) causes additional band folding, as observed in the band structure along the Γ-Z direction.

For the 100 K crystal structure, the essential features of the electronic structure remain similar to those at high temperature, as shown in the right panel of Figure 6.5. At low temperature, the 12 Ta atoms in the unit cell are classified into three groups: 4 Ta(1), 4 Ta(2), and 4 Ta(3). The occupancies of Ta(1) and Ta(2) are close to half-filled, while Ta(3) is more empty. The band gap increases slightly from 0.02 eV at high temperature to 0.03 eV at low temperature, indicating enhanced stability of the LT phase compared to

the HT phase. This tiny but non-zero gap and the increased band gap in the LT phase have been confirmed by three different methods: plane-wave, full-potential LAPW, and LMTO calculations. These results confirm that the compound remains semi-metallic, consistent with experimental observations.

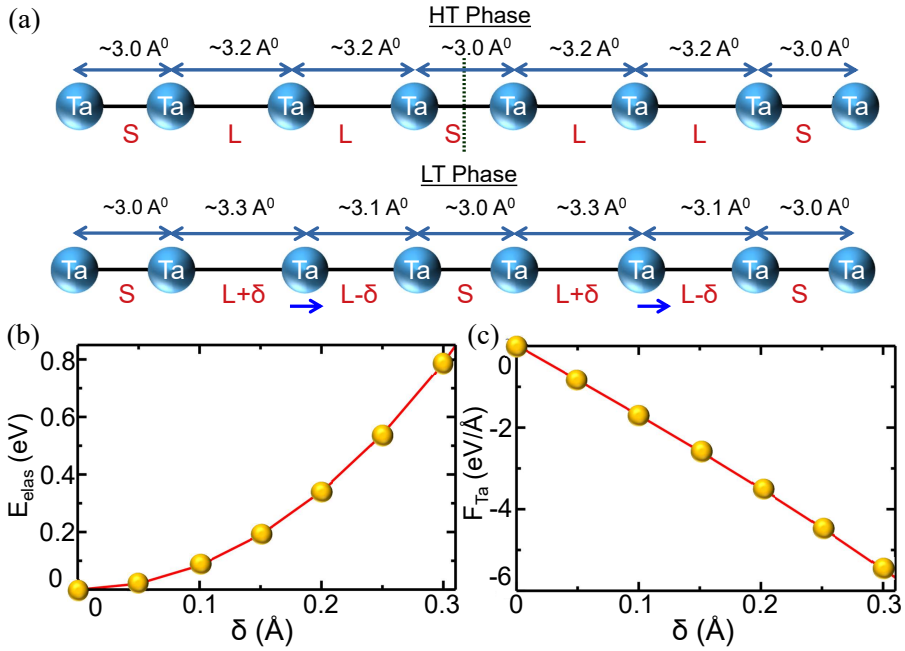

Figure 6.6: *(a) Schematic diagram illustrating the distribution of Ta-Ta bond lengths in the $TaSe_4$ chain for high-temperature (HT) and low-temperature (LT) crystal structures. The inversion center (marked by a dotted line) in the HT structure is disrupted in the LT structure due to the distortion δ. (b) Elastic energy and (c) force acting on Ta ions as a function of off-centric displacement (δ), as obtained from density functional theory (DFT) calculations.*

Our analysis revealed significant changes in the Ta-Ta bond lengths between the HT and LT phases, leading to a structural distortion. In the HT phase, the Ta-Ta bond sequence in the chain follows a …L-L-S-L-L… pattern. Upon transitioning to the LT phase, this sequence changes to …L-M-S-L-M… (see Figure 6.6(a)). This change breaks the inversion symmetry at the "S" bond in the HT phase, resulting in a noncentrosymmetric structure in the LT phase. The transition is analogous to an off-centric movement observed in ferroelectrics, where the centrosymmetric HT structure transforms into a noncentrosymmetric LT structure.

In ferroelectrics, such off-centric movements are driven by a balance between the hybridization energy gain and the elastic energy loss. To estimate the hybridization energy gain, we focused on a Ta-$3z^2$-r^2 only model. We noted that the bond length for the "S" bond remains approximately constant between HT and LT phases, while the "L" bond length splits into ≈ "L+δ" and ≈ "L-δ" in the LT phase. We employed the NMTO-downfolding method to construct a Ta-$3z^2$-r^2 model based on the DFT band structure of the HT phase.

The tight-binding Hamiltonian derived from this model provided estimates for the hopping parameter, t_{dd}, associated with the "L" bond.

The hopping parameter for the LT phase was obtained using a distance (l)-dependent scaling relation, $t_{dd} \sim 1/l^{\beta}$, where $\beta = \partial \ln t_{dd}/\partial \ln l$. For the HT phase, the estimated β was found to be approximately 2. The kinetic energy gain due to the additional off-centric distortion in the LT phase was calculated as:

$$\Delta E_{KE} = -2t_{dd}^2(L+\delta) - 2t_{dd}^2(L-\delta) + 4t_{dd}^2$$

The elastic energy cost due to the change in bond lengths was given by:

$$\Delta E_{elas} = \kappa \times \delta^2$$

where κ is the stiffness constant. We estimated κ from total energy calculations by varying δ, as shown in Figure 6.6(b). This was further corroborated by analyzing the force acting on Ta ions, leading to a stiffness constant of 16.8 eV/Å^2 from total energy and 17.0 eV/Å^2 from force estimates.

The calculated ΔE_{KE} of approximately -0.03 eV and ΔE_{elas} of approximately 0.01 eV indicate that the LT structure is stabilized by the net gain in hybridization energy. This theoretical analysis does not account for additional factors such as the distortion of Se rectangles and inter-chain interactions, but provides a valuable understanding of the phase transition. Despite the simplistic nature of the model, the estimated temperature scale for the transition, derived from the energy difference, is approximately 232 K, which is close to the experimentally observed transition temperature of $\sim$145 K.

Interestingly, the LT phase exhibits a non-polar space group $P\bar{4}2_1c$ (114), which is non-centrosymmetric but non-polar. This is attributed to the additional loss of inversion symmetry in the LT phase, which affects the polarization characteristics. For a uniform bonding sequence across chains, the LT phase would be expected to have a polar point group. This theoretical prediction aligns with the experimental findings and highlights the intricate interplay between hybridization and elastic effects in driving the phase transition.

6.5 Summary and Conclusions

In this work, we performed a detailed analysis of the single crystal X-ray diffraction (XRD) data to investigate the structural transition in $(TaSe_4)_3I$ around the transition temperature $T_s \sim 145\ K$. This transition is evidenced by resistivity, specific heat, and Raman scattering experiments. Our analysis reveals that the structural transition is characterized by a symmetry-lowering change in the Ta chains from a high-temperature (HT) phase with a

L-L-S sequence of Ta-Ta bonds to a low-temperature (LT) phase with a L-M-S Ta-Ta bond sequence. This transition results in the breaking of the center of inversion at the short Ta-Ta bond, leading to a transition between a high-temperature centrosymmetric structure and a low-temperature noncentrosymmetric structure, both belonging to the same tetragonal symmetry.

The origin of this structural phase transition was explored using first-principles DFT calculation and tight-binding modeling. Our theoretical investigations show that both the high-temperature and low-temperature structures exhibit semi-metallic behavior, consistent with recent experimental reports. Specifically, our theoretical analysis provides insights into the microscopic origin of the centrosymmetric-to-noncentrosymmetric transition. We identify that the transition is driven by the interplay between hybridization energy gain and elastic energy loss, resembling the mechanism observed in ferroelectric-paraelectric transitions.

In summary, the centrosymmetric to noncentrosymmetric structural phase transition is primarily driven by the balance between hybridization energy gain and elastic energy loss. Our calculations suggest that the hybridization energy gain dominates over the elastic energy loss, thereby stabilizing the off-centric structure at low temperature and the undistorted structure at high temperature. The temperature scale for the phase transition estimated from our model is in close agreement with the experimentally observed transition temperature.

Our work opens new avenues for exploring novel quantum phenomena in quasi-one-dimensional (1D) materials with broken inversion symmetry. It highlights the potential for discovering new quasi-1D materials with unique properties that could have significant implications for applications. Furthermore, our report of the centrosymmetric-noncentrosymmetric structural phase transition extends beyond the well-studied charge-density-wave transitions, unveiling an entirely new structural phase transition in this class of chain compounds.

Bibliography

[1] J. Zak. Symmetry criterion for surface states in solids. *Phys. Rev. B*, 32:2218, 1985.

[2] D. Gross. The role of symmetry in fundamental physics. *Proceedings of the National Academy of Sciences*, 93:14256, 1996.

[3] L. Lederman and C. Hill. *Symmetry and the beautiful universe*. Prometheus Books, 2007.

[4] L. Fu and C. L. Kane. Topological insulators with inversion symmetry. *Phys. Rev. B*, 76:045302, 2007.

[5] N. P. Armitage, E. J. Mele, and A. Vishwanath. Weyl and dirac semimetals in three-dimensional solids. *Rev. Mod. Phys.*, 90:015001, 2018.

[6] F. Zhang, H. Min, M. Polini, and A. H. MacDonald. Spontaneous inversion symmetry breaking in graphene bilayers. *Phys. Rev. B*, 81:041402, 2010.

[7] Y. Wang, G. Y. Cho, T. L. Hughes, and E. Fradkin. Topological superconducting phases from inversion symmetry breaking order in spin-orbit-coupled systems. *Phys. Rev. B*, 93:134512, 2016.

[8] P.-P. Shi, Y.-Y. Tang, P.-F. Li, W.-Q. Liao, Z.-X. Wang, Q. Ye, and R.-G. Xiong. Symmetry breaking in molecular ferroelectrics. *Chem. Soc. Rev.*, 45:3811, 2016.

[9] L. Du, T. Hasan, A. Castellanos-Gomez, G.-B. Liu, Y. Yao, C. N. Lau, and Z. Sun. Engineering symmetry breaking in 2d layered materials. *Nature Reviews Physics*, 3, 2021.

[10] E. Wang, X. Lu, S. Ding, W. Yao, M. Yan, G. Wan, K. Deng, S. Wang, G. Chen, L. Ma, J. Jung, A. V. Fedorov, Y. Zhang, G. Zhang, and S. Zhou. Gaps induced by inversion symmetry breaking and second-generation dirac cones in graphene/hexagonal boron nitride. *Nature Physics*, 12:1111, 2016.

[11] A. N. Berger, E. Andrade, A. Kerelsky, D. Edelberg, J. Li, Z. Wang, L. Zhang, J. Kim, N. Zaki, J. Avila, C. Chen, M. C. Asensio, S.-W. Cheong, B. A. Bernevig, and A. N. Pasupathy. Temperature-driven topological transition in 1t'-mote2. *npj Quantum Materials*, 3:2, 2018.

[12] M. Bode, M. Heide, K. von Bergmann, P. Ferriani, S. Heinze, G. Bihlmayer, A. Kubetzka, O. Pietzsch, S. Blügel, and R. Wiesendanger. Chiral magnetic order at surfaces driven by inversion asymmetry. *Nature*, 447:190, 2007.

[13] V. Vescoli, F. Zwick, J. Voit, H. Berger, M. Zacchigna, L. Degiorgi, M. Grioni, and G. Grüner. Dynamical properties of the one-dimensional band insulator $(NbSe_4)_3i$. *Phys. Rev. Lett.*, 84:1272, 2000.

[14] C. Pei, W. Shi, Y. Zhao, L. Gao, J. Gao, Y. Li, H. Zhu, Q. Zhang, N. Yu, C. Li, W. Cao, S. Medvedev, C. Felser, B. Yan, Z. Liu, Y. Chen, Z. Wang, and Y. Qi. Pressure-induced partial disorder and superconductivity in quasi-one-dimensional weyl semimetal $(nbse_4)_2i$. *Materials Today Physics*, 21:100509, 2021.

[15] D. Starešinić, P. Lunkenheimer, J. Hemberger, K. Biljaković, and A. Loidl. Giant dielectric response in the one-dimensional charge-ordered semiconductor $(NbSe_4)_3i$. *Phys. Rev. Lett.*, 96:046402, 2006.

[16] S. Kim, Y. Lv, X.-Q. Sun, C. Zhao, N. Bielinski, A. Murzabekova, K. Qu, R. A. Duncan, Q. L. D. Nguyen, M. Trigo, D. P. Shoemaker, B. Bradlyn, and F. Mahmood. Observation of a massive phason in a charge-density-wave insulator. *Nature Materials*, 22:429, 2023.

[17] PW Anderson and EI Blount. Symmetry considerations on martensitic transformations: ”ferroelectric” metals? *Phys. Rev. Lett.*, 14:217, 1965.

[18] Y Shi, Y Guo, X Wang, AJ Princep, D Khalyavin, P Manuel, Y Michiue, A Sato, K Tsuda, S Yu, et al. A ferroelectric-like structural transition in a metal. *Nature Materials*, 12:1024, 2013.

[19] M Sato and Y Ando. Topological superconductors: a review. *Reports on Progress in Physics*, 80:076501, 2017.

[20] K Matano, M Kriener, K Segawa, Y Ando, and GQ Zheng. Spin-rotation symmetry breaking in the superconducting state of cuxbi2se3. *Nature Physics*, 12:852, 2016.

[21] L Lu, Z Wang, D Ye, L Ran, L Fu, JD Joannopoulos, and M Soljačić. Experimental observation of weyl points. *Science*, 349:622, 2015.

[22] ZK Liu, LX Yang, Y Sun, T Zhang, H Peng, HF Yang, C Chen, Y Zhang, Y Guo, D Prabhakaran, et al. Evolution of the fermi surface of weyl semimetals in the transition metal pnictide family. *Nature Materials*, 15:27, 2016.

[23] P. Gressier, A. Meerschaut, L. Guemas, J. Rouxel, and P. Monceau. Characterization of the new series of quasi one-dimensional compounds (mx4)ny (m = nb, ta; x = s, se; y = br, i). *Journal of Solid State Chemistry*, 51:141, 1984.

[24] J. Rinjsdorp and F. Jellinek. Solid state chem. *Journal of Solid State Chemistry*, 25:325, 1978.

[25] P. Monceau, J. Richard, and M. Renard. Charge-density-wave motion in nbse3. i. studies of the differential resistance dv/di. *Phys. Rev. B*, 25:931, 1982.

[26] P. Gressier, M. H. Whangbo, A. Meerschaut, and J. Rouxel. Electronic structures of transition-metal tetrachalcogenides (mse4)ni (m = nb, ta). *Inorg. Chem.*, 23:1221, 1984.

[27] C. Roucau, R. Ayroles, P. Gressier, and A. Meerschaut. Electron microscopy study of transition-metal tetrachalcogenide (mse4)ni (m=nb, ta). *Journal of Physics C: Solid State Physics*, 17:2993, 1984.

[28] M. Izumi, T. Iwazumi, K. Uchinokura, R. Yoshizaki, and E. Matsuura. X-ray diffraction study of a structural phase transition in (nbse4)3i. *Solid State Communications*, 51:191, 1984.

[29] A. Meerschaut, P. Gressier, L. Guemas, and J. Rouxel. Preparation and structure of (nbse4)3.33 i. [i3nb10se40]. *Journal of Solid State Chemistry*, 51:307, 1984.

[30] A. Zwick, M. Renucci, P. Gressier, and A. Meerschaut. A raman study of the peierls transition in (tase4)2i. *Solid State Communications*, 56:947, 1985.

[31] M. Saint-Paul, P. Monceau, and F. Levy. Soft-acoustic-phonon mode at the phase transition in quasi-one-dimensional $(NbSe_4)_3$i. *Phys. Rev. B*, 37:1024, 1988.

[32] I. Taguchi, F. Levy, and H. Berger. Metal-insulator transitions in the quasi-one-dimensional compound (nbse4)3i. *Physica B+C*, 143:258, 1986.

[33] T. Sekine, M. Izumi, and E. Matsuura. Raman scattering in linear-chain compounds (nbse4)10/13i and (nbse4)3i. *Synthetic Metals*, 19:869, 1987. Proceedings of the International Conference on Science and Technology of Synthetic Metals.

[34] T. Sekine and M. Izumi. Successive phase transitions in the linear-chain semiconductor $(NbSe_4)_3$i studied by raman scattering and electrical resistivity. *Phys. Rev. B*, 38:2012, 1988.

[35] I. Sánchez-Ramírez, M. G. Vergniory, C. Felser, and F. de Juan. Band structures of $(NbSe_4)_3$I and $(TaSe_4)_3$I: Reconciling transport, optics, and angle-resolved photoemission spectroscopy. *Phys. Rev. B*, 107:205109, 2023.

[36] A. A. Balandin, F. Kargar, T. T. Salguero, and R. K. Lake. One-dimensional van der waals quantum materials. *Materials Today*, 55:74, 2022.

[37] D. Dominko, S. Vdović, H. Skenderović, D. Starešinčić, K. Biljaković, D. Ristić, M. Ivanda, J. E. Lorenzo, and J. Demsar. Static and dynamic properties of low-temperature order in the one-dimensional semiconductor $(NbSe_4)_3I$. *Phys. Rev. B*, 94:104113, 2016.

[38] J. Kusz, M. Zubko, A. Prodan, H. J. P. van Midden, J. C. Bennett, and H. Böhm. The phase transition in the $(nbse_4)_10/3i$ charge-density-wave system. *Acta Crystallographica Section A*, 66:s216, 2010.

[39] C. An, Y. Zhou, C. Chen, F. Fei, F. Song, C. Park, J. Zhou, H.-G. Rubahn, V. V. Moshchalkov, X. Chen, G. Zhang, and Z. Yang. Long-range ordered amorphous atomic chains as building blocks of a superconducting quasi-one-dimensional crystal. *Advanced Materials*, 32:2002352, 2020.

[40] J. Gooth, B. Bradlyn, S. Honnali, C. Schindler, N. Kumar, J. Noky, Y. Qi, C. Shekhar, Y. Sun, Z. Wang, B. A. Bernevig, and C. Felser. Axionic charge-density wave in the weyl semimetal $(tase_4)_2i$. *Nature*, 575:315, 2019.

[41] X.-P. Li, K. Deng, B. Fu, Y. Li, D.-S. Ma, J. Han, J. Zhou, S. Zhou, and Y. Yao. Type-iii weyl semimetals: $(TaSe_4)_2I$. *Phys. Rev. B*, 103:L081402, 2021.

[42] W. Shi, B. J. Wieder, H. L. Meyerheim, Y. Sun, Y. Zhang, Y. Li, L. Shen, Y. Qi, L. Yang, J. Jena, P. Werner, K. Koepernik, S. Parkin, Y. Chen, C. Felser, B. A. Bernevig, and Z. Wang. A charge-density-wave topological semimetal. *Nature Physics*, 17:381, 2021.

[43] Y. Zhang, L.-F. Lin, A. Moreo, S. Dong, and E. Dagotto. First-principles study of the low-temperature charge density wave phase in the quasi-one-dimensional weyl chiral compound $(tase_4)_2I$. *Phys. Rev. B*, 101:174106, 2020.

[44] Q.-G. Mu, D. Nenno, Y.-P. Qi, F.-R. Fan, C. Pei, M. ElGhazali, J. Gooth, C. Felser, P. Narang, and S. Medvedev. Suppression of axionic charge density wave and onset of superconductivity in the chiral weyl semimetal ta_2se_8I. *Phys. Rev. Mater.*, 5:084201, 2021.

[45] S. Ghosh, F. Kargar, N. R. Sesing, Z. Barani, T. T. Salguero, D. Yan, S. Rumyantsev, and A. A. Balandin. Low-frequency current fluctuations in quasi-1d $(tase_4)_2i$ weyl semimetal nanoribbons. *Advanced Electronic Materials*, 9:2200860, 2023.

[46] S. Kim, Y. Lv, X.-Q. Sun, C. Zhao, N. Bielinski, A. Murzabekova, K. Qu, R. A. Duncan, Q. L. D. Nguyen, M. Trigo, D. P. Shoemaker, B. Bradlyn, and F. Mahmood. Observation of a massive phason in a charge-density-wave insulator. *Nature Materials*, 2023.

[47] A. Bera, S. Gayen, S. Mondal, R. Pal, B. Pal, A. Vasdev, S. Howlader, M. Jana, T. Maity, R. Ali Saha, B. Das, B. Satpati, A. Nath Pal, P. Mandal, G. Sheet, and M. Mondal. Superconductivity coexisting with ferromagnetism in a quasi-one dimensional non-centrosymmetric $(tase_4)_3I$. *arXiv:2111.14525*, 2021.

[48] G. Kresse and J. Hafner. Ab initio molecular dynamics for liquid metals. *Phys. Rev. B*, 47:558, 1993.

[49] G. Kresse and J. Furthmüller. Efficient iterative schemes for ab initio total-energy calculations using a plane-wave basis set. *Phys. Rev. B*, 54:11169, 1996.

[50] P. Blaha, K. Schwarz, F. Tran, R. Laskowski, G. K. H. Madsen, and L. D. Marks. Wien2k: An apw+lo program for calculating the properties of solids. *The Journal of Chemical Physics*, 152:074101, 2020.

[51] P. Blaha, K. Schwarz, G. Medsen, D. Kvasnicka, J. Luitz, R. Laskowski, F. Tran, and L. Marks. *Wien2k: An augmented plane wave + local orbitals program for calculating crystal properties*. Karlheinz Schwarz, Techn. Universität Wien, Austria, 2018.

[52] O. K. Andersen. Linear methods in band theory. *Phys. Rev. B*, 12:3060, 1975.

[53] O. K. Andersen and T. Saha-Dasgupta. Muffin-tin orbitals of arbitrary order. *Phys. Rev. B*, 62:R16219, 2000.

[54] A. Bera, P. S. Rana, and et al. Tracking inversion symmetry breaking accompanied by structural phase transition in quasi-1d material, (TaSe4)3I by means of phonon modes renormalization. *Under preparation*, 2023.

[55] A. H. Wilson. *The Theory of Metals*. The Theory of Metals, 2011.

[56] L. Shulenburger, M. Casula, G. Senatore, and R. M. Martin. Correlation effects in quasi-one-dimensional quantum wires. *Phys. Rev. B*, 78:165303, 2008.

7

Observation of superconductivity and Weak Ferromagnetism in Quasi-1D chain compound, $(TaSe_4)_3I$ at Ambient Pressure*

7.1 Introduction and Motivation

In this chapter, we further extend our investigation into the quasi-one-dimensional compound $(TaSe_4)_3I$ (*n*-TSI). In chapter 6, we investigated the temperature-induced structural transition in *n*-TSI through a combination of experimental techniques and theoretical models. Our computational studies, based on first-principles calculations, revealed that the material transitions from a centrosymmetric to a noncentrosymmetric phase, driven by distortions in the Ta-chains. This symmetry-breaking phenomenon significantly impacts the electronic and lattice characteristics of the material.

This chapter expands on the results presented in chapter 6 by exploring the physical characteristics of the noncentrosymmetric phase. We focus particularly on its ability to host both superconductvity and magnetism-two quantum phenomena typically considered incompatible. Experimental data show that this unique phase, stable across a wide temperature range, exhibits metallic behaviour and unconventional superconductivity-properties not previously observed in similar materials.

*This chapter is based on publication: Arnab Bera, Riju Pal†, Buddhadeb Pal†, **Samir Rom**†, Suchanda Mondal†, Deepti Rana, Aastha Vasdev, Sandeep Howlader, Manish Jana, Tanmay Maiti, Rafikul Ali Saha, Biswajit Das, Tanusri Saha-Dasgupta, Prabhat Mandal, Atindra Nath Pal, Mintu Mondal, , (Under Review). († These authors contributed equally to this work)

As discussed in chapter 6, metallic chain-like systems $(M\mathrm{Se}_4)_n\mathrm{I}$ with MSe_4 chains (where M is Nb or Ta, and n is 2, 3, or 10/3) form a quasi-one-dimensional structure along the c axis, separated by iodine atoms[1–4]. These systems are notable for their diverse phase transitions and coexistences[1–9]. Tight-binding band structure calculations indicate that the electronic characteristics of these compounds are influenced by the value of n, which alters the band filling degree thus affecting the electronic properties [3, 4]. Although earlier studies suggested that for n =2, both $(\mathrm{NbSe}_4)_2\mathrm{I}$ [10] and $(\mathrm{TaSe}_4)_2\mathrm{I}$ [5, 8, 11] exhibit semiconducting properties, the latest research highlights a more intricate electronic nature. For n =3, both $(\mathrm{NbSe}_4)_3\mathrm{I}$ and $(\mathrm{TaSe}_4)_3\mathrm{I}$ are known to crystallize in a centrosymmetric structure with space group $P4/mnc$[2], suggesting that their electronic behaviors should be analogous. However, previous studies confirmed that while $(\mathrm{NbSe}_4)_3\mathrm{I}$ is semiconducting, $(\mathrm{TaSe}_4)_3\mathrm{I}$ displays weak metallic characteristics [2]. Furthermore, presented in chapter 6, our recent work has demonstrated that the newly stabilized noncentrosymmetric phase of $(\mathrm{TaSe}_4)_3\mathrm{I}$ exhibits enhanced metallic properties [12].

The proneness of quasi-one-dimensional conductors to experience a Peierls transition, resulting in a charge density wave (CDW) phase transition, adds complexity, leading to complex phase diagrams and novel quantum behaviors [13, 14]. Although theoretical models suggest that a true long-range order is unlikely in 1D systems [15], quasi-1D systems can still exhibit long-range superconducting and magnetic orders [16, 17]. The suppression of long-range order due to quantum and thermal fluctuations unveils unique physical phenomena such as phase slips [18–20], Cooper pair localization [17, 21, 22], and non-Fermi liquid behavior [23, 24]. For example, $(\mathrm{TaSe}_4)_2\mathrm{I}$ is known to host an exotic axionic CDW phase with strong electronic correlations [5, 8]. In addition, both $(\mathrm{TaSe}_4)_2\mathrm{I}$ [6, 25] and $(\mathrm{NbSe}_4)_2\mathrm{I}$ exhibit superconductivity under high pressure [26], with the latter predicted to follow a pressure-induced disorder mechanism. In superconductors, defects can cause pin vortices, which improves the stability and dynamics of the superconducting state [27]. In magnetic systems, these defects act as pinning centers for spin density waves (SDWs) and influence local magnetic interactions [28]. The interplay of superconductivity, magnetism, and CDWs, along with defects in these low-dimensional systems, offers a rich field for investigating new quantum states and phase transitions.

Experimental investigation into the quasi-one-dimensional compound $(\mathrm{TaSe}_4)_3\mathrm{I}$ (n-TSI) indicate that, upon cooling, the compound undergoes a long-range magnetic transition around 9 K, eventually attaining a superconducting ground state below 2.5 K, a coexistence typically deemed incompatible. As a plausible mechanism, supported by DFT calculations, we propose that Se_2 dimer vacancies play a crucial role in generating localized magnetic moments, which may drive the observed magnetism and enhance electronic properties. This study not only augments our understanding of the previously examined structural transition

but also elucidates the complex relationship between structural distortions and emergent quantum phenomena in *n*-TSI.

7.2 Computational Methodology

This chapter extends the first-principles approaches outlined in chapter 6, employing the VASP package with its plane-wave basis set [29, 30]. We continued to use the PBE exchange-correlation functional within the GGA approximation for accurate ground-state property calculations. Consistent with previous work, we applied an 8×8×4 Monkhorst-Pack k-point mesh and a 600 eV plane-wave cutoff to ensure reliable convergence of electronic properties for the pristine *n*-TSI structure.

In chapter 6, the focus was on comparing several basis sets (VASP, LAPW, and LMTO) to validate the semi-metallic solution. This chapter, however, employs the VASP and QUANTUM ESPRESSO (QE) software packages [31] for the analyses. To begin with, the Se_2 vacancy formation energy was calculated. To achieve this, a 3×3×1 supercell of $(TaSe_4)_3I$ was constructed, and convergence tests on the supercell size and k-point sampling were conducted to ensure accuracy in the defect calculations. Atomic positions were relaxed with a force convergence criterion of 0.01 eV/Å. The vacancy formation energy was determined by subtracting the total energy of the pristine structure from the sum of the energies of the structure containing the vacancy and the isolated defect [32].

Furthermore, we determined the superconducting transition temperature (T_c) of the low-temperature phase of *n*-TSI utilizing the anisotropic Eliashberg formalism [33, 34]. The effective Coulomb pseudopotential parameter (μ^*) was computed via the EPW (Electron-Phonon Wannier) code [35], which is integrated with density functional perturbation theory (DFPT) and maximally localized Wannier functions (MLWF) within the QE package [31]. Our computational simulations incorporated scalar-relativistic pseudopotentials with the PBE functional, utilizing a 4×4×2 k-point grid and an energy cutoff of 885 eV for the plane-wave basis. Dynamical matrices were computed using DFPT on a 2×2×1 q-point grid, and the electron-phonon coupling (EPC) constants were derived through Wannier interpolation employing the WANNIER90 library [36]. To achieve high numerical precision, electron-phonon matrix elements were calculated on dense 6×6×6 k and q grids.

7.3 Observations from Experimental Studies

This section summarizes the key experimental findings* based on which our theoretical work has been developed.

*Experimental observations are discussed in detail in the preprint [37]

7.3.1 Crystal Structure & Superconducting Transition

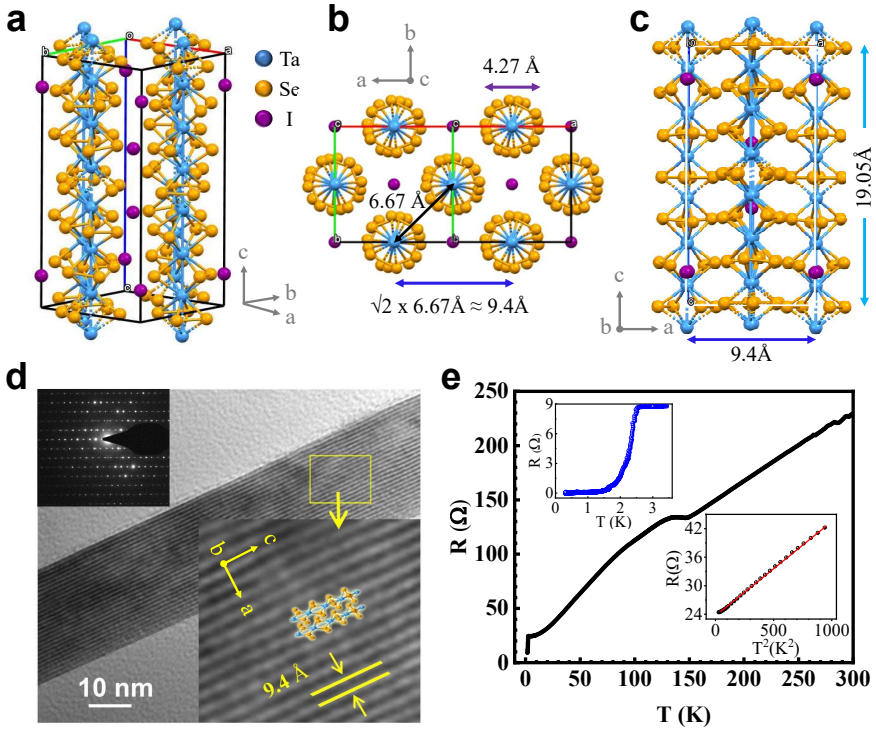

Figure 7.1: *Crystal structure & superconducting transition: (a) Oblique view of the simple tetragonal unit cell. (b) Projected view on the ab-plane. (c) Lateral view of the linear chains. (d) Quasi-1D structure as seen in high-resolution transmission electron microscopy (HRTEM). Upper inset: Selected area electron diffraction (SAED). Lower inset: Zoomed image showing an inter-chain separation of* ≈ 9.4 *Å. (e) Temperature dependence of resistance (R) measured using a conventional 4-probe method. The change in slope around 150 K signifies a charge density wave transition in n-TSI. Upper inset: Superconducting transition at zero magnetic field. Lower inset: Linear behavior of R* vs. T^2 *in the 5-25 K range, with zero magnetic field. Experimental observations are discussed in detail in the preprint [37].*

To contextualize our theoretical framework, key experimental results concerning *n*-TSI are outlined. Figure 7.1 depicts the crystal structure along with electrical transport measurements. The material is observed to crystallize within a tetragonal unit cell (space group $P\bar{4}2_1c$), characterized by lattice parameters $a = b = 9.4358(5)$Å and $c = 19.0464(11)$Å. High-resolution transmission electron microscopy identifies a linear $TaSe_4$ chain-like structure oriented along the *c*-axis, with inter-chain and intra-chain separations measured at 6.67Å and 4.27Å, respectively (Figure 7.1(a-d)).

Temperature-dependent resistivity measurements (Figure 7.1(e)) demonstrate metallic behavior down to low temperatures. The observed R vs. T^2 linearity in the 5-25 K range confirms Fermi liquid behavior. Notably, a resistivity slope change around 150 K corresponds to a structural phase transition from a centrosymmetric to a noncentrosymmetric

phase, as discussed in our previous theoretical work [12].

Crucially, below 2.5 K, the resistance exhibits a sharp decline, indicating a superconducting transition. Zero-resistance state is achieved below 1 K, confirming the intrinsic superconductivity of these quasi-one-dimensional crystals. Single-ribbon devices exhibit an even sharper zero-resistance transition, further supporting the material's intrinsic superconducting nature.

7.3.2 Ferromagnetism and Meissner Effect

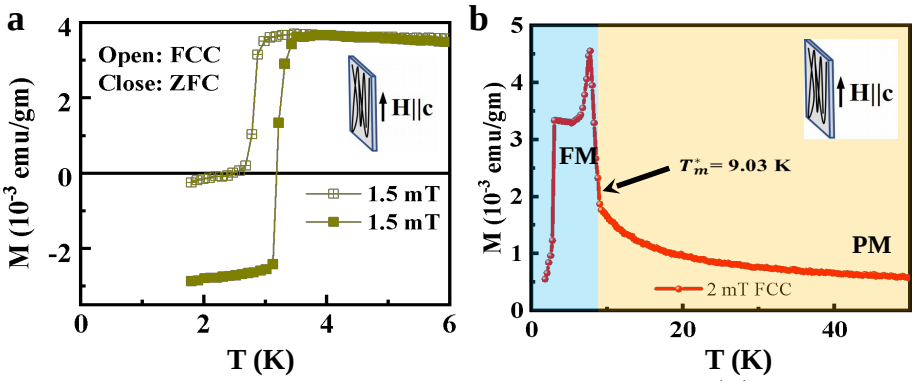

Figure 7.2: *(a) Temperature-dependent magnetization data at low field (1.5 mT), showing the Meissner effect below 3 K. (b) Field-cooled (FC) magnetization curve with $H \parallel c$ showing the paramagnetic-to-ferromagnetic phase transition in n-TSI. Experimental observations are further detailed in the preprint [37].*

Magnetization measurements reveal fascinating magnetic properties in *n*-TSI, providing essential insights for theoretical analysis. Key experimental observations are summarized in Figure 7.2.

Low-field magnetization measurements (Figure 7.2(a)) show a clear diamagnetic response below 3 K, which is a signature of the Meissner effect. This observation provides strong evidence for superconductivity. The superconducting volume fraction is estimated to be approximately 9%, confirming the existence of a superconducting ground state in this quasi-one-dimensional system.

Field-cooled (FC) magnetization measurements with the magnetic field applied parallel to the *c*-axis (Figure 7.2(b)) show a gradual increase in magnetization as the temperature decreases, peaking at around 9 K. This behavior is consistent with systems exhibiting helimagnetic order and suggests the presence of a ferromagnetic component. A Curie-Weiss analysis of the paramagnetic susceptibility gives a positive Curie-Weiss temperature ($T_{CW} \sim 5.5$ K), indicating dominant ferromagnetic interactions.

When the magnetic field is applied perpendicular to the *c*-axis, the magnetization decreases, and the magnetic transition becomes less distinct. Prominent hysteresis loops ob-

served across the superconducting transition temperature further highlight the anisotropy in both magnetic and superconducting properties. For details on these observations, refer to the preprint of the work [37].

These results provide compelling evidence for the coexistence of superconductivity and ferromagnetism in *n*-TSI, with significant anisotropy in their interplay. This unique combination of properties lays the foundation for further theoretical studies to explore the relationship between magnetic order and superconductivity in this material system.

7.4 Theoretical Caculation

The experimental observation of both superconductivity and weak ferromagnetism is intriguing, given the fact that recent first-principles studies [12, 38] on the pristine structure yield a non-magnetic, semi-conducting electronic structure with small gap $\sim$ 30 meV, as discussed in chapter 6. Thus to rationalize the experimental findings, we considered presence of chalcogen vacancies, which may form during the synthesis of the samples. It is worth mentioning at this point, that recently discovered magnetism in molybdenum dichalcogenides has been attributed to the presence of chalcogen vacancies [39, 40]. Considering the fact that the crystal structure of *n*-TSI hosts Ta atoms sandwiched between two Se_4 units with shorter side of the Se-Se bond of each Se_4 $\sim$ 2.35-2.36 Å, a typical distance for a $Se_2{}^{2-}$ dimer, in particular Se_2 dimer vacancy has been considered. This is further supported by the fact that the dimerization energy of the Se dimer in *n*-TSI structure was found to be -5.348 eV.

As shown in Figure 7.1, the crystal structure of *n*-TSI consists of parallel $TaSe_4$ chains separated by I atoms. In the low-temperature noncentrosymmetric structure, there are three inequivalent classes of Ta atoms, forming sequence of Ta-Ta bond lengths, characterized by –M-L-S-M-L–, commensurate with period three CDW (cf. Figure 7.3(a)). The S (short, 3.05 Å), M (medium, 3.12 Å), and L (long, 3.31 Å) bonds form between the Ta_1 and Ta_2, Ta_2 and Ta_3, and Ta_1 and Ta_3 atoms, respectively. Thus the $Se_2{}^{2-}$ dimer vacancy can be created either at coordination sites shared by Ta atoms that form S, or M, or L bonds. The formation energy of Se_2 dimer vacancies at these three possible locations was calculated (see the Computational Methodology section for computational details) considering a 3 $\times$ 3 $\times$ 1 supercell consisting of 576 atoms of $(TaSe_4)_3I$. The Se_2 dimer vacancy was placed on one of the 18 chains in the cell, resulting in a Se_2 dimer vacancy concentration of 0.46%. The Se_2 dimer vacancy was found to be preferentially formed on the L bond, followed by the M and S bonds with a vacancy formation energy of 3.47 eV on the L bond.

The calculated electronic structure of the compound containing the vacancy of the Se_2 dimer reveals two interesting aspects, i) the localized moments of $\sim$ 0.42-0.43 μ_B are

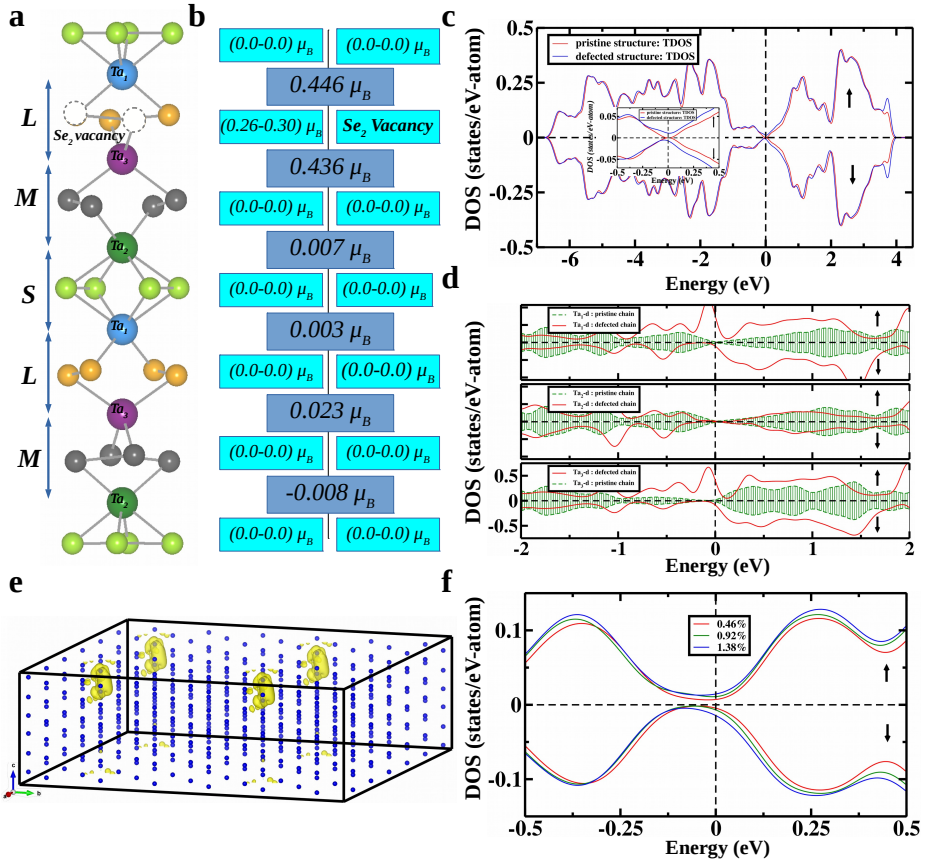

Figure 7.3: *First-principles Study: (a) The defected chain in $(TaSe_4)_3I$ with Se_2 dimer vacancy. Marked are the three inequivalent Ta atoms, Ta_1, Ta_2 and Ta_3, and the long (L), medium (M) and short (S) Ta-Ta bonds. (b) The calculated magnetic moment at the Ta and Se sites of the defected chain. The boxes correspond to Ta and Se layers, shown in (a). (c) The total density of states of the pristine (red) and vacancy bearing (blue) $(TaSe_4)_3I$, showing the semiconducting and metallic nature, respectively. The positive and negative y-axis correspond to density of states in up and down spin channels, respectively. The zero of the energy is set at Fermi level. The* inset *shows the zoomed plot. (d) The reconstructed density of states at Ta_1 (upper panel), Ta_2 (middle panel) and Ta_3 (bottom panel) sites of the defected chain in vacancy bearing structure (red) compared to that in the pristine structure (green dashed line with shading). (e) The plot of spin density in the vacancy bearing $(TaSe_4)_3I$. The isovalue in the plot is chosen as 0.0015 $1/\AA^3$. (f) The density of states of the undefected chains in vacancy bearing $(TaSe_4)_3I$ for increasing concentration of vacancy, 0.46% to 1.38%.*

formed at the Ta sites (Ta_1 and Ta_3) forming the L bond and hosting the Se_2 vacancy in their coordination. Appreciable local moments (0.26-0.30 μ_B) are also formed at the two Se sites of the neighboring Se_2 dimer which are oppositely aligned to each other, forming like a spin singlet (Figure 7.3(b). ii) The system becomes metallic with finite density of states at the Fermi level, as opposed to the small-gap semiconducting nature of the pristine compound (cf. Figure 7.3(c)). Thus, formation of Se_2 dimer vacancy, creates local moment as source of magnetism and makes the system metallic.

In the pristine compound, Ta is in the mixed valence state of 4.333+, which charge disproportionates into Ta_1 and Ta_2 in 4+ (d^1) nominal valence and Ta_3 in nominal 5+ (d^0) state. The resultant electronic structure shows a gap at the Fermi level due to the Peierls distortion of the trimerized structure, with occupied bonding states of Ta_1 and Ta_2, and unoccupied states of Ta_3, following the expectation of nominal valences. The introduction of a Se_2 vacancy with 0.46% concentration between the Ta_1 and Ta_3 holes dopes the system, making the average Ta valence 4.315+ instead of 4.333+ in the pristine structure. This hole doping makes the system metallic. The density of states projected to magnetic Ta_1 and Ta_3 sites in the vacancy bearing defected chain show major reconstruction compared to that in pristine compound, while that for Ta_2 remains more or less unaltered compared to the pristine compound (cf. Figure 7.3(d)).

The local moment formed around the Ta_1, Se-Se, Ta_3 unit, as evident in the spin density plot (cf. Figure 7.3(e)), magnetically interact with each other through the mobile conduction electron through the Ruderman-Kittel-Kasuya-Yosida (RKKY)-like exchange interaction. The total energies of the ferro-aperture (FM) and anti-ferromagnetic (AFM) alignment of the local moments between the defected chains are calculated considering $3 \times 6 \times 1$ supercell, containing two defected chains in the cell. The ferromagnetic configuration is found to be favored over the AFM configuration by an energy difference of ~ 0.55 meV (6.4 K), rationalizing the experimental observation of weak ferromagnetism.

Considering the observed low superconducting transition temperature, in the following we explore the phonon-mediated superconductivity. In this context we note the magnetic moment is highly localized at Ta and Se_2 dimer sites, adjacent to the vacant Se_2 dimer site. The undefected chains in the system, on the hand, remain nonmagnetic though metallic due to the hole doping effect. This is confirmed by the plot of the density of states contributed by the undefected chains in the vacancy-bearing compound, which shows the metallic, nonmagnetic nature (cf. Figure 7.3(f)). Interestingly, the density of states at Fermi level was found to increase upon increasing the vacancy concentration, as demonstrated by considering vacancy concentration of 0.46%, 0.92% and 1.38%.

To calculate the superconducting T_c arising from electron-phonon coupling mechanism, we determined the phonon spectra of *n*-TSI using first-principles DFPT theory (cf. Figure 7.4), and calculated the T_c from the modified McMillan formula[41]:

$$T_c = \frac{\omega_{log}}{1.2} \exp\left[\frac{-1.04(1+\lambda)}{\lambda - \mu^*(1+0.62\lambda)}\right]$$

where the dimensionless parameters λ and μ^* are coupling constants representing the electron-phonon interaction strength and effective coulomb pseudopotential, respectively.

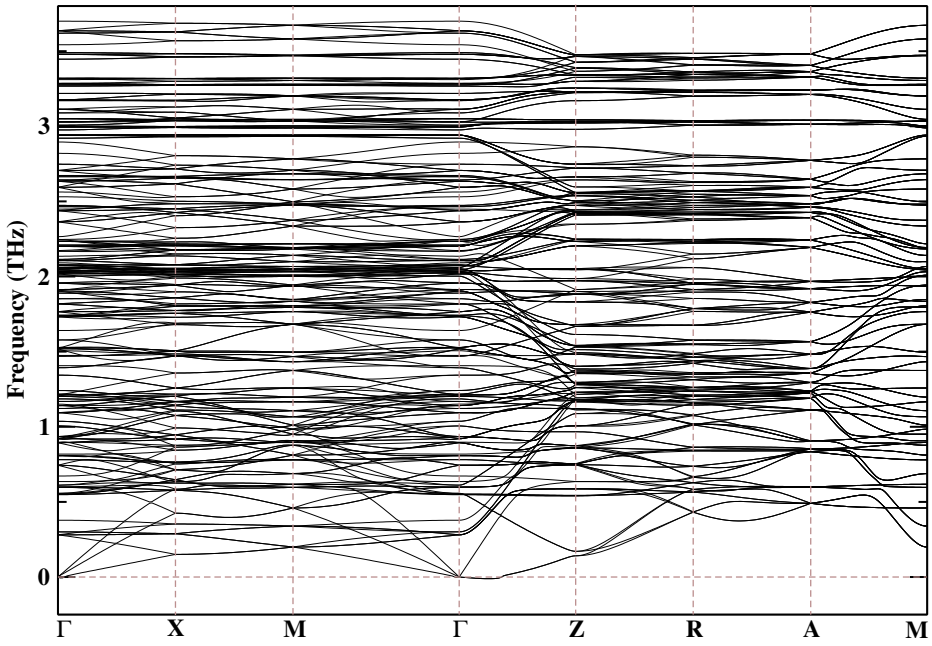

Figure 7.4: *Phonon band structure of pristine n-TSI at low temperature, plotted along the high-symmetry directions Γ-X-M-Γ-Z-R-A-M in the Brillouin zone. The absence of imaginary phonon frequencies across the Brillouin zone confirms the dynamic stability of the n-TSI structure, indicating that the lattice vibrations are stable and the crystal structure is robust under varying conditions.*

ω_{log} represents the logarithmically averaged phonon frequency, given by,

$$\omega_{log} = \exp\left[\frac{2}{\lambda}\int_0^\infty \frac{\alpha^2 F(\omega)}{\omega}\ln(\omega)d\omega\right]$$

The estimation of the Coulomb pseudopotential, μ^* from ab-initio calculations is difficult. However, for d-band metals, Bennemann and Garland [42] have proposed an estimation method that relates μ^* to the density of electronic states at the Fermi level $N(E_F)$, $\mu^* = \frac{0.26\times N(E_F)}{1+N(E_F)}$. Our estimate of μ^* for $(TaSe_4)_3$ I with a vacancy of 0.46% Se_2, considering the calculated value of $N(E_F)$ from undefected chains, turned out to be 0.11, which is in the range of 0.1-0.2 [43–45] commonly observed for BCS superconductors. Increasing the vacancy concentration to 0.92% and 1.38% μ^* is found to change slightly to 0.12, and 0.15 respectively, The calculated McMillan-Allen-Dynes superconducting transition temperature is found to be 2.04 K with 1.38% vacancy concentration which is in close agreement with the experimental observation of 2.5 K.

The theoretical analysis thus establishes that presence of Se_2 dimer vacancy may be a plausible means to give rise to weak magnetism through RKKY interaction between local moments formed at the vacancy bearing defected chains, while the metallic nature of hole doped electronic structure of undefected chains can support the phonon mediated superconductivity.

7.5 Summary and Conclusions

In conclusion, electrical and magnetization measurements on single crystals of the quasi-one-dimensional compound *n*-TSI reveal the coexistence of metallicity, weak ferromagnetism below 9 K, and superconductivity below 2.5 K. These experimental observations stand in contrast to first-principles calculations, which predict a semiconducting electronic structure for pristine $(TaSe_4)_3I$, indicating that defects may play a critical role in driving the material's unusual properties.

Our first-principles DFT calculations confirm that the formation of Se_2 dimer vacancies can induce metallic behavior, consistent with the observed transport measurements. Additionally, these vacancies create localized magnetic moments, which contribute to the weak ferromagnetism through the Ruderman–Kittel–Kasuya–Yosida (RKKY) exchange mechanism mediated by itinerant electrons. The vacancy-induced phase separation is characterized by magnetism originating from vacancy-bearing chains, while the vacancy-free chains remain nonmagnetic but metallic, thereby supporting phonon-mediated superconductivity.

This electronic phase separation leads to a complex ground state where the interaction between disorder, low-dimensionality, and unique electronic structure governs the material's properties. Our calculated ferromagnetic and superconducting transition temperatures, based on an assumed vacancy concentration of 1.38%, match with experimental values, further validating the theoretical model. This study highlights the importance of defect-induced phenomena in *n*-TSI and motivates further investigation into similar systems, which provide an ideal platform for exploring the interplay of magnetism, superconductivity, and low-dimensional electronic structures.

Bibliography

[1] P. Gressier, A. Meerschaut, L. Guemas, J. Rouxel, and P. Monceau. Characterization of the new series of quasi one-dimensional compounds(mx4)ny (m =nb, ta; x =s, se; y =br, i). *Journal of Solid State Chemistry*, 51(2):141–151, 1984.

[2] C Roucau, R Ayroles, P Gressier, and A Meerschaut. Electron microscopy study of transition-metal tetrachalcogenide (mse4)ni (m=nb, ta). *Journal of Physics C: Solid State Physics*, 17(17):2993, jun 1984.

[3] Pascal Gressier, Myung Hwan Whangbo, Alain Meerschaut, and Jean Rouxel. Electronic structures of transition-metal tetrachalcogenides (mse4)ni (m = nb, ta). *Inorg. Chem.*, 23(9):1221–1228, April 1984.

[4] Tomoyuki Sekine and Mitsuru Izumi. Successive phase transitions in the linear-chain semiconductor $(nbse_4)_3I$ studied by raman scattering and electrical resistivity. *Phys. Rev. B*, 38:2012–2020, Jul 1988.

[5] Wujun Shi, Benjamin J. Wieder, Holger L. Meyerheim, Yan Sun, Yang Zhang, Yiwei Li, Lei Shen, Yanpeng Qi, Lexian Yang, Jagannath Jena, Peter Werner, Klaus Koepernik, Stuart Parkin, Yulin Chen, Claudia Felser, B. Andrei Bernevig, and Zhijun Wang. A charge-density-wave topological semimetal. *Nature Physics*, 17(3):381–387, 2021.

[6] Chao An, Yonghui Zhou, Chunhua Chen, Fucong Fei, Fengqi Song, Changyong Park, Jianhui Zhou, Horst-Günter Rubahn, Victor V. Moshchalkov, Xuliang Chen, Gufei Zhang, and Zhaorong Yang. Long-range ordered amorphous atomic chains as building blocks of a superconducting quasi-one-dimensional crystal. *Advanced Materials*, 32(38):2002352, 2020.

[7] Yang Zhang, Ling-Fang Lin, Adriana Moreo, Shuai Dong, and Elbio Dagotto. First-principles study of the low-temperature charge density wave phase in the quasi-one-dimensional weyl chiral compound $(tase_4)_2I$. *Phys. Rev. B*, 101:174106, May 2020.

[8] J. Gooth, B. Bradlyn, S. Honnali, C. Schindler, N. Kumar, J. Noky, Y. Qi, C. Shekhar, Y. Sun, Z. Wang, B. A. Bernevig, and C. Felser. Axionic charge-density wave in the weyl semimetal (tase4)2i. *Nature*, 575(7782):315–319, November 2019.

[9] C. Tournier-Colletta, L. Moreschini, G. Autès, S. Moser, A. Crepaldi, H. Berger, A. L. Walter, K. S. Kim, A. Bostwick, P. Monceau, E. Rotenberg, O. V. Yazyev, and M. Grioni. Electronic instability in a zero-gap semiconductor: The charge-density wave in $(tase_4)_2\mathbf{I}$. *Phys. Rev. Lett.*, 110:236401, Jun 2013.

[10] V. Vescoli, F. Zwick, J. Voit, H. Berger, M. Zacchigna, L. Degiorgi, M. Grioni, and G. Grüner. Dynamical properties of the one-dimensional band insulator $(\mathrm{nbse}_4)_3 i$. *Phys. Rev. Lett.*, 84:1272–1275, Feb 2000.

[11] Sk Kalimuddin, Sudipta Chatterjee, Arnab Bera, Hasan Afzal, Satyabrata Bera, Deep Singha Roy, Soham Das, Tuhin Debnath, Bhavtosh Bansal, and Mintu Mondal. Exceptionally slow, long-range, and non-gaussian critical fluctuations dominate the charge density wave transition. *Phys. Rev. Lett.*, 132:266504, Jun 2024.

[12] Arnab Bera, Samir Rom, Suman Kalyan Pradhan, Satyabrata Bera, Sk Kalimuddin, Tanusri Saha-Dasgupta, and Mintu Mondal. Centrosymmetric-noncentrosymmetric structural phase transition in the quasi-one-dimensional compound $(\mathrm{TaSe}_4)_3\mathrm{I}$. *Phys. Rev. B*, 108:035112, Jul 2023.

[13] F.J. Di Salvo J.A. Wilson and S. Mahajan. Charge-density waves and superlattices in the metallic layered transition metal dichalcogenides. *Advances in Physics*, 24(2):117–201, 1975.

[14] Arnab Majumdar, Derrick VanGennep, Jérémy Brisbois, Dmitriy Chareev, Andrey V. Sadakov, A. S. Usoltsev, Masaki Mito, Alejandro V. Silhanek, Tapati Sarkar, Abdelwahab Hassan, Olof Karis, Rajeev Ahuja, and Mahmoud Abdel-Hafiez. Interplay of charge density wave and multiband superconductivity in layered quasi-two-dimensional materials: The case of $2\mathrm{H}-\mathrm{Nbs}_2$ and $2\mathrm{H}-\mathrm{Nbse}_2$. *Phys. Rev. Mater.*, 4:084005, Aug 2020.

[15] N. D. Mermin and H. Wagner. Absence of ferromagnetism or antiferromagnetism in one- or two-dimensional isotropic heisenberg models. *Phys. Rev. Lett.*, 17:1133–1136, Nov 1966.

[16] N. Giordano. Evidence for macroscopic quantum tunneling in one-dimensional superconductors. *Phys. Rev. Lett.*, 61:2137–2140, Oct 1988.

[17] H. P. Büchler, V. B. Geshkenbein, and G. Blatter. Quantum fluctuations in thin superconducting wires of finite length. *Phys. Rev. Lett.*, 92:067007, Feb 2004.

[18] C. N. Lau, N. Markovic, M. Bockrath, A. Bezryadin, and M. Tinkham. Quantum phase slips in superconducting nanowires. *Phys. Rev. Lett.*, 87:217003, Nov 2001.

[19] J. E. Mooij and Yu. V. Nazarov. Superconducting nanowires as quantum phase-slip junctions. *Nature Physics*, 2(3):169–172, 2006.

[20] I. M. Pop, I. Protopopov, F. Lecocq, Z. Peng, B. Pannetier, O. Buisson, and W. Guichard. Measurement of the effect of quantum phase slips in a josephson junction chain. *Nature Physics*, 6(8):589–592, 2010.

[21] A.M. eds Goldman and S.A. Wolf. Percolation, localization, and superconductivity. *NATO Science Series, Plenum Press, New York*, 1984.

[22] A. T. Bollinger, R. C. Dinsmore, A. Rogachev, and A. Bezryadin. Determination of the superconductor-insulator phase diagram for one-dimensional wires. *Phys. Rev. Lett.*, 101:227003, Nov 2008.

[23] Samuel Lederer, Yoni Schattner, Erez Berg, and Steven A. Kivelson. Superconductivity and non-fermi liquid behavior near a nematic quantum critical point. *Proceedings of the National Academy of Sciences*, 114(19):4905–4910, 2017.

[24] Ipsita Mandal. Superconducting instability in non-fermi liquids. *Phys. Rev. B*, 94:115138, Sep 2016.

[25] Qing-Ge Mu, Dennis Nenno, Yan-Peng Qi, Feng-Ren Fan, Cuiying Pei, Moaz ElGhazali, Johannes Gooth, Claudia Felser, Prineha Narang, and Sergey Medvedev. Suppression of axionic charge density wave and onset of superconductivity in the chiral weyl semimetal Ta_2Se_8I. *Phys. Rev. Mater.*, 5:084201, Aug 2021.

[26] C. Pei, W. Shi, Y. Zhao, L. Gao, J. Gao, Y. Li, H. Zhu, Q. Zhang, N. Yu, C. Li, W. Cao, S.A. Medvedev, C. Felser, B. Yan, Z. Liu, Y. Chen, Z. Wang, and Y. Qi. Pressure-induced a partial disorder and superconductivity in quasi-one-dimensional weyl semimetal (nbse4)2i. *Materials Today Physics*, 21:100509, 2021.

[27] A. P. Petrović, D. Ansermet, D. Chernyshov, M. Hoesch, D. Salloum, P. Gougeon, M. Potel, L. Boeri, and C. Panagopoulos. A disorder-enhanced quasi-one-dimensional superconductor. *Nature Communications*, 7(1):12262, 2016.

[28] I. Tüttö and A. Zawadowski. Theory of pinning of a spin-density wave by nonmagnetic impurities. *Phys. Rev. Lett.*, 60:1442–1445, Apr 1988.

[29] G. Kresse and J. Hafner. Ab initio molecular dynamics for liquid metals. *Phys. Rev. B*, 47:558–561, Jan 1993.

[30] G. Kresse and J. Furthmüller. Efficient iterative schemes for ab initio total-energy calculations using a plane-wave basis set. *Phys. Rev. B*, 54:11169–11186, Oct 1996.

[31] P. Giannozzi, S. Baroni, N. Bonini, M. Calandra, R. Car, C. Cavazzoni, D. Ceresoli, G. L. Chiarotti, M. Cococcioni, I. Dabo, A. Dal Corso, S. de Gironcoli, S. Fabris, G. Fratesi, R. Gebauer, U. Gerstmann, C. Gougoussis, A. Kokalj, M. Lazzeri, L. Martin-Samos, N. Marzari, F. Mauri, R. Mazzarello, S. Paolini, A. Pasquarello, L. Paulatto, C. Sbraccia, S. Scandolo, G. Sclauzero, A. P. Seitsonen, A. Smogunov, P. Umari, and R. M. Wentzcovitch. Quantum espresso: A modular and open-source software project for quantum simulations of materials. *Journal of Physics: Condensed Matter*, 21(39):395502, September 2009.

[32] S. Chatterjee, T. Saha-Dasgupta, and S. Sengupta. Visualizing frozen point defect tracks in fe-containing olivines. *Europhysics Letters*, 98(2):29001, apr 2012.

[33] A. B. Migdal. Interaction between electrons and lattice vibrations in a normal metal. *Soviet Physics JETP*, 7:996, 1958.

[34] G. M. Eliashberg. Interactions between electrons and lattice vibrations in a superconductor. *Soviet Physics JETP*, 11:696, 1960.

[35] S. Poncé, E.R. Margine, C. Verdi, and F. Giustino. Epw: Electron–phonon coupling, transport and superconducting properties using maximally localized wannier functions. *Computer Physics Communications*, 209:116–133, 2016.

[36] Giovanni Pizzi, Valerio Vitale, Ryotaro Arita, Stefan Blügel, Frank Freimuth, Guillaume Géranton, Marco Gibertini, Dominik Gresch, Charles Johnson, Takashi Koretsune, Julen Ibañez-Azpiroz, Hyungjun Lee, Jae-Mo Lihm, Daniel Marchand, Antimo Marrazzo, Yuriy Mokrousov, Jamal I Mustafa, Yoshiro Nohara, Yusuke Nomura, Lorenzo Paulatto, Samuel Poncé, Thomas Ponweiser, Junfeng Qiao, Florian Thöle, Stepan S Tsirkin, Małgorzata Wierzbowska, Nicola Marzari, David Vanderbilt, Ivo Souza, Arash A Mostofi, and Jonathan R Yates. Wannier90 as a community code: new features and applications. *Journal of Physics: Condensed Matter*, 32(16):165902, jan 2020.

[37] Arnab Bera, Sirshendu Gayen, Suchanda Mondal, Riju Pal, Buddhadeb Pal, Aastha Vasdev, Sandeep Howlader, Manish Jana, Tanmay Maiti, Rafikul Ali Saha, Biswajit Das, Biswarup Satpati, Atindra Nath Pal, Prabhat Mandal, Goutam Sheet, and Mintu Mondal. Superconductivity coexisting with ferromagnetism in a quasi-one-dimensional non-centrosymmetric $(tase_4)_3i$. *arXiv preprint*, 2111, Nov 2021.

[38] Irián Sánchez-Ramírez, Maia G. Vergniory, Claudia Felser, and Fernando de Juan. Band structures of $(nbse_4)_3I$ and $(tase_4)_3I$: Reconciling transport, optics, and angle-resolved photoemission spectroscopy. *Phys. Rev. B*, 107:205109, May 2023.

[39] Z. Guguchia, A. Kerelsky, D. Edelberg, S. Banerjee, F. von Rohr, D. Scullion, M. Augustin, M. Scully, D. A. Rhodes, Z. Shermadini, H. Luetkens, A. Shengelaya, C. Baines, E. Morenzoni, A. Amato, J. C. Hone, R. Khasanov, S. J. L. Billinge, E. Santos, A. N. Pasupathy, and Y. J. Uemura. Magnetism in semiconducting molybdenum dichalcogenides. *Science Advances*, 4(12):eaat3672, 2018.

[40] Bin Chen, Hasan Sahin, Aslihan Suslu, Laura Ding, Mariana I. Bertoni, F. M. Peeters, and Sefaattin Tongay. Environmental changes in mote2 excitonic dynamics by defects-activated molecular interaction. *ACS Nano*, 9(5):5326–5332, May 2015.

[41] P. B. Allen and R. C. Dynes. Transition temperature of strong-coupled superconductors reanalyzed. *Phys. Rev. B*, 12:905–922, Aug 1975.

[42] K. H. Bennemann and J. W. Garland. Theory for Superconductivity in d-Band Metals. *AIP Conference Proceedings*, 4(1):103–137, 02 1972.

[43] E. R. Margine and F. Giustino. Anisotropic migdal-eliashberg theory using wannier functions. *Phys. Rev. B*, 87:024505, Jan 2013.

[44] J. M. An and W. E. Pickett. Superconductivity of mgb_2: Covalent bonds driven metallic. *Phys. Rev. Lett.*, 86:4366–4369, May 2001.

[45] Mohammad Aslam, Chandan K Singh, Shekhar Das, Ritesh Kumar, Soumya Datta, Soumyadip Halder, Sirshendu Gayen, Mukul Kabir, and Goutam Sheet. Large enhancement of superconductivity in zr point contacts. *Journal of Physics: Condensed Matter*, 30(25):255002, jun 2018.

8

Summary and Outlook

8.1 Summary

In this thesis, we have investigated the electronic, magnetic, and topological properties of technologically significant materials using first-principles methods, focusing on Ce-based rare-earth lean permanent magnets, oxide perovskite heterostructures, and the quasi-one-dimensional compound $(TaSe_4)_3I$. Our study addresses critical challenges such as reducing the reliance on rare-earth elements, understanding interfacial phenomena in oxide heterostructures, and exploring novel quantum phenomena in low-dimensional materials. By employing a combination of density functional theory (DFT) and machine learning, we have predicted promising magnetic properties in $Ce_2Fe_{17-x}Co_xCN$ compounds, identified trends in interfacial charge transfer and anomalous Hall conductivity in $LaBO_3/SrIrO_3$ superlattices, and revealed the microscopic origin of a unique structural phase transition, vacancy-induced magnetism, and phononic superconductivity in $(TaSe_4)_3I$. These findings pave the way for future experimental and theoretical investigations. In this chapter, we summarize the main conclusions of our study and discuss potential directions for further research.

8.1.1 Chapter 3 : Prediction of the Properties of the Rare-Earth Magnets $Ce_2Fe_{17-x}Co_xCN$: A Combined Machine-Learning and Ab Initio Study

In this chapter, we have explored the potential of Ce-based 2:17 rare-earth transition-metal carbonitrides as cost-effective alternatives to existing permanent magnets. A combination

of machine learning, based on experimental data, and first-principles calculations has been employed. The main findings are:

- Machine Learning based regression model predicts $T_c > 600\,\mathrm{K}$, while classification models indicate $\mu_0 M_s > 1\,\mathrm{T}$ and $K_u > 0$ for $Ce_2Fe_{17-x}Co_xCN$ ($x = 1, \ldots, 7$).
- First-principles calculations confirm $\mu_0 M_s > 1.65\,\mathrm{T}$ and $K_u \geq 1\,\mathrm{MJ/m^3}$ at $T = 0\,\mathrm{K}$, with $Ce_2Fe_{17-x}Co_xCN$ ($x = 2, 5, 6, 7$) compositions showing comparable to $Nd_2Fe_{14}B$.
- Figures of merit for $(BH)_{\max}$ and H_a are in the range of 444–540 kJ/m^3 and approximately 1–14 T, respectively.
- Thermal stability, a key limitation for 2:17 magnets, is enhanced through carbon-nitrogen codoping, which raises vacancy formation energies by 35–40%, mitigating high-temperature degradation.
- The estimated price-to-performance ratio (0.03–0.22 USD/J) underscores the economic viability of these compounds.

This study highlights the promise of Ce-based carbonitrides as high-performance, thermally stable, and cost-effective permanent magnets, motivating future experimental validations.

8.1.2 Chapter 4 : Magnetism and Unconventional Topology in $LaCoO_3$/ $SrIrO_3$ Heterostructure

In this chapter, we have presented a first-principles investigation of the $LaCoO_3/SrIrO_3$ (LCO/SIO) heterostructure, providing microscopic insights into its counterintuitive ferromagnetism and topological properties. The main findings are:

- Interfacial charge transfer reduces the nominal valence of Co from 3+ to 2+, stabilizing an intermediate spin (IS) state for Co, which drives robust ferromagnetic exchange interactions. This contrasts with the non-magnetic low-spin (LS) state observed in bulk $LaCoO_3$.
- Strong ferromagnetic exchange interactions in the Co layer induce long-range ferromagnetic order in the SIO layer through Co–Ir interfacial ferromagnetic coupling, emphasizing the critical role of LCO in stabilizing magnetism in the heterostructure.
- The ferromagnetic, tetragonal $SrIrO_3$, constrained by the STO substrate, hosts charge-2 Dirac points, driven by orbital degeneracy, revealing intriguing topological properties.

- The results provide a microscopic explanation for the anomalous Hall effect (AHE) observed in experiments and highlight the potential of LCO/SIO as a platform for exploring novel quasiparticles beyond the conventional Dirac and Weyl points.

This study highlights the understanding of interfacial magnetism and topological phenomena within LCO/SIO heterostructure, simultaneously uncovering potential novel phases.

8.1.3 Chapter 5 : Trend in Interfacial Charge Transfer, Emergent Electronic and Magnetic Structure and Topological Properties in the 3d, 5d Superlattices $LaBO_3/SrIrO_3$ (B = Mn, Fe, Co, Ni)

In this chapter, we extend our investigation into the $LaCoO_3$(LCO)/$SrIrO_3$(SIO) system, presented in Chapter 4. Motivated by the experimental synthesis of $3d$,$5d$ superlattices $LaBO_3/SrIrO_3$ (LBO/SIO) with B = Mn, Fe, Co, Ni, we have theoretically studied these systems to uncover trends across the $3d$ transition metal (TM) series. Our key findings are:

- The polarity of the interface and the chemistry of the B-site cation significantly influence the interfacial properties.
  - For p-type interfaces, all superlattices exhibit identical interfacial charge transfer towards the SIO block.
  - For n-type interfaces, charge transfer occurs towards the LBO block for B = Ni and Co (with d occupancy greater than Ir^{4+} in SIO), while the transfer is reversed for B = Mn and Fe (with d occupancy equal or smaller than Ir^{4+}).
- The tetragonal SIO block exhibits varying degrees of ferromagnetism (FM) based on the interface type and B-site chemistry:
  - Strong FM for both n-type and p-type LCO/SIO, LNO/SIO, and p-type LMO/SIO.
  - Weak FM for p-type LFO/SIO.
  - Nearly non-magnetic for n-type LMO/SIO and LFO/SIO.
- An insulating interface is predicted for the n-type LFO/SIO superlattice, driven by charge transfer effects.
- Magnetic SIO in the LBO/SIO superlattice hosts $C = \pm 2$ double Weyl crossings, driving an intrinsic anomalous Hall conductivity (AHC) of 7-8 Ω^{-1} cm^{-1} for n-type and p-type LCO/SIO, LNO/SIO, and p-type LMO/SIO. Suppressed intrinsic AHC is expected for LFO/SIO due to weakened FM Ir–Ir interactions.

Our study not only provides theoretical insight into the trends observed in these 3d,5d superlattices but also aligns with recent experimental measurements, offering valuable guidance for future experiments aimed at exploring and utilizing these intriguing systems.

8.1.4 Chapter 6 : Centrosymmetric-noncentrosymmetric Structural Phase Transition in the Quasi-one-dimensional Compound $(TaSe_4)_3I$

In this chapter, we investigated the structural phase transition in $(TaSe_4)_3I$ around the transition temperature $T_s \sim 145$ K using single-crystal X-ray diffraction (XRD) data, supported by resistivity, specific heat, and Raman scattering experiments. The key findings are:

- The structural transition is characterized by a symmetry-lowering change in the Ta chains, transitioning from an L-L-S sequence of Ta–Ta bonds in the high-temperature (HT) phase to an L-M-S sequence in the low-temperature (LT) phase.
- This transition breaks the center of inversion at the short Ta–Ta bond, leading to a centrosymmetric-to-noncentrosymmetric transition within the same tetragonal symmetry.

To uncover the origin of this transition, we performed first-principles density functional theory (DFT) calculations and tight-binding modeling:

- Both HT and LT structures exhibit semi-metallic behavior, consistent with experimental reports.
- The centrosymmetric-to-noncentrosymmetric transition is driven by the balance between Hybridization energy gain and Elastic energy loss. The hybridization energy gain dominates, stabilizing the LT structure at low temperatures.
- The temperature scale for the transition estimated from our model aligns well with experimental observations.

This study highlights the centrosymmetric-to-noncentrosymmetric structural phase transition, which extends beyond the well-studied charge-density-wave transitions, unveiling a novel type of structural phase transition in this class of chain compounds.

8.1.5 Chapter 7 : Observation of superconductivity and Weak Ferromagnetism in Quasi-1D Chain Compound, $(TaSe_4)_3I$ at Ambient Pressure

In this chapter, we extend our investigation into the quasi-one-dimensional compound $(TaSe_4)_3I$ (*n*-TSI). Through a combination of experimental and theoretical approaches, we reveal the

presence of metallicity, weak ferromagnetism and superconductivity in single crystals of the *n*-TSI compound. The main findings are:

- **Experimental Observations:**
  - Metallic behavior is observed in transport measurements.
  - Weak ferromagnetism appears below 9 K.
  - Superconductivity emerges below 2.5 K.

  These observations deviate from first-principles predictions of a semiconducting ground state for pristine $(TaSe_4)_3I$, suggesting the crucial role of defects in shaping the material's unusual properties.

- **Theoretical Insights:**
  - First-principles DFT calculations reveal that Se_2 dimer vacancies induce metallicity, consistent with experimental transport measurements.
  - These vacancies generate localized magnetic moments that mediate weak ferromagnetism via the Ruderman–Kittel–Kasuya–Yosida (RKKY) exchange mechanism.
  - Phase separation induced by vacancies results in vacancy-bearing chains contributing to magnetism, while vacancy-free chains remain nonmagnetic and metallic, enabling phonon-mediated superconductivity.
  - Calculated ferromagnetic and superconducting transition temperatures, assuming a vacancy concentration of 1.38%, align with experimental values, further supporting the theoretical model.

This study highlights how disorder, low dimensionality, and unique electronic structures in *n*-TSI shape its complex ground state, emphasizing defect-induced phenomena and inspiring further exploration of similar systems to investigate the interplay of magnetism, superconductivity, and low-dimensional electronic behaviors.

8.2 Outlook

1. In Chapter 3, we predicted several rare-earth lean permanent magnets, particularly $Ce_2Fe_{17-x}Co_xCN$ compounds, using a combination of machine learning and first-principles calculations. This work opens several exciting avenues for future research.

   The predicted magnetic properties, such as high Curie temperature, large saturation magnetization, and strong magnetocrystalline anisotropy, suggest that these materials

could be excellent candidates for practical applications. Experimental synthesis and characterization of $Ce_2Fe_{17-x}Co_xCN$ compounds are essential to validate these theoretical predictions and to uncover any additional properties not captured by computational models. Collaborations with industries that rely on permanent magnets-such as renewable energy, automotive, and electronics-can help in tailoring these materials to specific needs.

The observed improvement in thermal stability through carbon-nitrogen codoping suggests the potential for exploring other combinations of interstitial dopants. Studying different dopant concentrations and alternative elements could lead to further enhancements in thermal stability and magnetic performance.

Another promising direction is extending the study to entirely rare-earth-free systems that share similar structural and magnetic characteristics. This could identify new candidates for high-performance, sustainable permanent magnets.

However, some key aspects still need to be addressed before these materials can be applied. For instance, the mechanical stability of these compounds was not studied in this work. Investigating their mechanical properties will be crucial for understanding their durability in real-world applications. Additionally, the calculation of anisotropy field (H_a) depends on specific mechanisms, and these should be studied and improved further to refine predictions.

These directions opens up possibilities for the discovery and application of sustainable, high-performance permanent magnets.

2. Building on the insights from Chapters 4 and 5, where we explored the interplay of magnetism, topology, and interfacial phenomena in $3d$-$5d$ superlattice systems $LaBO_3/SrIrO_3$ (B = Mn, Fe, Co, Ni), there are several directions for future research to expand our understanding and applications of these materials.

   One promising avenue is the use of external electric fields to tune magnetic and topological properties. For example, studying the anomalous Hall effect at $3d$-$5d$ interfaces under gating conditions could reveal mechanisms for controlling Berry curvature. This control is essential for the design of spintronic devices, where electric field manipulation of magnetic and topological properties could enable energy-efficient and multifunctional device operations.

   In this project, we primarily focused on superlattices of either n-type or p-type interfaces. However, other geometries, such as mixed n and p-type interfaces or thin film-substrate structures, remain unexplored. Studying these mixed geometries could provide new insights into the interplay of charge transfer, spin alignment, and mag-

netic coupling. Such investigations may lead to the discovery of novel phenomena and functionalities in these systems.

3. Building on the findings of defect-induced magnetism and superconductivity in $(TaSe_4)_3I$ (*n*-TSI) from Chapters 6 and 7, there are several exciting directions for future research to deepen our understanding of this material and its potential applications.

   One key focus could be on probing the unconventional superconductivity with possible topological implications in this noncentrosymmetric structure. The combination of defect-induced weak magnetism, superconductivity, and inversion symmetry breaking in *n*-TSI creates a unique platform for exploring topological features. This interplay could lead to the discovery of exotic quantum phenomena, such as topological superconductivity, Weyl fermions, and Majorana modes. These phenomena are heavily influenced by spin-orbit coupling and the material's distinctive electronic structure. Additionally, the electronic phase separation proposed in theoretical studies of *n*-TSI requires experimental validation.

   These investigations could unveil exciting quantum phenomena and help design new technologies, such as quantum computing components and advanced spintronic devices, that leverage the material's unique properties.